Surface Characterisation of Contact Materials for Thin Film CdTe Solar Cells

Thesis submitted in accordance with the
requirements of the University of Liverpool for
the degree of
Doctor in Philosophy by

David Hesp

January 2015

Abstract

Surface Characterisation of Contact Materials for Thin Film CdTe Solar Cells

David Hesp

The deposition of tellurium onto the low index faces of copper single crystals induces a range of structures such as the $(2\sqrt{3}\times2\sqrt{3})$R30° surface substitutional alloy on the Cu(111) surface. These structures have been studied using a combination of scanning tunnelling microscopy (STM), low energy electron diffraction (LEED), X-ray photoemission (XPS) and ultraviolet photoemission (UPS).

The deposition of tellurium on to the Cu(111) surface produced several structures including $(2\sqrt{3}\times2\sqrt{3})$R30° phase for a coverage of 0.17ML, For a coverage of 0.33ML a $(\sqrt{3}\times\sqrt{3})$R30° surface alloy was found. For coverages greater than 0.66ML a bulk alloy was formed which is consistent with the Cu_3Te_2 phase. The deposition of tellurium onto the Cu(110) surface produced a c(2×2) structure for a coverage of 0.5ML. Further deposition causes uniaxial compression of the over-layer as indicated by the LEED patterns. STM of this surface revealed two hexagonal domains rotated 30° with respect to each other.

The deposition of tellurium on to the Cu(100) surface produced a p(2×2) over–layer for a coverage of 0.25ML. Further deposition lead to a series of coincidence lattices showing co-existing structures including split c(2×2) spots in the LEED pattern. A heavily streaked split c(2×2) LEED pattern was observed for tellurium coverages over 1ML dosage where STM images revealed a heavily striped surface with two domains perpendicular to each other. The larger structures observed suggest 3D growth of these stripes. On all 3 surfaces the work function was found to increase upon tellurium deposition.

The electronic structure of indium oxide thin films was investigated after different treatments in ultra high vacuum using XPS and UPS. The (111) surface was investigated using a combination of hard and soft X-rays showing the lower portion of the valence band to be dominated by oxygen orbitals while the higher portion of the valence band indium orbitals. The valence band was then probed and the work function measured after different annealing treatments. For all 3 samples, (111) (110) and (100) the work function was found to increase when annealing in oxygen when compared to annealing in vacuum. This is attributed to the movement of the Fermi level as the carrier concentration at the surface is altered. The lowering of observed gap states when annealing in oxygen also suggests they may originate from oxygen vacancies within the surface.

Acknowledgements

I would like to thank my supervisors Dr. Vinod Dhanak and Prof. Christopher Lucas for all their help and support throughout my time as a research student. Special thanks to my colleagues on the publications including Katariina Pussi and her co-workers for their LEED I-V and DFT analysis.

I would like to thank Ian Mcleod for all his help and discussions in the lab during my studies. I would also like to thank any other colleagues within the Surface Science Centre and the Stephenson Institute for Renewable Energy who have helped me along the way.

Finally I would like to thank my family, my Mum and Dad for supporting me throughout my studies and Kat for doing all the things she does.

Author's contribution in collaborative work

Chapter 3

M.O. King, I.M. McLeod, D. Hesp, V.R. Dhanak, M. Kadodwala, D.A. MacLaren, "Growth and alloying of thin film Te on Cu(111)" Surface Science 606 (2012) p. 1353. D. Hesp, I.M. McLeod and M.O. King collected and analysed the experimental data. All authors were involved in the discussion of the findings. M.O. King authored the paper.

M. Lahti, A. Chaudhuri, K. Pussi, D. Hesp, I.M. McLeod, V.R. Dhanak, M.O. King, M. Kadodwala, D.A MacLaren. "The structural analysis of Cu(111)−Te($\sqrt{3}$×$\sqrt{3}$)R30° and (2$\sqrt{3}$×2$\sqrt{3}$)R30° surface phases by quantitative LEED and DFT" Surface Science 622 (2014) p. 35. D. Hesp, I.M. McLeod and M.O. King collected and analysed the experimental data. M. Lahti, A. Chaudhuri, K. Pussi performed the LEED IV and DFT calculations. All authors were involved in the discussion of the findings. K. Pussi authored the paper.

Chapter 4

The work in chapter 4 was carried out in collaboration with D. Martin.

Chapter 6

The samples and discussion were provided by K.H.L. Zhang.

Contents

Chapter 1

Introduction

Renewable energy is a hot topic for many reasons: dwindling fossil fuel supplies, global warming as a result of increasing greenhouse gases from burning these fossil fuels and reducing our carbon footprint. This along with the fact that many of our lifestyles increasingly revolve around the use of electricity and that the population of the Earth is increasing, means the energy demands of the human race will continue to climb. This has led to much research been done to find ways to generate a clean abundant source of energy. The aim is to also generate energy in a way that does not harm our environment, as we are aware our ecosystem is a delicate one and so we do not wish to perturb it to the point where it becomes inhabitable. There are many forms of renewable energy, solar, wind, geothermal, tides, hydroelectric and biofuels. The future energy landscape will not rely on just one of these methods however, but a combination, with consideration to the location specific needs and resources. Associated with each of these methods are pros and cons however in 2013 only around 15% of the Uk's energy was obtained from a renewable source, with coal making up 36%, gas 27%, nuclear 20% and 2% of others [1]. The total flux of solar energy incident on the Earth at any time is enough to meet the whole energy demands of the planet. The total solar energy flux intercepted by the earth on any particular day is 4.2×10^{18} Watt hours. This means that more energy falls on the Earth in an hour than humans use in one year [2]. There are 3 main ways that we can harvest energy of the sun on Earth: using photovoltaic materials to directly convert the energy of the photon to electricity, using the heat of the sunlight to

produce hot water and using the heat of the sunlight to heat an oil or a salt which can then be used to generate steam and provide electricity. In this thesis we will be looking at different parts of a solar device that uses the photovoltaic effect to directly produce electricity. In order to convert that energy in a cost effective manner using solar cells their effective cost must be cheap, this means either reducing the manufacturing costs or to improve the efficiency of the cells. The work on this thesis is concerned understanding the materials used to electrically contact the photovoltaic materials to the final device.

A photovoltaic (PV) device is one that converts incident light photons into electrical energy. One of the first observations of the photovoltaic effect was attributed to Becquerel in 1839 who measured a photo current generated by light illuminating an electrolyte solution [3]. Modern solar cells were first made in the 1950's, with crystalline silicon producing around a 6% conversion efficient device. Initially the idea was to use solar power in situations where power from the grid was unavailable such as in remote areas or on satellites, however with the supply of traditional fossil fuels dwindling alternative energy sources are becoming more important with solar PV one of the options as the Sun is the most abundant energy resource we have. To be able to convert as much of this energy as possible three steps must occur:

1. The device should absorb radiation from as much of the solar spectrum as possible. 2. This radiation then efficiently needs to generate electron-hole pairs within the device. 3. These charge carriers then need to be separated to prevent recombination and extracted to be used in an external circuit.

A solar cell is built from semiconducting materials, so the different types of semiconductor will be briefly discussed.

Semiconductors

A semiconductor is a material whose electrical conductivity lies between that of a metal and an insulator, with a band gap separating the valence and conduction bands. They can be categorized as either intrinsic or extrinsic and can be composed of single species of elements, elemental semiconductors, or compound structures. Gallium arsenide GaAs is a well-known example of a III-V binary compound semiconductor but you can also have ternary and quaternary compounds. In an intrinsic semiconductor the concentration of holes in the valence band is equal to that of electrons in the conduction band. At 0K there no electrons in the conduction band and the material behaves like an insulator. At temperatures above 0K the thermal energy may be enough to promote some electrons from the valence band into the conduction band, leaving behind the same number of holes as excited electrons. An extrinsic semiconductor is one that has been doped with another material in order to alter its electrical properties. By choosing the dopant with respect to the host material we can either end up with an excess of electrons in comparison to the un-doped material or a deficit. The level of doping is important as too high of a doping concentration leads to a narrow depletion region, making it easier for electrons to tunnel through the junction. Having too low of a doping concentration results in a very large depletion region where the layer becomes too resistive to allow charge to flow. When we have an excess of electrons we call this n-type doping, this is achieved by the addition of donor impurities such as group V elements from the periodic table for doping silicon, electron acceptor impurities such as group III elements are used to dope silicon, this results in an excess of holes

which is a p-type material. The majority charge carriers in an n-type material are electrons while in a p-type material they are holes. By adding these dopants to the material we also introduce new energy levels within the band gap as well as moving the position of the Fermi level as shown in figure 1.1.
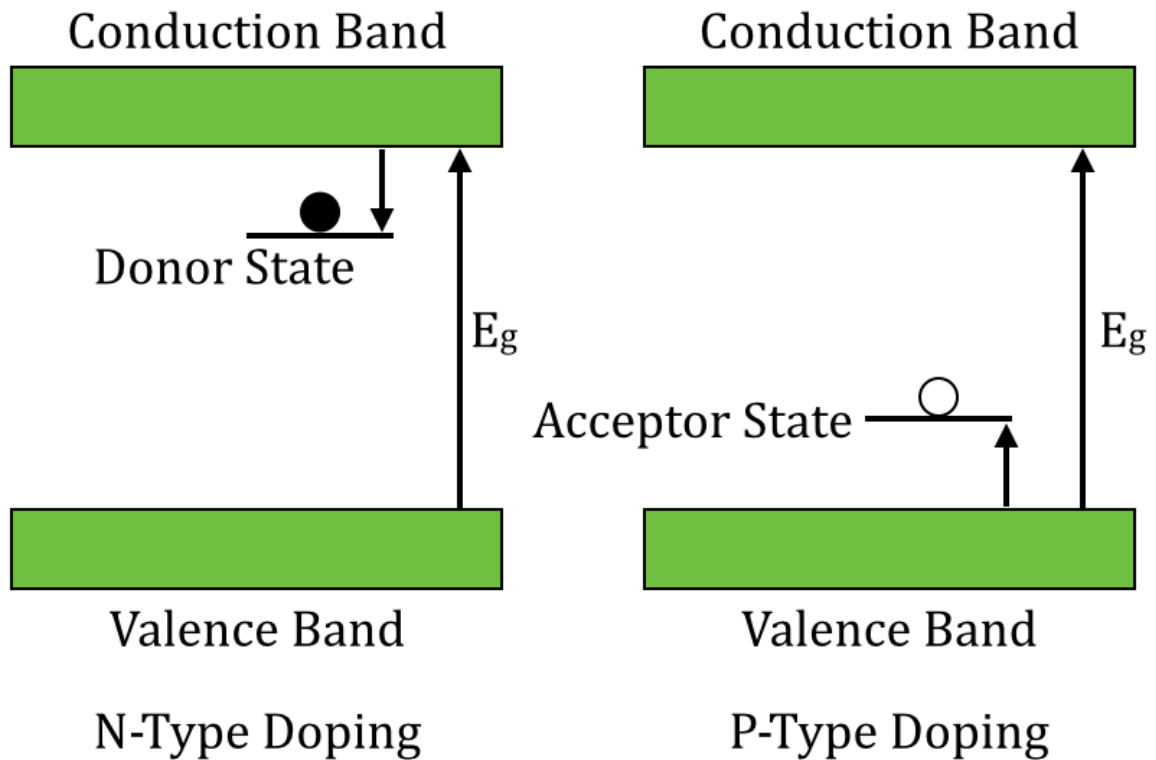

Figure 1.1: Energy Band diagram for n doped and p doped semi conductors

Depending on the band structure of the material a semiconductor can be said to have either a direct or an indirect band gap. For the electron to be promoted to the conduction band for a direct semiconductor it just needs enough energy to get over the band gap. For an in-direct semiconductor it not only needs to increase its energy but it also requires a change in momentum. This means it is easier for a direct semiconductor to absorb light, as no interaction with lattice is

required. For an indirect semiconductor a phonon must also be involved to change the momentum of the electron.

Semiconductor junctions

The basic structure of a solar cell is a junction between two semiconductors which have different properties, one of the materials will be p-doped, the other n-doped, bringing them together forming a p-n junction. When this occurs electrons from the n-type material at the interface will combine with holes in the p-type material to form negative ions, and leave behind positive ions, the separation of these ions either side of the junction leads to the built in electrical potential and the region with no mobile charge carriers is called the depletion region.

The magnitude of the built in potential V_{bi} is given by equation 1.1 [4]

$$V_{bi} = \frac{kT}{q} ln \left[\frac{N_A N_D}{n_i^2} \right] \tag{1.1}$$

where k is the Boltzmann constant, T is the temperature, q is the magnitude of electronic charge, N_A is the concentration of acceptors in the p-type material, N_D is the concentration of donors on the n-type side of the junction and n_i is the intrinsic charge carrier density.

The width of the depletion region formed w, shown in figure 1.2 is given by equation 1.2

$$w = \left[\frac{2\varepsilon}{q} \left(\frac{N_A + N_D}{N_A N_D} \right) V_{bi} \right]^{1/2} \tag{1.2}$$

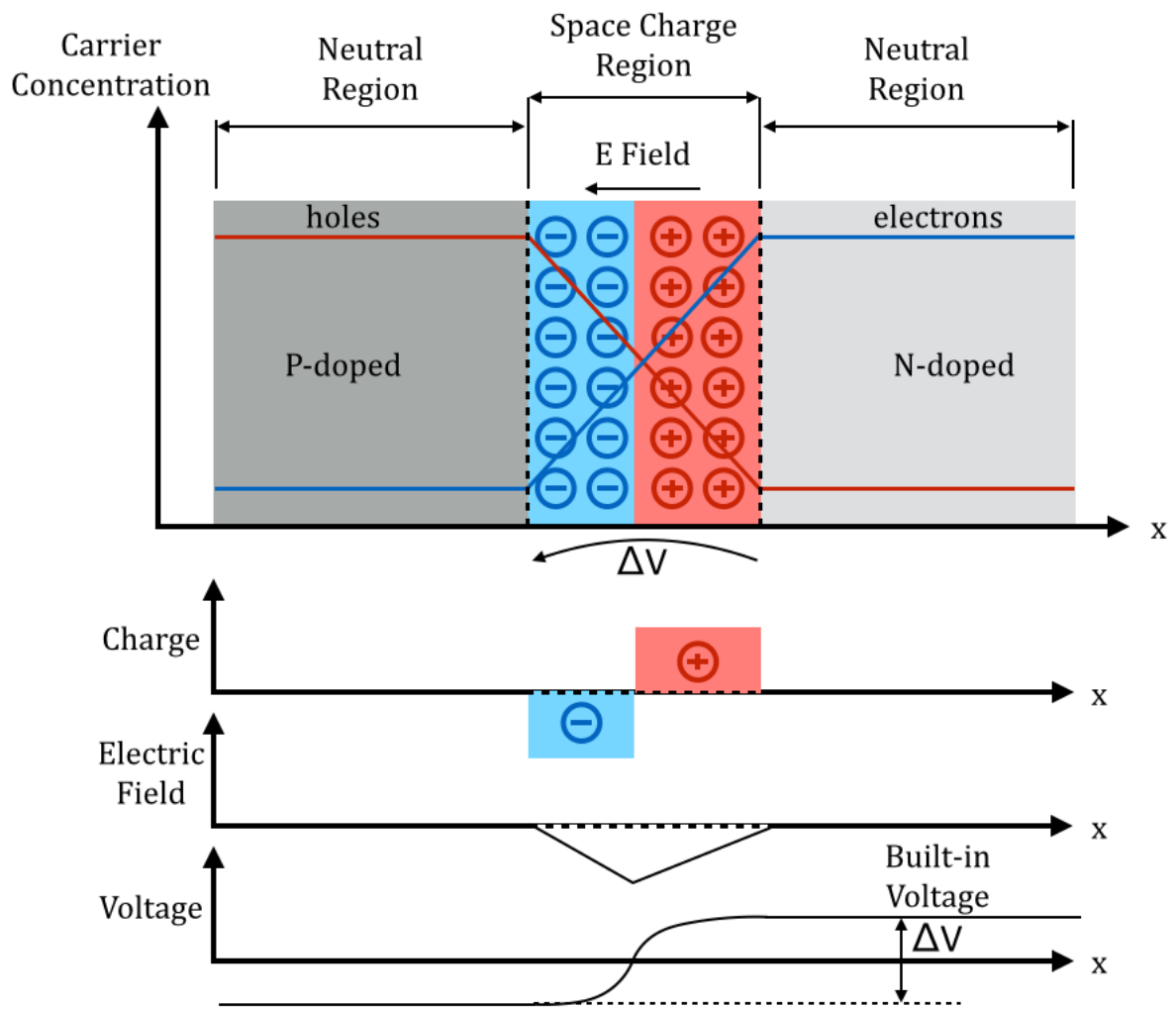where ε is the permittivity of the semiconductor.

Figure 1.2: Depletion region formed at a p-n junction

When light is incident on this junction, depending on the energy of the incoming photons an electron-hole pair may be generated [3]. If the photon's energy is greater than the band gap of the material then an electron can be promoted from the valence band to the conduction band leaving behind a hole, this electron hole pair is the separated by the built in electric field and forced to go through an external circuit in order to recombine. For photon energies lower than the band gap of the material there is insufficient energy to promote and electron to the conduction band, however in a non ideal system there may be inter-band states

for example due to vacancies in the lattice and so it is possible to promote an electron to such an inter-band state. If a high energy photon, typically more than twice the band gap, promotes an electron to the conduction band it will have an excess of energy, this energy may be sufficient enough to create further electron hole pairs, this mechanism is termed impact ionization.

The p-n junction within a solar cell can be created by either bringing together two different materials, a hetero-junction, or by doping one material to be p-type on one side of the junction and n-type on the other, a homo-junction. This is usually done by overcompensating for the existing dopant within a material. A sample can also be unintentionally doped, for example the presence of impurity atoms, these impurity energy levels can appear within the band gap which will affect the devices performance.
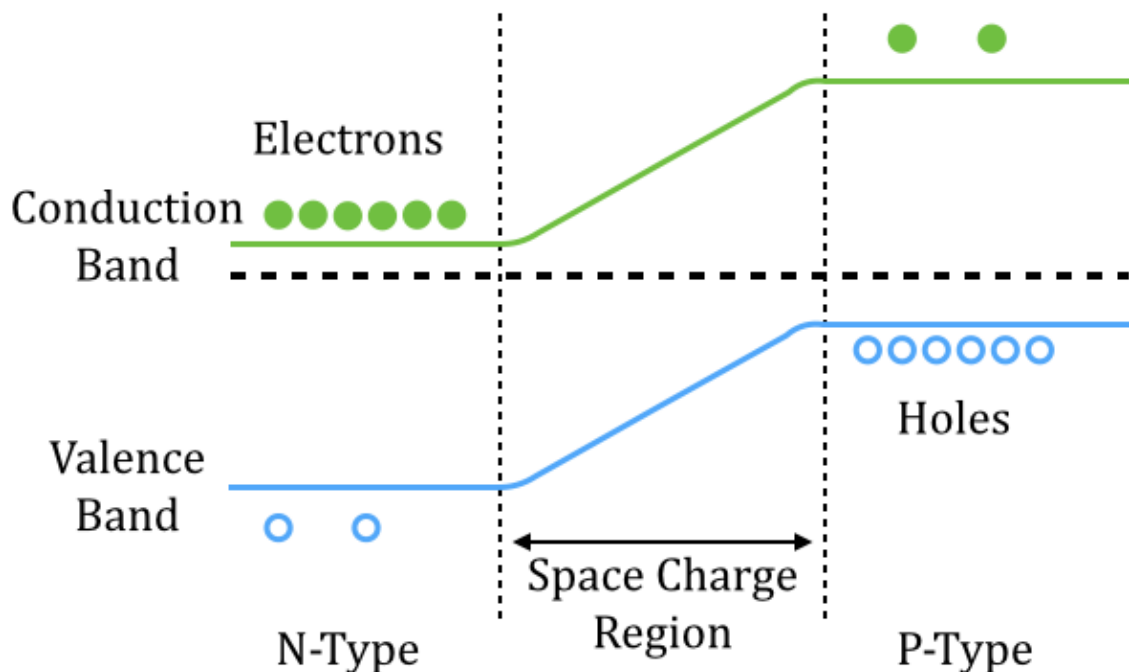

Figure 1.3: Energy diagram for a Homo-junction

The energy diagram for a homo-junction is shown in figure 1.3, as the two sides of the junction are formed from the same material they have the same band gap, this has the advantage of not forming barriers to charge flow as will be shown is a problem for hetero-junctions. This type of p-n homo junction is the device architecture for the current silicon photovoltaic industry.

Another method of creating a p-n junction is to bring together to different materials that have different band gaps. For solar cell applications there is usually a large band gap n-type window layer with a lower band gap p-type absorber layer. This is done to allow photons to pass through the window layer so they can be absorbed as close to the junction as possible.
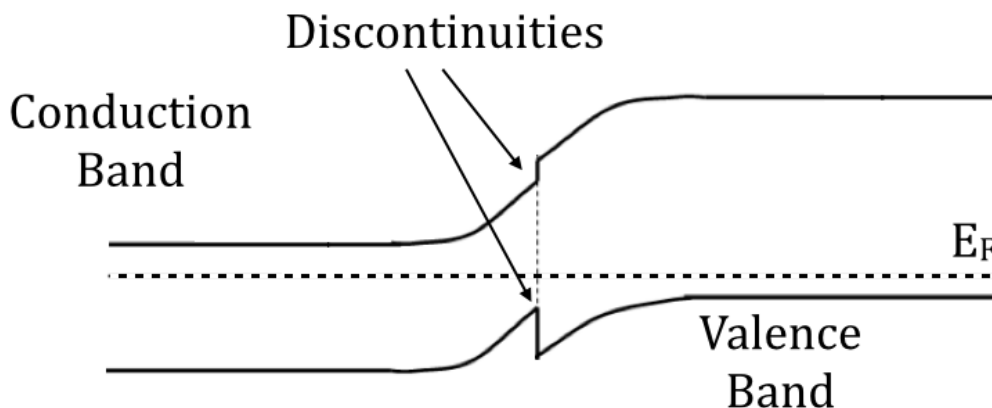

Figure 1.4: energy diagram for a Hetero-junction

In a homo-junction the materials properties are the same on both sides and so we have a continuous change in the positions of the energy bands. In a hetero-junction due to differences in the materials band gaps and electron affinities the bands may contain spikes (discontinuities) that act as barriers to charge flow, shown in figure 1.4.

There are other junctions in a solar device other than between the two active regions. One possible junction is that which is formed when a back contact is applied to the cell in order to extract the current. Back contacts are usually metallic and so a metal-semiconductor or Schottky junction is formed. This manifests itself due to the materials having a different Fermi level, when the materials are brought together charge will flow until the Fermi levels are in equilibrium and create a depletion or space charge region in the semiconductor. The difference in work function creates a built in junction potential which causes the bands to bend, for an n-type material the Fermi level is usually higher in energy than in the metal, so electrons flow into the metal, for a p-type material the Fermi level is lower in energy than in the metal so electrons flow into the semiconductor. As we will be contacting to the p-type absorber layer we will concentrate here on a p-type Schottky junction. Figure 1.5 shows the energy levels before and after contact is made.
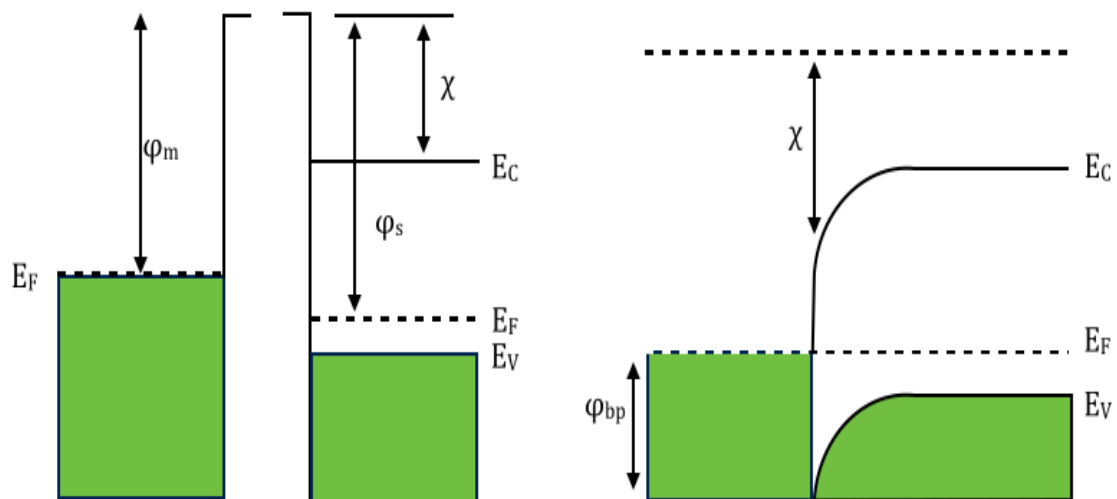

Figure 1.5: Schottky junction formed when contacting a metal to a semiconductor

The built in potential V_{bi} for a Schottky junction is given by equation 1.3 [5]

$$V_{bi} = \varphi_s - \varphi_m \qquad (1.3)$$

where φ_s and φ_m are the work functions of the semiconductor and the metal. The

barrier height for hole transport φ_{bp} is given by equation 1.4

$$\varphi_{bi} = E_g - (\varphi_m - \chi) \qquad (1.4)$$

where χ is the electron affinity of the semiconductor.
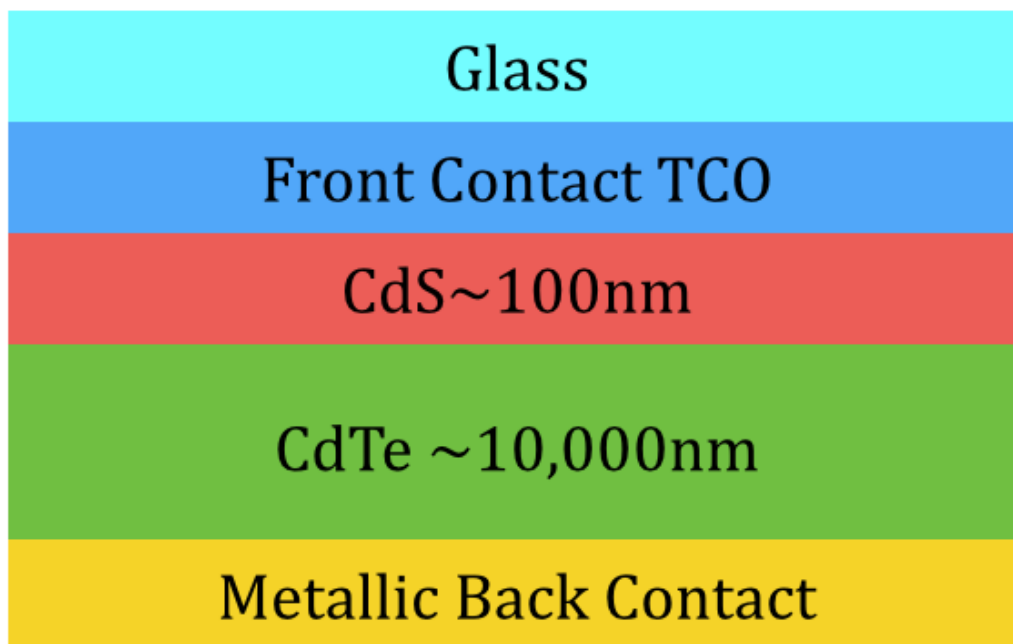
Cell architecture

Figure 1.6: Schematic of typical thin film CdTe solar cell architecture

The work in this thesis is concerned with the contacts formed at the front and

back of thin film solar cells. The typical architecture of a single junction thin film

device is shown in figure 1.6. The device consists of a p-n junction formed

between the absorber layer cadmium telluride and the window layer cadmium sulphide. This p-n junction is then sandwiched between the front and back contacts which are used for extracting charge carriers for use in an external circuit. The front contact is a transparent conducting oxide that is supported on the glass superstrate.

The Ideal solar cell

A circuit diagram equivalent to the structure of a solar cell is shown in figure 1.7.

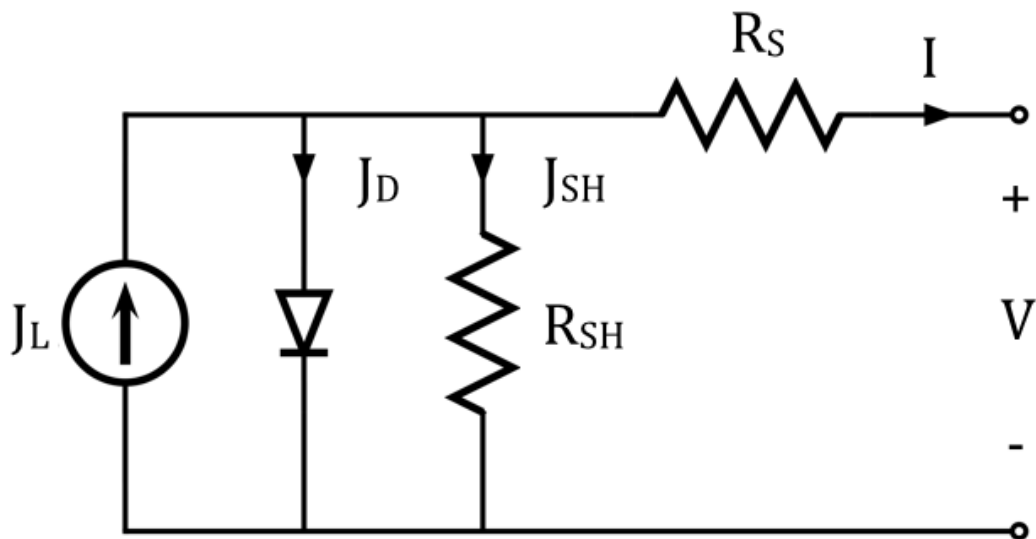**Figure 1.7: Circuit diagram representing a solar cell**

In figure 1.7 J_L is the light generated current density, J_D is the dark current density of a diode, R_{SH} and J_{SH} account for shunt resistances and currents within the cell and R_s is a series resistor. The diode in this diagram represents the p-n junction within the cell, the series resistance accounts for the resistivity of the

17

layers and the shunt resistance and current account for any leakages through the device. In an idealised device we assume that the series resistance is 0 ohms and the shunt resistance is infinite. Current density-voltage analysis is the standard method with which the efficiencies of solar cells are measured. This is done by measuring the current generated in the cell as a function of the applied bias, typically from -1V to + 1V. The measurement is carried not only under illumination but also in the dark as shown in figure 1.8. From measurements under illumination not only the efficiency of the cell can be worked out but also other important device parameters, such as the open circuit voltage V_{OC}, the fill factor FF and the short circuit current density J_{SC}. By running the measurement in the dark the diode current density J_D can be calculated using the Shockley diode relation given by equation 1.5 [6]

$$J_D = J_0\left(e^{qV/AkT} - 1\right)$$ (1.5)

where I_0 is the reverse saturation current density, a value related to the properties of the material, q is the charge on an electron, A is the quality factor of the diode, this describes how close to an ideal diode the system is, for an ideal diode this value is 1 however due to processes such as carrier recombination when moving through the depletion region for a real diode this value is usually around 1.1-1.2. Boltzmann's constant is k and T is the temperature. Under illumination equation 1.5 includes an additional term, the light generated current density J_L giving us equation 1.6.

$$J = J_0\left(e^{qV/AkT} - 1\right) - J_L$$ (1.6)

The short circuit current density is determined when the external terminals are short circuited, and so it is the current generated when no bias is applied to the

cell. In this scenario in the above equation when $V = 0$, the I_0 term becomes 0 and so we are just left with the light generated current density J_L.

The open circuit voltage V_{OC} is obtained when the terminals are open and therefore no current is flowing through the cell. It is the applied voltage at which there is no flow of charge through the external circuit. This can be calculated from the above equation by setting the total current to zero and re-arranging for V, gives equation 1.7

$$V_{OC} = \frac{Akt}{q} \ln\left[\frac{J_L}{J_D} + 1\right] \tag{1.7}$$

The Fill factor FF is the ratio of experimental power square to the theoretical power square and is given by equation 1.8

$$FF = \frac{V_m J_m}{V_{oc} J_{sc}} \tag{1.8}$$

where V_m is the maximum voltage and J_m is the maximum current.

The above parameters are shown in figure 1.8 on this typical I-V plot.

Using these parameters we can calculate the efficiency of the device η using equation 1.9, which is defined as the ratio of the maximum power generated by the device P_{mp} to the power of the radiation upon it P_s.

$$\eta = \frac{P_{mp}}{P_s} = \frac{V_{oc} J_{sc} FF}{P_s} \tag{1.9}$$

The efficiency values are usually determined using the AM 1.5 light spectrum which will be discussed in the next section where P_s is 1000 Wm^{-2}. In order to make a valid comparison of device efficiencies the above parameters need to be determined using a reference light spectrum. The sun can be approximated as a black body emitter whose temperature is 5800K which is the temperature of the sun's surface.
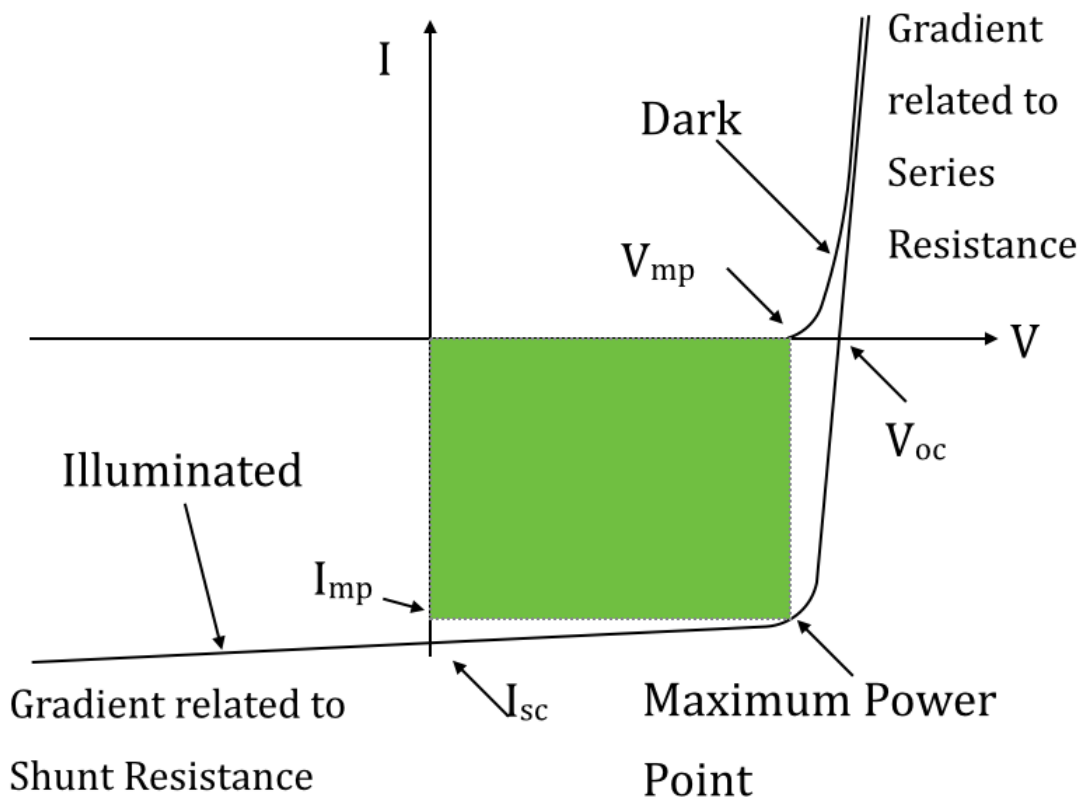
Figure 1.8: Typical I-V plot for a solar cell

The spectral emission of this idealised black body is shown in orange on the figure below. In reality the sun is not an ideal black body and so the actual spectrum that reaches the top of the Earth's atmosphere deviates from the black body spectrum and is shown in black on the figure below. The radiation that reaches the surface of the Earth is then modified again as the light travels through our atmosphere. The amount of atmosphere the light has to pass through is categorized using the AM system where AM stands for air mass. When the light travels through our atmosphere the radiation may be reflected, absorbed or scattered, which all attenuate the incoming flux. Light which reaches the edge of our atmosphere is therefore denoted as AM0 as it has not

been attenuated by our atmosphere, light which is incident on the surface of the earth perpendicular to it is AM1, and light which has an incidence angle of around 48° is AM 1.5. This is the standard spectrum used for analysing cell efficiencies. The Standard Test Condition STC used when certifying cells is done with the cell temperature of 25° C using the AM 1.5 spectrum with a power of 1000 Wm^{-2}.
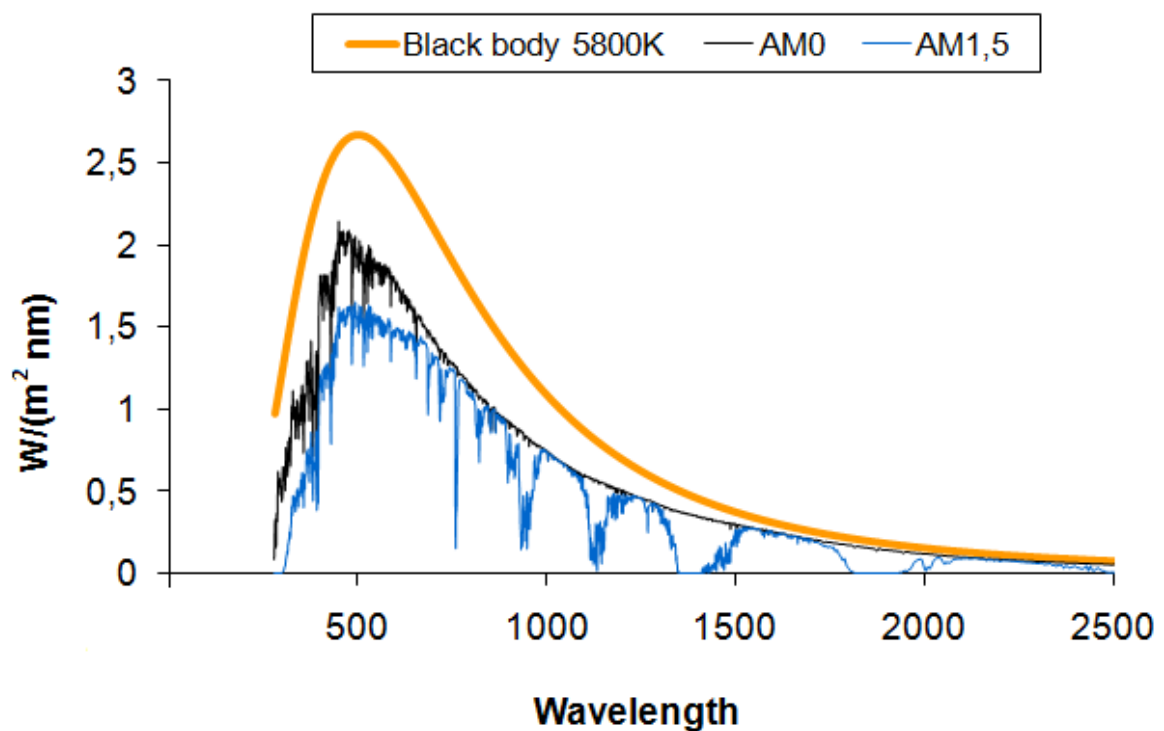

Figure 1.9: Solar spectrum from the Sun under different conditions, the orange line represents the sun as a perfect black body. The black line is the radiation before it has entered the Earth's atmosphere and the blue line is the remaining wavelengths that reach the Earth under an angle of ~ 48°. Figure reproduced without permission from [7]

As can be seen in figure 1.9 the AM 1.5 spectrum contains dips at different wavelengths, these are result of the radiation being absorbed in the atmosphere by molecules such as water, oxygen and ozone.

Fundamental Losses

In a single junction cell there is a fundamental limit on the efficiency due to intrinsic losses. These losses cannot be avoided for a given design structure. Extrinsic losses however in theory can be minimised or removed by design features and are not taken into account when calculating the limiting efficiencies [8]. The result of these losses is to either reduce the current available in the device or to reduce the operating voltage. The main sources of these intrinsic losses are due to thermalisation and excitations smaller than the band gap. In a device with a band gap of 1.3eV these losses account for 30% and 25% respectively. Thermalisation is when a photon is incident on a sample that has more than the required energy to promote an electron to the conduction band. In this case the excess energy is often converted and lost as heat meaning that really only energies just above *Eg* are available to excite pairs. If the photon doesn't have enough energy to excite an electron to the conduction band then the photon will be transmitted through the device and its energy will be lost. As well as intrinsic losses inherent to the device structure the cell also must be designed with the solar spectrum in mind. The light coming from the sun covers a range of wavelengths and therefore the band gap of the absorber layer plays an important role in determining the maximum power and therefore efficiency that the cell can achieve. A small band gap will only absorb a small section of the available solar spectrum, which results in a low photo voltage being generated. Too large of a band gap and a lot of the spectrum will be too low energy to excite electron-hole pairs and so the generated current will be small. This means a balance has to be struck to achieve the maximum efficiency. It is found that for a

single junction the cell, the ideal band gap is around 1.4eV where the maximum theoretical efficiency is around 33% [6].

These intrinsic losses given above cannot be minimized for a single junction device. However by using more complicated cell architectures such as tandem cells the maximum theoretical efficiencies can be increased. Extrinsic losses in the cell can theoretically be minimised or avoided which can improve cell efficiencies.

Extrinsic losses

Extrinsic losses can be split into 3 main areas, optical losses concerning the amount of light entering a cell, transmission losses within the cell and ohmic losses when extracting the carriers to be used in an external circuit.

Optical losses

In order for the light incident on the cell to excite carriers it needs to make it to the depletion region. Due to the difference in refractive index of the medium the light is travelling through, air $n \approx 1$, and the cell itself, a material with a higher refractive index, Si $n \approx 3.4$. This can be overcome by modifying the surface with an antireflective coating so that the maximum amount of light is transmitted through the device.

Certain cell designs have a metal grid on the top contact as to reduce the distance carriers have to travel before they are collected. Other cell designs use a transparent conducting oxide (TCO) to extract the carriers. In the first case

physical shading of the cell by the grid reduces the amount of photons entering the cell. In the case where a TCO is used the problem of shading is avoided however the TCO will absorb some of the light, as they are not completely transparent. The transparency of the TCO is related to its band gap, which can be affected by the properties of the TCO, for example, defects within the TCO can lead to gap states appearing within the band. These can affect the transparency of the TCO and therefore reduce the total flux of light incident on the active region.

Transmission through the cell occurs when the photon has energy lower than the band gap and so cannot excite carriers. Transmission can also occur though if the cell is too thin as the absorption coefficient of a material gives the likelihood of absorption per unit distance. However as most solar cells are designed to be thin to reduce manufacturing costs this is not a common problem. In thicker cells where this is an issue a reflective back contact can be used to try and harvest those transmitted photons.

Transmission losses, recombination, drift currents, minority carriers

Once the electron-hole pair has been created it needs to be separated and removed to be used in an external circuit. Recombination can occur before they can be extracted which will reduce the generated photocurrent. This recombination can occur at trap sites within the material created by defects such as grain boundaries or impurity atoms. Especially traps in the middle of the band gap which can be extremely detrimental to the devices performance. When recombination occurs in the depletion region it reduces the fill factor and

therefore efficiency [6]. An accepted approximation is that the built-in electric field due to the p-n junction is confined to the depletion region itself. This built in potential is responsible for separating the charge carriers however charge transport within the rest of the cell is governed by diffusion. When a minority carrier is created outside of the depletion region, for example if an electron-hole pair is created in the n-type layer the hole is the minority carrier. For it to contribute to the photocurrent it needs to make it to the p contact on the other side of the device. In order to do this it will need to diffuse to the edge of the depletion region where the in-built electric field can then sweep it across the junction to the p side where it is now a majority carrier. However before it reaches the depletion region, while it is diffusing through the n-type material it can re-combine with an available electron, of which there is a high concentration. This means that these minority carriers have a short lifetime. A good approximation is that only carriers generated within the diffusion length of the depletion region will be collected, with the others lost due to recombination. The diffusion length is the distance a carrier can travel during its average lifetime before recombining [6,9].

Ohmic losses

As described earlier a solar cell can be thought as equivalent to the circuit in figure 1.7. Where the shunt resistance accounts for leakage currents through the device, and the series resistance accounts for the resistivity of the layers used and the resistivity at interfaces such as back contacts. Shunt resistances are due to current pathways through the cell, often grain boundaries or defects, which

can introduce gap energy levels, making re-combination more likely. The higher the number of these leakage channels then the lower the effective shunt resistance of the cell. When we discussed the ideal device earlier we set the series resistance to be 0 ohm and we set the shunt resistance to have infinite resistance. In reality neither of these statements is true. The total current in equation 1.6 can be modified to include these two resistance terms as follows where R_s is the series resistance and R_{sh} is the shunt resistance giving equation 1.10 [6].

$$J = J_0\left(e^{(qV-R_s)/AkT} - 1\right) + \frac{(V - JR_s)}{R_{sh}} - J_L \qquad (1.10)$$

Shown in figure 1.10 are J-V curves where the values of the shunt and series resistant are varied to show their effect on the final device performance.
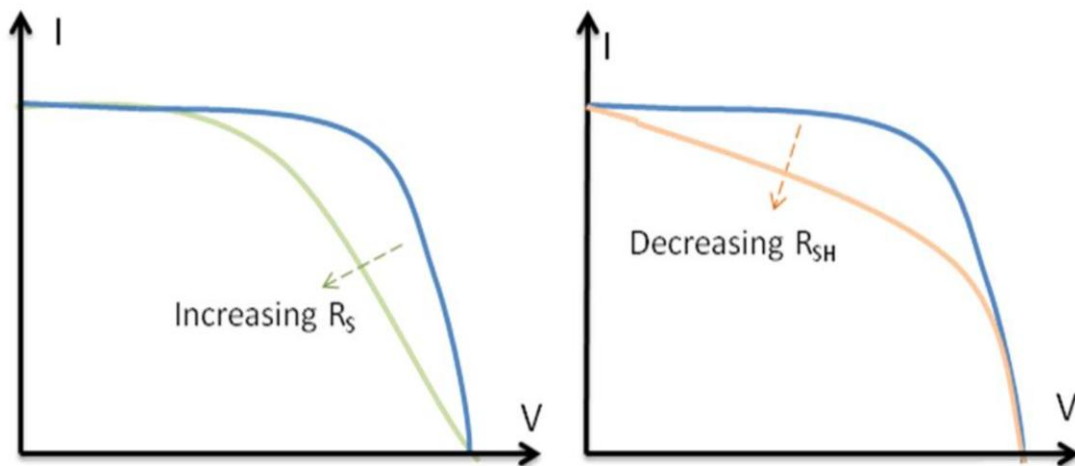

Figure 1.10: Effect of Series and shunt resistances on I-V curves, used without permission from [10]

The effect of these parasitic resistances can be seen from the effect they have on the I-V curve, and in both cases they reduce the *FF* value by reducing the

maximum power rectangle with respect to $J_{SC} \times V_{OC}$. When a metallic back contact is made to the semi conducting absorber layer a Schottky barrier may form, leading to non-ohmic behaviour, this is a prime source of the series resistance within a device as hole transport is impeded. The electron transport through the front contact can also be impeded if for example defects within the TCO give rise to states within the band gap, these sites can act as traps for the electrons and so can reduce the efficiency of the device. In this thesis different treatments of TCO's designed to probe oxygen vacancies are used to see how they affect the electronic structure of the TCO.

Copper telluride (CuTe) has been used as a component in high efficiency cadmium telluride (CdTe) solar cells, either intentionally where CuTe has been deposited or as a result of interfacial processes, namely alloying, between the CdTe layer and a copper back contact [11-16]. P-type CdTe has a high electron affinity and therefore a metal with an equally high work function is needed to make an ohmic contact [17]. However most metals which are used in the electronics industry for contacting such as copper or gold do not have a sufficiently high work function as when used as a back contact a Schottky barrier forms which reduces the overall efficiency of the cell. The expected barrier heights in the absence of any interface states are given by equation 1.11 [18].

$$\varphi_{bp} = E_g - (\varphi_m - \chi) \qquad (1.11)$$

The work function of the metal is φ_m, E_g the band gap and χ is the electron affinity of the semiconductor and the barrier height for hole transport is φ_{bp}. Inserting the values for CdTe we can see that ideally for a barrier of zero height we would need a metal with a work function of 5.95eV. One approach to

reducing the size of this barrier is to etch the surface of the CdTe prior to metal deposition. This etching process produces a Te rich surface [19,20]. Metal is then deposited onto this enriched surface and annealed, rendering an alloyed back contact. Understanding the alloying process will allow more suitable contacts to be made resulting in higher efficiency cells. For example certain phases of a material may be undesirable within a device, knowing which methods are likely to reduce these phases will therefore contribute to improving the device performance. As this alloying process will begin at the surface of these materials surface science techniques can shed light on the processes occurring and are therefore suitable for use in their investigation.

Transparent conducting oxide

A transparent conducting oxide (TCO) is a material which exhibits two usually contradictory behaviours, it is optically transparent due to wide band gap, greater than 3eV, with optical transmission greater than 80%, however it still conducts electricity with typical conductivity values of 10^4 Sm^{-1} [21-24]. This useful combination of properties result in TCO's being important in many technological applications, liquid crystal displays, touch screens, organic and inorganic solar cells and other optoelectronic devices [22,25-28].

A typical transparent material is an insulator with a filled valence band and an empty conduction band, separated by a band gap greater than 3eV. On the other hand a typical conductor is a material whose Fermi level lies within an energy band with a high density of states. These two properties can be achieved simultaneously by degenerately doping several transparent insulating metal

oxides, such as indium, tin and zinc oxide, In_2O_3, SnO_2 and ZnO. The most commonly used doped material is tin doped indium oxide ITO. Its market abundance is due to its ability to be deposited using routine thin film deposition techniques. Even though ITO is widely used their still remains interest into the conductivity of the host material In_2O_3. It has been shown that at the surface of these metal oxides there exists a high mobility electron gas. These electronic states were found on In_2O_3 [29], CdO [30] and $SrTiO_3$ [31]. The presence of these excess electrons has been attributed to surface dipoles and lattice vacancies [32]. For example an oxygen atom within the oxide will typically have an oxidation state of -2, and so by removing the oxygen from the lattice there are an additional 2 free electrons. These high surface electron densities have important implications when using the material in a device as some kind of contact has to be made to the surface. Several causes of this conductivity have been put forward in the past, including higher valence elements [33-35], defects such as vacancies within the lattice [36-38] and hydrogen incorporation [39,40]. Lany et al. showed that bulk vacancies cannot account for the large conductivities exhibited by these materials and showed their electrical properties are the result of charge carriers caused by surface donors [41]. Therefore understanding these surface donors is important when implementing these materials in working devices.

In Chapter 3,4 and 5 the deposition of tellurium on single crystal copper surfaces has been studied with several ultra high vacuum techniques. These were X-ray and ultra violet photoelectron spectroscopy, dynamical low energy electron diffraction and scanning tunnelling microscopy. In chapter 6 photoelectron

spectroscopy was used to study the effect of oxygen treatments on the valence band of low index high quality In_2O_3 films. In order to understand the effect of oxygen vacancies on the electronic structure of In_2O_3 the valence band was probed after different sample preparations, sputtering the samples, and annealing them in both an oxygen poor and an oxygen rich environment.

References

[1]   Government Report accessed November 2014

www.gov.uk/government/uploads/system/uploads/attachment_data/file

/337649/chapter_5.pdf

[2]   http://www.mpoweruk.com/solar_power.htm accessed November 2014

[3]   A. E. Becquerel. Les Compte Rendus des L'academie des sciences 9 (1839)

p. 561

[4]   S. M. Sze and Ng. K. Kwok, "Physics of Semiconductor Devices", Wiley-

Interscience, (2007) 3rd Edition

[5]   D. A. Neumann, "Semiconductor Physics and Devices", McGraw-Hill

Companies, Inc. (2003) 3rd edition

[6]   J. Nelson, "The Physics of Solar Cells", Imperial College press, London,

(2003)

[7]   Solar spectrum, http://rredc.nrel.gov/solar/spectra

[8]   L. C. Hirst, Prog. Photovolt. Res. Appl. 19 (2011) p. 286

[9]   H. A. Atwater and A. Polman. . Nature Materials, 9 (2010) p. 205□213

[10] "Photovoltaic   Cell   I-V   Characterization   Theory",   (2012)

http://www.ni.com/white-paper/7230/en/

[11] H. Uda, S. Ikegami, Sol. Energy Mater. Sol. Cells 50 (1998) p. 141

[12] J.H. Yun, K.H. Kim, Sol. Energy Mater. Sol. Cells 75 (2003) p. 203

[13] S.S. Hegedus, B.E. McCandless, Sol. Energy Mater. Sol. Cells 88 (2005) p. 75

[14] X. Wu, J. Zhou, S. Thin Solid Films 515 (2006) p. 5798

[15] K. Neyvasagam, N. Soundararajan, Vacuum 82 (2008) p. 72

[16] X. Wu, Sol. Energy 77 (2004) p. 803

[17] S.H. Demtsu, J.R. Site, Thin Solid Films 510 (2006) p. 320

[18]   J.L. Freeouf, J.M. Woodall, Appl. Phys. Lett. 39 (1981) p. 727

[19]   H.C. Chou, A. Rohatgi, J. Electrochem. Soc. 142 (1995) p. 254

[20]   D. Grecu, A.D. Compaan, Appl. Phys. Lett. 75 (1999) p. 361

[21]   C.G.Granqvist and A. Hultaker, Thin solid films 41 (2002) p. 1

[22]   C.G.Granqvist, Sol. Energy Mater. Sol. Cells 91 (2007) p. 1529

[23]   H.Y.Liu, V. Avrutin, Superlattices Microstruct. 48 (2010) p. 458

[24]   H. Hosono, Thin Solid Films 515 (2007) p. 6000

[25]   R. Baetens, B. P. Jelle, Sol. Energy Mater. Sol. Cells 94 (2010) p. 87

[26]   H. Mbarek, Physica Status Solidi C 4 (2007) p. 1903

[27]   T. Minami, Thin Solid Films, 516 (2008) p. 5822

[28]   D. Ginley and C. Bright, MRS Bulletin, 25 (2000) p. 15

[29]   P. D. C. King, T. D. Veal, Phys. Rev. Lett. 101 (2008) p. 116808

[30]   P. D. C. King, T. D. Veal, Phys. Rev. Lett. 104 (2010) p. 256803

[31]   W. Meevasana, P. D. C. King, Nat. Mater. 10 (2011) p. 114

[32]   E. Dagotto, Nature 469 (2011) p. 167

[33]   G. Frank and A. Kostlin, Appl. Phys. A 27 (1982) p. 197

[34]   G. B. Gonzalez, T.O. Mason, J. Appl. Phys. 96 (2004) p. 3912

[35]   S. Lany and A. Zunger, Phys. Rev. Lett. 98 (2007) p. 045501

[36] F. A. Kroger, "The Chemistry of Imperfect Crystals", North- Holland, Amsterdam, (1974) 2nd edition

[37]   J. H. W. de Wit, J. Solid State Chem. 13 (1975) p. 192

[38]   A. Ambrosini, G.B Palmer, Chem. Mater. 14 (2002) p. 52

[39]   C. G. van de Walle, Phys. Rev. Lett. 85 (2000) p. 1012

[40]   S. Limpijumnong, Phys. Rev. B 80 (2009) p. 193202

[41]   S.Lany A. Zakutayev , Phys. Rev. Lett. 108 (2012) p. 016802

Chapter 2

Theory and Instrumentation

This chapter gives a description of the experimental techniques used within this thesis and the instrumentation on which the experiments were performed. The work in this thesis concerns the properties at the surfaces of the materials studied and the techniques used are all extremely sensitive to these surface regions of the samples. The techniques used are X-ray photoelectron spectroscopy (XPS), ultra-violet photoelectron spectroscopy (UPS), low energy electron diffraction (LEED), dynamical LEED intensity-voltage calculations (LEED-IV) and scanning tunnelling microscopy (STM). These techniques all require ultra high vacuum (UHV) to operate. By using this combination of techniques both the geometric and the electronic structures of the surfaces can be investigated. The main system used in this thesis was a triple chamber system in the Nano-characterisation laboratory, originally based in the Chadwick building at the University of Liverpool but now relocated into the Stephenson Institute for Renewable Energy.

Ultra High Vacuum

The work in this thesis was carried out under ultra high vacuum. The necessity of the vacuum is due to two main factors. Sample stability and increasing the mean free path of electrons used in the experiments. In order to study the surfaces of materials on the atomic level we require that the surface remains unchanged for the duration of the experiment. This means for example if we

clean a metallic sample we need to be able to investigate the surface before it oxidizes and changes. This stability is achieved in vacuum by reducing the rate of molecular and atomic adsorption onto the surface; this rate of adsorption can be calculated with the kinetic theory of gases using equation 2.1 [1]

$$r = \frac{2.64x10^{22}P}{(TM)^{0.5}} \quad\quad\quad (2.1)$$

where r is the rate of arrival to the surface of atoms or molecules in $cm^{-2}s^{-1}$, P is the pressure in the chamber in mbar, T is the temperature in Kelvin and M is the average mass of the incident adsorbents. For example in an UHV system with a pressure of 1×10^{-10} mbar at room temperature the main residual gasses are H_2 CO and CO_2. Entering these into the above equation gives us a combined incident flux of 3×10^{10} $cm^{-2}s^{-1}$. The close packed surface of the Cu(111) has around 2×10^{15} atoms cm^{-2}. Assuming all incident atoms or molecules actually stick to the surface, a monolayer will be adsorbed after around 18 hours. If the working pressure in the chamber were 1×10^{-8} mbar then the adsorption of one monolayer would only take around 11 minutes, which is not sufficient time to carry out the measurements.

The main system used in this thesis shown in figure 2.1 was a triple chamber UHV system housed in the Nano-characterization lab within the Stephenson Institute for renewable energy. The three chambers are a preparation chamber where the samples were initially entered into the system and cleaned, an analysis chamber that contains the electron analyser for the PES measurements and a chamber to house the scanning tunnelling microscope. The system had a base operating pressure of 1×10^{-10} mbar where each of the chambers could be isolated using gate valves and individually pumped.
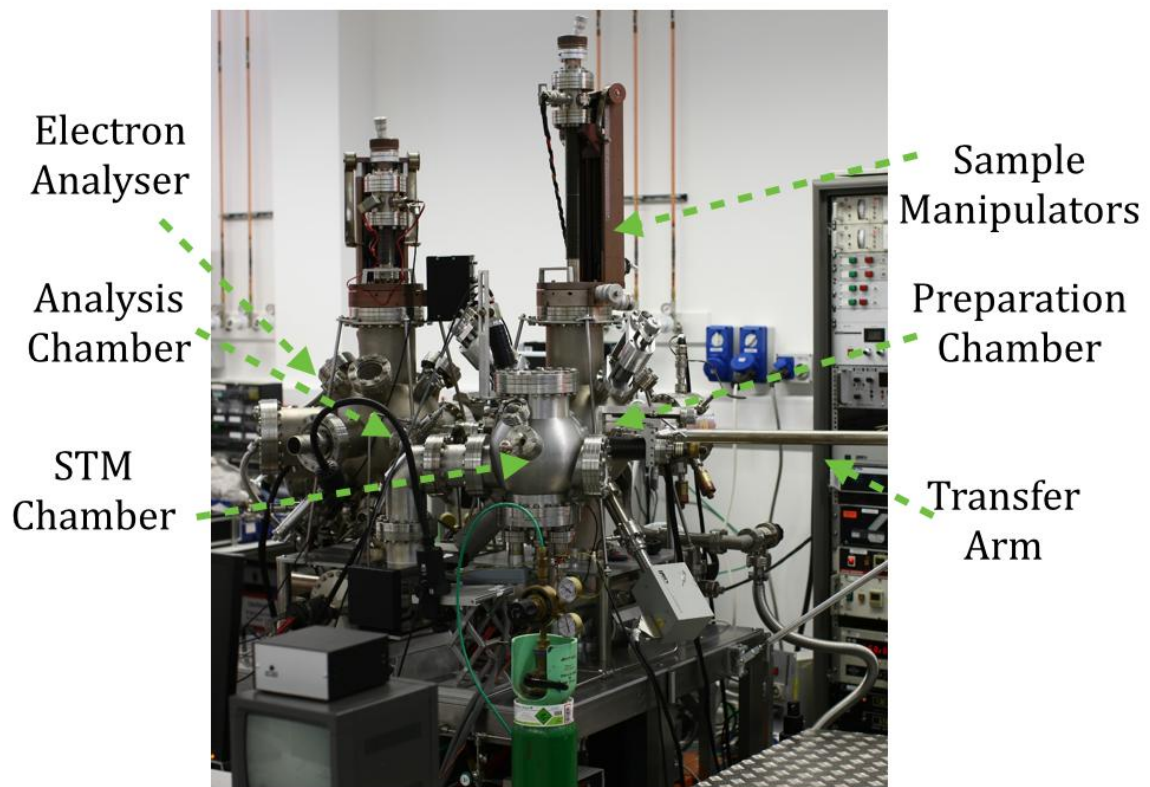
Figure 2.1: Labelled image of the UHV system in the Nano-characterisation laboratory

The samples were mounted on Omicron-style sample plates and were manoeuvred between the 3 chambers using a combination of magnetically coupled transfer arms and pincer headed wobble sticks. The copper single crystals were held to the sample plates by spot welding tantalum straps that slotted into pre made cuts in the edges of the crystals. The indium oxide samples had tantalum straps spot-welded over their edges to mechanically hold them and electrically connect the surface of the samples to the sample plate. The samples were then positioned onto 4-axis manipulators within the chambers so they could be positioned for cleaning and measurements. Ion bombardment guns

were used to clean the surfaces of samples via sputtering and the manipulators were equipped with heating stages to anneal the samples after they had been sputtered. Heating was achieved through an electron beam heater that can be used both with and without a bias. Without a bias it is a simple radiative filament, in this case tungsten. By passing a current through the filament thermionic electrons are emitted which hit the sample causing it to heat up. If higher sample temperatures are needed the sample can be positively biased with 500V as to accelerate the thermionic electrons into the sample. Sample cooling was also available by passing nitrogen gas through a condenser coil submerged in liquid nitrogen, this then flowed through capillaries down to a reservoir attached to the manipulator. Using these methods the sample temperature can be varied from 110K – 1100K. Sample temperature was typically measured using an infrared pyrometer in conjunction with a thermocouple attached to the manipulator. The thermocouple and infrared pyrometer both have an error value of $\sim 1\%$ as given by the manufacturer. The system also has a mass spectrometer that is mainly used for residual gas analysis in the chamber.

Tellurium was deposited onto the sample using a homemade Knudsen cell evaporator [2]; a schematic is shown in figure 2.2. This consisted of a sheet of tantalum folded over and spot welded along the sides to make a pouch. The pouch is welded to two terminals for passing a current through the pouch and providing mechanical support. Tellurium powder was placed in the bottom of the pouch and the top edge was then sealed with the spot welder leaving a small aperture in the centre. A thermocouple was also attached to the side of pouch to monitor its temperature so previous source deposition temperatures can be

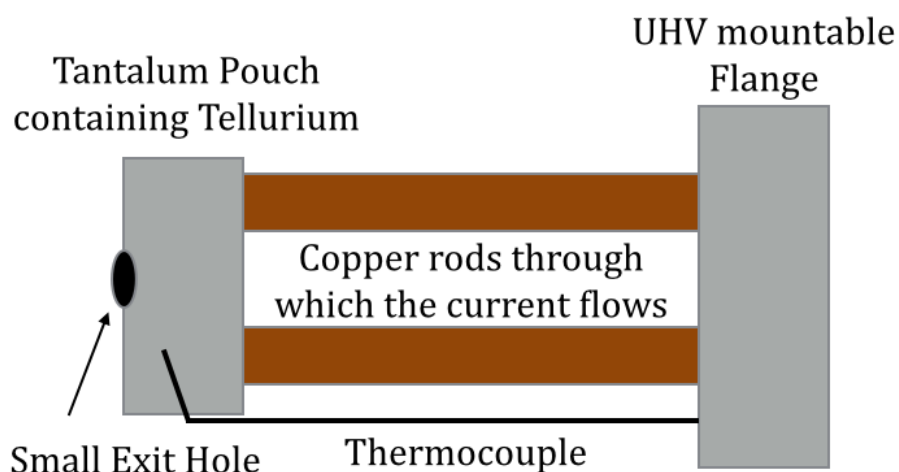reproduced to within 1% of the measured temperature in K.

Figure 2.2: Schematic of the homemade tellurium evaporator

The tellurium evaporator was de-gassed after the system was baked. This was achieved by heating the pouch around 10-15K above the deposition temperature for several hours. This deposition temperature was found by carrying out several test runs to ascertain the optimal operating temperature and sample position. Having a well de-gassed source meant that when the evaporator was used with a system starting pressure of 1×10^{-9} mbar, the overall pressure in the chamber did not exceed 2×10^{-9} mbar during operation. The sample was rotated to face the source at the start of evaporation, as no shutter was installed the sample was then rotated away from the source when the desired deposition time had been reached.

The observed LEED patterns were used to calculate the coverages and therefore to calibrate the evaporator. The flux of the evaporator was not directly

measured and was calculated from these known adsorbate structures. When known over-layer structures are identified the ratio of the over-layer to substrate core level peaks in photoemission are recorded and these ratios are used as an indicator of coverage.

Photoelectron Spectroscopy

Photoemission spectroscopy (PES) is the measurement of the kinetic energy of electrons emitted from a material after ionization by photons ranging in energy from tens to thousands of eV. The technique is used to study the energy levels of electrons within the sample. The photons can be generated by different types of sources, gas discharge lamps, X-ray tubes or synchrotron radiation, however they all involve the collection and measurement of photoelectrons ejected from the material.

In essence the fundamental principle of PES is the photoelectric effect, explained by Einstein in 1905 earning him the Nobel Prize in 1921. When a sample is illuminated by a source of photons, there is a probability that electrons residing within the energy levels of the material will absorb them. If the energy absorbed is high enough to overcome the binding energy E_b of the electron then the electron can be ejected from the surface. These ejected photoelectrons are then analysed with respect to their kinetic energy E_k. By knowing the energy of the incident radiation, and of the work function of the spectrometer, equation 2.2 can be used to calculate the binding energies of the ejected electrons

$$E_b = h\nu - E_k - \phi \tag{2.2}$$

where $h\nu$ denotes the photon energy and ϕ is the work function of the spectrometer. The sample and the spectrometer are connected to a common

ground. By studying the emitted electrons and their binding energies we can obtain not only compositional information from the ratio of electrons emitted from different elements, but also we can learn about the local environment from where the electrons originated. Studying shifts in binding energies can give information about the element's chemical state, for example seeing how the binding energies (chemical state) of the electrons are affected when the sample is oxidized.
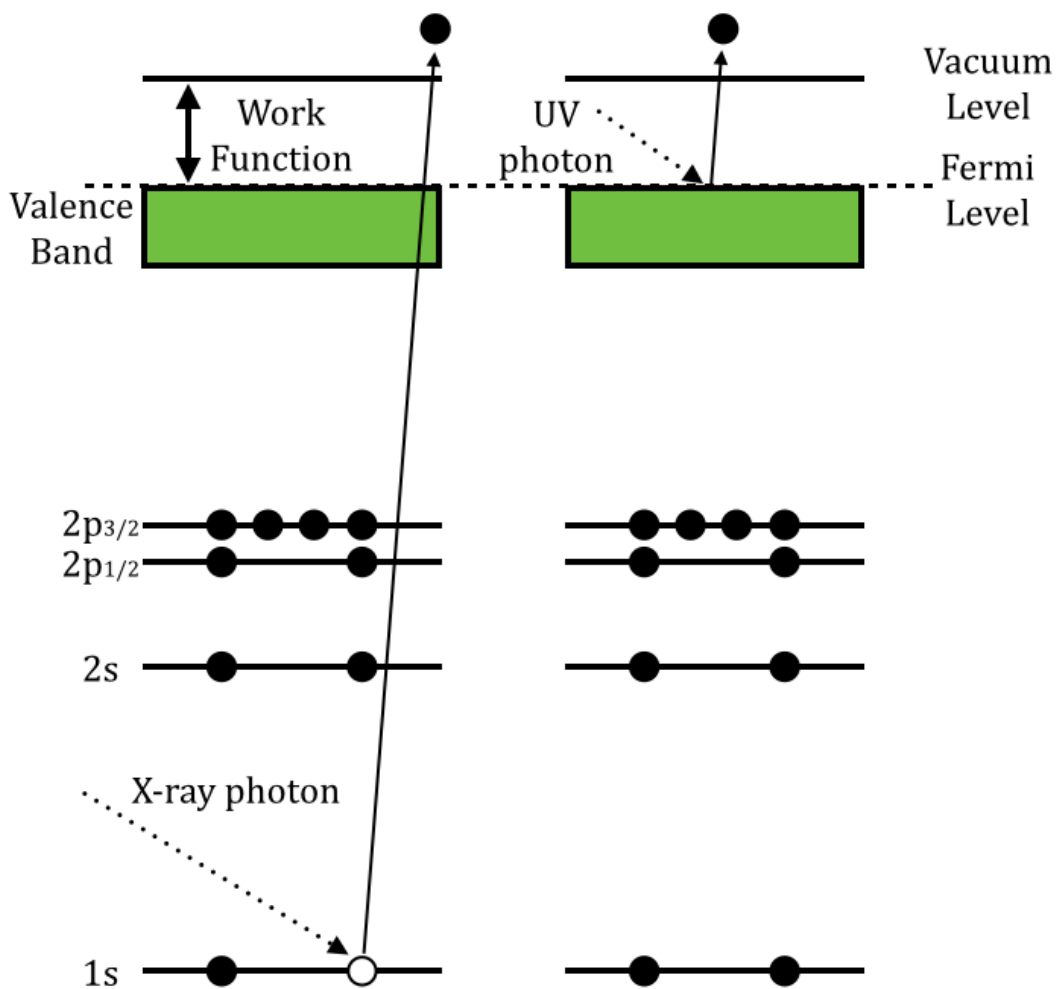

Figure 2.3: Diagram showing energy levels accessible with both X-rays and ultraviolet photons, core energy levels are denoted on the left by their quantum numbers *n,l* and *j*

A Schematic of the energy levels in a solid sample are shown in figure 2.3 with the core energy levels denoted by their quantum numbers *nlj*. The principal quantum number is *n*, the orbital angular momentum quantum number is *l* and the total spin is *j*. The schematic in figure 2.4 shows the set-up of a PES experiment: there is a source illuminating a sample, in this case X-rays, with an electron analyser capturing emitted photoelectrons. By varying the energy of electrons that are focused into the detector and discriminating unwanted energies, the intensity as a function of kinetic energy can be analysed.
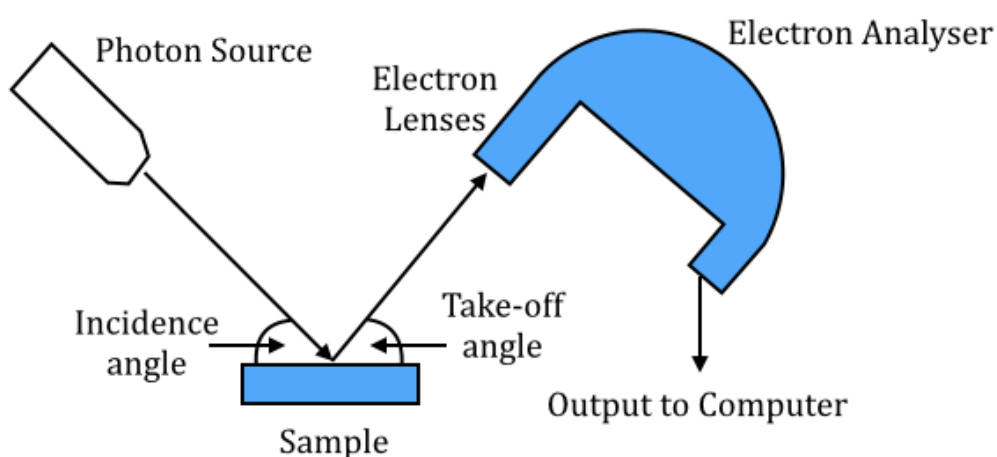
Figure 2.4: Setup of a typical PES experiment

PES is a surface sensitive technique due to the inelastic mean free path of the photoelectron. XPS only analyses the electrons that actually escape the surface. The mean free path of the electron will determine it's escape depth and whether or not the electron will escape. The intensity of electrons emitted *I* is determined by the depth of material through which an electron travels *d* and the inelastic mean free path of the electron λ and is given by equation 2.3.

$$I \propto e^{-\frac{d}{\lambda}} \qquad\qquad (2.3)$$

Figure 2.5 shows the universal curve for electron inelastic mean free paths. Although there is a general trend as described by the curve the mean free path does vary at the same energy for different materials. This is due to the different interaction strengths between the electron and the material that it is scattering from.
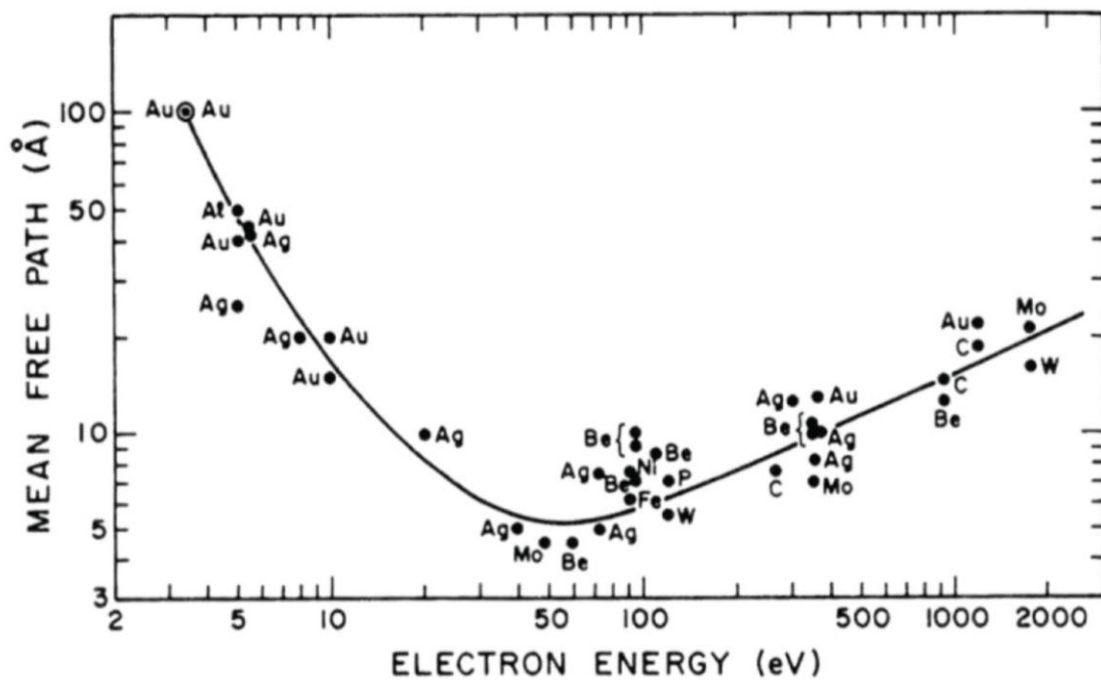

Figure 2.5: Universal curve showing the mean free path of electrons as a function of kinetic energy taken without permission from [3]

With typical kinetic energies in PES ranging from a few to 1000 eV we can see the mean free path λ is a few nm. This means that around 95% of the measured intensity will originate within 3 λ of the surface putting the sensitivity of the technique to within to first few nms of the surface. Varying the take-off angle of the electrons with respect to the analyser can increase this surface sensitivity. When the take-off angle θ is normal to the surface then the probing depth will be its maximum at 3λ, if we vary this angle then the probing depth will vary as

cos(θ)×3λ. For example the surface sensitivity goes from 3λ when θ=0° to 1.5λ when θ=60°. The resolution of the measurement on the binding energy of an electron is determined by three main factors. The line width of the photon source used for excitation, the natural line width of the energy level studied and the resolution of the energy analyser. Once the electron has been released from the surface it has to be collected by the analyser; so a high level of vacuum prevents the electron being lost to a collision before being collected. This coupled with the need for the sample to be clean for the duration of the experiment means that both UPS and XPS were done in an Ultra High Vacuum system.

The Source

The two types of photon sources that have been mainly used within this thesis are a gas discharge lamp for generating ultraviolet radiation, and a lab X-ray source with either aluminium or magnesium as an anode material. Synchrotron radiation was also used where the energy can be varied with far higher photon energies available than lab sources. At a synchrotron charged particles are accelerated in a circular orbit giving off radiation. This radiation is then focussed using optics to an end station where it is used as an excitation source. The gas discharge lamp was running He to generate the He1 discharge at 21.2 eV. The X-ray source generated photons of 1253.6eV(Mg) and 1486.6eV(Al). UPS is used to measure the valence band as it has a higher cross section for interaction than XPS and the source has a much narrower line width, a few meV for the Helium

lamp compared to around 1 eV for the X-ray source. However the limited energy range of UPS means that XPS must be used to look at deeper lying core electrons.

The main X-ray source used in this thesis was a conventional dual anode un-monochromated laboratory source as shown in figure 2.6. This schematic has been modified from the manufacturers manual [4]. The two anodes were magnesium and aluminium with K-alpha emission energies of 1253.6 and 1486.6eV respectively. The FWHM of the magnesium K-alpha emission is around 0.7eV and for the aluminium emission 0.9eV.
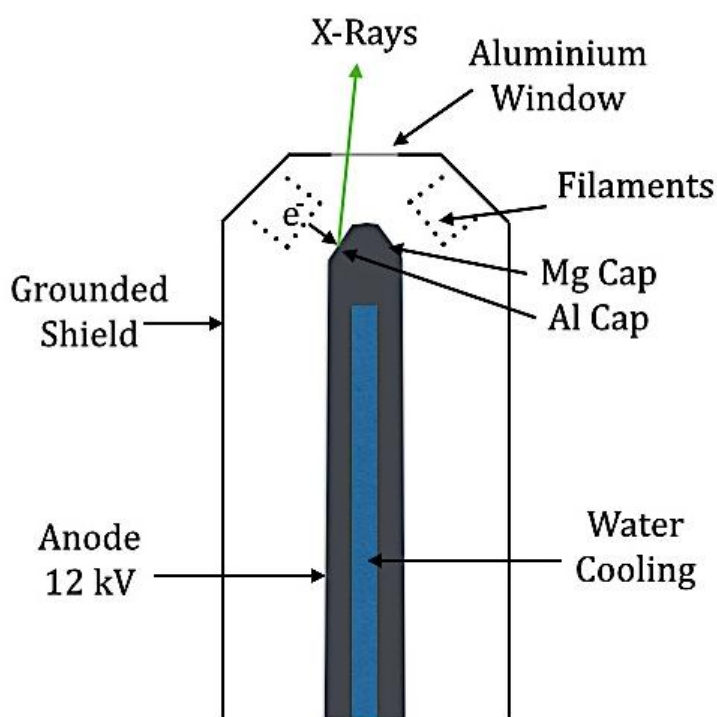
Figure 2.6: Schematic of a dual anode X-ray source modified from [4]

The ultraviolet radiation was generated in a gas discharge lamp attached to the UHV chamber where the discharge is confined by a quartz capillary tube. In order to operate the lamp a relatively high pressure of helium is required, this means that the lamp must be differentially pumped so that the sample and

analyser remain at a workable pressure. The pumping system for the lamp consists of a rotary pump (rough pump) and a turbo molecular pump (fine pump).

A high voltage is applied between an anode and a cathode at the back of the capillary tube, typically 1 keV. This applied voltage ionizes the gas molecules liberating electrons, which in turn ionize further gas molecules resulting in a plasma. These exited gas molecules relax giving off characteristic radiation in the process. To increase the purity of the gas used in the lamp the helium was fed through a condenser coil submerged in liquid nitrogen.

The Analyser

The kinetic energies of the emitted electrons were measured using an electron energy analyser. In order to make spectroscopic measurements the analyser needs to be able to select and count different kinetic energies with a good resolution. There are three main established methods for measuring the energy of the electrons; acceleration in an electric field, change in orbit in a magnetic field and time of flight. In this thesis the analyser uses the acceleration in an electric field. A schematic of the hemispherical analysers used in this thesis is shown in figure 2.7.
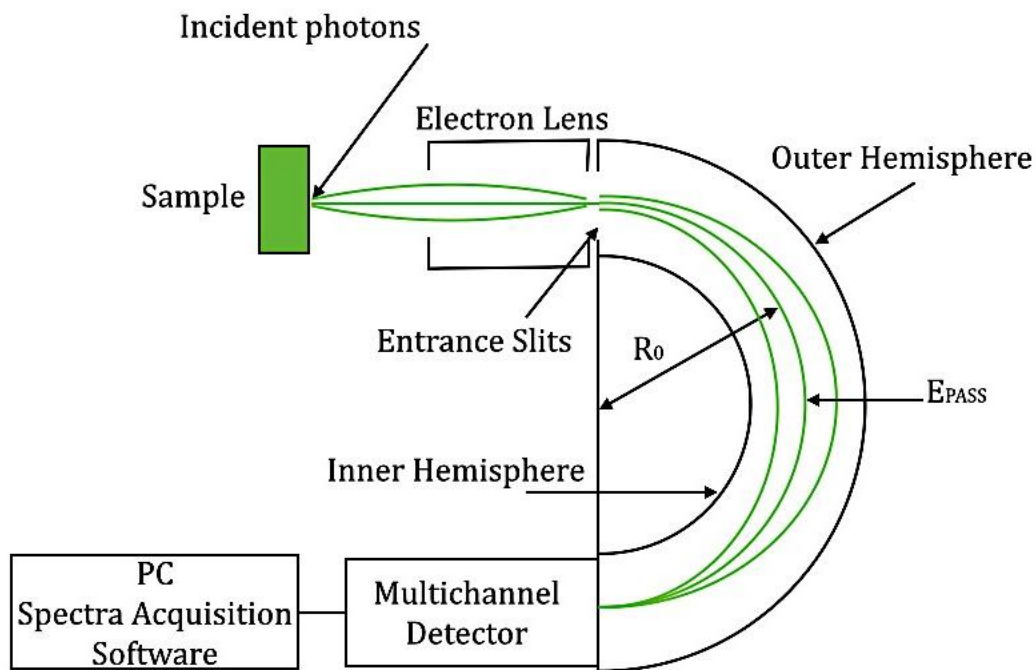
Figure 2.7: Schematic of a hemispherical analyser

The analysis of the electron energies requires 3 steps: first the liberated photoelectrons must be collected, they must then be filtered so only a narrow energy range is transmitted so to improve the resolution, and they must then be detected.

The analyser can be operated with a range of different pass energies, the energy of electrons that make it successfully through the hemisphere, with trade offs between intensity and resolution varying for different pass energies. In the high pass energy mode (50eV in this system) we have a higher count rate with a lower resolution. Running with a lower pass energy (20 or 10eV) allows greater energy resolution at the cost of lower count rates. The resolution improvement with decreasing pass energy can be seen below as the resolution of the analyser is given by the equation 2.4 [5,6]

$$\Delta E = E_0 \left(\frac{\omega}{2R_0} + \frac{\alpha^2}{4} \right) \tag{2.4}$$

where ΔE is the energy resolution of the analyser, E_0 is the pass energy used, ω is the average width of the entrance and exit slits, R_0 is the radius of path that electrons with the pass energy will take and α is the acceptance angle of the analyser. This expression is dominated by the first term containing R_0 and so in general increasing the size of the analyser will increase the resolution. In this thesis the majority of the work was done with an analyser with a radius of 120mm. Changing the size of the slits can also affect the resolution at the expense of decreasing counts. The analyser has a range of slits available however a slit width of 5mm was mainly used. Using the above equation with a pass energy of 20eV gives the energy resolution of the analyser as 0.42eV.

The Resolution

The total resolution of a PES experiment is affected by 3 main factors: the energy level being probed, the photon source and the analyser. Each orbital has an intrinsic width that is related to its lifetime known as core-hole broadening. When an electron is ejected from a core level it will leave behind a hole, an electron in a higher energy orbital can then relax into this hole; this process takes a finite time. The length of time that the hole exists is inversely proportional to the width of the energy level. As holes in the valence band are relatively more quickly populated than holes in core levels, valence levels are naturally broader. The line width of the illuminating radiation is a physical property of the source used. In the majority of the work in this thesis an un-

monochromated source was used so as well as getting satellites from non primary transitions, the width is around 0.7eV for the magnesium anode and 0.9eV for the aluminium. A lower line width can be achieved by either using a monochromator or by using synchrotron radiation. The broadening of the analyser can be reduced by running the system with different pass energies, however this is done at the cost of intensity and so in order to obtain results within a reasonable time frame a pass energy of 20eV was used for the high resolution scans. When running with a pass energy of 20eV with the Mg anode the overall resolution of the system is 0.84eV and we were able to detect binding energy shifts of the order of 0.1eV.

The Theory of the emission process

Each element has characteristic electron energy levels denoted by their principal quantum numbers n (1,2,3,4 etc.), their orbital angular momentum quantum number l (labelled s,p,d,f for l=1,2,3,4 etc.) and their total angular moment j (1/2,3/2,etc.). The s orbitals are a single energy level however for all other orbitals the spectra is split into a doublet due to spin-orbit coupling. Spin-orbit splitting of the energy levels is to do with the interaction of the electron's spin magnetic moment $\boldsymbol{s}$ with the magnetic field created by its motion, its orbital magnetic moment $\boldsymbol{l}$. The total angular momentum $\boldsymbol{j}$ is given by equation 2.5.

$$\boldsymbol{j} = \boldsymbol{l} + \boldsymbol{s} \qquad\qquad (2.5)$$

As the electrons spin can be either ± ½ this means each level of $\boldsymbol{l}$ is split into two states $|\boldsymbol{j}| = |\boldsymbol{l} \pm 1/2|$ and each of these states has $2\boldsymbol{j} + 1$ degenerate sub-states, labelled by m_j with values ranging from $\boldsymbol{j},\boldsymbol{j}$-1...-$\boldsymbol{j}$. The lower value of $\boldsymbol{j}$ from the

pair occurs at the higher binding energy. The population of these two energy levels is governed by their degeneracy and is called the branching ratio. This ratio is determined by the orbital angular momentum of the energy level. For a p orbital (*l*=1) the ratio is 2:1, d orbital (*l*=2) 3:2 and f orbital (*l*=3) a ratio of 4:3 with the level with the highest value of *j* is the most populated. For example with *l*=1, *j* can be either 3/2 or 1/2. This results in a $p_{3/2}$ level with four-fold degeneracy and a $p_{1/2}$ level with two-fold degeneracy. Therefore the ratio of the peak populations is 4:2 and hence 2:1. A spin orbit split Cu 2p level is shown in figure 2.8. These different orbitals all have different lifetimes and ionization cross-sections.
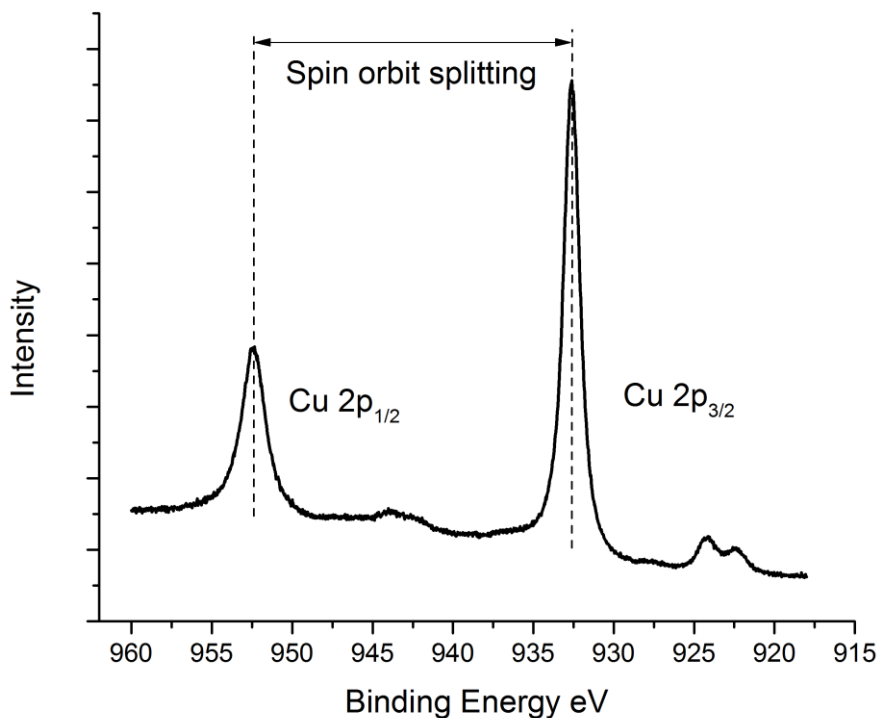
Figure 2.8: Spectrum showing the spin orbit splitting observed for the Cu 2p orbitals

The binding energy "felt" by an electron is sensitive to the local environment of the electron and the atom's charge state, as chemical shifts change that local environment they can be probed with XPS. This is due to a re arrangement of the electrical density when a chemical change occurs. In a simple approximation these shifts can be seen as a change in the shielding of the attraction from the nuclear core. The removal of an electron from an atom for example when a metal is oxidized, where an electron from the metal is then re-located to the oxygen atom, and so the charge density around the metal atom has been reduced. This means the remaining electrons "feel" a stronger nuclear force as there is less shielding and this can be seen as shifts in binding energies measured with XPS. Multiple chemical states may be present in a sample, for example if a metal has a thin oxide, only some of the metal atoms will be oxidized and so both chemical states will be seen as shown in figure 2.9. Shifts can also be caused when a material changes structure, for example a Mott transition when a metallic system becomes an insulating one, due to the redistribution of charge with respect to the anions and their relevant overlap of orbitals [7]. By measuring these shifts in energy different species in binding sites and their relative intensities can be identified.

The simplified view of XPS is that the system remains unchanged after the creation of the hole [1]. In reality the system will re adjust with the remaining electrons partially shielding the charge the ejecting electron feels from the nucleus. This appears as an apparent increase in kinetic energy and is known as intra-atomic relaxation [8].
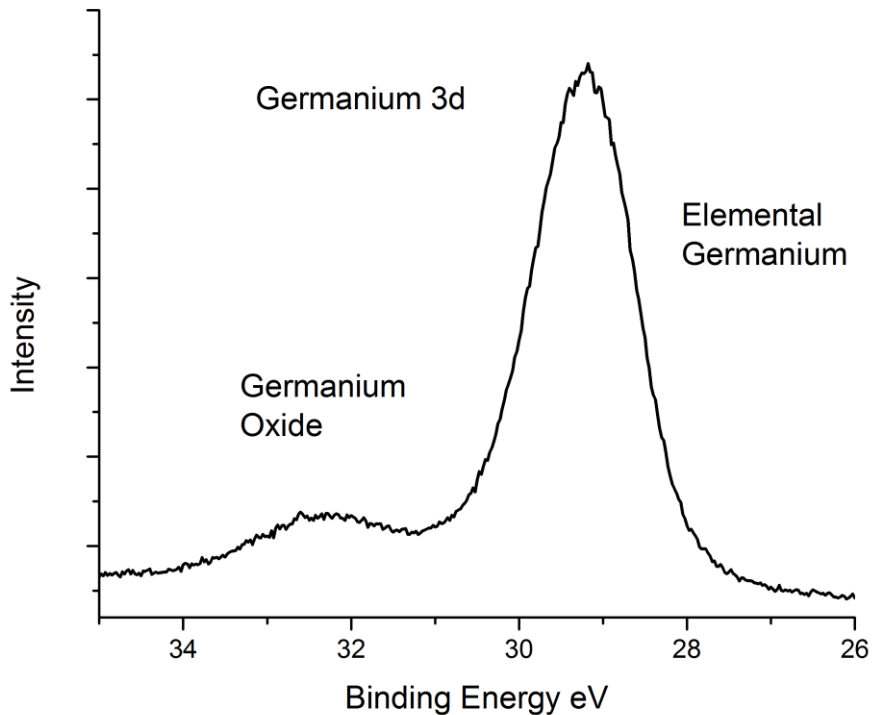
Figure 2.9: Spectrum showing signal arising from both the oxide (surface) and clean germanium (bulk) of a wafer

In a solid material where valence electrons can be more mobile as they are weakly bound, especially in metals, they can also re-arrange to shield the potential of the hole created during ionization. This once again is seen as an apparent shift in kinetic energy. In a solid material with a band structure with available states around the Fermi level the outgoing photoelectron can interact and excite a valence electron, seen as an increase in its binding energy equal to the energy needed to excite the electron to an available orbital. The interaction leading to electron hole pairs manifests itself as a tail on the higher binding energy side of the core level peaks of systems with a high number of electrons near the Fermi level, such as metals. The electron can also interact with

plasmons during its journey to the surface and the study of these satellites can give information about electronic states around the Fermi level.

The analysis of PES spectra

The analysis of XPS spectra involves fitting peaks to the experimental data in order to extract information about binding energies and compositions. Although the energy levels probed are discrete and sharp the measured peaks are broadened due to experimental effects. The line shapes routinely used in the XPS fitting in this thesis are the product of a Gaussian and a Lorentzian or the asymmetric Doniach-Sunjic line shape for metal samples due to the high number of electrons close to the Fermi level. A peak analysis package using a least squares fitting routine is used to fit these peaks to the data. In this thesis the commercial software CASA XPS was used [9]. In order to attribute for both the Gaussian nature of the statistics when counting, and the Lorentzian broadening due to the lifetime of the states a convolution of these line shapes is employed. This convolution of two broadening features is known as a Voigt function, and the form of the Voigt function used in this thesis is the product of a Gaussian and a Lorentzian (GL) given by equation 2.6 [10].

$$GL(x:F,E,m) = \frac{e^{-4ln2\left(1-\frac{m}{100}\right)\left(\frac{x-E}{F}\right)^2}}{1+\frac{4m}{100}\left(\frac{x-E}{F}\right)^2} \qquad (2.6)$$

The numerator in this expression is the Gaussian contribution while the denominator is the Lorentzian contribution. F is related to the FWHM of the peak, E is related to the centroid value of the peak and m is the mixing ratio of

Gaussian to Lorentzian, a value of *m=0* reduces the equation to the first term and is completely Gaussian.

An asymmetric line shape is needed to fit metallic peaks as mentioned above and the Doniac Sunjic line shape was used in this thesis [10], given by equation 2.7

$$DS(x{:}\,\alpha, F, E) = \frac{cos\left[\frac{\pi a}{2} + (1 - \alpha)\tan^{-1}\left(\frac{x - E}{F}\right)\right]}{(F^2 + (x - E)^2)^{(1-\alpha)/2}} \quad (2.7)$$

where α is an asymmetry parameter. This line shape is convoluted with a Gaussian to account for instrumental broadening. The effect of varying the asymmetry parameter is shown in figure 2.10.
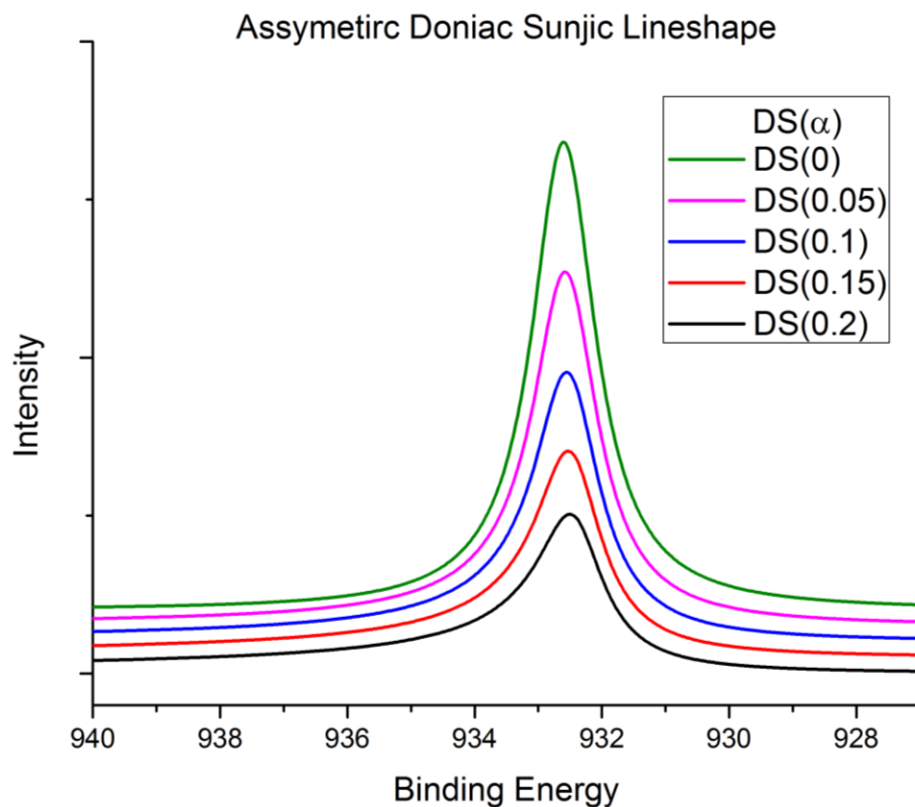
Figure 2.10: Doniac Sunijc line shapes showing the effect the asymmetry parameter α has on the peak. The lines have been offset in intensity to allow for easier comparison

The peaks in an XPS spectrum sit on top of a background generated by electrons that have lost energy after being ejected from the orbital on their path to the surface. A widely used background in XPS analysis is the Shirley background in which the intensity of the background is proportional to the intensity of the total peak area above the background in the lower binding energy peak range as shown in figure 2.11 [11].
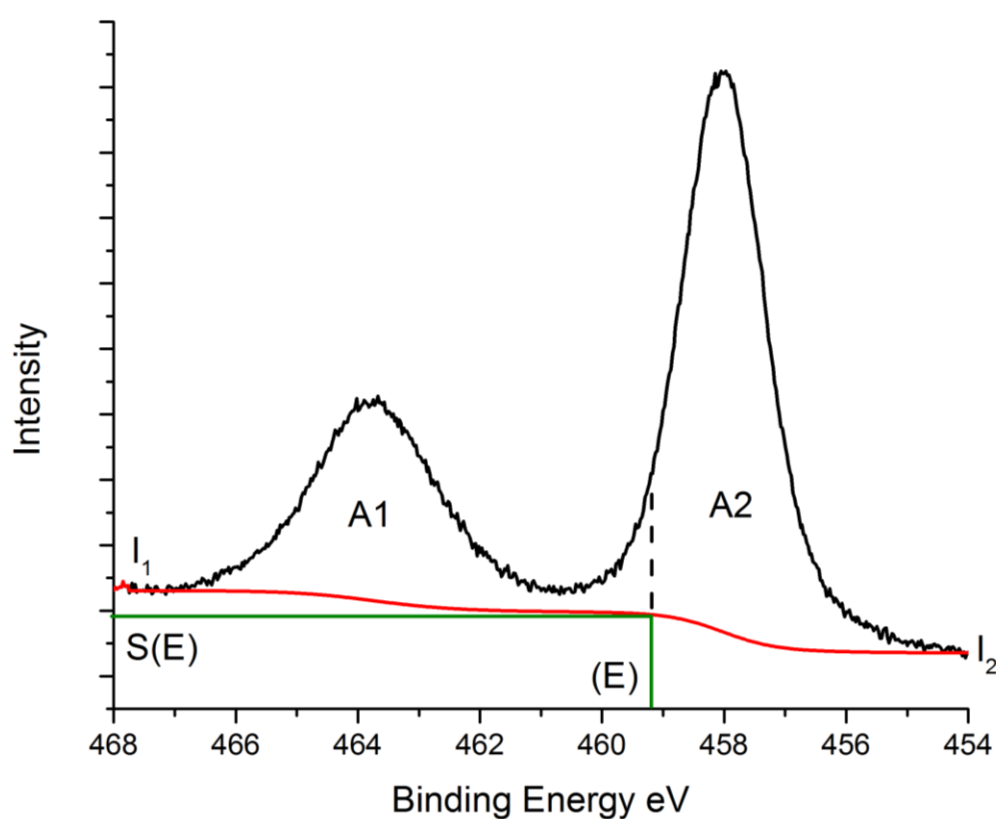

Figure 2.11: Spectrum showing Shirley background for a doublet peak

The intensity of the Shirley background shown in figure 2.11 is given by equation 2.8 [10]

$$S(E) = I_2 + \kappa \frac{A2(E)}{A1(E) + A2(E)} \tag{2.8}$$

where I_2 is the intensity at the low binding energy edge of the region to be evaluated and κ defines the step in the background from the start of the region to

the end, and is given by ($I_1 - I_2$).

The line shapes and background above were used to evaluate different chemical species in the sample. The errors when extracting peak areas were given by the CASA XPS software and were calculated by running a Monte Carlo routine that looks at how many different ways the data could be fitted. By minimising the difference between the data set and the sum of the fitted functions the above line shapes were fitted to the experimental data. As multiple species may be present in a spectrum it is often useful to use reference spectra. By fitting these elemental reference spectra, for example a clean copper sample, parameters such as the FWHM and the asymmetry can be obtained and used in later fitting procedures.

Once the spectra have been processed using the peak fitting procedures quantitative analysis can be done. Binding energy shifts can be used and compared to literature values to ascertain the different chemical species in the surface region. In order to calculate information on the stoichiometry, the composition of the sample is analysed by comparing the areas of the different energy levels. A wide energy survey scan is first done like the one in figure 2.12. In figure 2.12 as well as peaks relating to emission from core levels we also see peaks related to the Auger process. The Auger process occurs after the ionisation of a core level. An electron from a higher energy relaxes into the now available vacancy, the energy it gains from this transition is transferred to another electron ejecting it from the material. This ejected electron is called an Auger electron whose energy depends not only on the core levels involved in the transition but also the excitation energy [1].
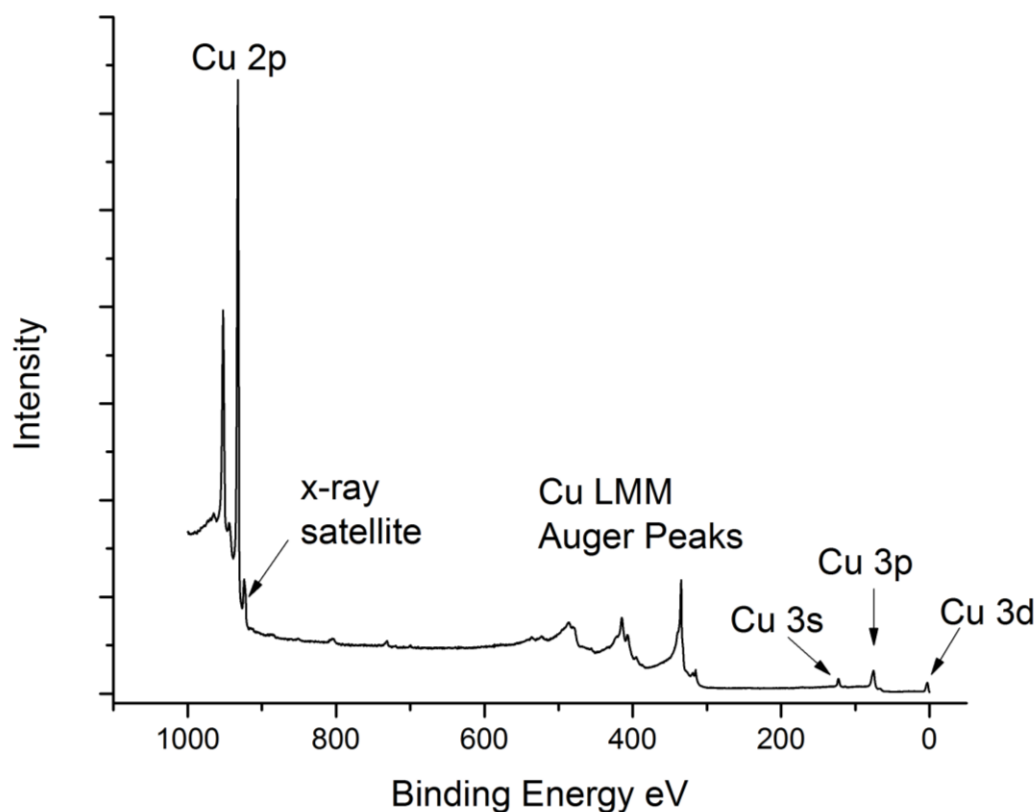
Figure 2.12: Survey spectrum from a clean copper sample taken with a magnesium anode hv = 1253.6eV

From this survey spectrum the different elements present in the sample can be identified. Higher resolution scans are then done on the strongest orbitals for each of the elements and other regions of interest such as the valence band. The measured intensities of these orbitals first need to be corrected to allow for their different cross sections for ionization. These cross sections are empirical values and dependent on the source and the geometry of the experiment. These atomic sensitivity factors were sourced from the Wagner handbook of XPS and the values for the geometry closest resembling our experimental set up were used [12]. These cross sections are used to correct the measured intensities and calculate the fractional atomic composition using equation 2.9 [12-15]

$$\chi_A = \frac{\dfrac{I_A}{S_A}}{\sum_i \dfrac{I_i}{S_i}} \qquad\qquad (2.9)$$

where the fractional composition of element A in the sample is χ_A, I_A is the measured peak intensity from A with S_A the sensitivity factor for the orbital. All other elements need to be accounted for in the summation in the denominator, where I_i is the measured peak intensity from element I with sensitivity factor S_i. This normalisation using cross sections arises from the fact that the ratio of XPS signals when normalised, is proportional to the relative atomic ratio of species within a homogeneous sample [11].

Ultraviolet photoemission spectroscopy

Ultraviolet photoemission spectroscopy (UPS) is used to study the valence bands due to the high cross sections for absorption of ultraviolet radiation and its narrow line width. As well as providing information on valence orbitals it can also be used to calculate the work function of the surface as detailed below. A UPS spectrum from a clean copper single crystal is shown in figure 2.13. There are three main features in the UPS spectrum. They are the secondary electron cut-off, the valence bands and the Fermi level. Electrons at the cut-off are those who have been excited by the source, but then have lost energy through interactions and left with the minimum energy needed to escape the surface.
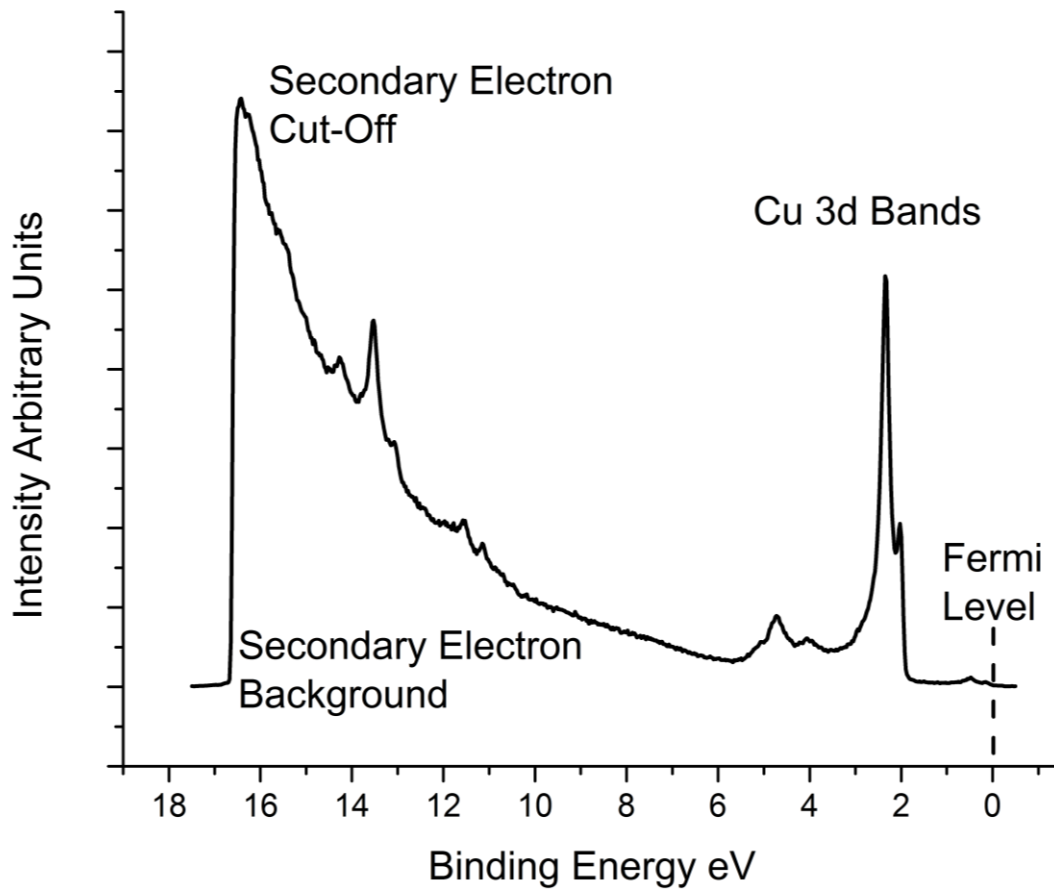
Figure 2.13: UPS spectrum from a clean Cu(110) single crystal

Inelastically scattered electrons like those at the secondary cut-off are the origin of the background in the UPS measurement. This means that by knowing the energy of the ionizing radiation and the energy of the cut-off the work function Φ of the surface can be calculated using equation 2.10.

$$\phi = h\nu - w \qquad (2.10)$$

where the photon energy used $h\nu$, was 21.2eV (He 1 line) and w is the energy difference between the most and least energetic photoelectrons, the Fermi edge

and the secondary cut-off respectively. The position of the Fermi edge is determined by fitting a step up function to the edge using the CASA XPS software [9]. A fitted Fermi edge for a copper sample is shown in figure2.14. At OK the Fermi level is a Heaviside step function that is broadened at higher temperatures. The position of the edge determined by the fitting is then set as 0eV binding energy.
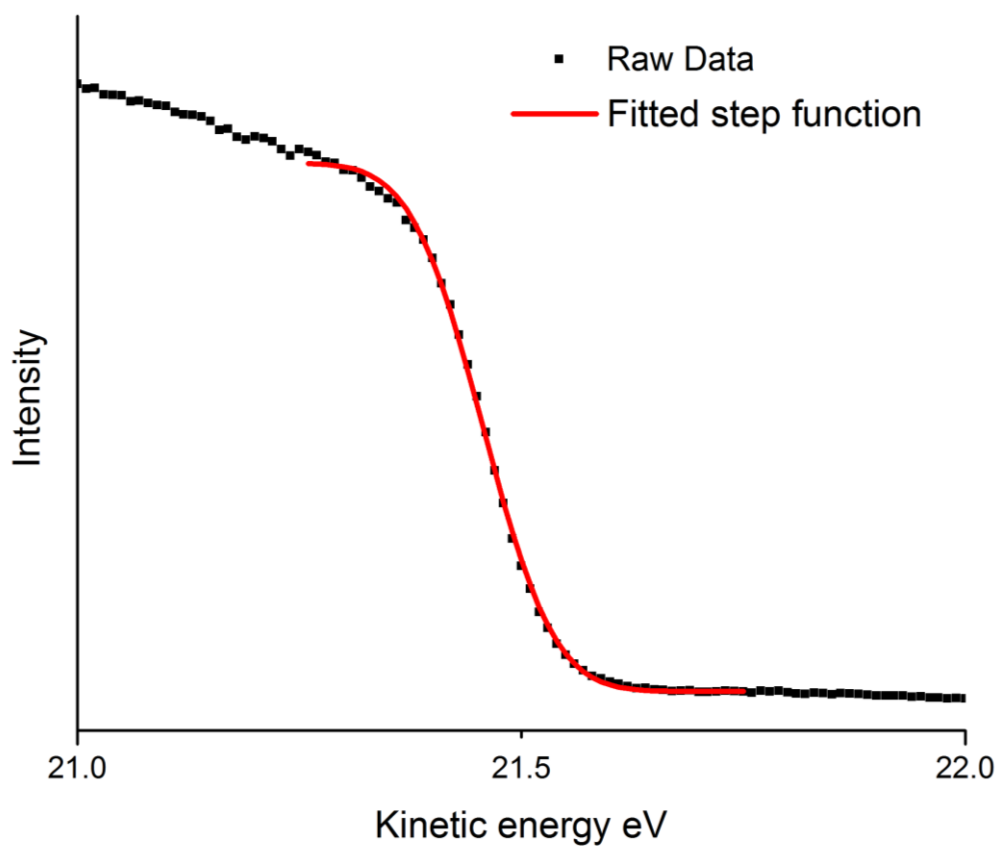
Figure 2.14: Step function fitted to the Fermi edge of copper sample

The position of the secondary electron cut-off was determined by linear extrapolation of the edge to the background level as in other studies [1617]. The UPS spectra were measured with a pass energy of 2eV, using equation 2.4 gives the analyser resolution as 0.1eV. There are several techniques available to measure the work function of a sample that can be divided into two categories,

absolute and relative. Absolute methods measure electrons emitted from the surface such as UPS and thermionic emission at high sample temperatures. Relative methods measure the difference in contact potential between the sample and a reference probe such as Kelvin probe force microscopy (KPFM). This requires a good knowledge of the work function of the reference probe. The other main difference between the techniques is the area of the sample that is studied. As the work function can vary across a surface the area sampled is important. The value found for the work function when using UPS is the lowest value on the illuminated part of the sample, KPFM gives a much more localised value but can be used to produce work function maps of the surface.

Contamination or absorbing materials onto a surface may alter the work function and this is detected as a movement of the secondary cut-off position. Changes of the order of 1eV in the work function are common for metals and semiconductors. Electric dipoles present at the surface can be modified which change the energy an electron requires to leave the sample. The value of the work function of a surface is important in semiconductor junctions where barriers can arise from work function differences. Due to the sensitivity of the work function to the condition of the surface it can provide information about its chemical state, such as the quenching of surface states with sub monolayer adsorbate layers. When measuring the secondary cut-off it is necessary to place a negative bias on the sample. If no bias is applied, signal from secondary electrons generated within the analyser after collision from photoelectrons will overlap with the secondary electrons ejected from the sample [16]. By biasing the sample these electrons are shifted away from the cut-off allowing better

determination of its position. It position can be determined to within 0.1eV, and this is the error on the assigned values of the work function.
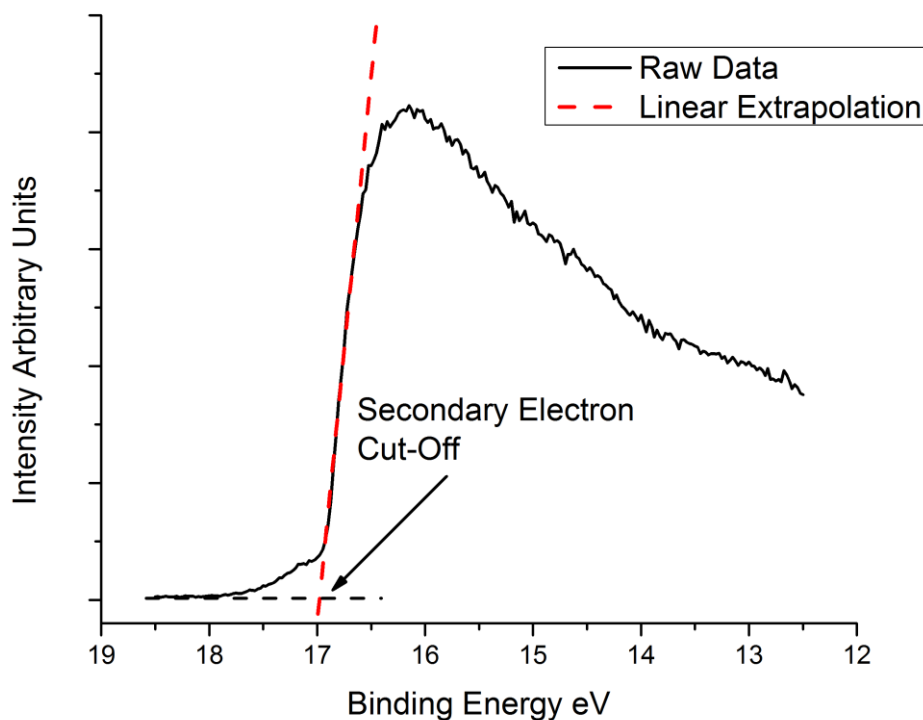

Figure 2.15: Showing the linear extrapolation of the secondary electron cut off for determining the work function of a surface

Low energy electron diffraction

Low energy electron diffraction (LEED) is a useful technique when studying the crystallographic structure of a surface and is commonly used to assess the quality of the surface. There are two ways in which the data from a LEED experiment can be used.

By inspecting the size and symmetry of the diffraction pattern observed information about the unit cell and subsequent over-layers can be deduced, such

as the spacing of the over-layer and its rotational symmetry with respect to the unit cell. The sharpness of the peaks observed also give an indication to the long-range order of the surface, when looking at a clean surface random defects or crystallographic imperfections will broaden the diffracted peaks. When single crystal metal samples where prepared by cycles of sputtering and annealing their cleanliness was first checked with XPS and the quality of the surface was then assessed with LEED.
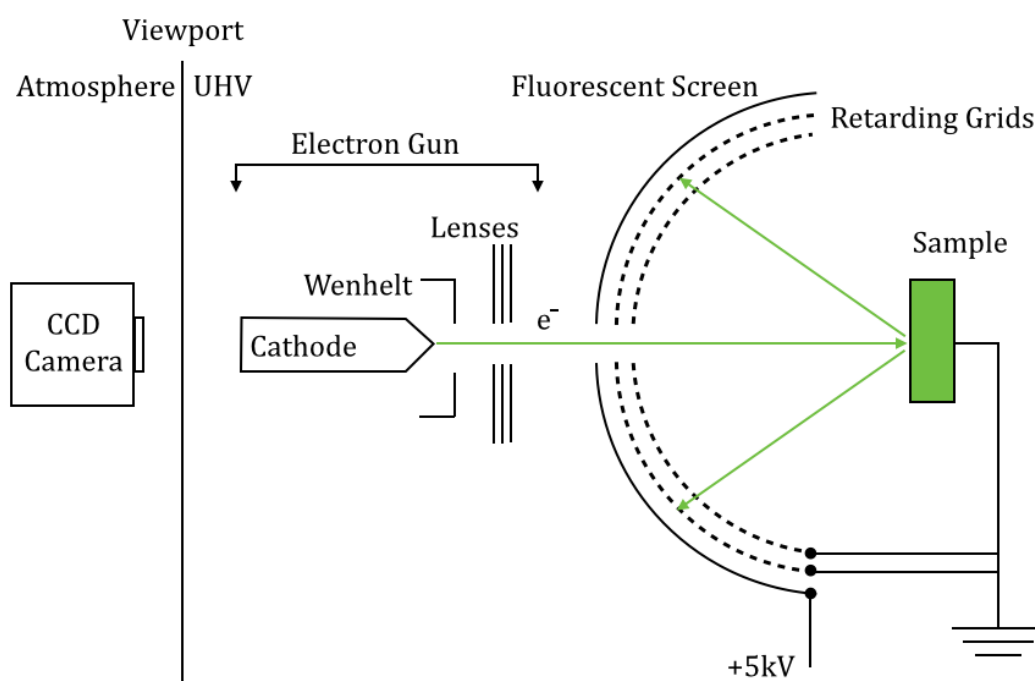

Figure 2.16: Schematic diagram of a typical rear view LEED optics

Measuring the intensities of the diffracted beams as a function of the incident electron beam energy can produce a more quantitative study. The experimental intensity vs. voltage (IV) curves can be compared to a theoretical model, where the electron diffraction is simulated and the intensities recorded. Refinement of

parameters in the model to allow the theoretical curves to resemble the experimental ones enables atomic co-ordinates to be calculated.

The diffraction patterns are produced using a LEED optic instrument, a schematic representation is shown in figure 2.16. The electron gun consists of a cathode (a thoriated tungsten filament) to generate the electrons with a Wenhelt ring and lenses to focus and accelerate them toward the sample. The grids then filter the backscattered electrons allowing only those elastically scattered to pass through to impinge on the phosphor screen and fluoresce. Typical electron energies used range from 20-500eV meaning that they have an inelastic mean free path of around 5 – 10 Å. The result is that the information obtained from LEED is extremely surface sensitive with all the information arising from the top few monolayers. The de Broglie wavelengths λ of the electron is given by equation 2.11

$$\lambda = \frac{h}{p} \qquad (2.11)$$

where h is Planck's constant and p is the momentum of the electron. By substituting in the electrons momentum under the accelerating potential this gives equation 2.12

$$\lambda = \frac{h}{\sqrt{2m_e eV}} \qquad (2.12)$$

where m_e is the mass of the electron, e is the elementary charge and V is the accelerating potential. For the electron energies used in LEED the de Broglie wavelengths range from 2.8 Å at 20eV to 0.5 Å at 500eV. These wavelengths are equal or smaller than the atomic spacing at the surfaces of solids and therefore are able to produce diffracted beams from these structures. Due to the periodic arrangement of the atoms in a surface some of the electrons will undergo elastic

scattering where they are diffracted back towards the screen with the same energy they were accelerated to by the gun. However other electrons will undergo inelastic scattering due to interactions within the sample. These electrons will have lost energy and so if they make it out of the sample will head towards the screen with a lower energy than those that were emitted by the gun. Little useful information can be obtained from these inelastic electrons and so to improve the ability to detect the elastically scattered beams a series of grids to which negative potentials are applied retards them. The sample must be grounded so as to not charge up from the electron beam and is typically orientated at normal incidence to the optics resulting in the diffraction pattern occurring at the centre of the phosphor screen. The grounding of the sample also ensures a field-free region between the sample and the first grid in the LEED optics. In order for the electrons to have a high enough energy to cause fluorescence upon impacting the screen they are first accelerated by a potential, typically around 5 kV, producing a pattern like the one in figure 2.17. This LEED image is obtained from a clean single crystal Cu(110) surface. The rectangular symmetry of the surface can be seen with the unit lattice vectors *a** and *b** overlaid onto the image. In order to record images of the diffraction patterns and to carry out LEED-IV analysis a CCD camera is attached to system and is programmed to capture images as the electron beam energy is being varied using the OCI Vacuum MultLeed interface [18]. Line profiles were taken through the diffraction patterns to measure the reciprocal lattice vectors of the clean surfaces. The lattice vectors of later structures are then given relative to the clean substrate for which the lattice values are known. In order to compare

these images care needs to be taken to ensure the sample is at the epicentre of the spherical optics.
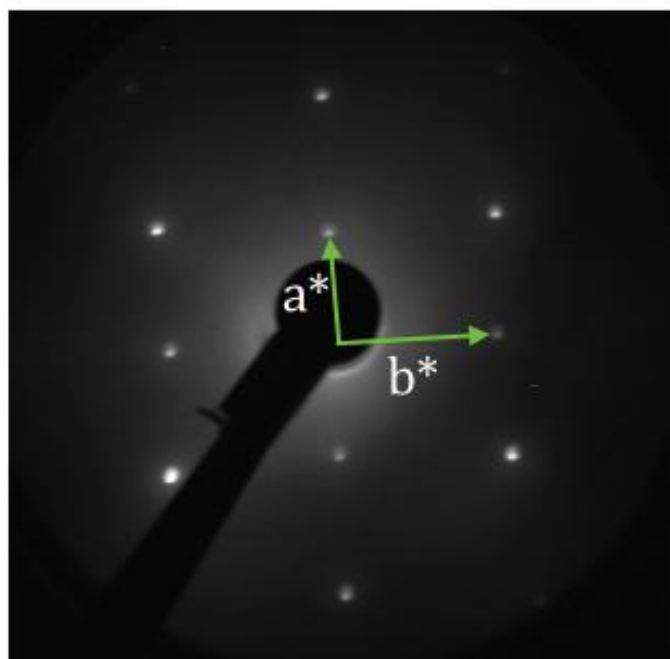

Figure 2.17: LEED pattern from a clean Cu(110) single crystal taken with a beam energy of 212eV

The reciprocal lattice vectors were then measured by taking line scans through the images to determine the peak position. The working distance for this LEED optic is 75mm and the sample was positioned using the sample manipulator. The accuracy of the sample stage position is 0.1mm, so that is an error of ~1%. This leads to an error due to sample position on where the beam hits the phosphor screen. The error in this beam position is found to be 0.2%, so when comparing lattice vectors in terms of a percentage increase or decrease there is an error of ±0.1%, where the fractional errors on each vector value were added in quadrature.

The transfer width of a LEED system is related to the coherence length of the incoming wave of electrons and determines the largest resolvable structures. In the theory of LEED the incoming electrons are described as a plane wave and therefore all electrons emitted at the same time will be coherent. The real case however is that the wave front is that of a spherical wave, and so even for electrons which were emitted at the same time there is only a certain length of the beam where they are coherent. The coherence length depends on both the energy spread of the electrons emitted and their angular divergence. For a typical LEED experiment this coherence length is around 10-20nm. As the spot size of the electron beam can be $1mm^2$ in size this means we have signal from many domains contributing to the final LEED pattern. If domains on the surface are larger than the transfer width, then scattering between the domains is incoherent and so the intensities of diffracted beams are summed. If the domains on the surface are smaller than the transfer width then scattering between domains is coherent, the amplitudes of the diffracted beams are added and so the LEED pattern will contain broadened peaks with possible interference patterns [1].

Theory of LEED

When looking at systems where one ordered structure has formed over another, such as adsorbates on a well ordered substrate, it is useful to define how they are related to each other. There are two main methods for doing this, the more general of which is the matrix notation proposed by Park and Madden [19]. The

over-layer vectors are related to the substrate vectors by a transformation matrix as in equation 2.13

$$G \begin{pmatrix} \boldsymbol{a_1} \\ \boldsymbol{b_1} \end{pmatrix} = \begin{pmatrix} \boldsymbol{a_2} \\ \boldsymbol{b_2} \end{pmatrix} \qquad (2.13)$$

where $\boldsymbol{a_1}$ and $\boldsymbol{b_1}$ are the substrate vectors, $\boldsymbol{a_2}$ and $\boldsymbol{b_2}$ are the surface vectors and the matrix G is defined as equation 2.14.

$$G = \begin{pmatrix} G_{11} & G_{12} \\ G_{21} & G_{22} \end{pmatrix} \qquad (2.14)$$

This gives the surface lattice vectors as equations 2.15 and 2.16.

$$\boldsymbol{a_2} = G_{11}\boldsymbol{a_1} + G_{12}\boldsymbol{b_1} \qquad (2.15)$$

$$\boldsymbol{b_2} = G_{21}\boldsymbol{a_1} + G_{22}\boldsymbol{b_1} \qquad (2.16)$$

The unit cells made up of these 2d lattice vectors are referred to as the mesh of the structure. The determinant of the matrix G ($det.G$) describes the type of relationship between the substrate and the adsorbate lattices:

a) $det.G$ is integral and all matrix components are integral, the two lattices are simply related with both sharing the same translational symmetry. The two lattices are commensurate.

b) $det.G$ is a rational fraction or if $det.G$ is integral and with some of the matrix components are rational fractions; the lattices are rationally related. The lattices are still commensurate however the actual surface mesh is larger than both the substrate and the adsorbate lattice. The size of this surface mesh is dictated by the distance over which the two lattices come into coincidence at regular intervals, this is known as a coincidence lattice.

c) *det.G* is irrational; the two lattices are incommensurate with no true surface lattice, the adsorbate forms a structure irrespective of the underlying substrate. [1]

These coincidence or superlattices can be seen as Moiré patterns which originate due to the mismatch of the adsorbate lattice to the substrate lattice. A Moiré pattern is used to describe the beating of any two short range periodic patterns to create a single long range quasi-periodic pattern [20]. Moiré patterns have been reported for many superlattices such as graphene on hexagonally symmetric metallic substrates and can be seen with STM or as additional peaks in the LEED pattern. The periodicity of the Moiré pattern can be used to calculate the mismatch between the two lattices.

While the matrix notation is entirely general and can accommodate structures where the over-layer is incommensurate with the underlying substrate, for most situations the more convenient Wood notation is used. In this notation the ratio of the length of the surface and substrate meshes are defined along with the angular rotation needed to align the two pairs of primitive translational vectors. For the (*hkl*) surface of material *X*, if the surface lattice vectors are given by $|\boldsymbol{a_2}| = p|\boldsymbol{a_1}|$ and $|\boldsymbol{b_2}| = q|\boldsymbol{b_1}|$ for adsorbate *A* and the surface mesh has to be rotated by an angle φ then the Wood notation for this structure is given in equation 2.17.

$$X(hkl) - (p \times q)R\varphi° - A \qquad\qquad (2.17)$$

Small modifications to this notation can occur for example to indicate when you have a centred unit cell instead of a primitive one. A primitive unit cell is one which contains only one atom, for example the p(2×2) over-layer shown in figure

2.18, the quarter of one atom is in each corner and so there is one whole atom within the unit cell. In a centred unit cell, such as a c(2×2) over-layer has an additional atom at the centre of the unit cell as well as those in the corners.
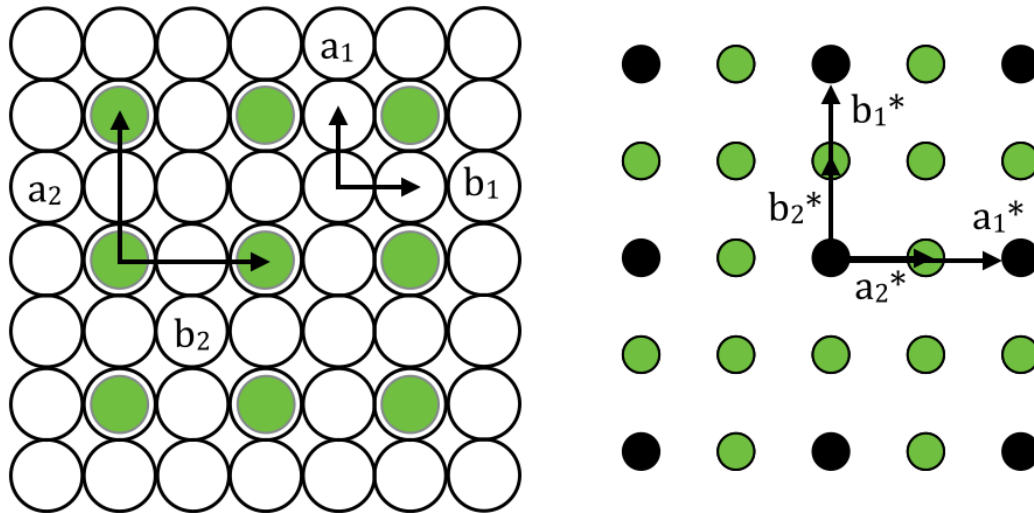

Figure 2.18: Example of an ordered p(2x2) over-layer on a cubic 100 surface with the corresponding LEED pattern produced. *a1*, *b1*, *a2* and *b2* are the lattice vectors for the substrate and over-layers respectively. *a1**, *b1**, *a2** and *b2** are the corresponding reciprocal lattice vectors

Diffraction techniques are important methods for investigating the structure of periodic systems. In these methods coherent elastic scattering is needed to form diffraction beams, these diffracted beams reveal the reciprocal lattice of the structure from which information about the translational symmetry can be obtained. As described by Bragg constructive interference will occur between beams reflected from parallel planes when the condition in equation 2.18 is fulfilled [21].

$$n\lambda = 2d \sin\theta \qquad (2.18)$$

The order of diffraction is n, λ is the wavelength of the beam, d is the spacing between adjacent planes and θ is the angle between the incident beam and the scattering planes as shown in figure 2.19
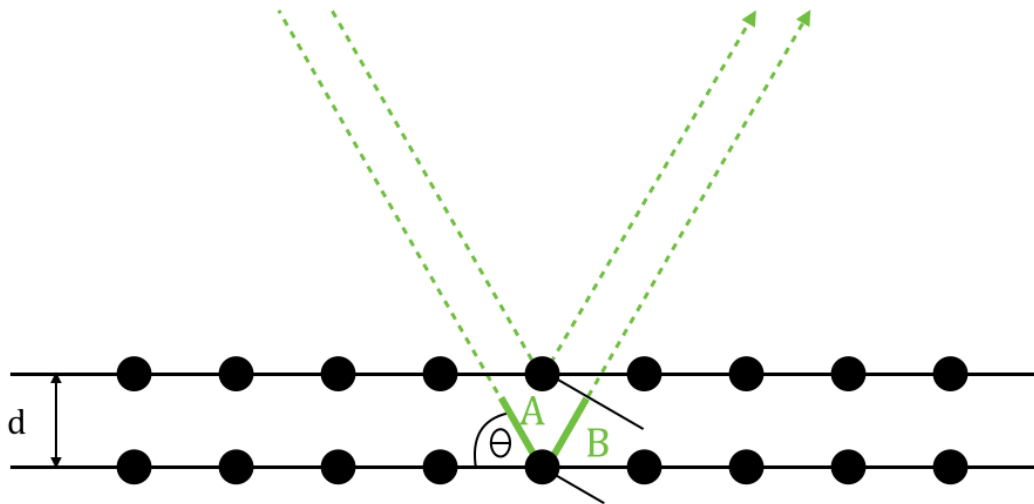
Figure 2.19: Model showing diffraction from parallel planes, the bold green sections A and B represent the different path lengths

The optical path difference (OPD) of the beams is the sum of lengths $A + B$ in figure 2.19. This gives the condition for constructive interference as equation 2.19.

$$OPD = 2d \sin \theta \qquad (2.19)$$

When the path difference is equal to an integer number of the wavelength constructive interference will occur. Within a crystalline sample there are many of these different atomic planes that are labelled by their Miller indices. The planes that we can see in a diffraction experiment are governed by the wavelength used and the geometry. Viewing diffraction in terms of these many planes can be difficult and so a different method was prosed by Laue [21]. For coherent elastic scattering to occur both the energy and momentum of the

scattered electrons must be conserved. For an incident wavevector k and the scattered wavevector k' the conservation of energy leads to equation 2.20.

$$k^2 = k'^2 \tag{2.20}$$

The conservation of momentum leads to equation 2.21

$$k' = k + G_{hkl} \tag{2.21}$$

where G_{hkl} is a reciprocal lattice vector for a structure periodic in 3 dimensions where h,k and l are integers.

$$G = ha^* + kb^* + lc^* \tag{2.22}$$

The reciprocal lattice vectors a^*, b^* and c^* are related to the real lattice vectors **a**, **b** and **c** by equation 2.23.

$$a^* = \frac{2\pi}{a}, \quad b^* = \frac{2\pi}{b}, \quad c^* = \frac{2\pi}{c} \tag{2.23}$$

Ewald's sphere allows us to visualise which diffraction peaks should be observed for a given wavevector. This 3d situation is the one encountered in synchrotron X-ray diffraction (XRD) and is used to asses the periodic quality of structures by assessing the width of the diffracted beams, as a loss of long range order leads to the diffracted beams broadening. It is constructed by drawing a sphere in reciprocal space whose tip is on a lattice point so the circumference passes through it as shown in figure 2.20 with a radius given by the magnitude of the wave vector k. Any of the reciprocal lattice points that intercept the sphere will satisfy the Laue condition and a diffracted beam will be produced.
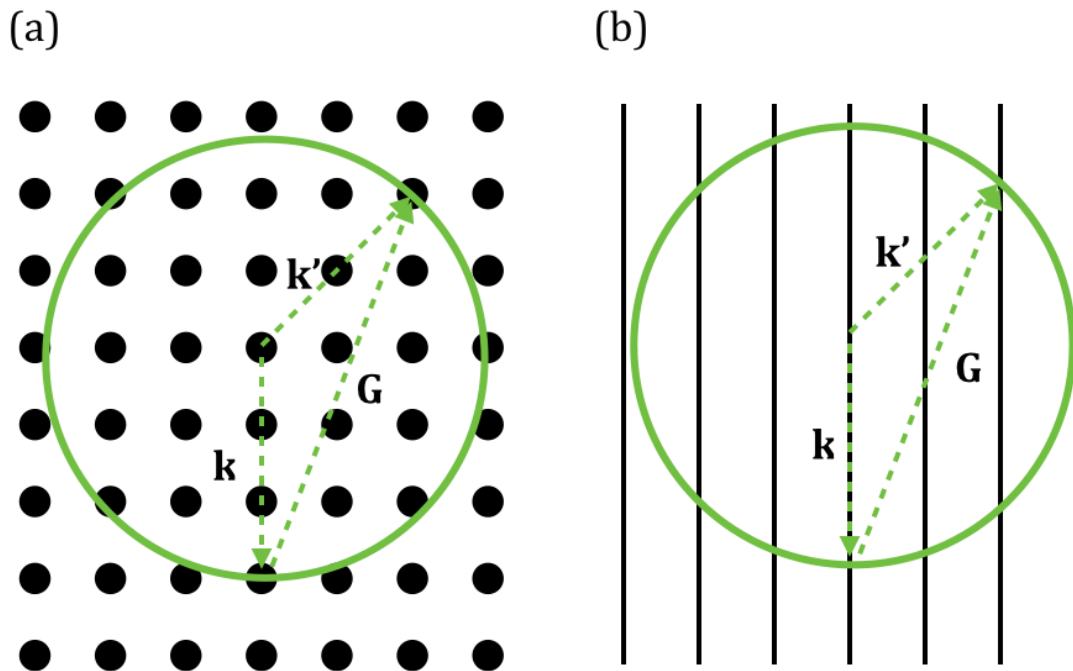
Figure 2.20: Ewald sphere in (a) 3D and (b) 2D situation, this 2D situation is the one encountered for LEED measurements

When diffracting from a material that is only periodic in two dimensions, for example the surface of a crystal, then the situation is modified. This is due to the lack of periodicity perpendicular to the surface, meaning that the wavevector's momentum parallel to the surface $\boldsymbol{k}_{\parallel}$ must be conserved but not the perpendicular momentum $\boldsymbol{k}_{\perp}$. The relaxation of the diffraction conditions changes the lattice points in figure 2.20 (a) to reciprocal lattice rods that extend perpendicular to the surface shown in figure 2.20 (b). The conservation of energy is the same as in equation 2.20 but now the conservation of momentum is given by equation 2.24

$$\boldsymbol{k}_{\parallel}' = \boldsymbol{k}_{\parallel} + \boldsymbol{G}_{hk} \tag{2.24}$$

where $\boldsymbol{G}_{hkl}$ is a reciprocal lattice vector for a structure periodic in 2 dimensions as in equation 2.25.

$$G = h\boldsymbol{a}^* + k\boldsymbol{b}^* \qquad\qquad (2.25)$$

The reciprocal lattice vectors $\boldsymbol{a}^*$ and $\boldsymbol{b}^*$ are related to the real lattice vectors $\boldsymbol{a}$

and $\boldsymbol{b}$ by equation 2.26

$$\boldsymbol{a}^* = \frac{2\pi}{a}, \quad \boldsymbol{b}^* = \frac{2\pi}{b} \qquad\qquad (2.26)$$

The atoms in a metallic system are arranged in such a way as to maximise the

number of bonds with neighbouring atoms by minimising the amount of open

space between them. Such an arrangement of atoms is known as close packing

[22]. In copper the atoms are arranged in a periodically repeating face centred

cubic (FCC) lattice. This lattice describes the locations of atoms within the bulk

of the material. When we cleave this bulk crystal to reveal a surface depending

on which plane of the crystal is cleaved, a different crystallographic surface will

be produced.
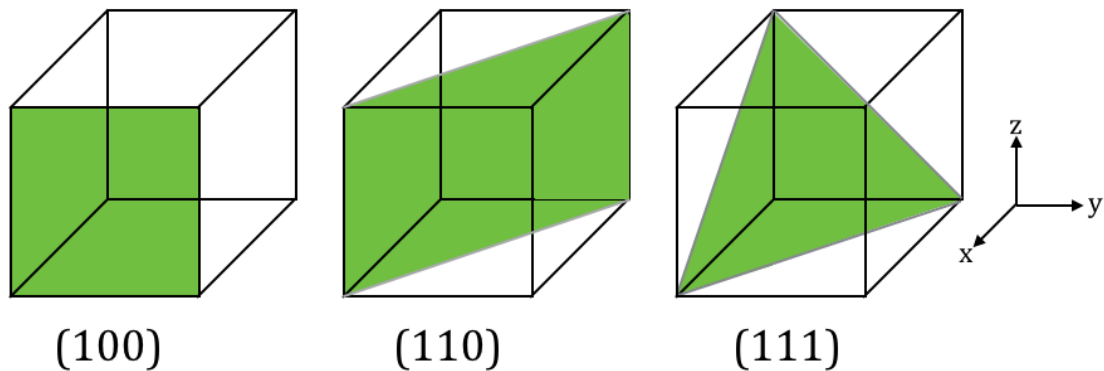
Figure 2.21: Low index faces for a cubic system with their Miller indices

The low index surfaces are the most widely studied as they have the most

ordered structures with the lowest amount of adsorption sites making their

study relatively more easy than high index surfaces [23]. Planes within crystal

are denoted with round brackets whereas directions within crystals with square

brackets. The planes cleaved are assigned Miller indices h,k and l. The low index planes of a cubic system are shown in figure 2.21. These indices are determined by first identifying where the plane intercepts the x, y and z-axis. These intercepts are than given in fractional co-ordinates of the unit cell, for example if we have a cubic cell with lattice constant a then we express then the fractional co-ordinates will be $\left(\frac{x}{a},\frac{y}{a},\frac{z}{a}\right)$. So for the plane in figure 2.22 whose intercepts are $(a,0,0)$ the fractional co-ordinates are $\left(\frac{a}{a},\frac{0}{a},\frac{0}{a}\right)$ and so $(1,0,0)$. The reciprocals of the fractional intercepts are then taken to produce the miller indices for the plane, in this case the (100) plane.
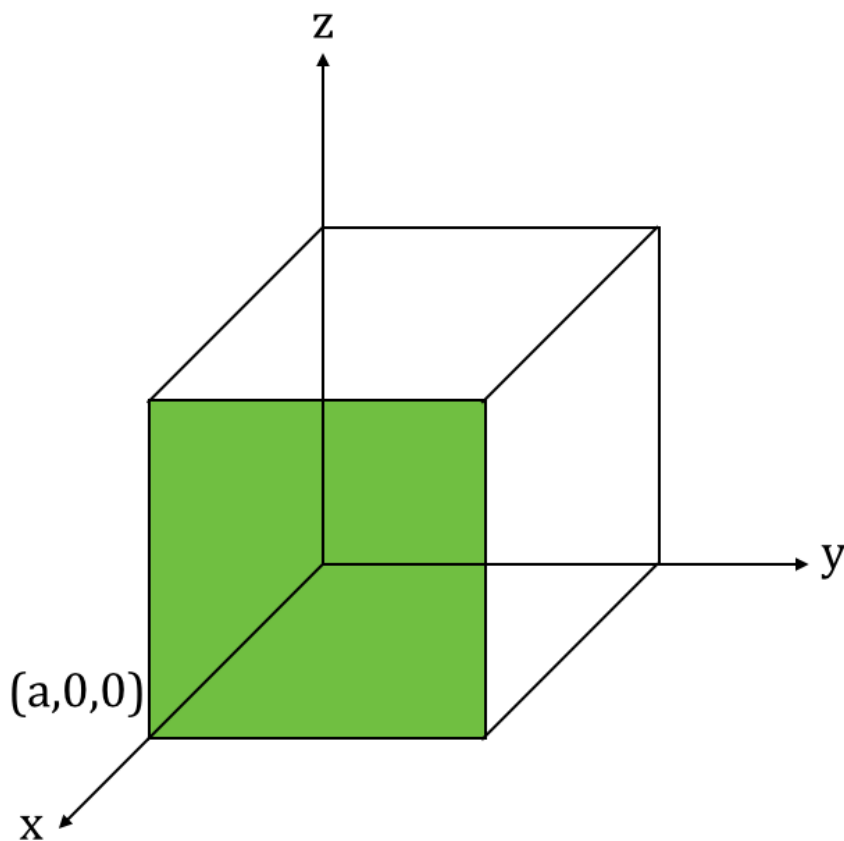
Figure 2.22: Plane to show assignment of miller indices

By cleaving the bulk crystal along the (111), (110) and (100) planes we can produce the 3 low-index surfaces of copper shown in figure 2.23.
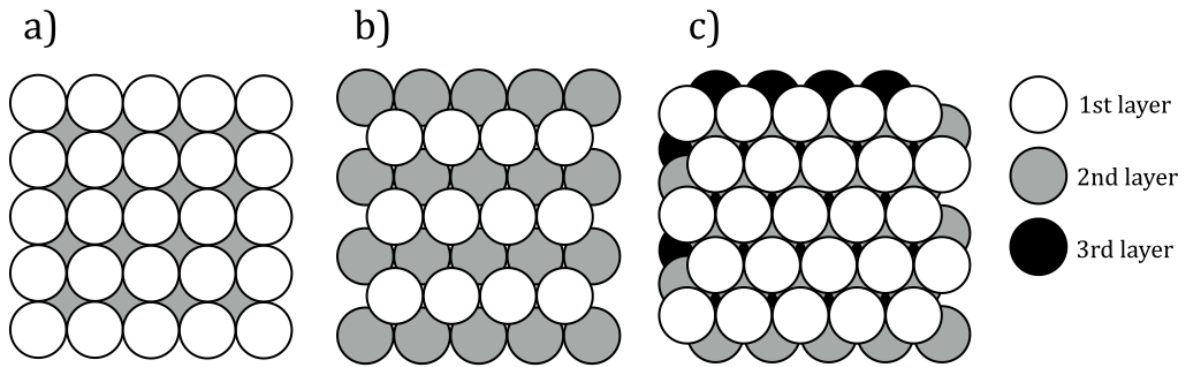
Figure 2.23: The 3 low index faces of an FCC material such as copper

A measure of how tightly packed the atoms are on these different surfaces is given by the planar packing fraction (PPF). This is calculated using the following equation 2.27.

$$PPF = \frac{area\ of\ atoms\ on\ plane}{area\ of\ plane} \tag{2.27}$$

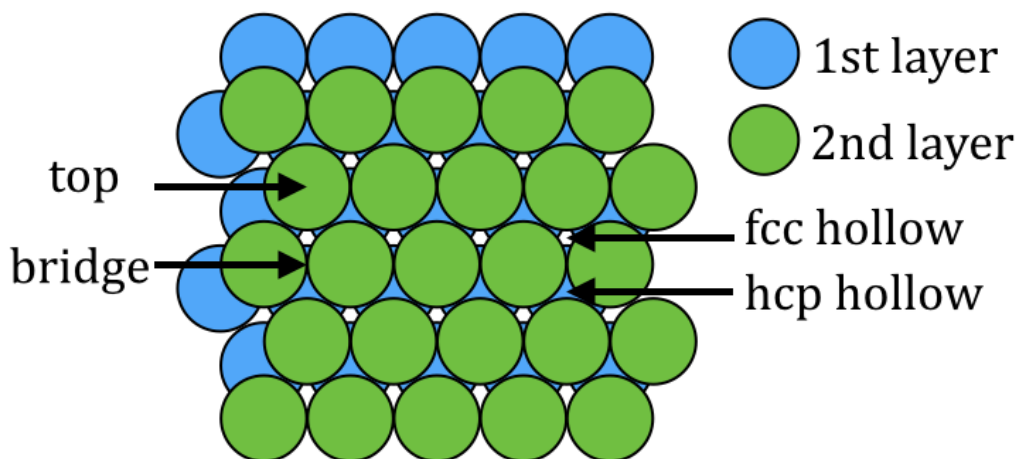The PPF for the 3 low index surfaces are 0.91, 0.79 and 0.56 for the (111), (100) and (110) surface respectively.

Figure 2.24: Adsorption sites on the Cu(111) surface

The adsorption sites of the Cu(111) surface are shown in figure 2.24. They are the top site, sitting directly above a copper atom, the bridge site, bridging above

two surface atoms and the FCC and hexagonal close packed (HCP) 3-fold hollow sites, sat within the depression between three surface atoms. The difference between the FCC and HCP hollow sites is due to the stacking of the FCC crystal. When building the crystal layer by layer we place the 2nd layer so that the atoms are sitting in the hollow sites of the first layer. We now have a choice when placing the third layer as to which hollow sites we place the atoms in. There are now two non-equivalent hollow sites on the 2nd layer, those where the atoms of the first layer lie directly beneath, and those that lie above the hollow sites of the first layer. If we place the atoms in the latter we arrive at the stacking sequence of layers for an FCC crystal, therefore this is called the FCC hollow site. If instead we put the atoms directly above those in the first layer (the HCP hollow site) then we produce the stacking sequence for a HCP crystal. Faults in this crystal stacking can occur for example if the surface layer atoms adopt the HCP sites instead of the FCC sites, the surface is said to be a faulted one.

Adsorbate atoms may also substitute the atoms within the surface to form an alloyed layer. If there is a size difference between the two atoms then incorporating the larger atom into the substrate lattice is expected to cause an expansion of the surface lattice vectors. The atomic radii of copper and tellurium are 128pm and 143pm respectively, that is an 11.7% difference in size and so we would expect the lattice to expand in the case of an alloy formation. This 2d expansion of the surface introduces biaxial strain to the layer as seen in several systems such as the surface alloying of silver on Cu(100). In this system the strain in the surface layer at higher coverages is large enough to drive a de-alloying of the silver leading to the growth of islands [24].

When we have a material such as a metal oxide made up of two elements, for example indium oxide, then the plane we produce can either consist of both the oxygen and metal atoms or it can be terminated by just one of them. Due to the ionic nature of the bonding in these metal oxides if we produce a plane that only consists of one of the elements then we will produce a dipole between the top plane and the plane below, this dipole will be repeated through the crystal and is known as a polar surface. However if we cleave the crystal to reveal a plane that contains both the metal and oxygen atoms then each of the layers of the crystal will be charge neutral and we will generate a non-polar surface. There are three types of repeating structure available as categorised by Tasker that are shown in figure 2.25 [25].
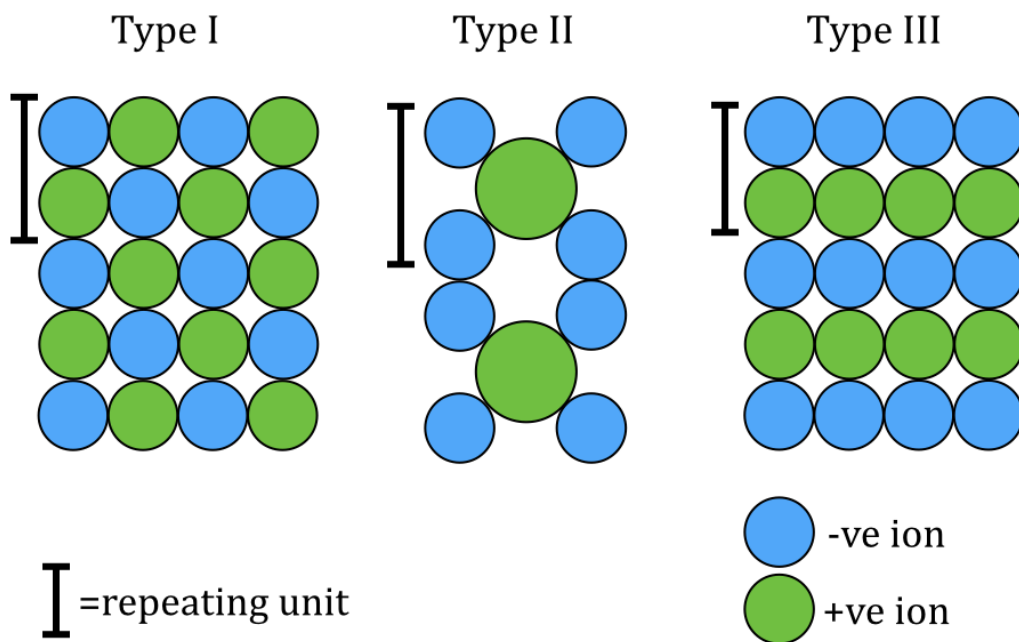
Figure 2.25: Tasker classification of polar surfaces, image modified from [25]

In the type I structure the repeating unit is charge neutral and there is no dipole. For the type II structure the individual layers are charged however the repeating

unit is charge neutral with no dipole. Both type I and type II structures are non-polar surfaces. In type III structure there is a dipole in the repeating unit and this produces a polar surface.

When a bulk crystal is cleaved to produce a surface the atoms at the surface may undergo reconstructions or relaxations to minimise the energy of the newly formed surface. For example the interlayer spacing between the surface atoms and the row of atoms beneath it may differ from that found in the bulk of the sample. Parallel to the surface atoms can also undergo a reconstruction, changing the periodicity of the surface [1].

Dynamical LEED

Basic geometric information about the surface can be obtained by examining individual LEED images, such as its symmetry, however for a more detailed description of the atomic co-ordinates at the surface a dynamical analysis is needed. Experimental intensity-voltage (IV) curves are collected by taking an image of the diffraction pattern for a range of energies, the individual peaks are then analysed by tracking their movement across the image with increasing beam energy. A box is placed around the peak that tracks the spot as well as calculating the intensity at each energy. This is done by taking the intensity of the pixels in the four corners of the box to be the background, then counting the intensity in the rest of the box above the background as the peak. In Dynamical LEED calculations a surface structure is proposed and modelled. Simulated IV curves are then produced and compared to the experimental data. Parameters within the model are optimized such as interlayer spacing until the best

agreement between experiment and theory is achieved. As this is a multi-parameter calculation an automated optimization package is used to find the structures which best match the experimental data. The calculations were performed using the Barbieri/Van Hove Symmetrized Automated Tensor LEED package (SATLEED) [26]. Due to the symmetry of the single crystals there are planes within the crystal that are symmetrically equivalent. For example the 6 planes that make up the faces of the FCC structure. Diffracted beams from these planes are symmetrically equivalent and therefore when analysing them they can be averaged together to improve the signal to noise ratio in the experimental data. [27]. As well as the geometrical parameters varied in the simulation there are other factors, such as the Debye temperature. This is used to calculate the Debye-Waller factor which accounts for the damping of diffracted intensities dues to atomic vibrations.

The commonly used quantitative measure for the level of agreement is the Pendry reliability or R factor [28]. This Pendry R factor places more importance on the positions of the maxima and minima in the *IV* curves rather than their relative intensities. The Pendry R factor uses the logarithmic derivatives *L(V)* of the intensity *I* of a diffracted beam as a function of incident beam energy *V* which is given by equation 2.28 [29].

$$L(V) = \frac{d(\log_e I(V))}{dV} \tag{2.28}$$

Another function needed to determine the level of agreement is the so-called *Y* function that is given by equation 2.29

$$Y(V) = \frac{L(V)^{-1}}{L(V)^{-2} + V_{oi}^2} \tag{2.29}$$

where V_{oi} is the imaginary part of the electron self-energy, this is related to the widths of the peaks in the IV curves. The Pendry R factor R_p is then given by equation 2.30

$$R_p = \sum_g \frac{\int \left(Y_{gth} - Y_{gexp}\right)^2 dV}{\int \left(Y_{gth}^2 + Y_{gexp}^2\right) dV} \qquad (2.30)$$

where the summation is taken over g diffracted beams. The subscripts *th* and *exp* denote the theoretical and experimental values. If there is a good correlation between the experimental and theoretical curves then the numerator will be small and the R factor will tend to zero. An R factor of R_p=1 represents a situation where there is no correlation between the theoretical and experimental curves. The lower the value of the R factor the more reliable the determined structure. Generally values of R_p< 0.2 is considered to be a good agreement, 0.2 < R_p <0.3 is considered a mediocre fit with values above 0.3 considered a bad fit. The error bars for the determined structures were calculated using the Pendry RR-function [29]. The variance of the R-factors was then calculated as the product of the minimum R-factor value and the RR function. This Pendry variance is then used to discount possible structures if their R-factor was larger than the sum of the minimum R-factor plus the variance. During the calculations each diffracted beam has its own R-factor. The overall R factor for the structure is obtained by weighting the individual R factors by their individual energy range, so those beams with the largest data sets more heavily influence the overall R factor.

Density Functional Theory

Density functional theory (DFT) was used to calculate the adsorption energies of tellurium at different sites on the copper substrate. This is the energy difference between the clean surface and the trialled structure. The calculations were performed using the Vienne ab-initio simulation package VASP [30-34]. The copper surface slab was modelled with 6 layers of copper atoms. Periodic boundary conditions are applied to the central cell so that it is reproduced periodically throughout out the xy plane.

The adsorption energy of a Te atom for the non-alloyed sites is defined as equation 2.31

$$E_{ads} = \frac{1}{N_{Te}} (E_{tot} - E_{clean} - N_{Te}E_{Te}) \qquad (2.31)$$

where E_{tot} is the total energy of the relaxed Cu/Te system, E_{clean} is the total energy of the relaxed clean Cu slab, N_{Te} is the number of Te atoms and E_{Te} is the energy of one atom in bulk Te metal. This is modified for the substitutional alloy structures to equation 2.32

$$E_{ads} = \frac{1}{N_{Te}} (E_{tot} - E_{clean} - N_{Te}E_{Te} + N_{Te}E_{Cu-bulk}) \qquad (2.32)$$

where $E_{Cu-bulk}$ is the total energy of a Cu atom in the bulk.

Scanning Tunnelling Microscope

A STM is used to provide information on the atomic structures of surfaces by measuring the interaction of a tip with the electron density of the surface. The high resolution of this technique, around 0.01nm resolution can be achieved in

the vertical direction and around 0.1nm resolution in the horizontal planes, allows individual atoms to be viewed and manipulated. Depending on the system to be studied a STM can be operated in either atmospheric conditions, within an electrolyte or under vacuum. In this thesis the STM used was housed in its own chamber on the UHV system.

The STM uses the process of quantum mechanical tunnelling to assess the height of a tip above the surface. When a bias is applied between the tip and the sample electrons quantum mechanically tunnel between them. The tunnelling voltages typically applied range in from a few meV to a few volts.
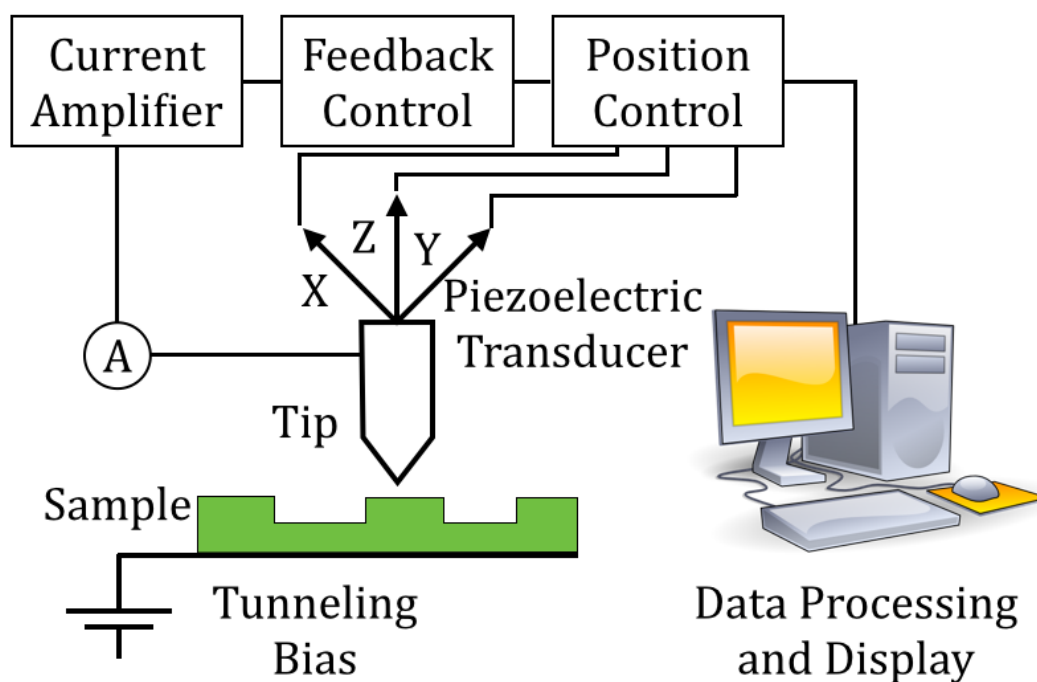
Figure 2.26: Typical setup for STM. An atomically sharp tip is brought close to the surface until a tunnelling current is observed. This tunnelling current is measured as the tip scans the sample to reveal surface details

Classically if an electron does not have the energy required to overcome a barrier it will not be able to penetrate it. However in quantum mechanics the wave function of the electron is predicted to exponentially decay within the barrier. This means there is a reduced but finite chance of the electron tunnelling through the barrier, it is only the probability of finding the electron that is reduced by the barrier not its energy, an electron that elastically tunnels through the barrier will have the same energy it did before encountering the barrier. Equation 2.33 shows the effect a barrier has on the incident wave function ψ.

$$\Psi(d) = \Psi(0)e^{-\kappa d} \tag{2.33}$$

The distance between the tip and the sample is d and κ is the inverse decay length. The larger the value κ the more rapidly the wave function decays within the barrier, κ is given by equation 2.34 [35]

$$\kappa = \frac{\sqrt{2m(\Phi - E)}}{\hbar} \tag{2.34}$$

where m is the mass of the electron, Φ the size of the potential barrier, E is the energy of the electron and $\hbar$ is Planck's constant. Due to this exponential relationship atomic changes in the height of the tip will result in measurable changes in the tunnelling current. By raster scanning the tip over the sample the topography can be plotted to reveal the electronic density of the surface.
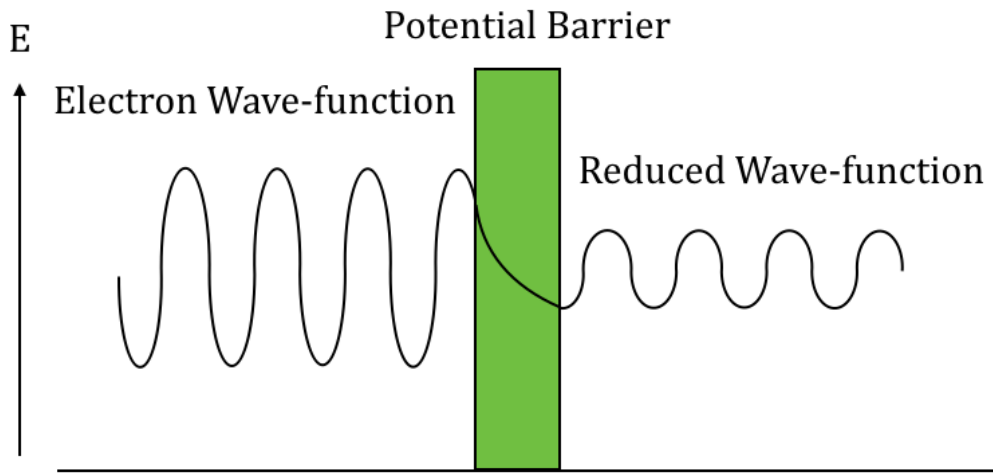
E

Potential Barrier

Electron Wave-function

Reduced Wave-function

Figure 2.27: Illustration of the decay of the electron wave function when travelling through a potential barrier

With the tip and sample both held at the same electrical potential their Fermi levels will line up and no current will flow. However by applying a bias between them we effectively raise one of their Fermi levels with respect to the other as shown in figure 2.28. So electrons in the higher energy states will tunnel into the now available lower energy states. This means the polarity of the bias between the tip and the sample determines whether electrons are tunnelling from the sample to the tip or vice versa. When a negative bias is applied to the sample its Fermi level is raised with respect to the tip's, so the tunnelling provides information from the occupied states of the sample to the unoccupied states of the tip.
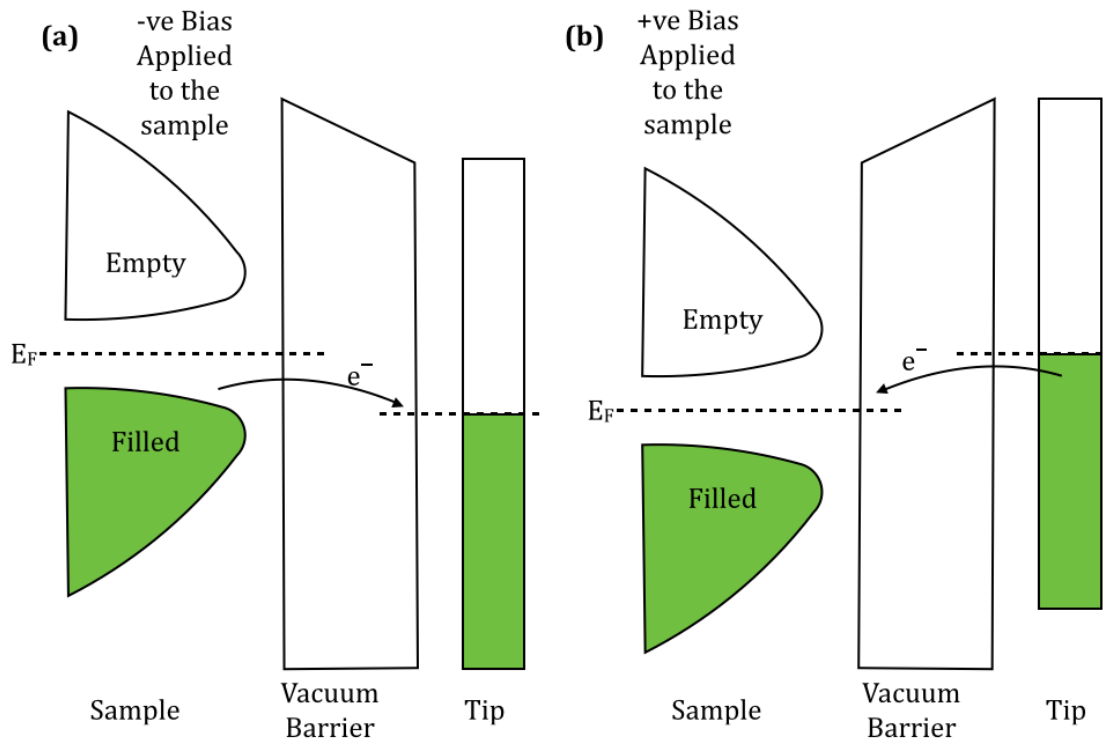
Figure 2.28: Energy level alignment between tip and sample when (a) a negative bias is applied to the sample and (b) a positive bias is applied to the sample

With a positive bias applied to the sample the opposite occurs as electron tunnels from occupied states within the tip to unoccupied states within the sample. As the orbitals that make up the occupied and unoccupied states can vary so can the images obtained when the bias is reversed.

Figure 2.29 shows a typical STM image of the surface of highly ordered pyrolytic graphite HOPG which shows the hexagonal symmetry known to exist on this surface.
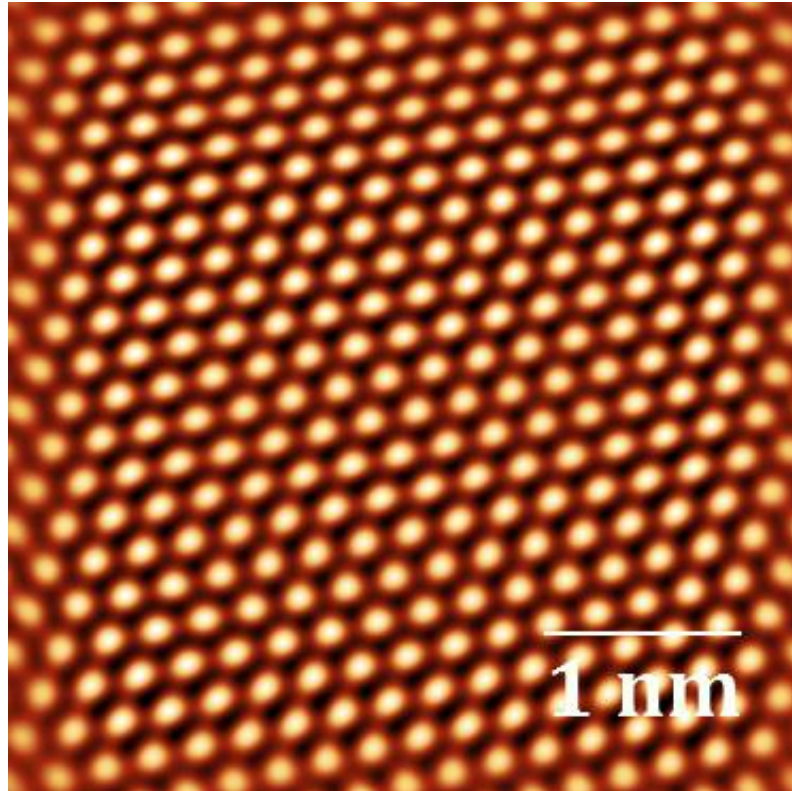
Figure 2.29: Atomic resolution STM image of HOPG taken with a sample bias of +0.3V and a tunnelling current of 500pA.

Two approaches can be taken with relation to control of the tip to sample distance in STM. It can either be operated in constant current mode or constant height mode. In both modes the tip is mounted on a scanner consisting of 3 piezoelectric arms, x y and z, and the sample mounted on a courser scanner for initial tip positioning and looking at different macro regions. Piezoelectric materials are ones whose physical dimensions can be altered by the application of an electrical potential. Likewise deformation of a piezoelectric material produces an electrical potential. This allows the position of the tip to be controlled and read back to the control system with a high precision.
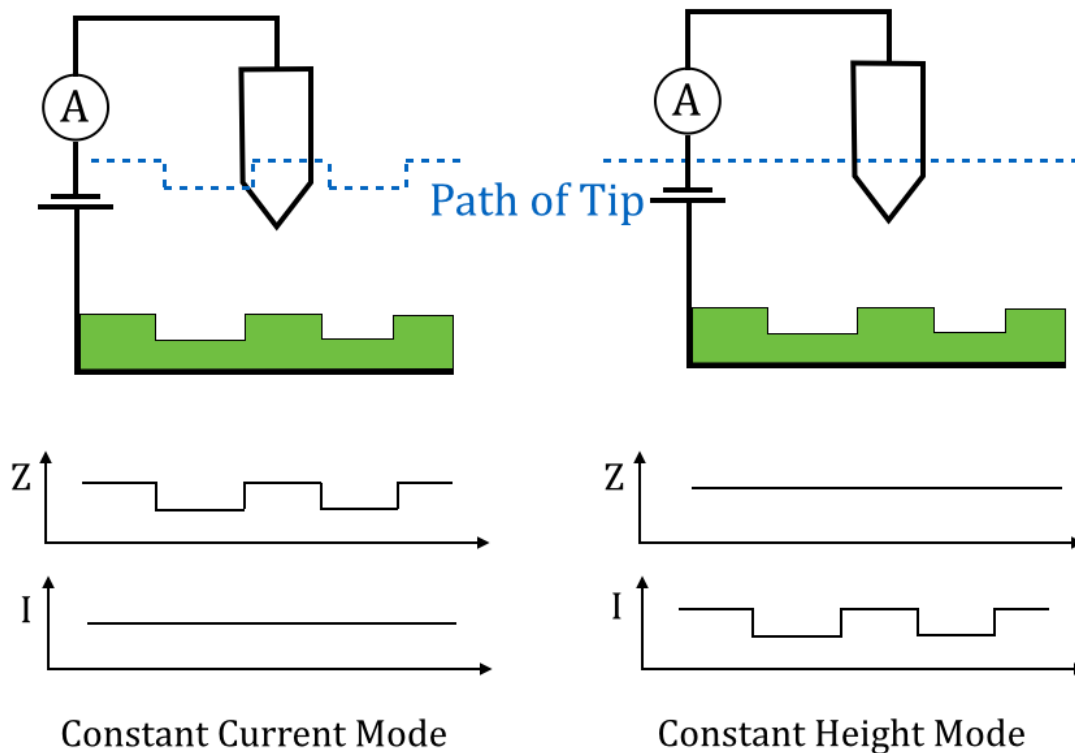
Figure 2.30: Two modes of operating an STM, constant current mode and constant height mode. The path of the tip as it scans the surface is shown for the two modes

In constant current mode the z piezo controlling the height of the tip is connected to a feedback loop, which maintains the set tunnelling current by varying the tips height as it is scanned horizontally over the surface. Plotting this tip height against the *x-y* co-ordinates allows us to view the electron density of the surface. In constant height mode the feedback loop is used in order to achieve the tip height required but it is then disconnected. The tip scans the surface at the fixed height determined by the size of the tunnelling current. For this method the sample needs to be extremely clean and flat as the tip will not move out of the way of defects or adsorbents and so can easily be damaged.

In order to achieve clear images an atomically sharp tip must be used. There are different methods of producing these tips such as cutting platinum iridium wires or electrochemically etching them from tungsten. In this thesis the tips were etched in a solution of potassium hydroxide KOH. The 0.28mm diameter tungsten wire was first cleaned with wire wool to remove any oxide and was then held vertically into the electrolyte and connected to the etching circuit.
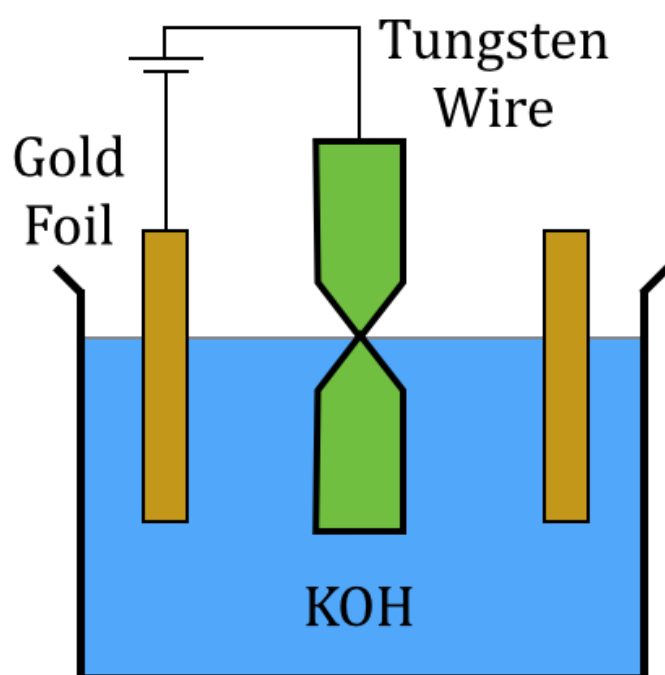

Figure 2.31: Diagram of the set-up for electrochemically etching tungsten STM tips

A gold foil is used as the other electrode and is placed into the electrolyte; the setup is shown in figure 2.31. When a bias is applied to the cell the tungsten begins etching away at the meniscus formed around it where it penetrates the liquid. This causes the wire to thin out until it too thin and cannot support the weight of the remaining wire. The wire breaks off leaving a sharp tip behind. It

is crucial that the bias is switched off here, as further etching will cause the tip to be blunt. That is why the power supply in the etching circuit is connected to a switch that detects the drop in current due to the wire snapping off and shuts off the applied voltage. The tip is then rinsed with distilled water to remove any electrolyte and then examined under an optical microscope. Suitable tips are then mounted on the tip plates, they are annealed in UHV and then conditioned while being used until they produce atomic resolution. This tip conditioning involves applying voltage pulses to the tip during scanning. These pulses serve to both clean and sharpen the tip however they must be performed on areas of the sample not to be imaged, as the pulse may disturb the area of interest. A Scanning electron microscope image of a suitable STM tip is shown in figure 2.32, where the radius of curvature for a good tip is around 10-30nm.

Due to the high resolution needed to image surfaces mechanical and atomic vibrations need to be minimized. Mechanical vibrations can be insulated against by the use of damping systems such as eddy damping magnets. In order to minimize thermal vibrations the sample must be cooled and so most new high quality STMs are designed to be operated at 4K using liquid helium cooling. The STM used in this thesis was operated at room temperature. In order to calibrate the piezoelectric drives a freshly prepared HOPG surface was scanned and used as a reference. The calibration settings of the piezo were then adjusted until the lattice vectors of the acquired image agreed with the reported literature values of 2.46±0.1Å.
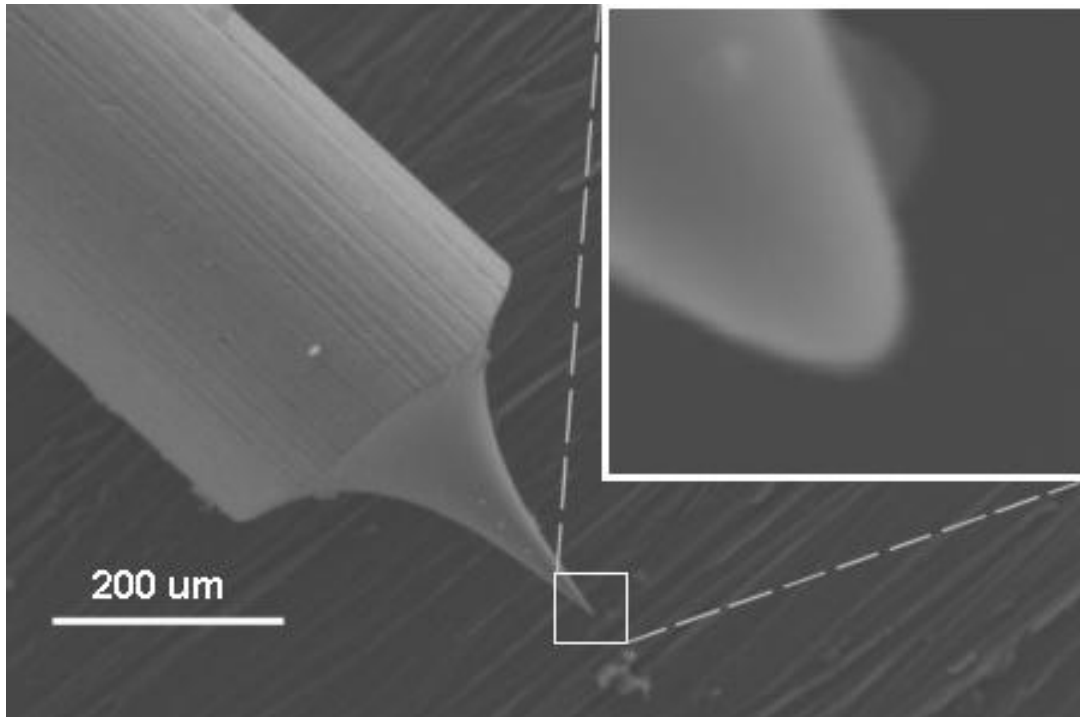
Figure 2.32: Electron microscope image of a typical STM tip. Image taken without permission from [36]

This lattice vector is determined by taking a Fourier transform of the image. Line profiles where then taken across the Fourier image to determine to reciprocal lattice spacings using the Gwyddion software package [37]. These reciprocal lattice spacings were then inverted to reveal the dimensions of the imaged surface.

DFT was used to simulate STM images for the different adsorption sites of tellurium on copper. This was done using the p4VASP [38] code that is a visualisation suite for the VASP code [30].

References

[1]   D.P. Woodruff, T.A. Delchar, "Modern Techniques of Surface Science", Cambridge University Press (1994) 2nd edition

[2]   N.J. Taylor, Surface Science 4 (1966) p. 161

[3]   S. Hüfner, "Photoelectron Spectroscopy: Principles and Applications". Springer, (1995)

[4]   PSP, X-ray instruction Manual TX-400

[5]   G. King, "An Introduction to Electron Optics", (2005), Lecture notes taken from: http://es1.ph.man.ac.uk/george-king/gcking.html [August 2013]

[6]   J.F. Watts, J. Wolstenholme, "An introduction to surface analysis by XPS and AES" Wiley (2003) p. 212

[7]   M. Cyot, Le Journal de Physique 33 (1972) p. 125

[8]   G.F. Drake, "Handbook of atomic and orbital physics" Springer (2006)

[9]   N. Fairley, http://www.casaxps.com, Casa software Ltd. (2005)

[10]   Casa XPS Manual 2.3.15 rev 1.3. Published by Casa Software Ltd. (2009)

[11]   D. Briggs, M.P. Seah, "Practical Surface Analysis by Auger and X-ray Photoelectron Spectroscopy", Wiley (1983) p. 204

[12]   C.D. Wagner, "Handbook of X-ray photoelectron spectroscopy", Perkin-Elmer Corporation (Physical Electronics), (1979) 1st edition

[13]   S. Evans, Surf. Interface Anal. 17 (1991) p. 85

[14]   P.J. Cumpson, M.P. Seah, Surf. Interface. Anal. 25 (1997) p. 430

[15]   C.J. Powell, A. Jablonski, J. Electron Spectrosc. 178-179 (2010) p. 331

[16]   R. Schalf, J. Elec. Spec. Rel. Phen., 120 (2001) p.149

[17]   M.D. Williams, D.W. Hess, Graphene 2 (2013) p.55

[18]   OCI MultLEED version 5.5, (2006) http://www.ocivm.com

[19]   R.L. Park, H.H. Madden, Surf. Sci. 11 (1968) p.188

[20]   J. Wallbank, "Electronic Properties of Graphene Heterostructures with Hexagonal Crystals", Springer (2014)

[21]   N.W. Ashcroft, N.D. Mermin, "Solid State Physics", Brooks/Cole (1976)

[22]   D.F Shriver, P.W. Atkins, "Inorganic Chemistry", Freeman New York (1999) 3rd edition

[23]   E.M. McCash "Surface Chemistry", Oxford University press Inc. (2007)

[24]   P.T. Sprunger, E. Laesgaard, Phys. Rev. B 54 (1996) p. 8163

[25]   P.W. Tasker, J. Phys. C: Solid State Phys. 12 (1979) p. 4977

[26]   A. Barbieri, M.A. Van Hove, Private communication

 http://www.ap.cityu.edu.hk/ personal-website/Van-Hove.htm

[27]   A.   Morawiec,   "Orientations   and   Rotations: Computations   in Crystallographic Textures", Springer (2004)

[28]   K. Heinz, G.J. Besold, Phys. C: Solid State Phys. 16 (1983) p. 1299

[29]   J.B. Pendry, Journal of Physics C-Solid State Physics 13 (1980) p. 937

[30]   G. Kreese, J. Hafner, Phys. Rev. B 47 (1993) p. 558

[31]   G. Kreese, J. Hafner, J. Phys. Condens. Matter 6 (1994) p. 8245

[32]   G. Kreese, J. Hafner, Phys. Rev. B 49 (1994) p. 14251

[33]   G. Kreese, J. Furthmuller, Comput. Mater. SCi. 6 (1996) p. 15

[34]   G. Kreese, J. Furthmuller, Phys. Rev. B 54 (1996) p. 11169

[35]   F. Bechstedt, "Principles of Surface Science", Springer (1965) p.46

[36]   SEM   image   of   STM   tip   accessed   2014 http://std2.fic.uni.lodz.pl/~pkowa/pic/tip1ttrawiona.png

[37]   Gwyddion open source software version 2.31 http://gwyddion.net

[38]   p4 VASP code http://www.p4vasp.at/

Chapter 3

Tellurium deposition on the Cu(111) surface

Abstract

The chemisorption of tellurium onto the low index Cu(111) surface has been studied under ultra high vacuum using a combination of low energy electron diffraction, photoelectron spectroscopy, scanning tunnelling microscopy and density functional theory. We report on three different coverage regimes for the tellurium on copper and the structures formed. The initial stage of growth up to 0.33 ML was an ordered $(2\sqrt{3}\times2\sqrt{3})R30°$ phase. At 0.33ML an ordered $(\sqrt{3}\times\sqrt{3})$ phase is formed. Above 0.66ML a Cu_3Te_2-like alloy is formed. For the two lower regimes quantitative LEED and DFT indicate that substitutional surface alloying begins at very low coverages.

Introduction

Copper chalcogenides such as copper sulphide, copper selenide and copper telluride have been show to perform as p-type semiconductors due to copper vacancies. This makes them suitable materials for a range of applications such as photovoltaics, batteries and thermoelectrics [1]. Copper telluride has been studied for several decades due to its technological importance. It has a high conductivity which makes it suitable for use within electrical circuits. It is a component in several thin film solar cells where the absorber layer is made of cadmium telluride, the back contact is often CuTe, this is either intentionally deposited or a copper back contact has been deposited which has then undergone alloying due to interfacial reactions [2-7]. The junction between the back contact and the active layer is crucial as any resistances the carrier

experiences when travelling through the junction will increase the series resistance of the overall cell and therefore decrease its efficiency. The back contact also has to be stable under operation so that the diffusion of material from the contact into the active region is minimised as it has been shown that copper migration into the cell results in a decrease in device performance and lifetime. So in order to minimise the series resistance of the cell ideally an ohmic (where the current increases linearly with the voltage following Ohm's law) contact would be formed to extract the carriers [8,9]. Due to the difference in work functions when joining a metal to a semiconductor as described earlier a Schottky barrier can form which prevents the ohmic behaviour of the back contact and hence limits the efficiency of the device. One approach to reducing the size of this barrier is to etch the surface of the CdTe prior to metal deposition [4]. This etching process produces a Te rich surface, metal is deposited onto this enriched surface and then annealed, rendering an alloyed back contact. A large range of CuTe alloys are known to exist with copper telluride having the most complicated phase diagram of all the copper chalcogenides [10,11]. These alloys range from metallic to semiconducting and differ in suitability when used in devices due to their varying resistances. In order to understand this alloying process recent studies have been done on mainly polycrystalline samples [12-15]. The growth of Cu_xTe alloys by evaporating Cu onto a Te rich surface of CdTe was done by Zhoue et al [13]. Using X-Ray diffraction (XRD), it was found that the deposition of Cu onto the Te surface created a range of alloys, including Cu_2Te, $Cu_{2.8}Te_2$, $Cu_{3.18}Te_2$, Cu_4Te_3 and CuTe. The properties of these alloys range from semiconducting to metallic. Each of these alloys has a different resistance and stability making some of the phases more desirable than others for the back

contact. For example the Cu_2Te alloy has the highest conductivity however it is unstable leading to copper diffusion into the cell, causing a reduction in device performance [5]. The Cu_2Te alloy was most prevalent at room temperature. XRD and photoemission were used to study the deposition of Cu onto a Te enriched polycrystalline CdTe sample [14]. The XRD data showed that a $Cu_{2-x}Te$ alloy formed with × varying between 0.1 and 0.5. The XPS spectra showed shifts relative to elemental Cu of 0.4-0.6eV. The deposition of Cu onto CdTe(111) was investigated with XPS and UPS. It was found that the deposition of Cu onto CdTe(111) reduced the work function and led to the precipitation of Cu_2Te by the substitution of Cd by Cu [15]. Understanding this alloying process will allow more suitable contacts to be as preferable phases can be grown.

In this chapter the alloying of tellurium with copper has been investigated on the close packed (111) face of single crystal copper. There were only 2 previous studies of the adsorption of Te on Cu(111). The first of those assessed the sub-monolayer growth of Te/Cu(111) using LEED[16]. They reported unalloyed $(2\sqrt{3}×2\sqrt{3})R30°$ and $(\sqrt{3}×\sqrt{3})R30°$ phases for Te coverages of 0.08 ML and 0.33 ML, respectively. Another study used surface extended X-ray absorption fine structure (SEXAFS) to analyse the geometry of 0.33 ML over-layer of Te on Cu(111). They found that Te substituted for a Cu atom in the outermost Cu layer, residing 0.084 nm above the Cu nuclear plane [17]. The adsorption of tellurium on the (100) surface of copper has also been previously studied. Two LEED studies showed that Te forms a p(2×2) over-layer with Te occupying the four-fold hollow sites for a coverage less than 0.25 ML[18,19]. Above this coverage, a structure forms that is incommensurate with the substrate. This assignment was

confirmed by both photoelectron diffraction and SEXAFS finding the four-fold hollow site as the adsorption geometry [17,20].

The work in this chapter has been published in the following papers

M.O. King, Surf. Sci. 606 (2012) p. 1353 [21]

M. Lahti, Surf. Sci. 622 (2014) p. 35 [22]

Experimental

Tellurium was deposited onto a clean single crystal using a homemade thermal evaporator. This tellurium effusion cell was operated at 570K with the deposition rate for the sub monolayer coverage calculated to be about 0.2 ML/min. The adsorption was monitored by comparing the intensity of the $Cu2p_{3/2}$ and $Te3d_{5/2}$ XPS spectra. The coverages are expressed in terms of monolayers where 1 ML is equal to the number of atoms present in an ideal Cu(111) surface. The Cu(111) single crystal was cleaned in situ by cycles of argon ion bombardment to remove adsorbates followed by annealing to restore the order at the surface disrupted by the sputtering process. This procedure was repeated until the XPS showed no detectable contamination and a sharp (1×1) LEED pattern was observed. The cleaning conditions for this crystal were an ion energy of 1kV with a sample flux of around 10μA followed by annealing to ~870K. Once the superstructures were observed by LEED the sample was annealed to increase the order and the cooled down to 140K for the dynamic LEED measurements. By cooling the sample for the LEED work the contrast and sharpness of the observed LEED spots is improved. The intensities of the diffracted beams were recorded with a CCD camera as a function of the ingoing electron energy. The LEED work was done at normal incidence angle. The

spectra were extracted using the OCI LEED software where the intensity above the background is plotted. In order to further reduce experimental noise in addition to cooling the sample symmetrically equivalent beams were averaged together. The extracted LEED-IV curves were analysed by Pussi et al in Finland. The theoretical IV curves were generated using the Barbieri/Van Hove Symmetrized Automated Tensor LEED package [23]. The Barbieri/Vanhove phase shift package was used to compute the electron phase shifts. The agreement between the theoretical and the experimental curves quantified using the Pendry R factor [24]. The quality of the clean copper sample was verified by a dynamical LEED calculation. Five non-equivalent beams were collected at room temperature with the calculation giving a good agreement between the experimental and theoretical curves with a Pendry R factor of 0.14.

Low coverage (2$\sqrt{3}$×2$\sqrt{3}$)R30° Phase

Tellurium was deposited at room temperature with the corresponding LEED images for different coverages shown below. The (2$\sqrt{3}$×2$\sqrt{3}$)R30° Phase was found for a coverage of 0.17ML. The observed LEED pattern shown in figure 3.1 is in good agreement with previous work [16]. The LEED images in figure 3.1 were collected at room temperature with an electron beam energy of 111eV. The dashed lines show the unit cell vectors of the Cu(111) substrate whose lattice constant is 2.55Å. From 0.08ML onwards the pattern displays (2$\sqrt{3}$×2$\sqrt{3}$)R30° symmetry with the sharpest pattern observed for a coverage of 0.17ML.
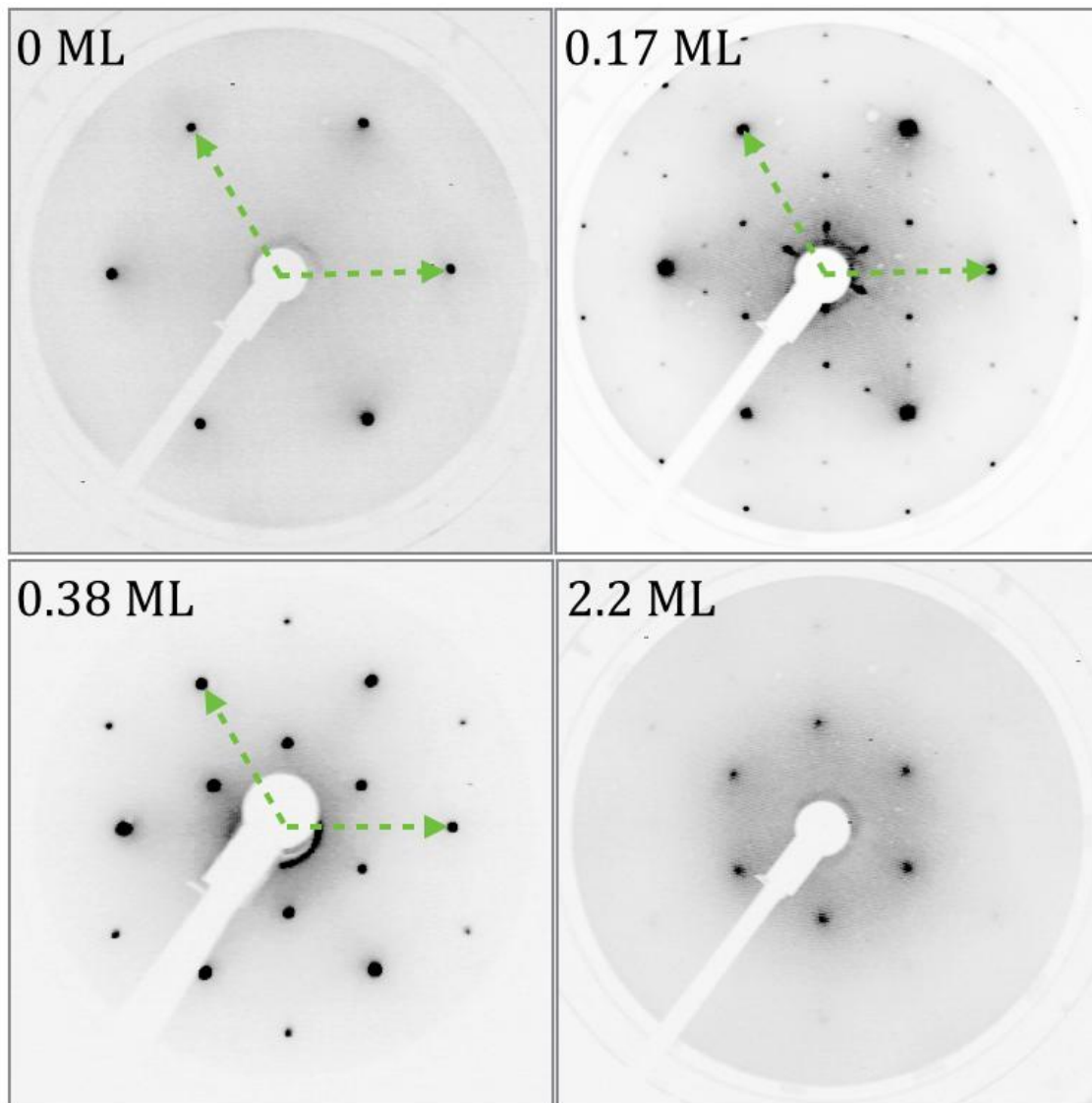
Figure 3.1: LEED patterns obtained at different tellurium coverages. The reciprocal lattice vectors of the substrate for the sub monolayer coverages are shown. The images were collected with a beam energy of 111eV at room temperature.

As further tellurium is deposited the observed peaks become more diffuse indicating a decrease in the long range order as it is no longer possible for the tellurium to occupy the $(2\sqrt{3} \times 2\sqrt{3})$ sites. Inspection of the peak positions indicate there has been an expansion of the surface lattice vector of $\sim 2.8 \pm 0.1\%$

when compared to the clean substrate, increasing to 2.63Å from the original 2.55Å. Due to the larger size of the tellurium this could be due to strain originating from alloying of the larger atom in to the copper lattice. Line profiles were taken through the LEED images to determine the relative expansion as shown in figure 3.2. Gaussian peaks were fitted to the line scans to determine the peak positions.
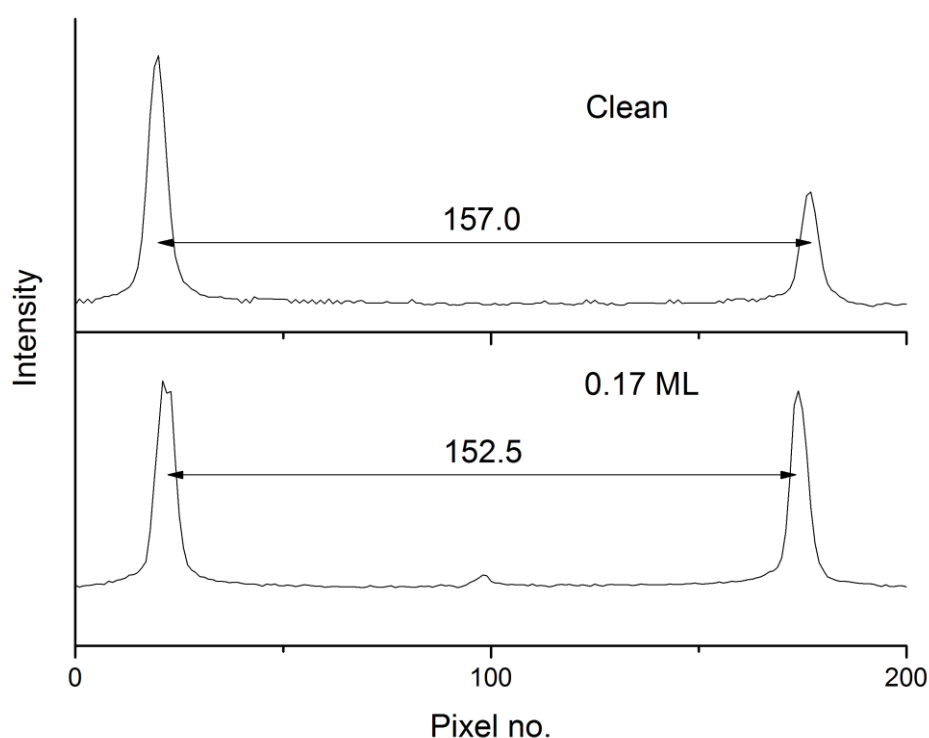
Figure 3.2: Line scan taken through LEED images to determine relative expansion of surface lattice vectors

XPS data was taken after the LEED images were captured which also suggest that the surface is alloying as it agrees with previous results on Cu_xTe systems [25-27]. Survey spectra and the main core levels were obtained. The acquired spectra were fitted using Doniac-Sunjic line shapes. They were fitted in agreement with previously reported studies where the binding energy for the

elemental copper peak is 932.4eV and the binding energy for elemental tellurium peak is 573.1eV. The binding energy for the elemental tellurium was calculated by depositing a thick layer of tellurium ~22ML and XPS data collected. No signal from the underlying copper substrate was detected. When information about species has been obtained from references their position and FWHM are fixed, the intensity of the individual species is varied by the fitting program to best represent the experimental data. The peaks are asymmetric in shape consistent with other work done on similar systems. The XPS spectrum for the tellurium shown in figure 3.5 for the $(2\sqrt{3}\times2\sqrt{3})R30°$ phase is fitted with a single peak and found to be 572.3eV. This is shifted 0.8eV lower in binding energy with respect to the data collected for elemental tellurium. In order to fit the $Cu2p_{3/2}$ two components were used, one of the signals corresponding to the original elemental signal from the bulk and one shifted by 0.2eV, shown in figure 3.4. The shift 0.8eV to lower binding energy with respect to the elemental tellurium indicates a partial transfer of charge between the tellurium and the copper. Similarly the XPS data from the copper shows a species which has shifted 0.2eV with respect to the bulk elemental reference which also indicates a partial charge transfer. Signal from the underlying copper still occurs at the elemental reference. This data suggests that formation of a surface substitutional alloy (SSA) begins with very low amounts of tellurium. The XPS signal attributed to the SSA is also detected for the lowest available coverages where no tellurium structure was observed with the LEED. This suggests that as soon as tellurium is deposited onto the Cu(111) surface it is immediately incorporated in to the surface forming an alloy. The valence band was investigated using UPS and the clean Cu(111) spectra showed similar features to those previously reported [28],

with sharp peaks associated with the 3d orbitals between 2eV-4eV and a surface state around 1eV below the Fermi level.   For low the low coverage of tellurium the only change in the UPS spectra was the quenching of the surface state that is typical after adsorption [29]. There was also a small change in the work function as measured by UPS. The work function for the clean Cu(111) surface was found to be 4.9±0.1eV which is in agreement with previous studies [30].   For the (2√3×2√3)R30° phase with a coverage of around 0.18ML the work function had increased to 5.0±0.1eV.

STM images of the 0.18ML surface were obtained at room temperature with sample displaying a sharp (2√3×2√3)R30° LEED pattern. The STM image shown in figure 3.3 is consistent with the observed LEED pattern as it shows (2√3×√3)R30° domains that are expected with further tellurium adsorption after all the available (2√3×2√3)R30° adsorption sites are filled. The tellurium strains the copper lattice as it is incorporated due to its larger size and sits slightly above the copper plane as revealed by previous SEXAFS work [17]. This vertical protrusion means the bright features in the STM images are taken to be Te atoms as in similar studies of Te/Pt111 [31,32]. The dimensions of the unit cell for the surface structure shown in figure 3.3 were found to be a=4.5±0.1Å and b=9.1±0.1Å. These dimensions were calculated using a Fourier transform of the image. The lattice spacing for the expanded Cu(111) from the LEED is 2.63Å so they should have values of 4.55Å and 9.10Å so the measured surface vectors are in good agreement with this.
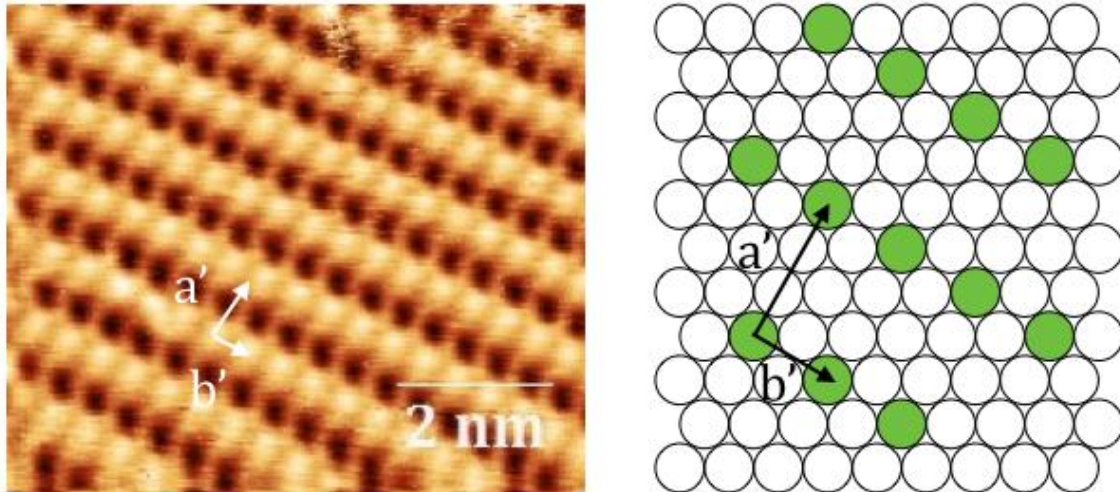
Figure 3.3 STM image taken from published work of (2√3×√3)R30° domain with a corresponding atomic model. Obtained at room temperature with a sample bias of +1.8V and a tunnelling current of 800pA.

As further tellurium is deposited the XPS and LEED data suggests that it is incorporated into the surface alloy without causing a further expansion of the surface lattice vectors. This continues up to a coverage of 0.33ML where a (√3×√3)R30° LEED pattern is observed. As tellurium was deposited it can be incorporated between the lines on the atomic model in figure 3.3 and so it naturally progresses into the (√3×√3)R30° structure.

Intermediate Coverage (√3×√3)R30°

At 0.33ML the LEED pattern shown in figure 3.1 has (√3×√3)R30° symmetry. Measurement of the lattice constant showed no further increase from the (2√3×2√3)R30° phase. The XPS data in figure 3.5 for 0.33ML suggests that the tellurium is still being incorporated into the surface in the same way, however a

new peak appears related to the bulk alloy phase. As further tellurium is adsorbed the LEED still displays a (√3×√3)R30° structure however with increasing coverage the signal becomes weaker and more diffuse. An STM image taken for a coverage of 0.38ML is shown in figure 3.6. The UPS data showed the work function had increased to 5.1±0.1eV.
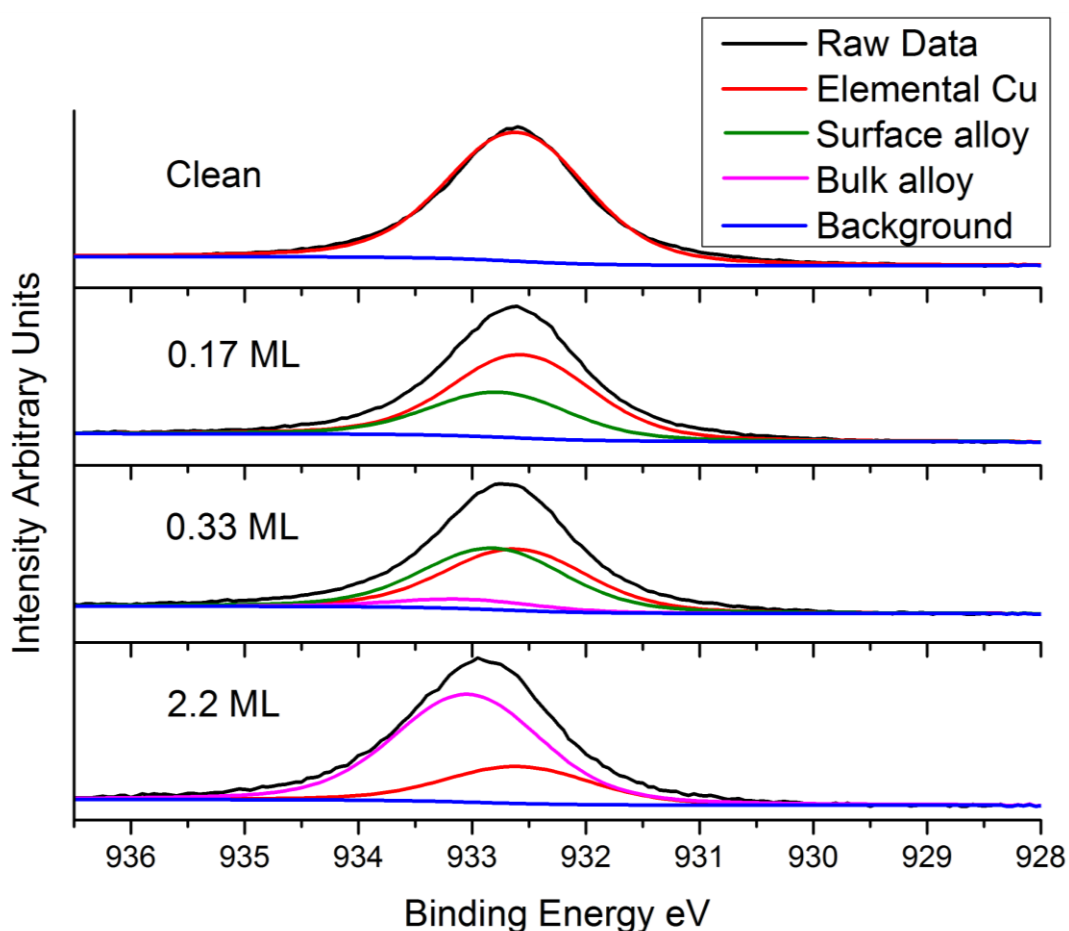
Figure 3.4: XPS spectra of the Cu 2p$_{3/2}$ for increasing Te coverages

The dimensions of the unit cell from the Fourier transform are 4.5±0.1Å that is consistent with the distances measured with LEED. The triangular defects have a shape and size that is consistent with vacancies in the surface alloy. These

were seen to occur at a high frequency and may allow dispersion of strain within the film.

The XPS data showed an additional species of tellurium present for coverages greater than 0.33ML, this additional component corresponds to tellurium with an oxidation state of Te^{2-} with a binding energy 0.6eV higher than elemental Te [25-27]. This signal may be arising from the bulk alloy (BA) phase which was found to form for higher coverages. As further tellurium is deposited the signal arising from the SSA decreases while the signal from the Te^{2-} increases suggesting a gradual transition from SSA to BA.
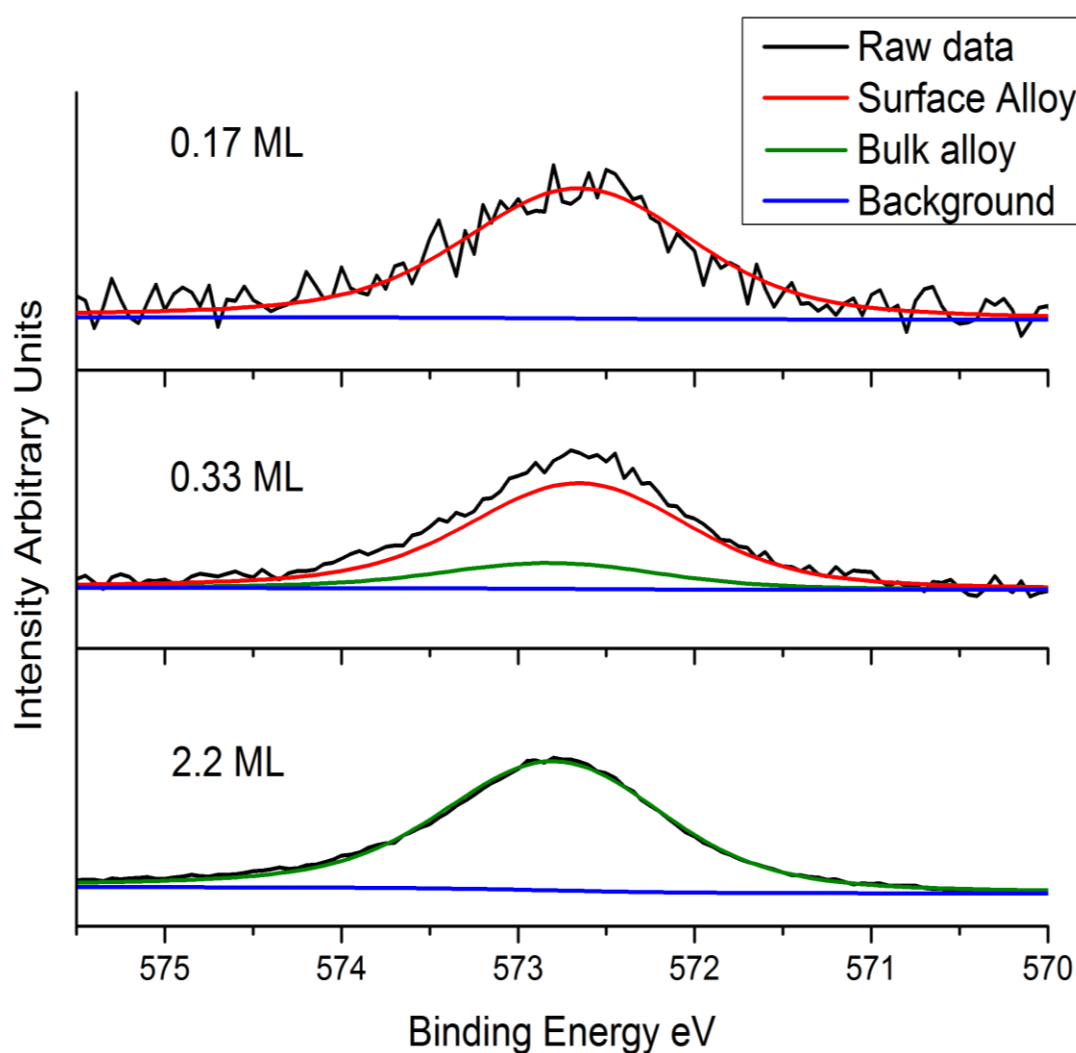
Figure 3.5: XPS spectra of the Te3d$_{5/2}$ for increasing Te coverages
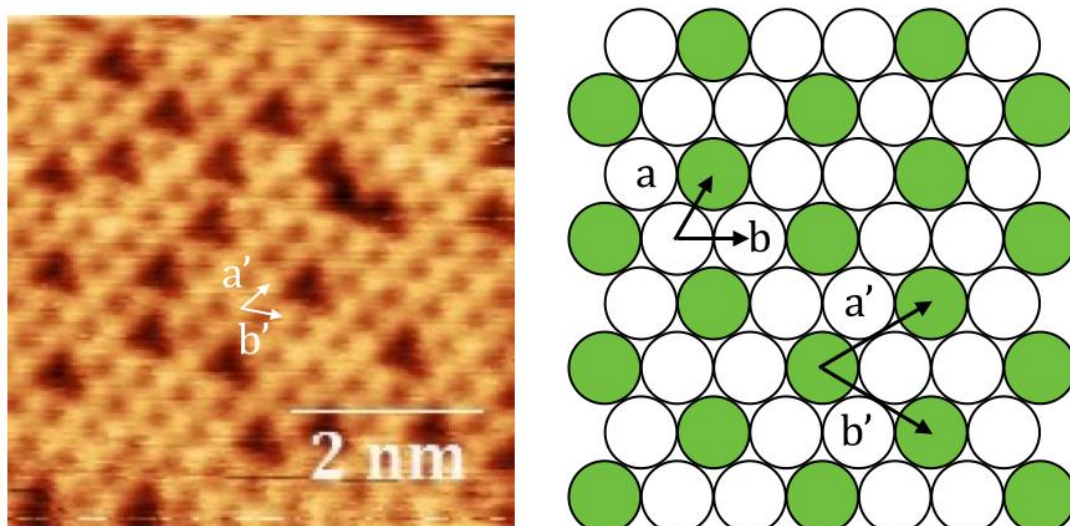
Figure 3.6: STM image of the ($\sqrt{3}\times\sqrt{3}$)R30° surface substitutional alloy at 0.38ML. Image taken from published work and was obtained at room temperature with a sample bias of +1.7V and a tunnelling current of 1.9nA. The image size is 5.3nm², alongside is shown the atomic model.

Bulk Alloy Phase coverage over 0.66 ML

The LEED patterns for this coverage show the same ($\sqrt{3}\times\sqrt{3}$)R30° symmetry, however measurement of the peak positions in the LEED images show that the lattice constant has contracted with respect to the Cu(111) substrate by ∼ 3.2%, from 2.55±0.1Å to 2.48±0.1Å . The sharpest LEED image was obtained for a coverage of 2.2ML, shown in figure 3.1, further deposition above this reduced the long range order. Only two of the previously reported bulk alloy phases of $Cu_{1-x}Te_x$ were shown to possess hexagonal symmetry, the most common alloy Cu_2Te [33] and the Cu_3Te_2 [34]. The XPS components attributed to the SSA phase were not present at this coverage suggesting a complete bulk alloy phase

has been formed. By correcting the measured intensities in the XPS spectra with appropriate cross sections the ratio of Cu/Te is 1.4±0.1 which suggest the Cu_3Te_2 as the phase of the alloy.

STM image of the BA phase shown in figure 3.7 is consistent with the observed LEED pattern. As well as displaying the hexagonal symmetry observed with LEED we also observe long range periodicity. This is attributed to a Moiré effect, producing a superlattice similar to that observed in a many other systems and originates from the mismatch of the over-layer structure with the underlying substrate lattice. [35,36] . The unit cell of the surface is found to be 4.3±0.1Å that is smaller than for the SSA phase. Further evidence that suggest the Cu_3Te_2 phase for the alloy is the step height measured with STM. The step heights for the Cu_2Te and Cu_3Te_2 phases differ significantly, 4.24Å and 3.49Å respectively. The measured step height was found to be 3.2±0.1Å, which does not agree well with the Cu_2Te phase but a reasonable agreement with the Cu_3Te_2 stoichiometric phase. This contraction in lattice spacing with respect to the bulk value may be accounted for by a different a slightly off 3:2 ratio as many other $Cu_{1-x}Te_x$ compounds are known to exist. A line scan through a defect is shown as the inset to figure 3.7 indicating it is a vacancy within the lattice.
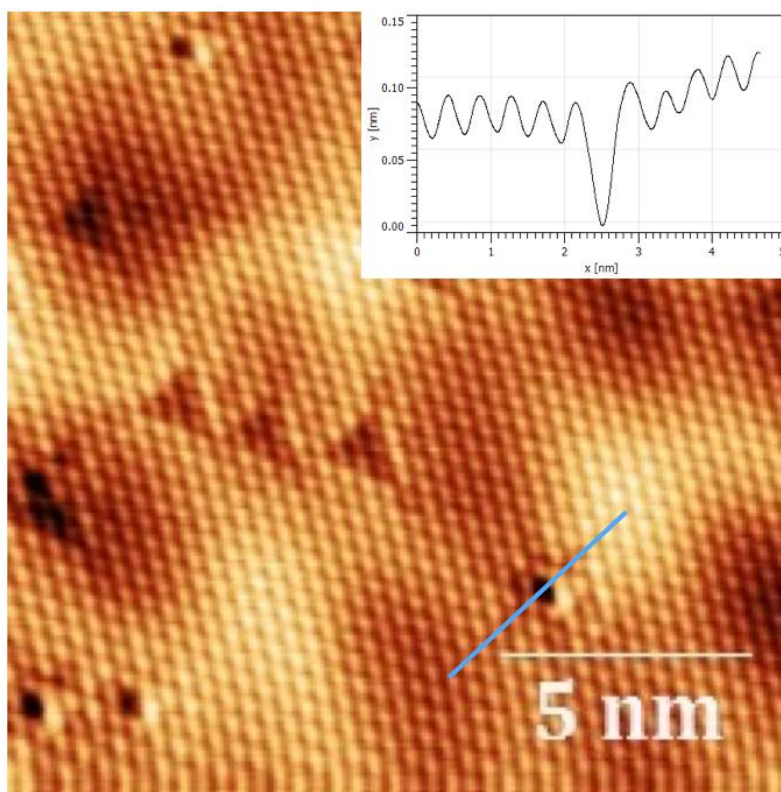
Figure 3.7: STM image of bulk alloy formed by 2.2 ML deposition of tellurium at room temperature. Image size is 15.5 nm² and was obtained with a sample bias of +1.8V and a tunnelling current of 800pA. Inset shows the profile of the blue line

The UPS spectrum for the BA phase shown in figure 3.8 also favours a Cu_3Te_2 like phase. The data resembles previously reported spectra on copper telluride alloys with a composition $Cu_{0.58}Te_{0.42}$. The spectra show a strong step at the Fermi level, this is in contrast to the reported spectra for the Cu_2Te phase and hence our results are more consistent with the Cu_3Te_2 than the Cu_2Te phase [37,38].
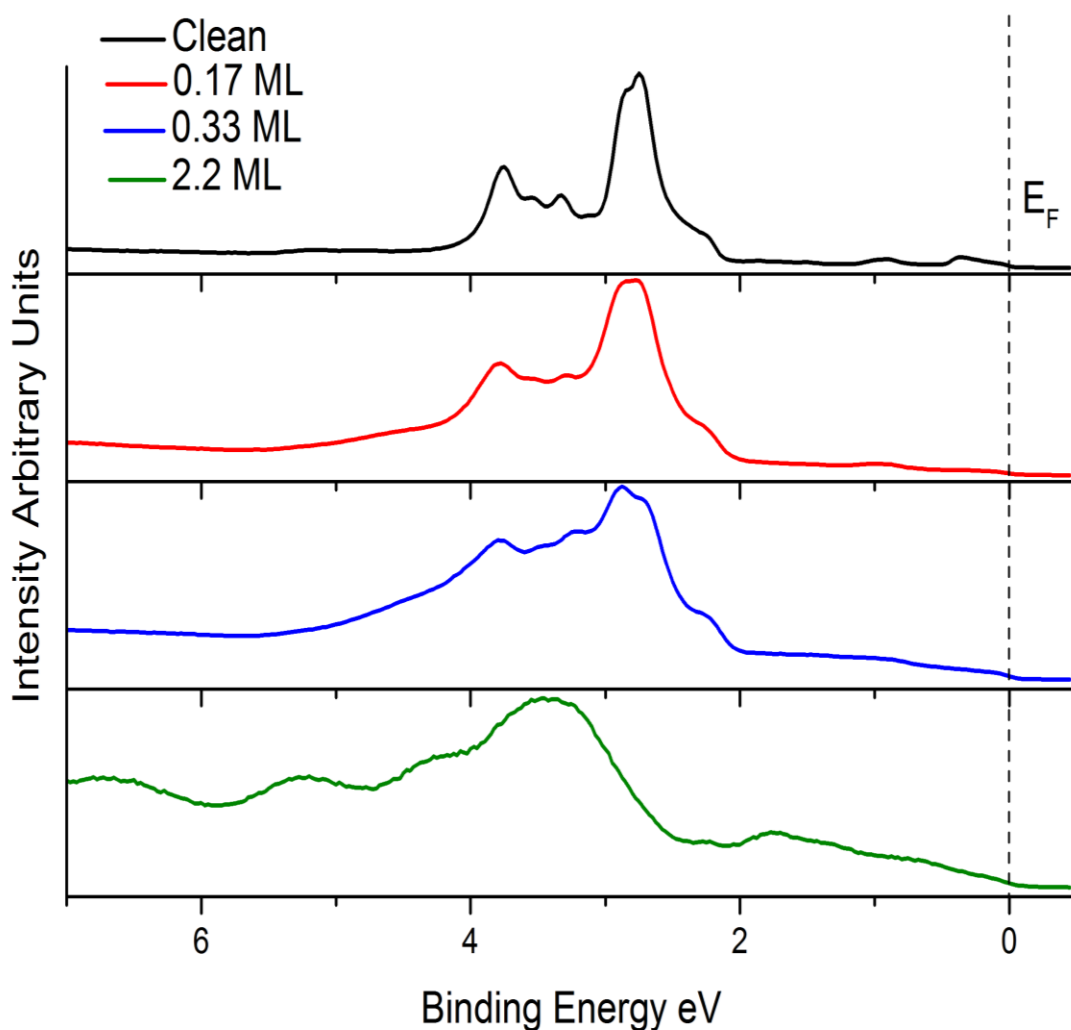
Figure 3.8: UPS spectra taken at normal emission for a range of Te coverages

LEED IV

A more detailed analysis of the surface structure was provided by LEED-IV analysis. For the simulations a start geometry of a bulk terminated Cu (111) crystal with Te in the appropriate site was used with a hard sphere, atomic radii of Cu and Te 1.28A and 1.48A respectively. In the first stage of the calculation

the position of the Te and first Cu layers are allowed to relax. The bond length between the Te and Cu atoms is *d(Te-Cu)* while the spacing between the planes of Te and the first row of Cu atoms is $dz_{Te\text{-}Cu}^1$. An automated optimization technique is used in the SATLEED code that searches for minima in the R factor values. Once these distances have been optimized the second Cu layer is allowed to relax with its spacing from the first layer $dz_{Cu^1\text{-}Cu}^2$. The spacing of the third Cu layer $dz_{Cu^2\text{-}Cu}^3$ was then allowed to relax after the second layers position had been optimized. Once the structural parameters were obtained non-structural parameters such as the Debye temperatures were optimized. The Debye temperature is used to calculate the Debye-Waller factors which accounts for the damping of diffracted intensities dues to atomic vibrations. The initial Debye temperatures used in the first stages of the calculation were the bulk values of 343K and 153K for Cu and Te respectively.

The calculations were done for a coverage of 0.08ML where a $(2\sqrt{3}\times2\sqrt{3})R30°$ LEED pattern was observed. The intensity plots for nine non-equivalent diffracted beams were collected and used in the calculation. Four out of the nine beams collected were integer diffraction peaks while the other five beams were fractional order diffraction spots. The electron energies used during collection ranged from 60eV to 400eV with the mean current held constant. The cumulative energy range used in the calculation was 1250eV. The observed LEED pattern only tells us about the symmetry of the over-layer with respect to the bulk, it does not tell us the adsorption site that the tellurium is in. In order to determine the adsorption site 6 different models were tested two of which were alloyed structures. In these alloyed structures a surface copper atom is substituted for a tellurium atom. The four non-alloyed sites tested were the on

top site, the bridge site and two 3-fold coordinated hollow sites, one for the FCC hollow and one for the HCP hollow. The different adsorption sites tested are displayed in figure 3.9. Only four sites out of the six are shown in the image as only the first copper layer is included, therefore faulted an un-faulted alloy look the same and so do the HCP and FCC hollow sites.
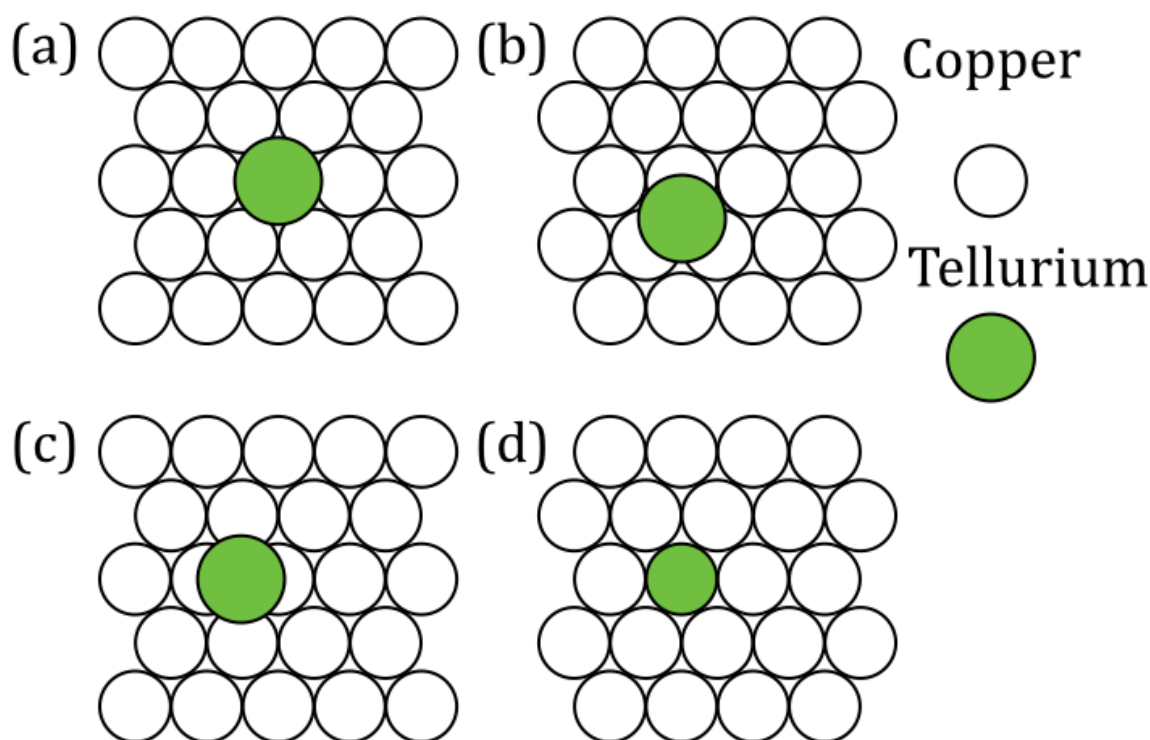

Figure 3.9: Different adsorption geometries tested in the LEED-IV calculations: (a) top site, (b) 3-fold hollow site(FCC or HCP), (c) bridge site and (d) surface substitutional alloy(faulted or un-faulted)

For the substitutional alloy phase two structures were tested, in the first alloyed structure one of the surface copper atoms is swapped for a tellurium atom, leaving 11 copper atoms and one tellurium atom in the unit cell. For the second alloyed structure once again one copper atom was substituted however in this

model a stacking fault is also introduced to the surface layer [39]. This shifts the surface layer so that the atoms in the top layer that would have been sat in FCC hollow sites are now sitting in HCP hollow sites. A representation of a faulted structure is shown in figure 3.10. The correct stacking sequence for a FCC structure is ABCABC shown on the left hand side of the figure, the stacking sequence for the faulted structure is ABCABA shown on the right hand side.
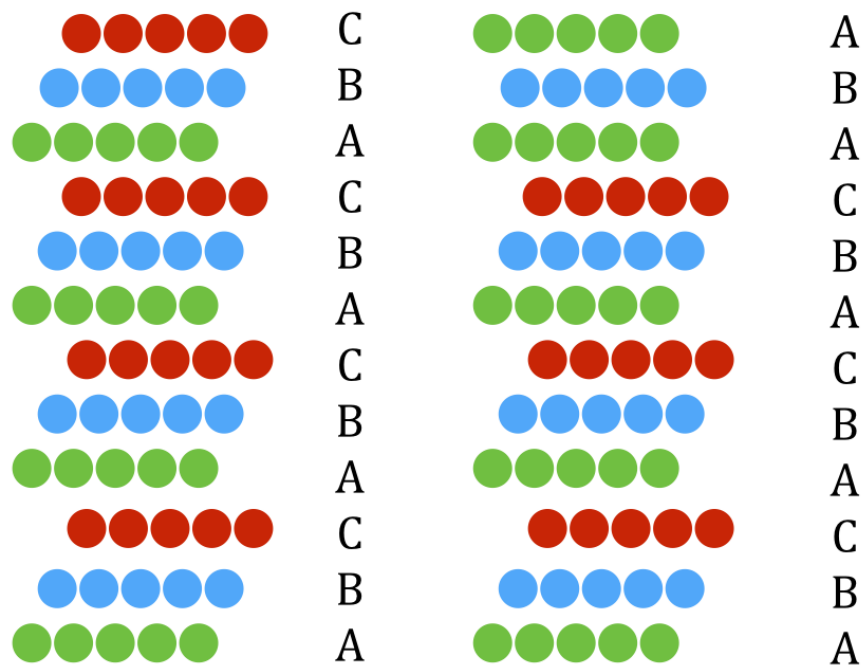

Figure 3.10: Stacking fault used in the second alloyed structure tested. Green circles represent atoms in the A site, blue atoms are those in the B sites and red atoms are those in the C sites

This stacking fault was previously reported where antimony had been deposited onto the Cu(111) surface [39]. The majority of the data set used for the $(2\sqrt{3}\times2\sqrt{3})R30°$ phase shown in figure 3.11 consisted of information from integer diffraction beams with only 250eV of the total 1250eV originating from fractional order beams. However it has been previously shown by Braun and

Held that an accurate determination of the structure can be obtained just using integer diffracted beams [40].
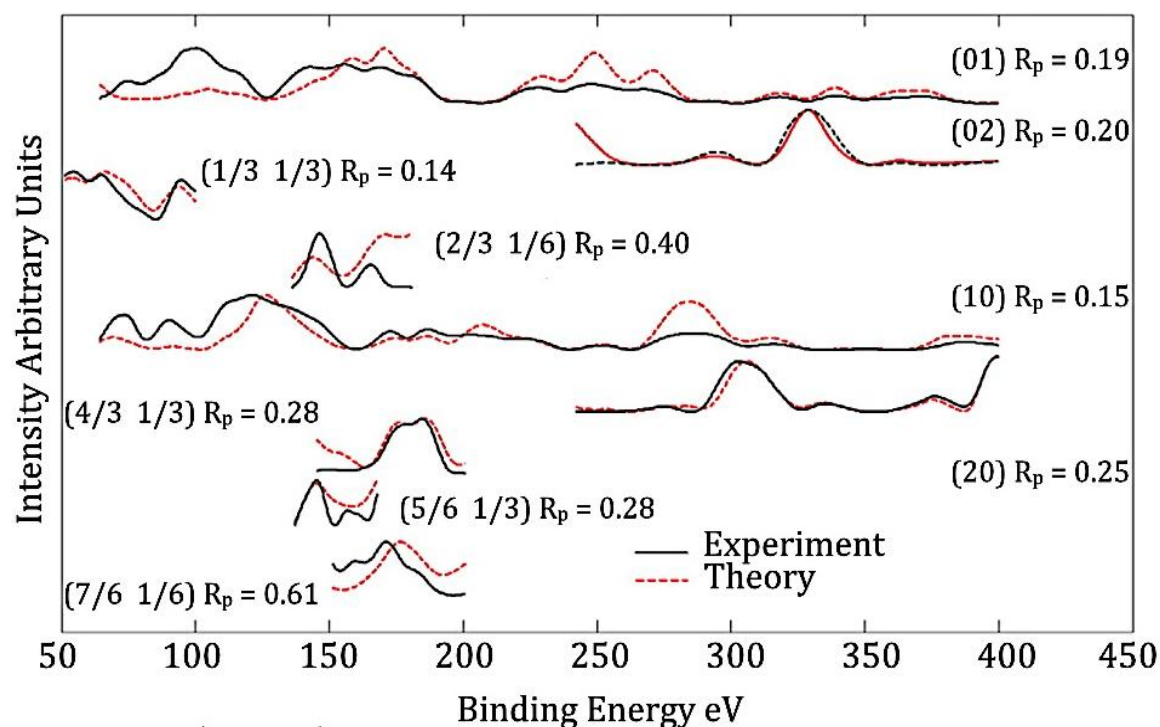

Figure 3.11: LEED IV curves compared with experimental data for the $(2\sqrt{3}\times2\sqrt{3})R30°$ phase with the HCP hollow model. The overall R factor was 0.22 with the individual R factors shown for each beam

The LEED IV plots for the fractional order peaks are considered to be dominated by the adsorption sites whereas integer spots have large contributions from diffraction below the surface, in the bulk-like layers where the structure is better known and more easily described by the standard muffin tin potentials used in standard LEED theory. The best agreements for 0.08ML coverage between the experimental and simulated IV curves were found for the HCP hollow site and the alloyed surface, with Pendry R factors of 0.22 and 0.24 respectively. The

111

Pendry RR function was used to calculate the Pendry variance [24], this allows us to rule out geometries whose R factor is greater then the sum of this Pendry variance and the minimum R factor value found. The Pendry R factors for all six adsorption sites are given in table 3.1.

Geometry	Pendry R Factor $(2\sqrt{3}\times2\sqrt{3})$	Pendry R Factor $(\sqrt{3}\times\sqrt{3})$
Top	0.26	0.70
FCC Hollow	0.29	0.67
HCP Hollow	**0.22**	**0.36**
Bridge	0.59	0.54
Alloy	**0.24**	0.54
Faulted Alloy	0.48	**0.41**
Variance	0.03	0.06

Table 3.1: Pendry R Factors for the different adsorption geometries. Viable structures allowed by the Pendry variance are highlighted in bold

By running the simulation with both geometries present the possibility of a mixed surface was tested. By mixing the structures 50:50 on the surface a slight improvement in the Pendry R factor to 0.21 was found when compared to the individual geometries. However this improvement is small when compared to the Pendry variance. This improvement could be due to the fact that in the mixed phase there are more free parameters, and more free parameters allow a better fit of the data. The optimized structural parameters for the calculations are shown in table 3.2 and are demonstrated on figure 3.12.

Geometry	d(Te-Cu)	dz $_{Te-Cu}^{1}$	dz $_{cu^{1}-cu^{2}}$	dz $_{cu^{2}-cu^{3}}$	dz $_{cu^{3}-cu^{4}}$
($2\sqrt{3}\times2\sqrt{3}$)					
HCP Hollow	2.76±0.02Å	2.33±0.02Å	2.06±0.03Å	2.06±0.04Å	
Alloy	2.71±0.03Å	0.91±0.03Å	2.08±0.04Å	2.00±0.04Å	
($\sqrt{3}\times\sqrt{3}$)					
HCP Hollow	2.74±0.04Å	2.31±0.04Å	2.06±0.04Å	2.04±0.07Å	2.09±0.10Å
Faulted Alloy	2.70±0.05Å	0.88±0.05Å	2.12±0.06Å	2.03±0.07Å	2.06±0.09Å

Table 3.2: Some optimized structural parameters from the LEED IV analysis with the best fit geometries for both coverages. d(Te-Cu) is the Te-Cu bond length, dz$_{Te-Cu}^{1}$ is the distance between the planes of the Te and Cu in the first layer. dz$_{Cu^{1}-Cu^{2}}$ is the distance between the first and second planes of copper atoms and so on.
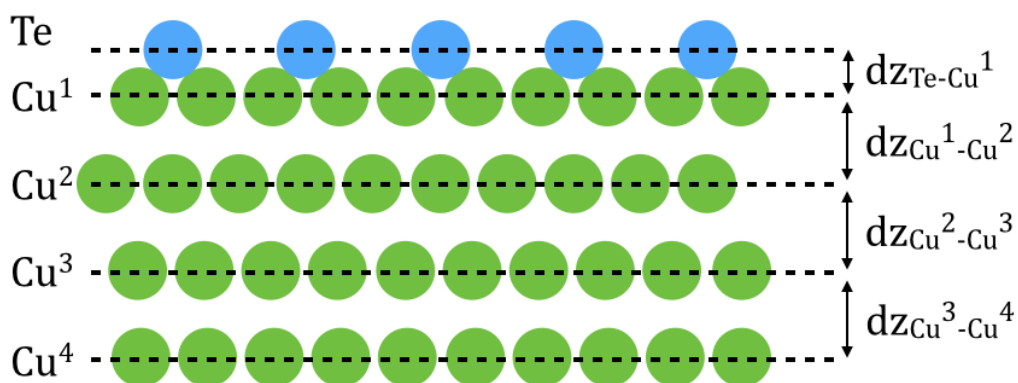
Figure 3.12: Model showing the relaxation parameters in the LEED IV calculations

DFT calculations were also done to reveal the adsorption energies for the different sites. DFT was also used to simulate STM images for comparison with the experimental images. The calculated adsorption energies are shown in table 3.3.

Geometry	Adsorption Energy eV (2√3×2√3)	Adsorption Energy eV (√3×√3)
Top	-	-0.93
FCC Hollow	-1.53	-1.23
HCP Hollow	-1.50	-1.23
Bridge	-1.46	-1.26
Alloy	-1.60	-1.39
Faulted Alloy	-1.50	-1.29

Table 3.3: DFT adsorption energies for the six tested different geometries.

The DFT for the 0.08ML coverage showed no real preference towards any adsorption site other than the top site being energetically unstable. The simulated STM images that best resembled the experimental images were for the alloy and the faulted alloy structures. The other simulated images displayed a strong Moiré pattern that was not observed experimentally. The simulated images for the (2√3×2√3) phase are shown next to the experimental images in figure 3.13. The XPS, LEED and STM data show that Te is gradually incorporated into the surface as it is deposited. The Te displaces a Cu atom to create a surface alloy and expand the lattice in the process due to their different size. At 0.08ML the favoured adsorption sites from the LEED IV calculations were the HCP hollow and the alloy.
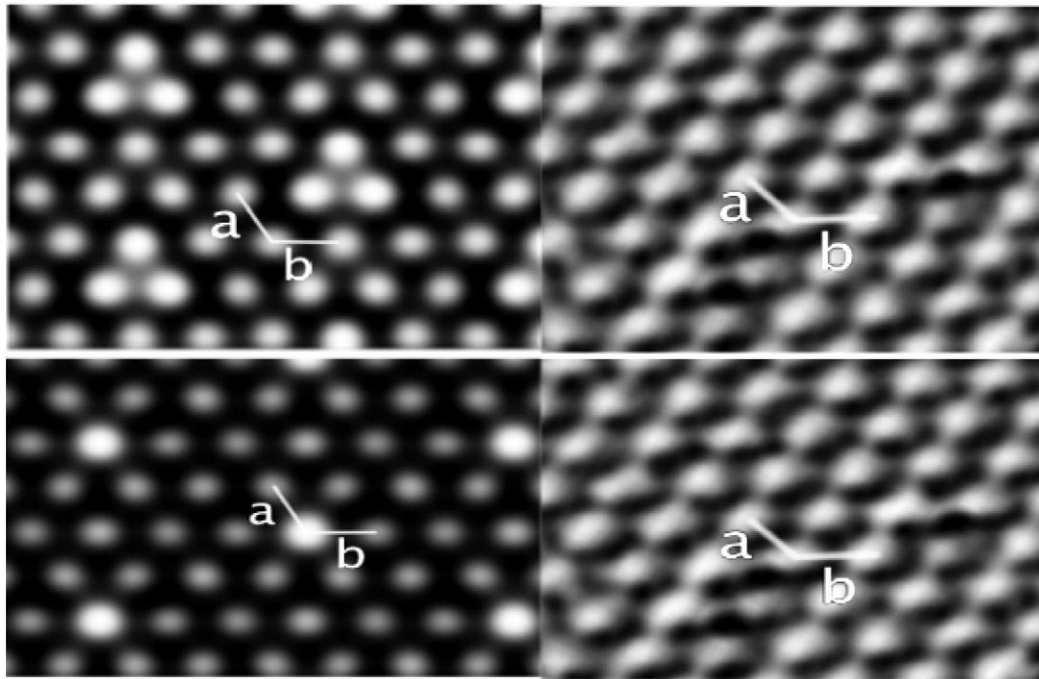
Figure 3.13: On the left DFT simulated STM images for the alloy (top) and faulted alloy (bottom) structures for the (2√3×2√3) phase. On the right the measured STM image obtained with a sample bias of +2.3V and a tunnelling current of 2nA, image has been Fourier filtered.

For the LEED IV calculations of the (√3×2√3) phase the intensities of diffracted beams were collected between 30eV and 350eV. The cumulative energy of the data set was 1675eV with five integer beams and six fractional order beams. The same six adsorption possibilities were tested as for the lower coverage. The overall R factor is a weighted average of the individual R factors by the length of each dataset. The best agreement was found for the HCP hollow site and the faulted alloy structure however with Pendry R factors of 0.36 and 0.41 respectively they are not in excellent agreement. Once again the possibility of a mixed surface was tested, mixing these two phases together led to a considerable improvement in the R factors. The lowest R factor was found to be 0.26 when the structures were mixed with a ratio of 40:60 of HCP hollow to faulted alloy.

This suggests that the alloying of the surface is not yet complete. The experimental and simulated curves are shown in figure 3.14.
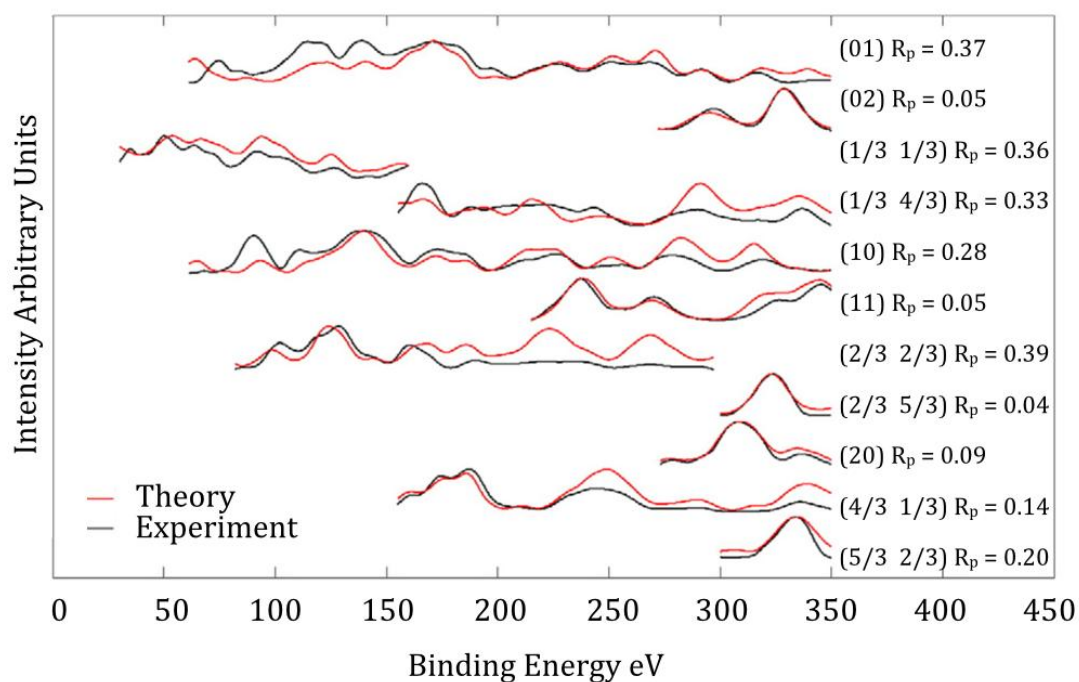

Figure 3.14: LEED IV curves for the ($\sqrt{3}\times\sqrt{3}$)R30° phase using a mixed geometry (40:60 mix of HCP hollow and faulted alloy). The overall Pendry R factor is 0.26 with the individual R Factors shown for each beam

The optimized structural parameters for this coverage were shown in table 3.2, with the height of the Te above the copper plane for the HCP hollow site 2.31±0.04Å. This agrees with an earlier study that reported the distance the tellurium sits above the copper plane as 2.34Å [16]. The mixed phase structures improvement in R factor when compared to the variance suggests it is a viable option for the structure. The DFT calculations show the surface alloy is energetically favoured over the other structures. The simulated STM image that best matches the experimental image is for the alloy structure. The simulated images are shown in figure 3.15.
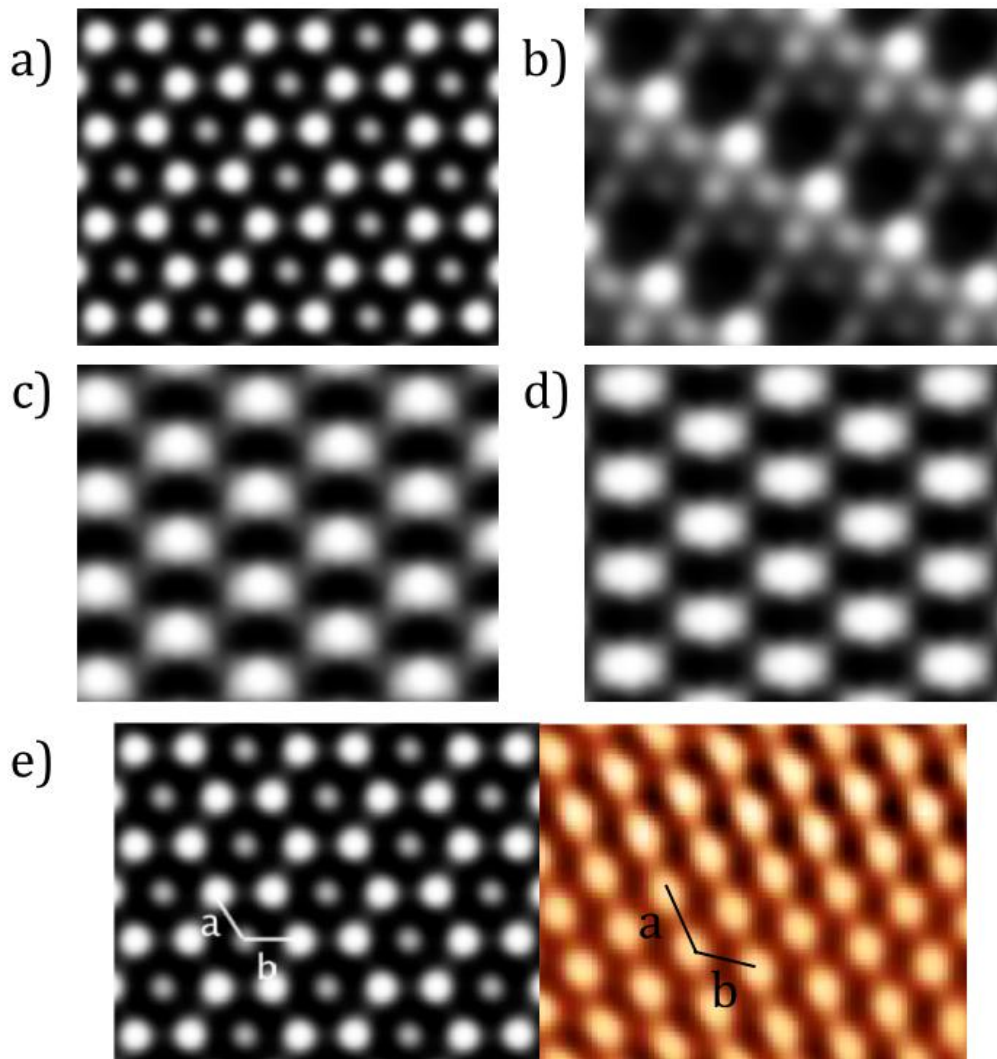
Figure 3.15: DFT simulated STM images ($\sqrt{3}\times\sqrt{3}$)R30° phase, a) alloy, b) faulted alloy, c) FCC hollow, d) HCP hollow and e) the comparison of the best matched image with the Fourier filtered experimental data. The image was obtained with a sample bias of +1.5V and a tunnelling current of 1.7 nA.

In the simulated HCP and FCC hollow sites the tellurium protrudes high out of the surface. These vertical protrusions were not seen experimentally and hence those structures were discarded.

Conclusion

In this chapter the deposition of Te on the Cu(111) surface has been investigated using a combination of LEED, STM, XPS, UPS, LEED IV and DFT. For coverages below 0.33ML we found a substitutional surface alloy with an ordered (2√3×2√3) R30° phase for a coverage of 0.08ML and an ordered (√3×√3) R30° phase for a coverage of 0.33ML. For coverages greater than 0.66ML a bulk alloy phase was found which best resembles a Cu_3Te_2 like alloy. The adsorption sites for the low coverages was explored using quantitative LEED and DFT. Our results indicate that substitutional surface alloy formation starts at very low coverages. For the 0.08ML coverage the adsorption energies from DFT are almost equal for the hollow sites, bridge site and the two alloyed structures. There was a preference in the LEED results for the HCP hollow and alloy structures therefore it is possible to say that the surface alloy formation has started at this low coverage. The DFT showed that for the 0.33ML coverage the surface alloy is the energetically favoured structure. The LEED results found a mix of the HCP hollow site and the faulted alloy to give the best agreement, This suggests that the alloying is not yet complete. The LEED and DFT results are consistent with the XPS results indicating that alloying begins from the lowest coverages however it also indicated that the alloy flips to the faulted alloy structure at a coverage of 0.33ML.

References

[1]   J. Mater. Chem. A, 2 (2014) p. 985

[2]   H. Uda, Sol. Energy Mater. Sol. Cells 50 (1998) p. 141

[3]   J.H. Yun, K.H. Kim, Sol. Energy Mater. Sol. Cells 75 (2003) p. 203

[4]   S.S. Hegedus, B.E. McCandless, Sol. Energy Mater. Sol. Cells 88 (2005) p. 75

[5]   X. Wu, J. Zhou, A. Duda, Y. Yan, S. Thin Solid Films 515 (2006) p. 5798

[6]   K. Neyvasagam, N. Soundararajan, Vacuum 82 (2008) p. 72

[7]   X. Wu, Sol. Energy 77 (2004) p. 803.

[8]   H.C. Chou, A. Rohatgi, J. Electrochem. Soc. 142 (1995) p. 254

[9]   D. Grecu, A.D. Compaan, Appl. Phys. Lett. 75 (1999) p. 361

[10]   A.S. Pashinkin, L.M. Pavlova, Inorg. Mater. 41 (2005) p. 939

[11]   A.S. Pashinkin, V.A. Fedorov, Inorg. Mater. 39 (2003) p. 539

[12]   G. Teeter, Thin Solid Films 515 (2007) p. 7886

[13]   J. Zhou, X. Wu, A. Duda, G. Teeter, Thin Solid Films 515 (2007) p. 7364

[14]   B. Spath, K. Lakus-Wollny, J. Fritsche, Thin solid films 515 (2007) p. 6172

[15]   G. Teeter, J. Appl. Phys. 102 (2007) p. 034504

[16]   S. Andersson, I. Marklund, J. Martinson, Surf. Sci. 12 (1968) p. 269

[17]   F. Comin, P. Citrin, P. Eisenberger, J. Rowe, Phys. Rev. B 26 (1982) p. 7060

[18]   D.E. Andersson, S. Andersson, Surf. Sci. 23 (1970) p. 311

[19]   A. Salwén, J. Rundgren, Surf. Sci. 53 (1975) p. 523

[20]   P.D. Johnson, D.P. Woodruff, H.H. Farrell, Surf. Sci. 129 (1983) p. 366

[21]   M.O. King, Surf. Sci. 606 (2012) p. 1353

[22]   M. Lahti, Surf. Sci. 622 (2014) p. 35

[23] A. Barbieri, M.A. Van Hove, Private communication http://www.ap.cityu.edu.hk/ personal-website/Van-Hove.htm.

[24] J.B. Pendry, J. Phys. C Solid State Phys. 13 (1980) p. 937

[25] H. Neumann, M. Mast, Cryst. Res. Technol. 31 (1996) p. 75

[26] A.J. Ricco, H.S. White, M.S. Wrighton, J. Vac. Sci. Technol. 2 (1984) p. 910

[27] F. Debbagh, E.L. Ameziane, M. Azizan, Mater. Sci. Eng. 38 (1996) p. 223

[28] S. Hufner, G.K. Wertheim, Solid State Commun. 17 (1975) p. 417

[29] D. Westphal, A. Goldmann, Surf. Sci. 131 (1983) p. 113

[30] W. Wallauer, Surf. Sci. 331 (1995) p. 731

[31] C.K. Rhee, C. Jung, B. Ku, J. Solid State Electrochem. 9 (2005) p. 247

[32] P. Rodriguez, E. Herrero, Langmuir 22 (2006) p. 10329

[33] H.N. Nowotny, Z. Metallk. 37 (1946) p. 409

[34] A.L.N. Stevels, G.A. Wiegers, Recl. Trav. Chim. Pays-Bas 90 (1971) p. 352

[35] H.C. Galloway, J.J. Benitez, M. Salmeron, Surf. Sci. 298 (1993) p. 127

[36] Y.C. Kim, C. Westphal, R.X. Ynzunza, Surf Sci. 416 (1998) p. 68

[37] S. Kashida, W. Shimosaka, M. Mori, J. Phys. Chem. Solids 64 (2003) p. 2357

[38] A.J. Brunner, H. Bretscher, R. Lapka, J. Phys. C. 20 (1987) p. 5233

[39] S.A. de Vries, W.J. Huisman, P. Goedtkindt, Surf. Sci. 414 (1998) p. 159

[40] W.Braun, G.Held, Surf. Sci. 594 (13)(2005) p. 1

Chapter 4

Tellurium deposition on the Cu(110) surface

Abstract

The chemisorption of tellurium onto the low index Cu(110) surface has been studied under ultra high vacuum using a combination of Low energy electron diffraction, photo electron spectroscopy and scanning tunnelling microscopy. For a coverage of 0.5ML a c(2×2) substitutional alloy forms with the alloying process beginning as soon as tellurium is adsorbed. As the coverage exceeds 0.5ML we start to see the structure becoming uniaxially compressed as indicated by the LEED patterns. For coverages over 1ML we see 3d island growth in the STM with two domains detected rotated ~ 30° with respect to each other.

Introduction

2d materials and 2d surface alloys are interesting for many fundamental and technological applications. They allow material properties to be adjusted from those of the bulk materials. Most of the 2d alloy systems previously reported are formed by bi-metallic elements [1]. The deposition of tellurium onto copper is an interesting system as they are two different types of element, a semiconductor and a metal. No previous studies of this system have been performed however several systems that may be similar have been studied, including silicon, sulphur and iodine adsorption on the Cu(110) surface. Tellurium adsorption on the Cu(111) plane was discussed in the previous chapter with the previous studies finding that a surface substitutional alloy forms for 0.33ML coverage [2,3]. The only other tellurium adsorption studies

done on copper were performed on the (100) surface. For the (100) surface a commensurate c(2×2) structure with the tellurium occupying the four fold hollow sites for a coverage of 0.25ML [4-7]. Differing to the (111) surface were surface alloying was found. Above this coverage on the (100) surface the over-layer becomes incommensurate with the underlying copper lattice.

One of the similar systems which has been studied is the adsorption of silicon on the Cu(110) surface. This was first done by Martin-Gago et al where using photoelectron diffraction they found that at 0.5ML an ordered c(2×2) alloyed structure is formed with Si replacing one out of every two copper atoms [8]. The deposition was looked at in more detail by studying the surface at several instances leading up to the 0.5 ML [9]. For coverages of around 0.1ML they found regularly sized but randomly distributed islands orientated along the [112] surface direction. However only the (1×1) LEED pattern of the clean surface was found. With further deposition they found these islands coalesced and grew forming extended alloy regions. For a coverage of 0.5ML as previously they found the entire surface was covered by the alloy structure. As further Si was deposited three further islands of alloy grew on top of the alloy as well as clusters of Si being detected. High resolution PES work showed that signal originating from these additional islands and clusters is present for 0.5ML coverage [10]. They found the islands to also have the same structure as the alloy underneath it and attributed mass transport via surface diffusion as the mechanism responsible for the completion of the surface alloy. Further high resolution PES work showed that the ratio of these islands and clusters with respect to the alloy was constant from the beginning of deposition, suggesting they are present and grow with the alloyed surface from the start [11]. The fact

that these structures were observed for such low coverages suggests that Si has a high diffusion length in copper [11]. Rojas et al. also performed a LEED IV experiment on the 0.5ML c(2×2) structure which found the same 2d alloyed top layer with the silicon atoms displaced inwards with respect to the copper plane by 0.26Å [12]. Studies of antimony adsorbed on Cu and Ag (110) surfaces have also found that a substitutional c(2×2) surface alloy forms for a coverage of 0.5ML [13-15]. They found a buckled surface layer with the Sb atoms residing 0.25Å above the plane of the copper atoms.

The deposition of sulfur on Cu(110) is relevant as it is also a chalcogenide coming from group 16 of the periodic table. Oudar and co-workers studied the dissociative chemisorption of hydrogen sulphide on Cu(110) surfaces using LEED [16,17]. They found a range of structures for increasing sulfur coverage starting with a c(2×2), then a p(5×2) and finally a p(3×2) structure. These structures were confirmed by an STM study by Carley et al. [18]. They also proposed new models for the p(5×2) and p(3×2) structures in which the upper copper/sulfur layer is compressed by 16.3% and 24.5%, respectively, resulting in surface buckling.

Similar in size and properties to tellurium the adsorption of iodine on Cu(110) is also relevant. The atomic structure of the over-layers was determined with LEED and STM [19]. A commensurate c(2×2) structure was found for a coverage of 0.5ML. Further adsorption lead to the uniaxial compression of the over-layer along the [110] direction indicated by a splitting of the fractional order peaks in LEED. This compression included the formation of heavily striped domain walls revealed via STM. The formation of striped domain walls is a well-known mechanism of a commensurate–incommensurate phase transition [20,21].

Under this mechanism, an initially commensurate structure is compressed by forming areas with higher densities of atoms (domain walls) at regular intervals, leaving the areas between them unchanged. With increasing coverage the distance between the walls decreases [19].

In this chapter the chemisorption of Te onto the low index Cu(110) surface has been investigated for a range of coverages using a combination of LEED, STM and PES techniques.

Experimental

Tellurium was deposited onto a clean single crystal using a homemade thermal evaporator. This tellurium effusion cell was operated at 570K with the deposition rate for the sub monolayer coverage calculated to be about 0.2 ML /min. The adsorption was monitored by comparing the intensity of the Cu $2p_{3/2}$ and Te $3d_{5/2}$ XPS spectra and examining the LEED patterns. The coverages are expressed in terms of monolayers where 1 ML is equal to the number of atoms present in an ideal Cu(110) surface. The Cu(110) single crystal was cleaned in−situ by cycles of argon ion bombardment to remove adsorbents followed by annealing to restore the order at the surface disrupted by the sputtering process. This procedure was repeated until the XPS showed no detectable contamination and a sharp (1×1) LEED pattern was observed. The cleaning conditions for this crystal were an ion energy of 1kV with a sample flux of around 10µA followed by annealing to ~870K. The STM images were analysed using the Gwyddion software package [22].

Results

0.5 ML coverage

Tellurium was deposited onto the clean Cu(110) crystal in UHV. Following deposition the LEED pattern was observed to see if an over-layer structure had formed. The tellurium was deposited in small doses with XPS data taken along with LEED data for each coverage shown in figure 4.1. For the first deposit even though we do detect tellurium with the XPS we see no additional ordered structure with the LEED still displaying the (1×1) pattern of the clean surface. After an additional 60 seconds of deposition we start to see the c(2×2) spots appear in the LEED pattern, slightly diffuse with additional spots at the c(2×8) position which could be the initial growth stage. These c(8×2) spots were fairly diffuse and we were not able to get a coverage where we could only see the c(8×2) over structure independent of the c(2×2). These c(8×2) diffraction spots disappear when either additional tellurium is deposited or by gently annealing the sample to around 300° C. This gentle annealing of the surface provides the energy needed for the surface structure to become more ordered. After further tellurium is deposited we now have a sharp c(2×2) pattern, this corresponds to a coverage of 0.5ML. The position of the sample was altered to examine different sections with the electron beam in LEED. This was done to check how uniform the c(2×2) structure was and it was found to be constant and sharp over the whole surface.
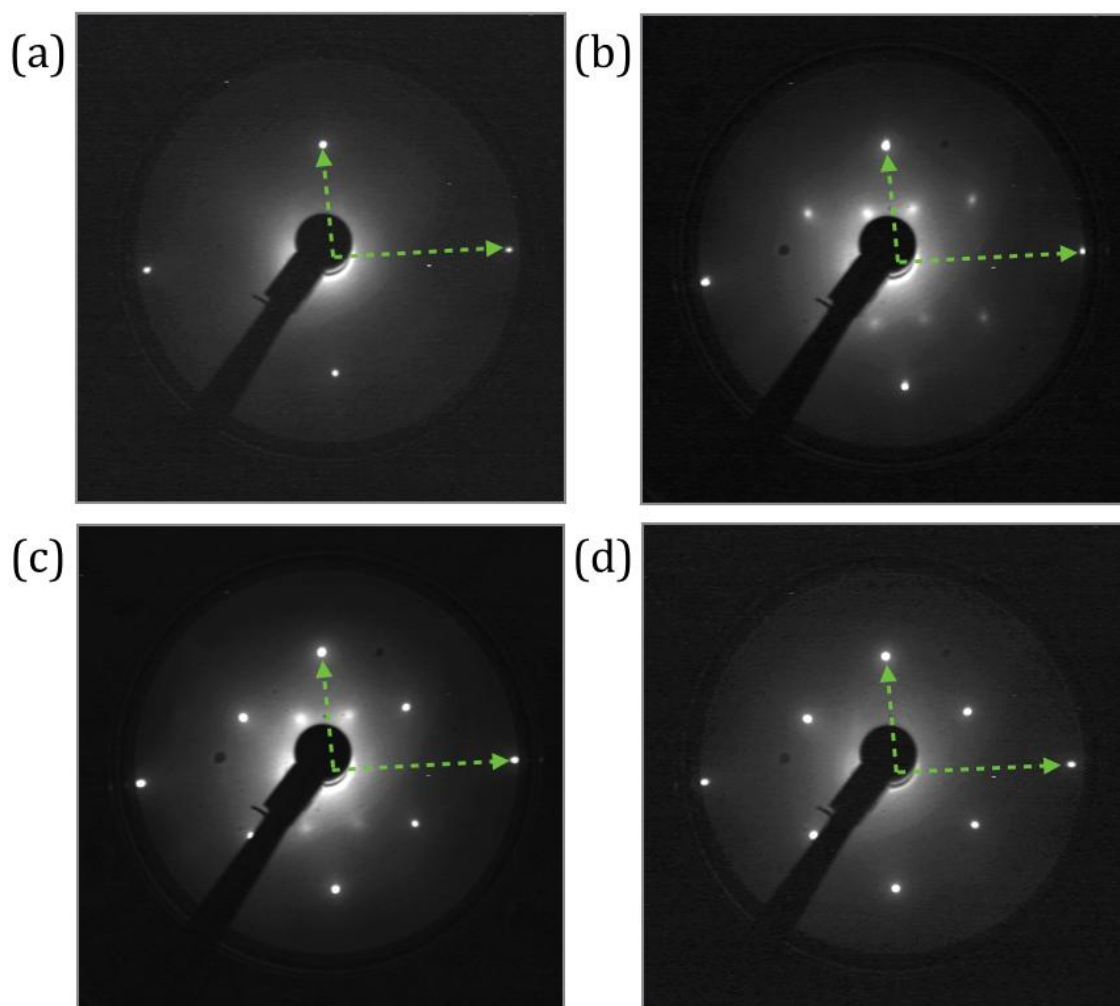
Figure 4.1: LEED patterns obtained for increasing dosing times. (a) 0 seconds, (b) 60 seconds, (c) 90 seconds and (d) 120 seconds. The unit cell of the copper (110) is shown in the images. All of the images were taken with an electron beam energy of 70eV

The atomic model corresponding to a c(2×2) over-layer at 0.5ML coverage is shown in figure 4.2 with the corresponding diffraction pattern. The XPS data for this coverage showed just one species of tellurium to be present while the main change in the UPS data was a dampening of the Cu 3d orbitals.
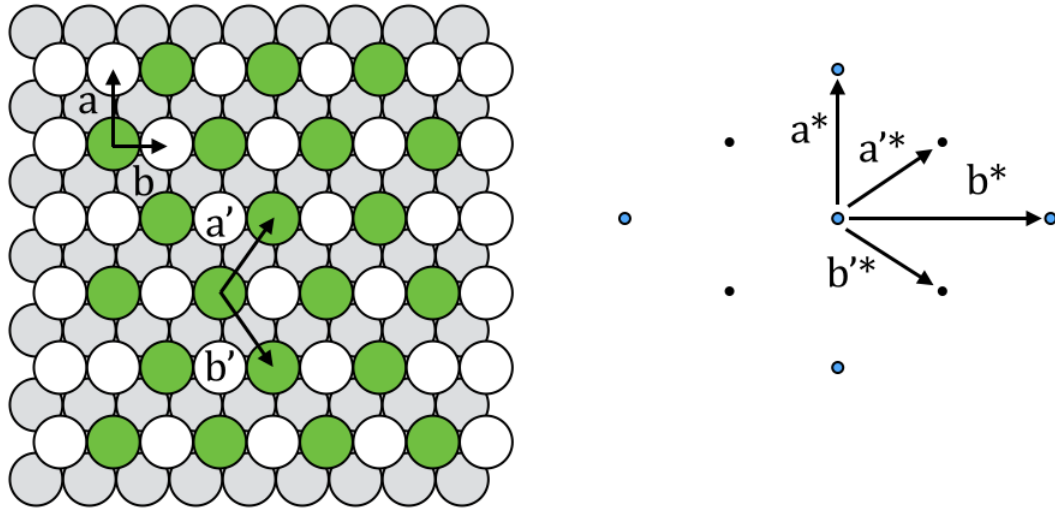
Figure 4.2: Atomic Model of c(2×2) over-layer with corresponding diffraction pattern

STM images of this phase were consistent with the observed LEED patterns showing a quasi-hexagonal symmetry as is expected for the c(2×2) over-layer. In figure 4.3 a step can be seen running diagonally down the image with the c(2×2) structure decorating both of the terraces. This was typical of the images obtained at this coverage. The Fourier transform of the image is shown adjacent showing the c(2×2) symmetry. We were not able to image an area with a lower coverage or more disorder which may have suggested the origin of the diffuse c(8×2) spots seen in the LEED. The section highlighted by the green box has been blown up and Fourier filtered using the Gwyddion software package to clearly reveal the hexagonal structure [22]. The lattice constant for this over-layer was measured to be 4.6±0.1Å which is consistent with the expected distance for a c(2×2) over-layer on Cu(110) which is 4.4Å.
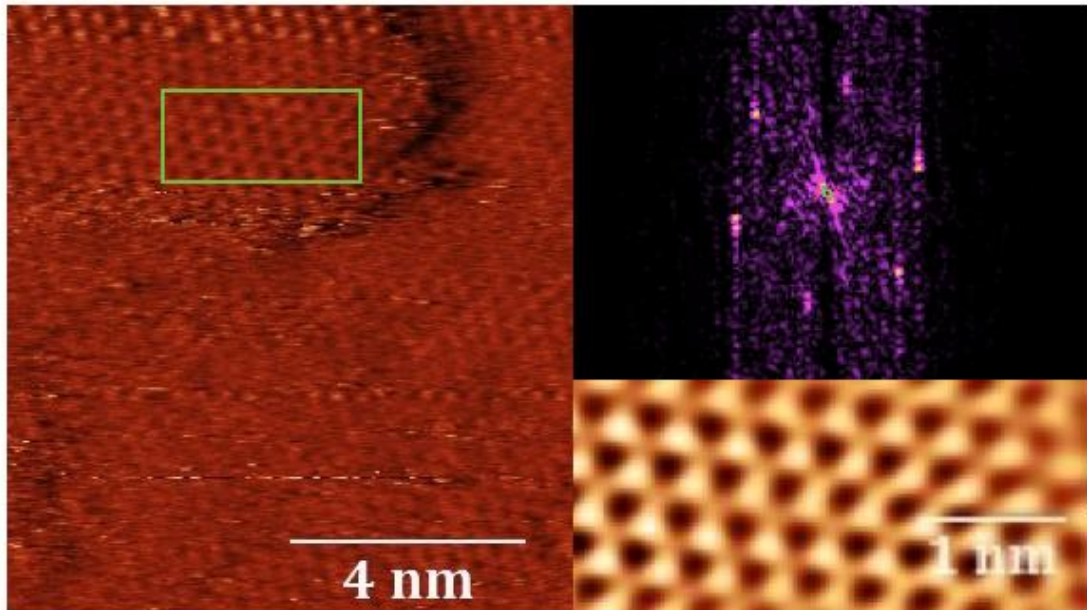
Figure 4.3: STM image of the c(2×2) phase taken at room temperature. The section within the green box has been enlarged and Fourier Filtered and is shown in the bottom left. The Fourier image is shown in the top right. The image was obtained with a sample bias of +0.3v and a tunnelling current of 0.3nA.

Coverage > 0.5ML

As further tellurium was deposited after the c(2×2) was completed the half order spots begin to split along the [110] direction, this indicates uniaxial compression of the over-layer structure which is seen on other (110) systems such as iodine adsorption on Cu(110) and Ag(110) surfaces [19,23]. Once the c(2×2) structure is complete additional tellurium atoms will displace atoms sitting in the [110] rows of the surface causing the over-layer to become compressed. In similar studies a quantity known as the splitting parameter Q is introduced to quantify the size of this spot splitting. The value of Q is given by the ratio of the distance

between moving spots of the over-layer *d1* to the distance between the (0 0) and

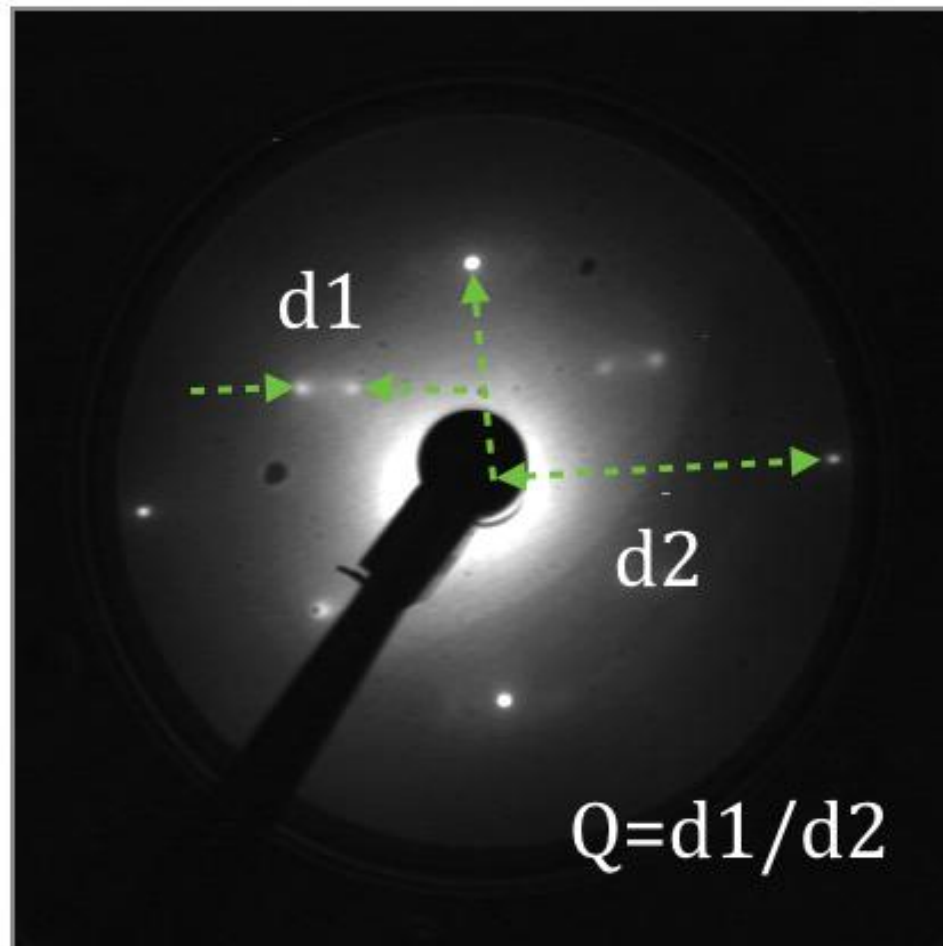(1 0) spots of the substrate *d2* as shown in figure 4.4.

Figure 4.4: LEED pattern showing the split spot structure after a tellurium

dosage of 240 seconds taken with an electron beam energy of 70eV. The

distances *d1* and *d2* used calculating *Q* are also shown

It has been shown for a high-order commensurate structure on Cu(110), the

splitting parameter *Q* can be expressed in terms of *M* and *N*, where *M:N* denote

the commensurability for example 5Te:6Cu is 5:6. Equation 4.1 is then used to

calculate *Q* [19].

$$Q = \frac{M - N}{N} \tag{4.1}$$

Figure 4.4 displays the maximum splitting observed as a function of deposition time before the split spot structure was no longer observed. For the lower coverage where the split spots were seen the Q value was 0.14 while for the image shown in figure 4.4 the Q value was 0.16. Using the above equation these correspond roughly to M and N values of 6:7 for the least split spots and 5:6 for the most split spots. Previous STM studies imaged a high order commensurate phases coinciding with the split spot phase as domain boundaries, however we were not able to observe them for our sample [19,24].
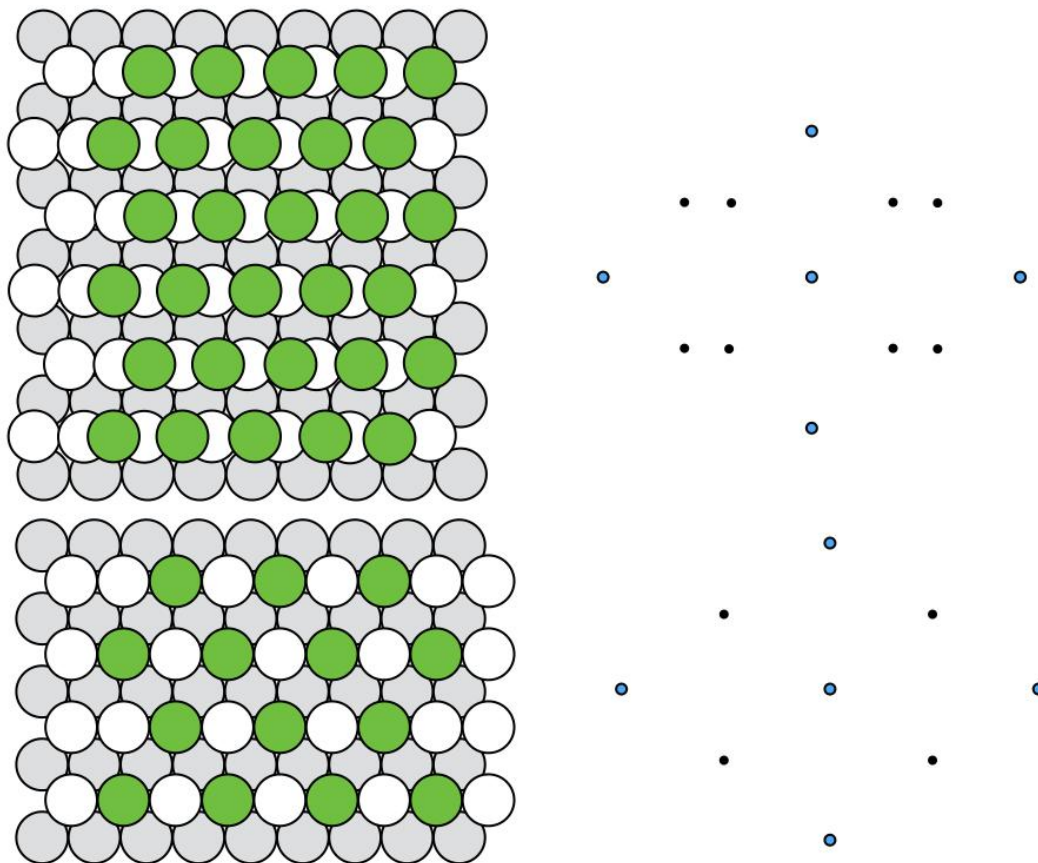
Figure 4.5: Atomic model of a compressed over-layer and the corresponding diffraction pattern. The original structure is shown below.

Coverage > 1ML

For a heavy deposition we do not see this split spot structure just a hexagonal symmetry in the LEED pattern shown in figure 4.6, however the energy range over which patterns could be seen was reduced suggesting a loss in long-range order. For this coverage we have layers of the c(2×2) alloy on top of other buried regions of c(2×2) as indicated by the STM and XPS data.

Figure 4.6: LEED image after a heavy tellurium dose no longer showing c(2×2) symmetry but instead hexagonal. Image taken with an electron beam energy of 70eV

The STM images for this section showed a hexagonal symmetry in agreement with the LEED however the structure was rotated 30° with respect to the hexagonal structure of the lower coverage c(2×2) phase. An STM image after a deposition of 360 seconds corresponding to ∼ 1.2ML is shown in figure 4.7. Measurement of the peak positions in the LEED show that this hexagonal pattern has equal vector lengths unlike for the c(2×2) structure. In the case of the c(2×2) symmetry the quasi-hexagon is formed by the four over-layer spots and the two

of the spots form the substrate. So the vector lengths should be the lattice constant a for the substrate and the over-layer should be $\sqrt{3/2}a$. The lattice constant for the c(2×2) structure measured from the position of the peaks in the LEED was found to be 4.3±0.1Å which is in agreement with the expected distances for the c(2×2) over-layer. The change in rotation of domains is clear when comparing the Fourier transforms of the two phases. Only two of the previously reported bulk alloy phases of $Cu_{1-x}Te_x$ were shown to possess hexagonal symmetry, the most common alloy Cu_2Te [25] and the Cu_3Te_2 phase [26].
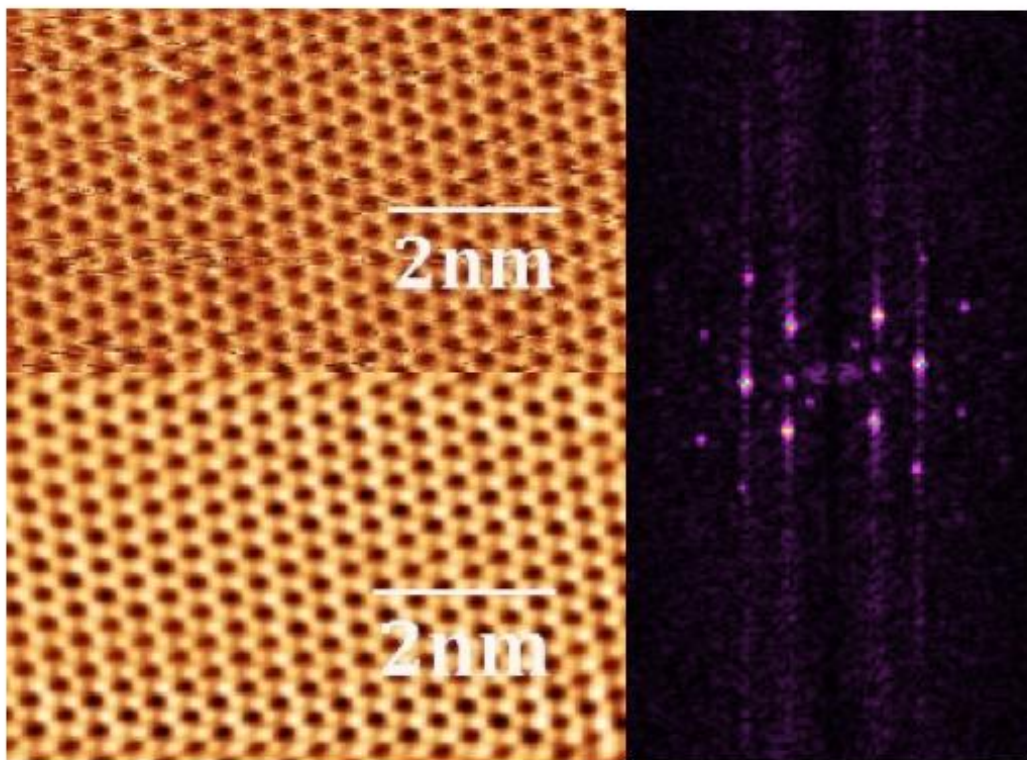
Figure 4.7: STM image showing the rotated hexagonal structure for the heavy deposition taken at room temperature. The image size is 6.7×4.2nm and was obtained with a sample bias of +0.3V and a tunnelling current of 0.3nA. The raw image is shown in the top left with is Fourier transform on the right. The lower left image has been Fourier filtered.

For a heavier tellurium deposition of 590 seconds a 3d surface was observed with regions showing both the normal and the rotated structures. The c(2×2) domains appear to have grown on top of the rotated hexagonal phase.
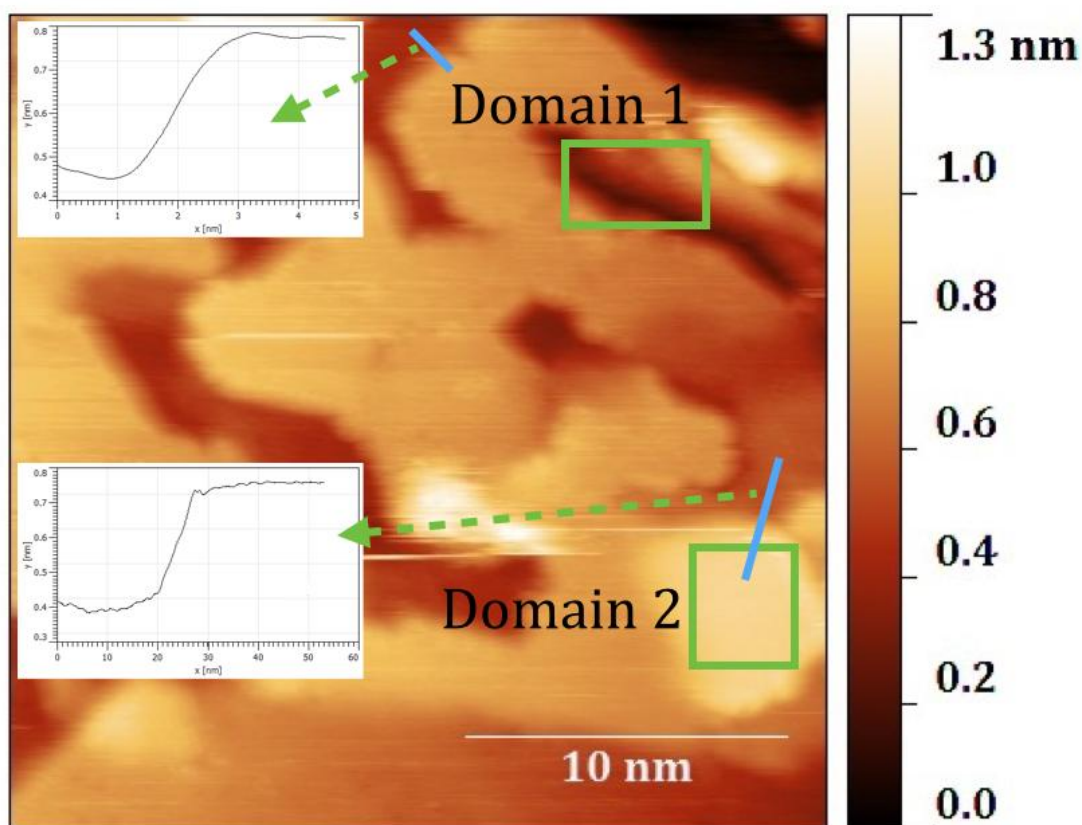

Figure 4.8: STM image for the heavy deposition showing a 3D surface. Insets show the step heights taken across the 2 blue lines. The image is 25.2nm^2 and was obtained with a sample bias of +0.5V and a tunnelling current of 3nA

The 2 domains highlighted in image 4.8 have been blown up to show the rotational difference between them in figure 4.9. The islands are not aligned in any particular direction and vary in size and shape however there are several whose borders display a ~60° angle demonstrating the hexagonal structure of

the islands. The average height of the islands was measured by taking line scans over the image producing an average island height of 3.7±0.1Å.
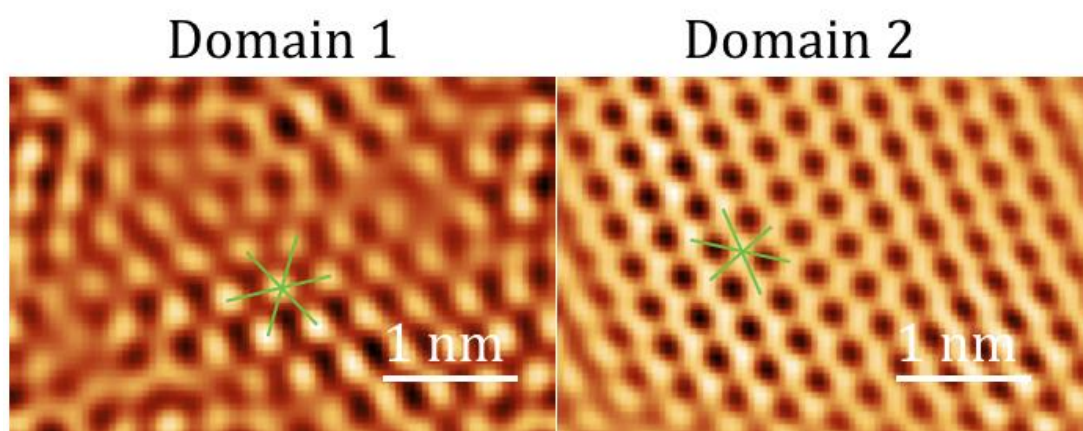

Figure 4.9: Blown up domains from figure 4.8 highlighting the change in rotation of the two domains

The hexagonal directions for the images have been highlighted to show the rotation of ~ 30° in figure 4.9. The lattice constants for the two domains were found to be the same as at the lower coverage. The images that contained both domains were dominated by regions with the same rotation as domain 2 however most images obtained at this coverage only showed domain 2. We were not able to image domain 1 independently suggesting it may be the precursor to the next layer.

In the large scale STM image shown in figure 4.10 many islands of varying size can be seen. A lot of these islands are either triangular or have a hexagonal shape to them. The islands vary in height ranging from 0.26±0.1Å to 0.56±0.1Å when measured by taking line scans through the image. This 3D island growth suggests that a simple layer by layer growth mode is not present.
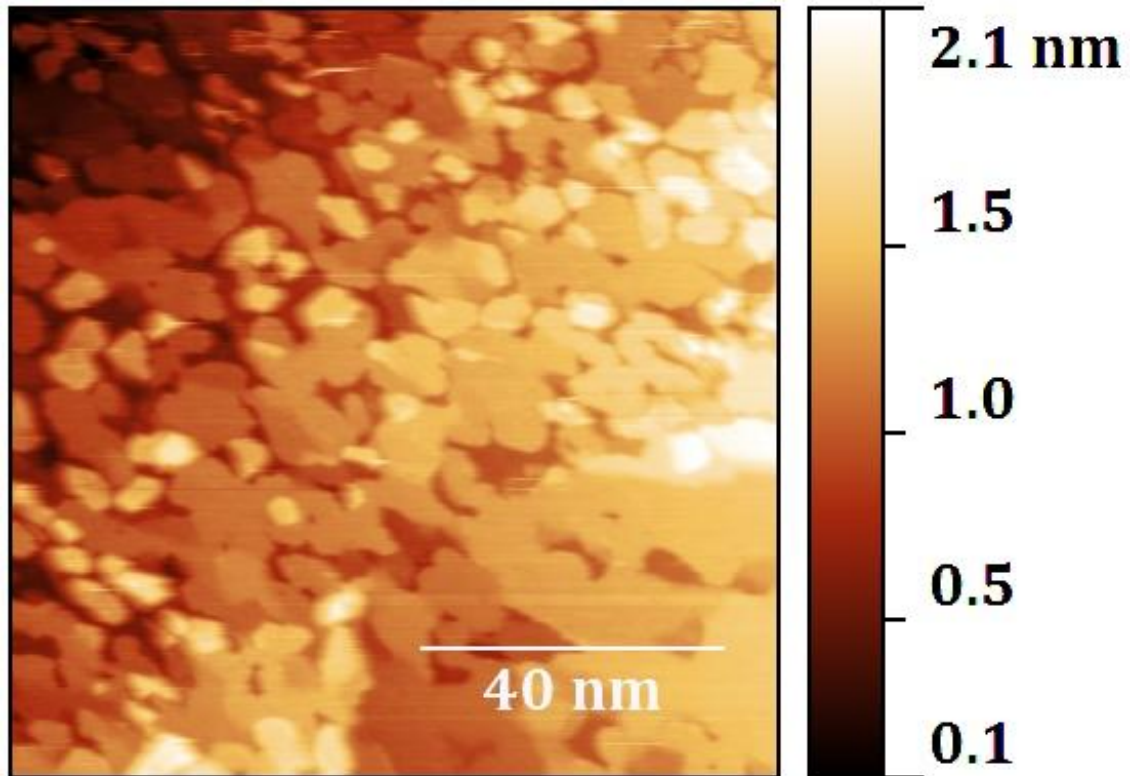
Figure 4.10: STM image of the 3D growth of islands taken at room temperature. The image size is 100nm² and was obtained with a sample bias of +0.6V and a tunnelling current of 2nA.

The expansion of the lattice was measured with LEED for the different coverages and was found to expand for the ordered c(2×2) structure respect to the clean Cu(110) lattice vectors. This expansion was found to be around 3.6±0.1% for the c(2×2) structure with the substrate lattice vector measuring 2.64±0.1Å. This expansion may arise due to strain caused by incorporating the larger tellurium atom within the copper plane. The lattice spacing extracted from the heavy deposition revealed a hexagonal symmetry with both lattice vectors measuring the same 3.70±0.1Å. This corresponds to diffraction peaks in the same position as was observed in the split spot earlier. This could reveal a bulk alloy phase formation with the split spots seen earlier indicating an interference between

the surface alloy and the forming bulk alloy. It could also be a compressed phase of the surface alloy that bears the hexagonal symmetry as was observed for the adsorption of iodine on the Ag(110) surface [27].
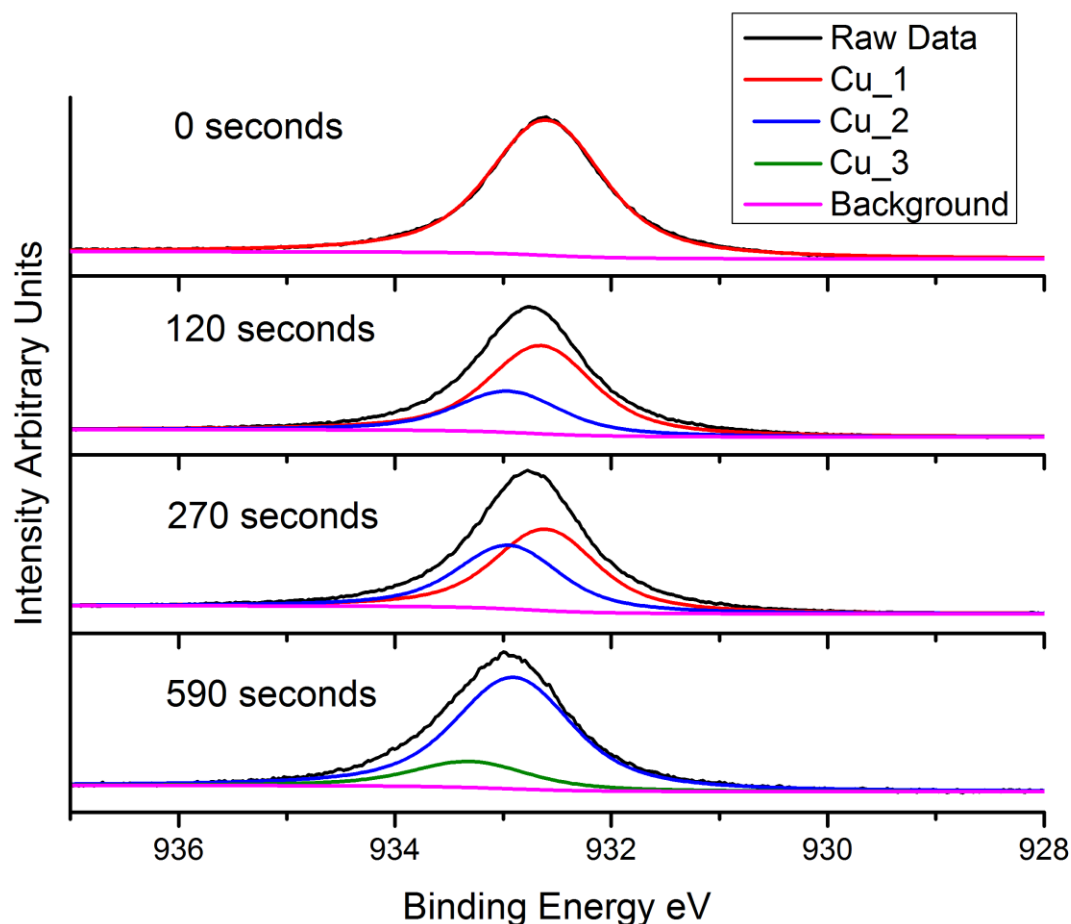

Figure 4.11: XPS spectra for the Cu 2p orbital for different dosage times of tellurium

The XPS spectra for the copper 2p orbitals were fitted with 2 components for the lower coverage as shown in figure 4.11. The two components used relate to the elemental copper obtained from the clean sample and a signal originating from copper bonded to tellurium at the surface with binding energies 932.6eV and 933.0eV. An asymmetric Doniac-Sunjic DS line shape was used as is common for the peak fitting of metals [28]. The FWHM used was 1.3eV with the asymmetry factor in the DS line shape set to 0.0001. The intensity of the orbital associated

with copper bonded to tellurium increases as we increase tellurium coverage as shown in figure 4.13, however it does not shift in binding energy suggesting the bonding is similar for all the coverages. This copper peak may be associated to the Cu^{2+} species as in the earlier chapter on the Cu(111) surface. Examining the Cu signal after a heavy deposition of tellurium the main peak originated from the signal of copper in the alloy with only a small amount of the underlying elemental copper still detectable, however another peak was also detected shifted 0.4eV to higher binding energy. A similar peak was found for the tellurium orbital for the heavy deposition. This may arise from copper in the alloy that is not at the surface and so may have been buried by additional alloy growth on top of it. The fitting for the Te 3d level was done using the Te $3d_{3/2}$ instead of the $3d_{5/2}$. This was due to using a non-monochromatic X-ray source and the satellite from the $3d_{3/2}$ sits underneath the $3d_{5/2}$ peak. Therefore it is easier to fit the $3d_{3/2}$ and then convert the areas and energies using the branching ratios and spin orbit splitting values. The tellurium peak was also fitted with two asymmetric line shapes with binding energies 572.7eV and 573.1eV respectively. The line shapes used were more asymmetric than that for the copper with asymmetries of 0.04. For the sub monolayer coverages the tellurium data is fitted with just one component at 572.7eV. The higher binding energy component was only detected for the heavy depositions over 1ML and so may originate from an alloyed section that is buried underneath another alloyed section. The fact that the binding energy is constant for the sub monolayer tellurium data suggests that the surface is alloying and that the alloying process begins for very low coverages. If initially an over-layer of tellurium were forming we would expect to see this as a shifted component as the local

environment will be different for surface adsorbed tellurium to that alloyed into the surface. We only see a decrease in the elemental copper with the ratio of copper telluride peak to the tellurium peak remaining constant with further tellurium deposited. By looking at the ratio of tellurium to copper which coincide with our sharp c(2×2) LEED pattern we can try to calibrate the coverage in terms of XPS signal. A growth curve of tellurium deposition time against the ratio of $Cu2p_{3/2}$ to $Te3d_{5/2}$ is displayed in figure 4.23, showing a linear relationship. This indicates that the mechanism by which tellurium is adsorbed on to the surface is constant for these deposition times. This growth curve allowed us to reproduce known structures at a later time even if the output of the source increases.
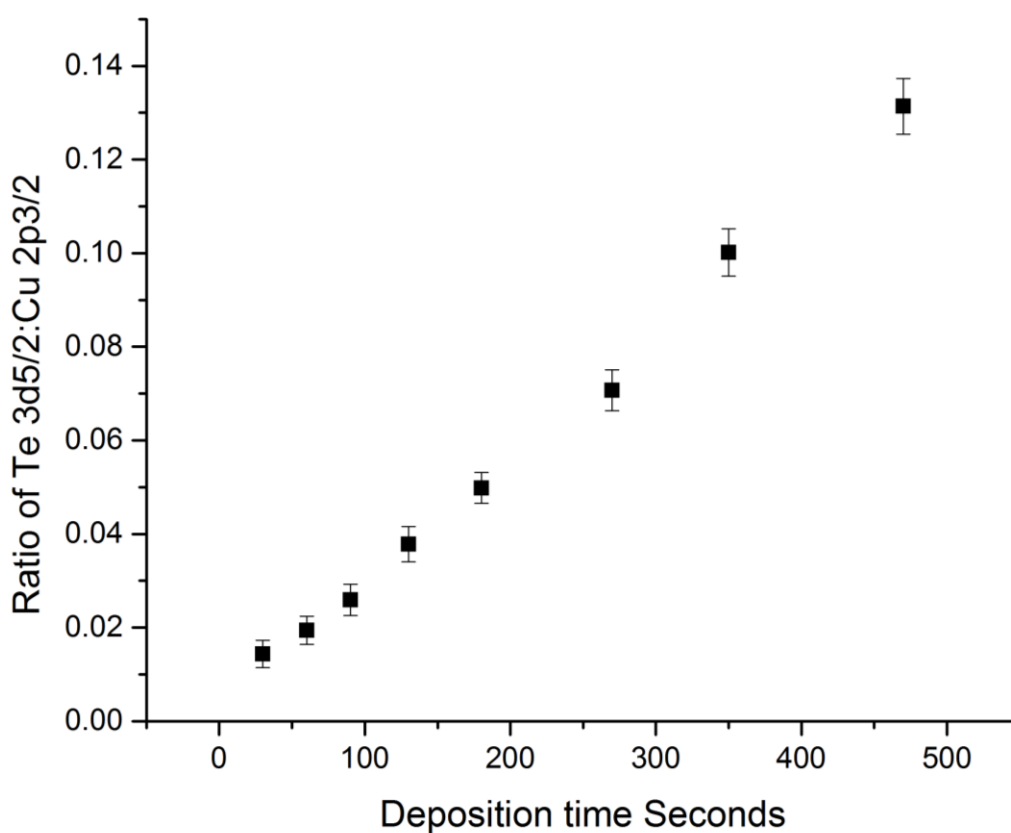

Figure 4.12: Growth curve of Te on Cu(110) measured by XPS with the Te source operated at a temperature of 320°C
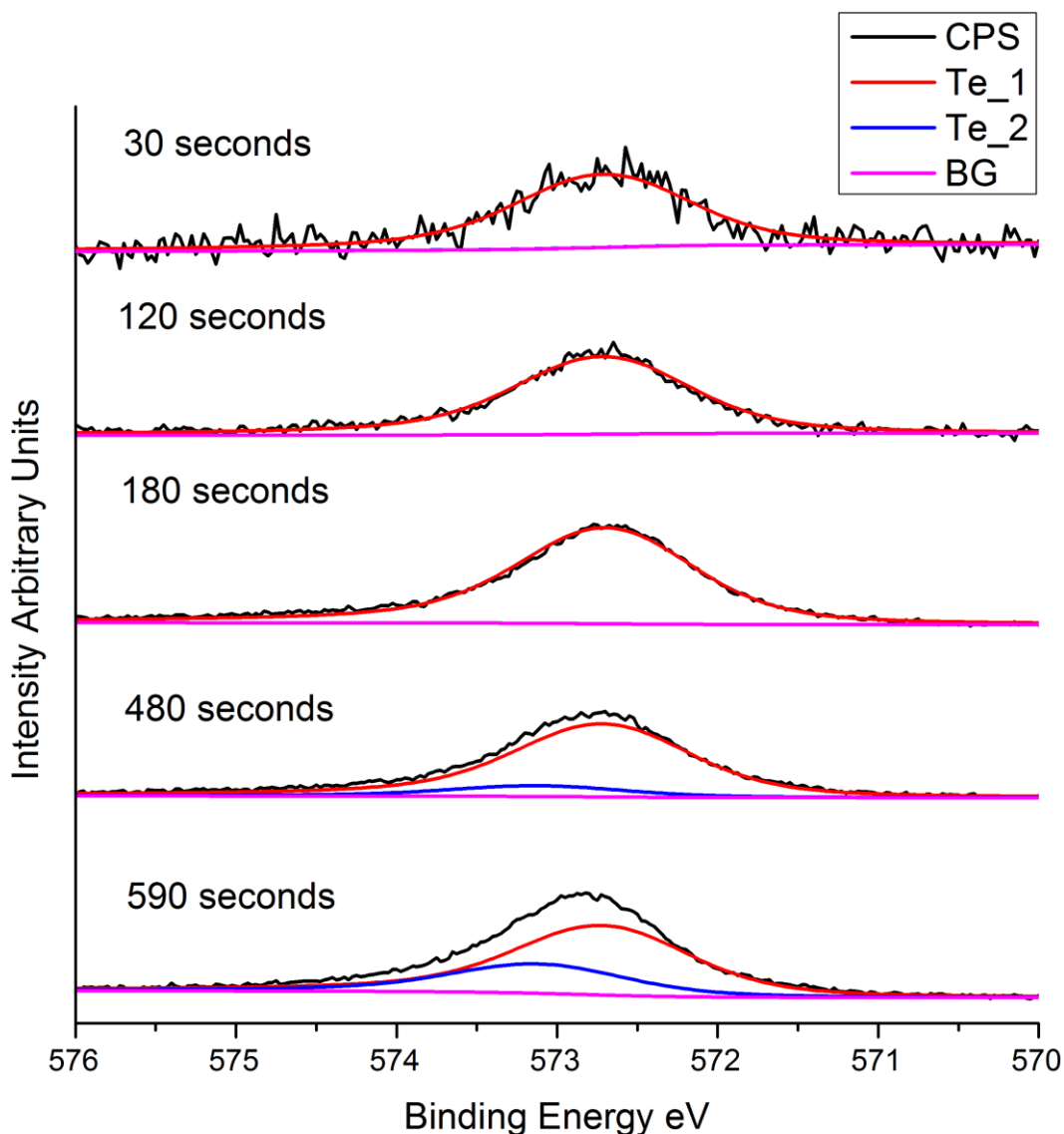
Figure 4.13: XPS spectra for Te 3d$_{5/2}$ orbital for a range of tellurium dosage times

The atomic ratio Cu:Te calculated for 590 second deposition was 1.9±0.1. The UPS spectra were measured at normal emission for a range of increasing coverages. The Clean Cu(110) spectrum is displayed at the top of figure 4.15, this is similar to previously reported spectra with the main 3d peaks occurring from 2−3eV [29]. As we deposit tellurium the main initial change is the damping of signal from the Cu 3d orbitals. With increasing coverage we start to see an

increase in intensity both sides of the Cu 3d bands that are attributed to Te 5p orbitals [30]. The change in work function of the sample was calculated using the position of the secondary electron cut-off and the Fermi level. A plot of the change in the value of the work function against deposition time is shown in figure 4.14.
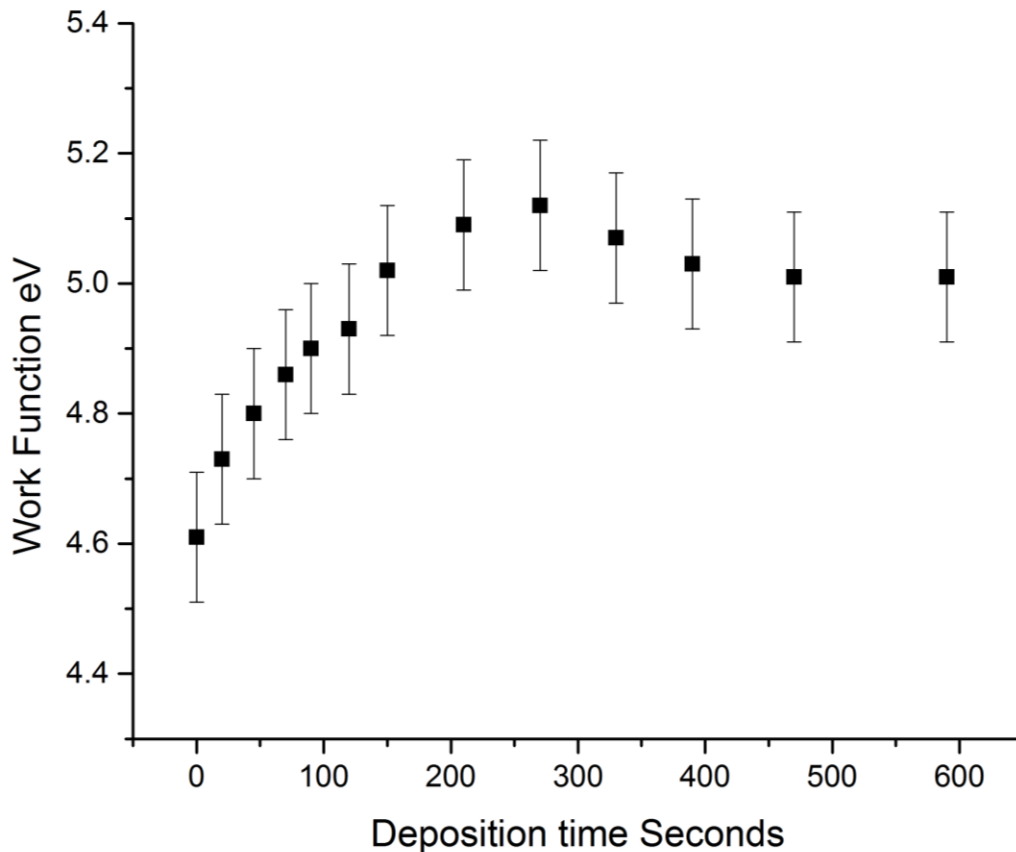

Figure 4.14: Plot of the measured work function vs. tellurium deposition time

The initial measured value of the work function for the clean Cu(110) surface was found to be 4.6±0.1eV which is in agreement with other studies [31]. For the first stages of deposition the work function increases with tellurium coverage. We see a maximum in the work function for a deposition time of 200 seconds with an increase of 0.5eV from the clean surface to 5.1±0.1eV. Further tellurium deposition brings about a small decrease in this value until above 1 ML

of deposition this value plateaus to a value of 5.0±0.1eV. This could indicate the change to a bulk alloy from a surface alloy as this is the coverage where we start to see a higher binding energy component in the Te 3d XPS data.
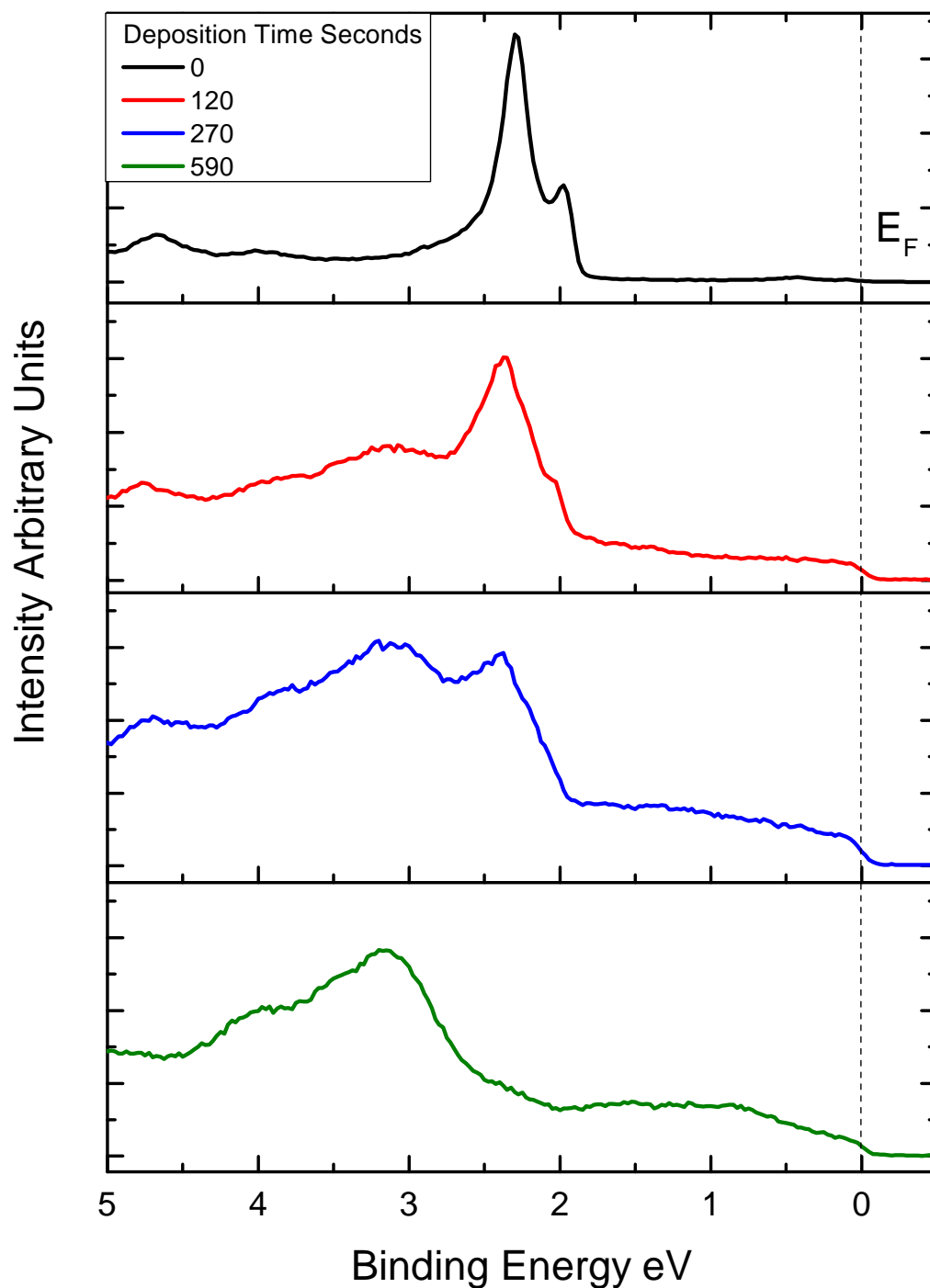

Figure 4.15: UPS spectra collected at normal emission for different tellurium dosage times with the Fermi level set to 0eV binding energy

The largest change in work function corresponds to the spectra where we no longer see strong emission from the elemental Cu 3d orbitals. After this the valence band is more similar to that of an alloyed surface than the clean one, with the valence band showing a close resemblance to the Cu_3Te_2 as opposed to the Cu_2Te due to a sharp edge present at the Fermi level [32,33].

Conclusion

The adsorption of tellurium on the Cu(110) surface has been studied using a combination of XPS, UPS, STM and LEED. For a coverage of 0.5ML a c(2×2) structure was observed, the position of the Te 3d peak in the XPS data suggests that the surface alloys from the beginning of deposition. Further work needs to be done to confirm whether or not a surface substitutional alloy has formed or just an over-layer however the LEED data was not suitable for dynamical analysis. Above this coverage we start to see the emergence of an incommensurate structure highlighted by the spot splitting observed in the LEED patterns. This splitting along the [110] direction indicates a uniaxial compression of the over-layer with respect to the under-lying lattice. For coverages over 1ML 3D island growth was observed with the STM revealing two co-existing domains of the c(2×2) structure rotated by 30° with respect to each other. The UPS spectra for this coverage revealed a similarity to that reported for the Cu_3Te_2 bulk alloy phase.

References

[1]   J.A. Rodriguez, Surf. Sci. Rep. 24 (1996) p. 223

[2]   S. Andersson, I. Marklund, J. Martinson, Surf. Sci. 12 (1968) p. 269

[3]   F. Comin, P. Citrin, P. Eisenberger, J. Rowe, Phys. Rev. B 26 (1982) p. 7060

[4]   D.E. Andersson, S. Andersson, Surf. Sci. 23 (1970) p. 311

[5]   A. Salwén, J. Rundgren, Surf. Sci. 53 (1975) p. 523

[6]   P.D. Johnson, D.P. Woodruff, Surf. Sci. 129 (1983) p. 366

[7]   F. Comin, P. Citrin, P. Eisenberger, Phys. Rev. B 26 (1982) p. 7060

[8]   J.A. Martin-Gago, Phys. Rev. B 55 (1997) p. 12896

[9]   C. Polop, Surf. Sci. 402-404 (1998) p. 245

[10]   J.A. Martin-Gago Phys. Rev. B 59 (1999) p. 3070

[11]   C. Rojas, Surf. Sci. 454-456 (2000) p. 778

[12]   C. Rojas, Phys. Rev. B 57 (1998) p. 4493

[13]   K. Pussi, Surf. Sci. 583 (2005) p. 151

[14]   H.Y. Xiao, Chemical Physics 325 (2006) p. 519

[15]   V.B. Nascimento, Surf. Sci. 572 (2004) p. 337

[16]   J.L. Domange, J. Oudar, Surf. Sci. 11 (1968) p. 124

[17]   M. Kostelitz, J. Oudar, Surf. Sci. 27 (1971) p. 176

[18]   A.F. Carley Surface Science 447 (2000) p. 39

[19]   B.V. Andryushechkin, K.N. Eltsov, Surf. Sci. 584 (2005) p. 278

[20]   A. Bondi, J. Phys. Chem. 68 (1964) p. 441

[21]   A. Gavezzotti, J. Am. Chem. Soc. 105 (1983) p. 5220

[22]   Gwyddion software version 3.27 http://gwyddion.net

[23]   U. Bardi, G. Rovida, Surf. Sci. 128 (1983) p. 145

[24]   B.V. Andryushechkin Surf. Sci. 608 (2012) p. 135

[25]   H.N. Nowotny, Z. Metallk. 37 (1946) p. 409

[26]   A.L.N. Stevels, G.A. Wiegers, Recl. Trav. Chim. Pays-Bas 90 (1971) p. 352

[27]   W.F. Temesghen, J.B. Abreu, R.J. Barriga, Surf. Sci. 385 (1997) p. 336

[28]   S. Doniach, M. Sunjic, J. Phys. C 3 (1970) p. 285

[29]   M Bowker and R J Madix Surface, vol. 95 (1980) p. 190

[30]   T. Ichikawa J. Phys. Soc. Jap. 36 (1974) p. 1213

[31]   B. Quiniou, V. Bulovic′, Phys. Rev. B 47 (23)(1993) p. 15890

[32]   A.J. Brunner, H. Bretscher, R. Lapka, J. Phys. C. 20 (1987) p. 5233

[33]   S. Kashida, W. Shimosaka, M. Mori, J. Phys. Chem. Solids 64 (2003) p. 2357

Chapter 5

Tellurium deposition on the Cu(100) surface

Abstract

The chemisorption of tellurium onto the low index Cu(100) surface has been studied under ultra high vacuum using a combination of low energy electron diffraction, photoelectron spectroscopy and scanning tunnelling microscopy. An ordered 2d over-layer was found for 0.25ML with p(2×2) symmetry. Above this coverage the over-layer becomes compressed and incommensurate with the substrate. LEED patterns revealed one of the phases to be a coincidence structure with 5 Te surface lattice vectors coinciding with 6 Cu unit cell lattice vectors. At the highest coverage STM images revealed a heavily striped surface consisting of c(2×2) domains.

Introduction

Continuing the theme of tellurium adsorption on single crystal copper surfaces to understand how the surface structure can affect the work function and therefore its performance within a device. As mentioned earlier CuTe is a compound which either intentionally or unintentionally is a component in several thin film solar cells [1-6]. It appears as a back contact for cadmium telluride devices. Understanding the interaction of tellurium with copper is therefore important for device optimization and single crystal work allows us to more easily probe the structure of these systems.

The adsorption of tellurium on the (100) surface of copper has been previously studied for sub monolayer regimes. Two LEED studies showed that Te forms a p(2×2) over-layer with Te occupying the fourfold hollow sites for a coverage less than 0.25 ML [7,8]. This assignment was confirmed by both photoelectron diffraction [9] and SEXAFS [10] with the SEXAFS work finding the four-fold hollow site as the adsorption geometry. Above this coverage, a structure formed that was found to be incommensurate with the substrate. This structure was described as a coincidence lattice where 5 Te surface lattice vectors corresponded to 6 Cu unit cell lattice vectors [7]. For higher coverages after they annealed the sample to 800K they also found a disordered hexagonal Te layer as the structure became more compressed.

Many other studies have been done concerning adsorption on FCC (100) surfaces with many of them finding a p(2×2) over-layer for low coverages followed by a c(2×2) over-layer for higher coverages. Relevant systems to tellurium will be discussed below. Previous studies on the adsorption of Iodine on the Cu(100) surface reported LEED patterns for several different iodine structures with increasing coverage [11]. They begin with a sharp p(2×2) structure for 0.25ML. Additional deposition causes these p(2×2) spots to become blurry becoming diffuse stripes aligned along the [10] and [01] direction centred at the (½ 0) spot positions. The p(2×2) peaks then begin splitting until further deposition produces a c(6×2) phase. This pattern persists with additional iodine however new spots appear relating to a split c(2×2) symmetry. The p(2×2) spots then fade with additional iodine until only a split c(2×2) pattern remains. The adsorption of sulphur onto the Cu(100) surface has received much attention and studies such as dynamical LEED and SEXAFS have

shown that for the p(2×2) phase, corresponding to 0.25ML, that the sulphur sits in the four-fold hollow sites [12,13]. It has also been shown that sulphur occupies the four-fold hollow sites when the same structure is formed on Ni(100) [14]. The deposition of tin on to the Cu(100) surface also found a p(2×2) structure a splitting of the diffracted LEED beams as we observe here [15]. This splitting was attributed to anti phase domain boundaries formed at the surface [16]. They also found a range of structures for increasing coverage and imaged these domain walls with STM. The adsorption of antimony Sb onto the Cu(100) surface was found to produce a p(2×2) surface substitutional alloy despite the large mismatch in size between the copper and the antimony [17]. This surface alloying was shown by Xiao et al. to be favoured on all three low index surfaces of copper [18]. An STM study showed nano-stripes of electrochemically deposited Sb on the Cu(100) surface where they also found a coincidence lattice between the over-layer and the substrate [19].

In this chapter we study a range of over-layers formed by Te on a single crystal Cu(100) sample. The structures were probed with a combination of LEED and STM while the electronic properties were explored using XPS and UPS.

Experimental

Tellurium was deposited onto a clean single crystal using a homemade thermal evaporator. This tellurium effusion cell was operated at 570K with the deposition rate for the sub monolayer coverage calculated to be about 0.2 ML /min. The adsorption was monitored by comparing the intensity of the Cu $2p_{3/2}$

and Te $3d_{5/2}$ XPS spectra. The coverages are expressed in terms of monolayers where 1 ML is equal to the number of atoms present in an ideal Cu(100) surface. The Cu(100) single crystal was cleaned in situ by cycles of argon ion bombardment to remove adsorbates followed by annealing to restore the order at the surface disrupted by the sputtering process. This procedure was repeated until the XPS showed no detectable contamination and a sharp (1×1) LEED pattern was observed. The cleaning conditions for this crystal were an ion energy of 1kV with a sample flux of around 10μA followed by annealing to ~870K. The STM images were analysed using the Gwyddion software package [20].

Results

p(2×2) Phase 0.25ML

Tellurium was deposited at room temperature onto the cleaned copper substrate. The initial stage of growth was a p(2×2) over-layer with a deposition of 0.25ML. Below this coverage diffuse peaks were seen in the (½ 0) positions at very low beam energies only. With further deposition these became sharp producing a well ordered p(2×2) structure. The LEED patterns shown in figure 5.1 were taken with a beam energy of 67eV.
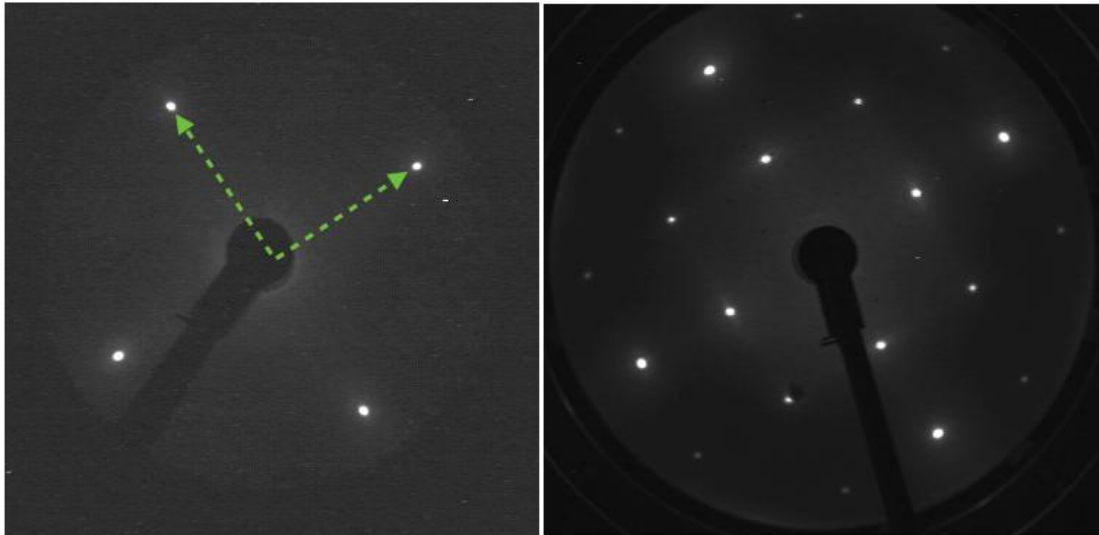
Figure 5.1: LEED images obtained for the clean surface and the p(2×2) structure a room temperature with an electron beam energy of 67eV

The structural model for this phase is shown in figure 5.2 with the tellurium atoms (green) located in the four-fold hollow sites as found by a previous SEXAFS and LEED studies [7,10].
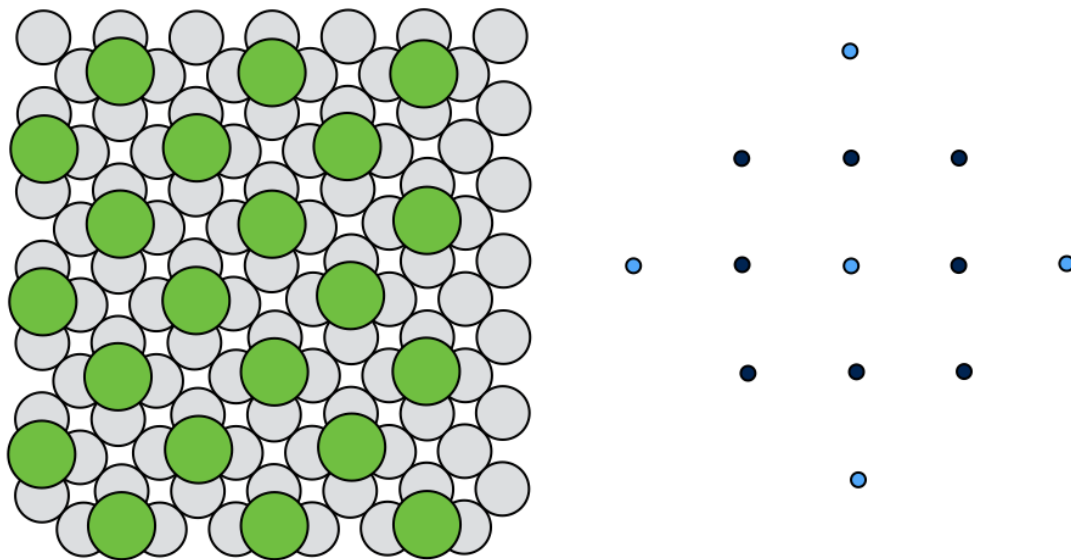

Figure 5.2: Structural model of p(2×2) over-layer on Cu(100) with the corresponding diffraction pattern

STM images obtained at this coverage were consistent with the observed LEED patterns displaying the p(2×2) structure aligned along the directions of the underlying copper substrate. The lattice vectors for the over-layer imaged in figure 5.3 were measured to be a=5.2±0.1Å and b=5.3±0.1Å, consistent with twice the atomic distance in the copper (100) substrate (2.55Å). The image was cleaned up using a Fourier transform to remove experimental noise. The vectors were not measured to be identical due to asymmetries with the STM scanner. For the same reason the observed angle between the vectors is 84° and not the expected 90°.
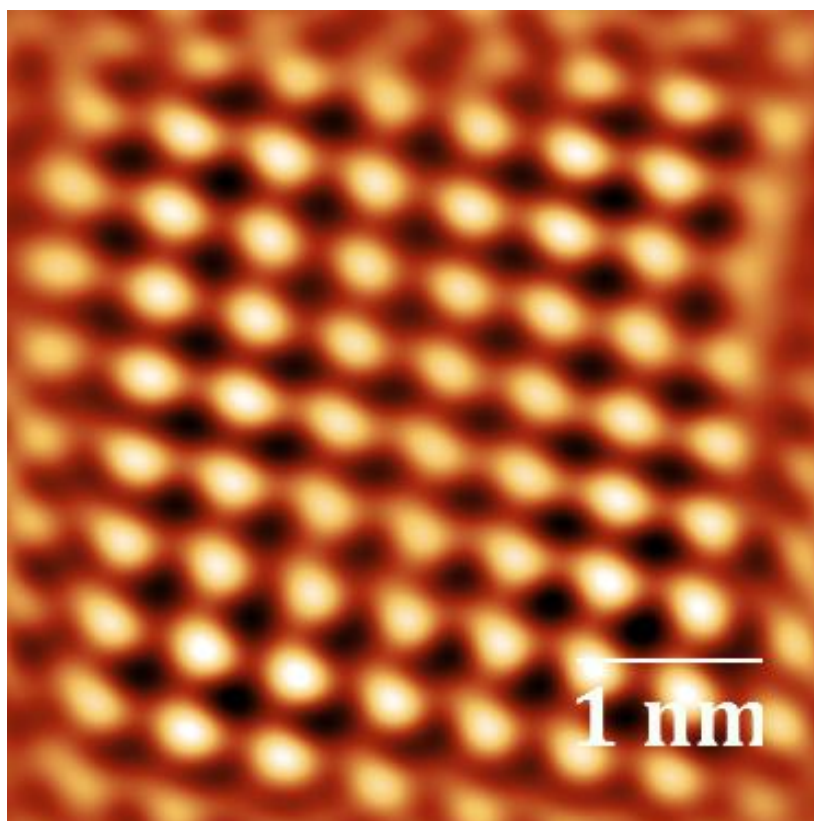

Figure 5.3: STM image of p(2×2) phase of Te/Cu(100) taken at room temperature. The size of the image is 4.4nm² and was obtained with a sample bias of +0.3V and a tunnelling current of 1.8nA. Image has been Fourier filtered

The STM of this coverage revealed large flat domains of the p(2×2) structure with occasional defects corresponding to missing tellurium atoms from the p(2×2).
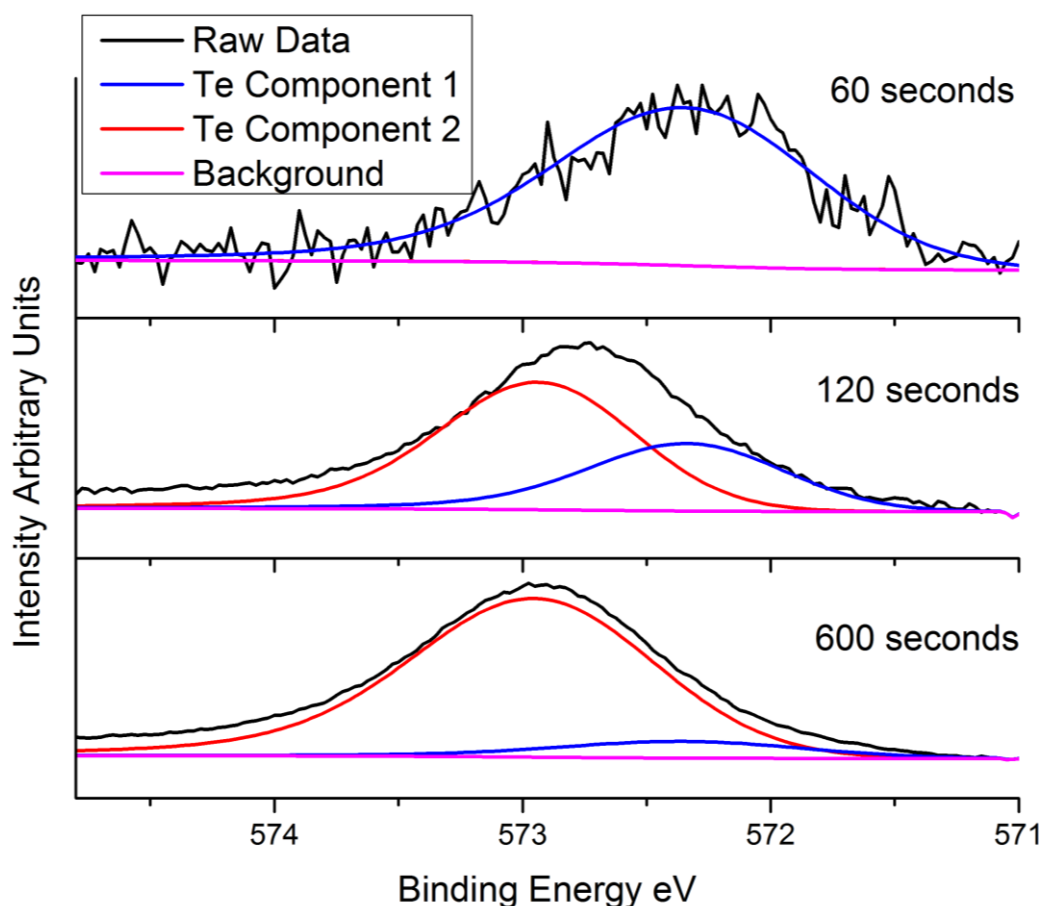

Figure 5.4: XPS spectra for increasing dosage times for the Te 3d$_{5/2}$ orbital

XPS data was collected after LEED and STM images were captured. The spectra showed the surfaces to be clean of contamination from oxygen after imaging with only detectable signal arising from copper and tellurium. The peaks were fitted with asymmetric Doniac-Sunjic [21] line shapes with two components for each element after the removal of a Shirley background. For the Cu 2p$_{3/2}$ orbital the binding energy for the clean surface was found to 932.7eV while a higher

binding energy component was found at 933.0eV for the heavy tellurium deposition shown in figure 5.5. This shift to a higher binding energy for the heavy deposition could indicate an alloying process as was seen on the other surfaces of copper. Indication of this possible alloying process is also given by the UPS spectra where for the heavy coverage it resembled the valence band of Cu_3Te_2 measured by Brunner [22].
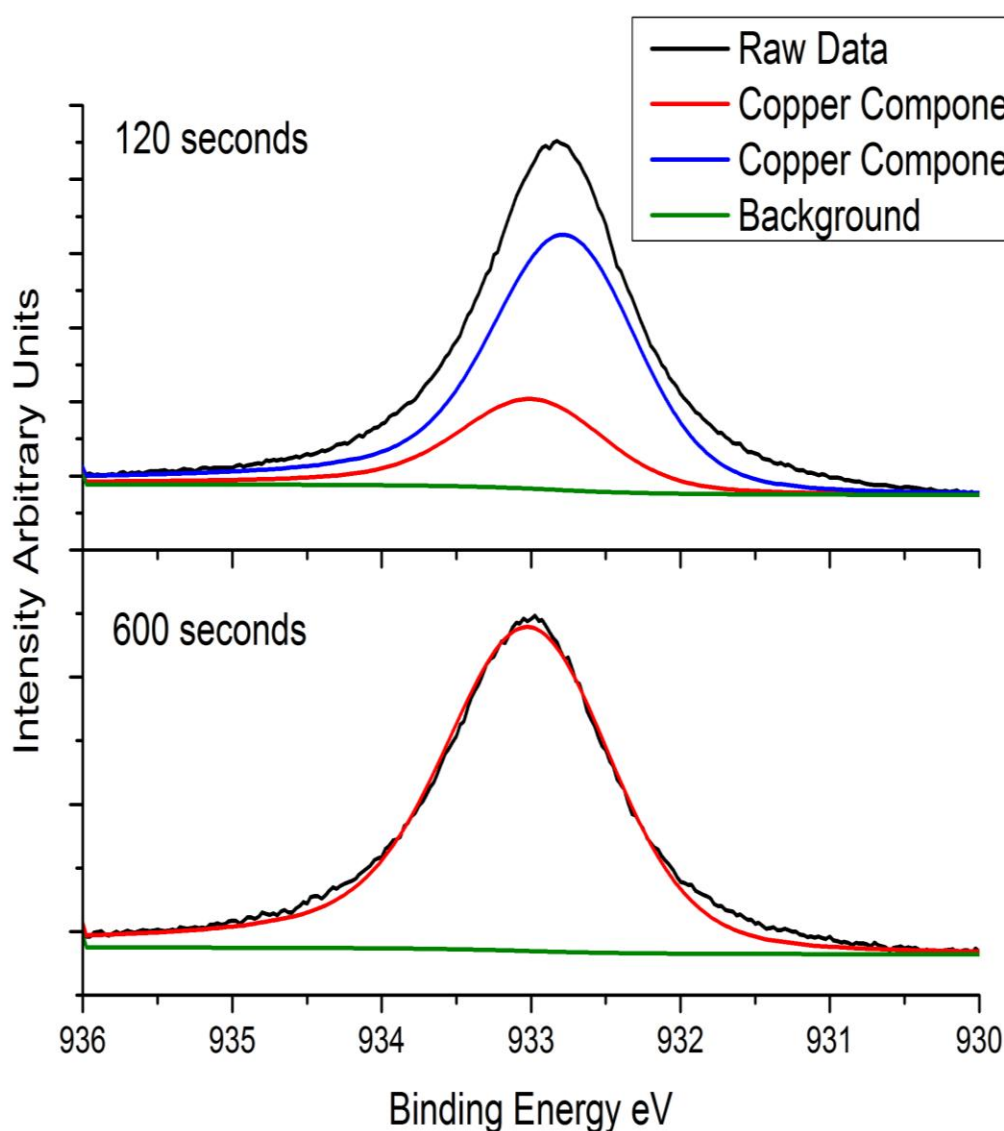

Figure 5.5: XPS spectra for two different dosage time for the Cu $2p_{3/2}$ orbital

For the tellurium data set two components were also used for the fitting shown in figure 5.4. One determined from the heavy coverage relating to tellurium in the striped c(2×2) domains observed with STM at 572.9eV and one for the low coverage p(2×2) phase shifted to a lower binding energy of 572.3eV in agreement with previously reported XPS values for copper telluride systems [23-25]. This shift to a higher binding energy is consistent with XPS studies on the growth of iodine over-layers on the Cu(100) surface, where a similar transition of structures was proposed [26]. The valence band was investigated using UPS and is shown in figure 5.6. The clean Cu(100) spectrum showed similar features to those previously reported [27], with sharp peaks associated with the 3d orbitals between 2-4eV and a sharp Fermi edge. UPS spectra for this p(2×2) coverage shows a dampening of signal from the Cu 3d orbitals as is usual [28] with a higher binding energy shoulder appearing on them attributed to the Te 5p orbitals [29]. The work function for the different coverages was calculates using equation 2.10. The work function of the surface was found to increase from 4.6±0.1eV for the clean surface to 4.9±0.1eV for the p(2×2) structure. This increase in work function upon tellurium deposition was seen earlier on the other low index surfaces of copper. This value for the work function remained constant for all other sub monolayer coverages until the heavy deposition of tellurium, when the work function increased to 5.0±0.1eV. This increase in work function could be related to heavily striped surface that is viewed with STM. The UPS spectra for the heavy deposition resembles that reported by Brunner for the Cu_3Te_2 alloy phase where there is a sharp Fermi edge present [22].
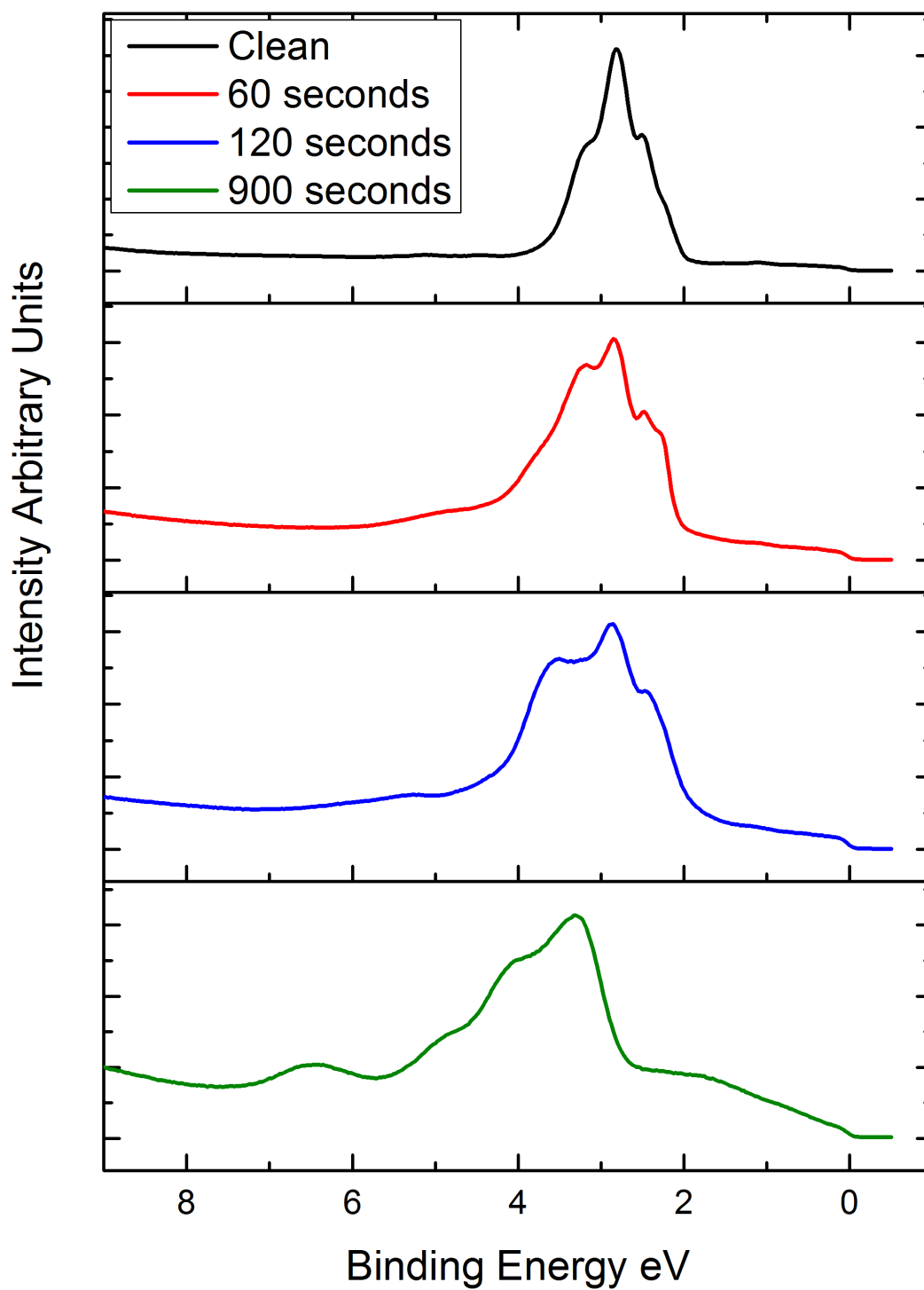
Figure 5.6: UPS spectra obtained at normal emission for different dosage times where the Fermi level has been set to 0eV binding energy

Mixed Phase

For coverages above 0.25 ML we see a transition in the LEED patterns beginning with the p(2×2) pattern becoming diffuse and streaked slightly in the [01] and [10] directions with no satellite spots detected around the integer beams of the substrate, indicating a loss in the long range order of the over-layer. Increasing coverage sees a range of very interesting diffraction patterns where the p(2×2) spots have split as well as intensity in the split c(2×2) positions. There are many other coincidence spots suggesting several differently sized domains present. The LEED patterns in figure 5.7 were taken with a beam energy of 31eV and so the substrate spots are only just coming in at the edge of the LEED optics. They have also been inverted to help with the contrast of the many weak over-layer spots.
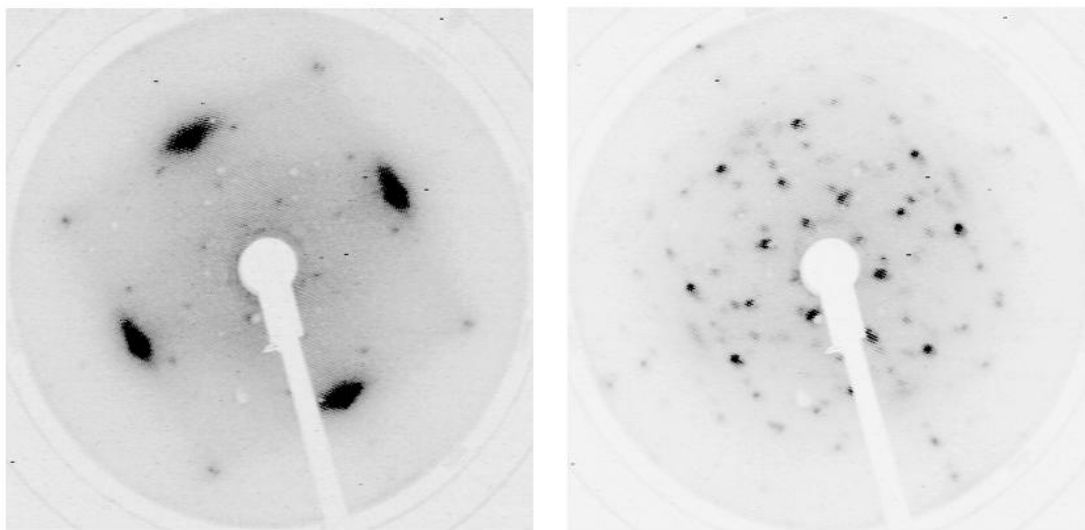

Figure 5.7: Left hand LEED image is the streaked p(2×2) structure obtained for 75 second deposition, the right hand image is after a deposition time of 90 seconds. Both images are taken with an electron beam energy of 31eV.

The (½ 0) spots in the left hand image of figure 5.7 have become diffuse and streaked in the [01] and [10] directions. There is also the emergence of additional peaks which may be the beginning of a higher coincidence lattice. The right hand image shows this coincidence lattice more clearly with the diffuse streaks in the (½ 0) position no longer present. Measurement of these extra peaks reveals that the majority if them lie on a (6×6) grid. This is agreement with the previous work where a coincidence lattice of 5 Te surface lattice vectors = 6 Cu unit lattice vectors was observed [7]. Obviously a true (6×6) would mean there is less tellurium on the surface than for the p(2×2) structure and so a coincidence lattice is the more likely explanation with increasing dosage. This is confirmed by the difference in intensity of the peaks on the 6×6 grid due to the interference of the over-layer lattice with the substrate.

With further deposition the LEED pattern still shows the symmetry seen in the left hand image of figure 5.7 however there are now no additional spots in the split c(2×2) position, shown in the left hand image of figure 5.8. This suggests the co-existence of both of these domains. The STM images of this surface did find both a p(2×2) structure and a c(2×2) striped structure but not in the same image. However the spot size of the LEED is far larger than the imaging size of the STM and so covers a much larger section of the surface. If domains on the surface are larger than the transfer width of the LEED optics, then scattering between the domains is incoherent and so the intensities of diffracted beams are summed. This means seeing multiple domains with LEED is much more likely than with STM.
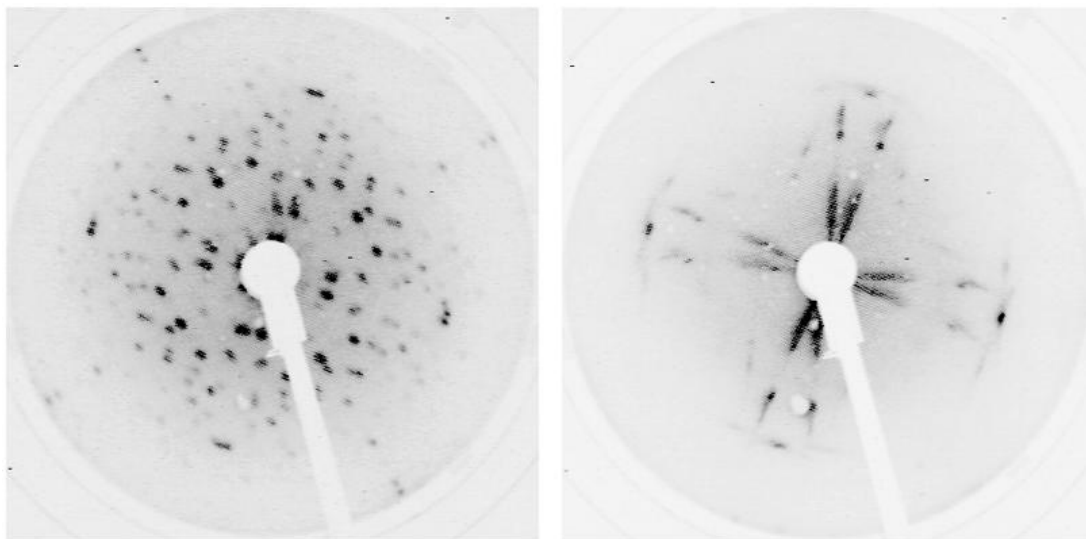
Figure 5.8: The left hand LEED image is for a deposition time of 120 seconds, the right hand image is a deposition time of 180 seconds taken with an electron beam energy of 31eV

The final LEED pattern shown in the right hand side of figure 5.8 no longer showed any intensity in the (6×6) spot positions or the p(2×2) positions with the split c(2×2) peaks visible at low energies. At higher energies only streaks in the [½ ½] directions and as satellites around the substrate peaks. There are also satellite spots around the substrate spots for the (6×6) and the mixture of phases. This transition from p(2×2) to c(2×2) is similar to that seen for iodine adsorbed on the Cu(100) surface [11]. It has been suggested that the splitting of the spots can be attributed to domain boundaries [16], which we clearly see with the STM for this split spot coverage.

The STM images for these high coverages showed two main structures. One was a square structure aligned to the substrate but with a far larger unit cell than the p(2×2) shown in figure 5.9. The bright protrusions in the image have a height of

70±10pm Measuring the lattice vector for this structure revealed it to be $a = 1.27\pm0.01$nm and $b = 0.96\pm0.01$nm. This corresponds to approximately a (5×4) structure with relation to the copper substrate. This exact over-layer was not imaged with the LEED however it may co-exist with other structures such as the (6×6) phase.
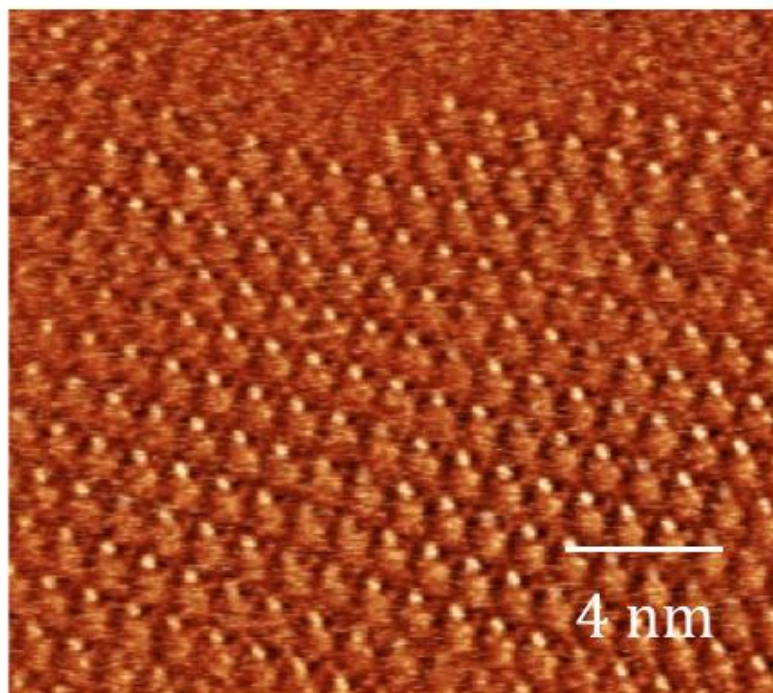
Figure 5.9: STM image of the coincidence (5×4) of Te/Cu(100) taken at room temperature. The image was obtained with a sample bias of +0.1V and a tunnelling current of 1.8nA

The other main structure imaged at this coverage was a striped structure shown in figure 5.10, with the stripes along the [½ ½] direction. The average width of these stripes was found to be 0.36±0.05nm. Due to the corrugation of the surface imaging was difficult however on the following image atomic resolution was achieved along the edge of one of the stripes. These striped domain boundaries are similar to those reported previously [30]. These stripes are different domains of the same symmetry. However the streaks in the LEED

pattern suggest that there are many different sized domains present with different coincidences to the substrate. Similar coexisting domains were found in a study of electrochemically deposited tellurium on Au(100). They found a range of over-layer structures starting from a p(2×2) and becoming more compressed leading to striped domains forming. These stripes were the result of anti-phase domain boundaries [31].
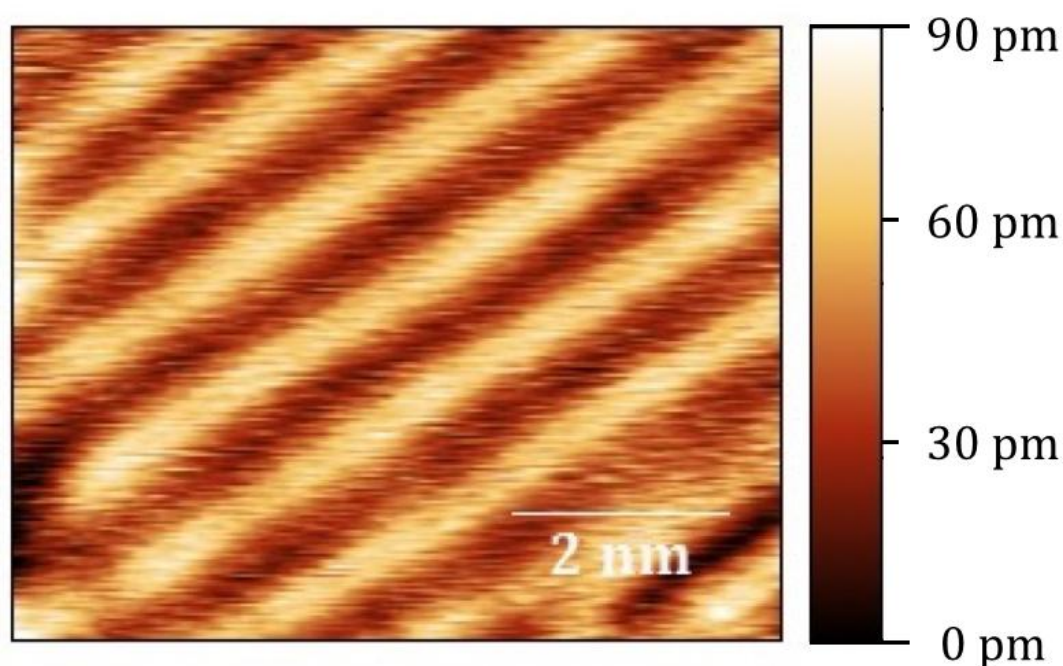
Figure 5.10: STM image of the striped c(2×2) structure taken at room temperature. The image size is 10.8nm^2 and was obtained with a sample bias of +0.3V and a tunnelling current of 1.6nA

These stripes are similar for those observed for the electrochemical growth of Sb on Cu(100) [19]. In that study the 3D stripes aligned along the [01] and [10] directions all evenly spaced of monatomic height. They proposed that the orientation of the stripes was dependent on the underlying structure which suggests we may have a c(2×2) structure underneath the stripes we observe. If the underlying structure were the original p(2×2) then the stripes should be

aligned along the [01] and [10] directions not the [½ ½] directions as is observed. For higher coverages the split c(2×2) LEED pattern was observed with varying degrees of background present in the images. The LEED spots were only visible at lower energies, at higher energies satellite peaks were detected around the substrate spots. This splitting of the (½ ½) spots into satellites is similar to other over-layer structures previously reported on the Cu(100) surface such as lead [32]. The fact that no splitting occurs around the integer beams suggests the splitting is a consequence of anti phase domain boundaries [15].
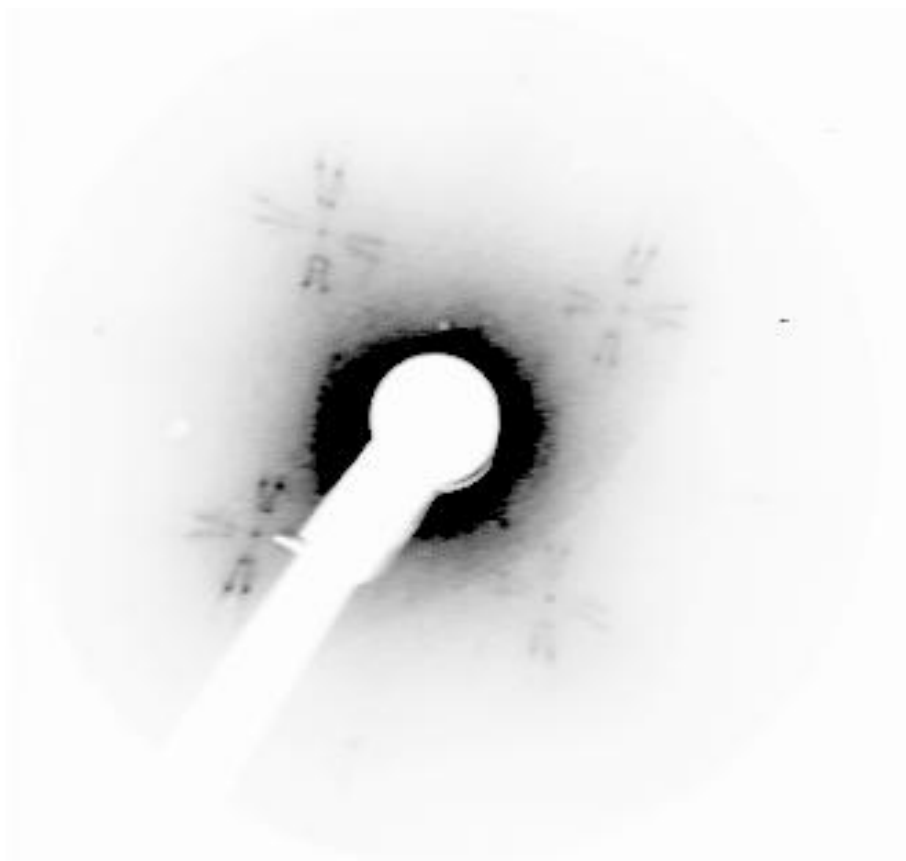
Figure 5.11: LEED image for the heavy deposition taken with an electron beam energy of 133eV. Satellite spots in the split c(2×2) positions can be seen around the substrate spots

The STM images for the higher coverage also revealed the same heavily striped structure. The image in figure 5.12 domains aligned in different directions. The width of the horizontal stripes was found to be 1.1±0.1nm while the vertical stripes 0.7±0.1nm. Domain boundaries where the rows are at 90° with respect to each other were also observed which agrees with the LEED patterns where the splitting of the spots and the streaks were seen in both directions. None of the previously flat p(2×2) like domains were imaged for this coverage indicating a complete transition to the heavily striped surface.

Figure 5.12: STM image showing two sets of perpendicular rows taken at room temperature. The image size is 20nm² and was obtained with a sample bias of +0.3V and a tunnelling current of 1.9nA

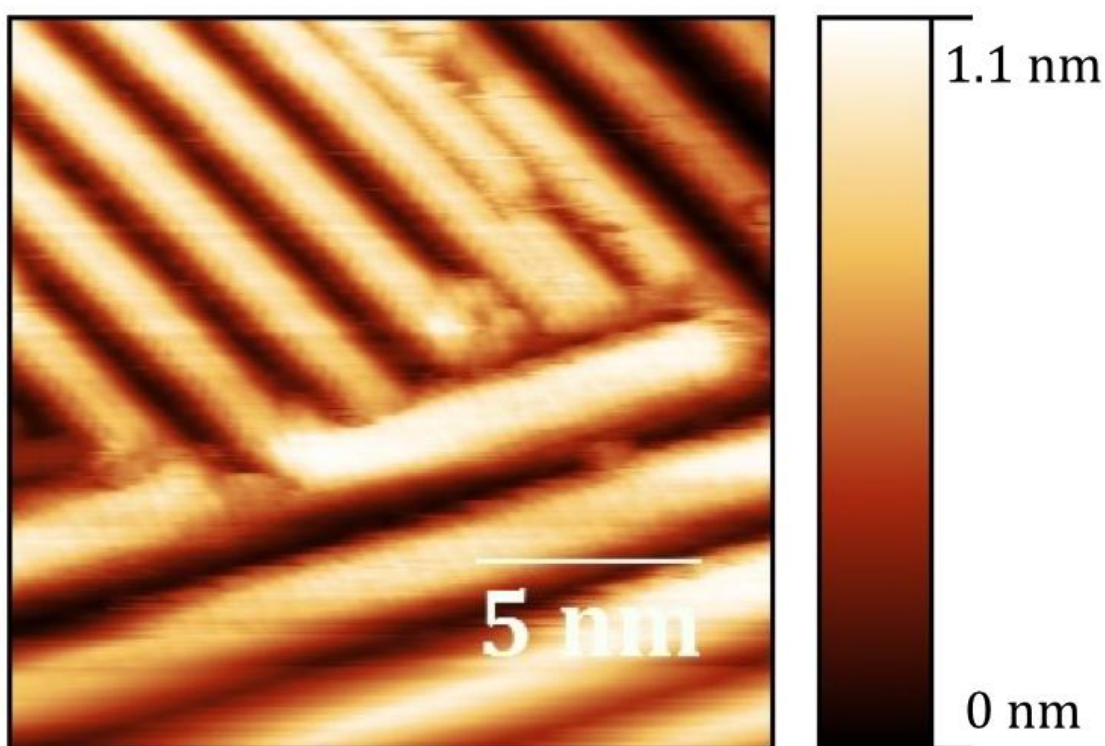Shown in figure 5.13 are two rows, the one in the upper left has a width of 3.6±0.1 nm while the thicker stripe to in the centre has a width of 6.4±0.1nm. These striped domains are much larger than those imaged at lower coverage and could indicate 3D growth as their heights are 1.09±0.01nm and 0.54±0.01nm respectively. 3D growth of tellurium was seen on Au(100) where the final compressed over structure acted as a nucleation site for high aspect ratio domains of close packed tellurium atoms [31]. In that study they also found a range of coincidence lattices indicated by the LEED patterns and suggested several domains that produce domain boundaries or walls the compression mechanism the random introduction of Te chains between the (2×2) structures.
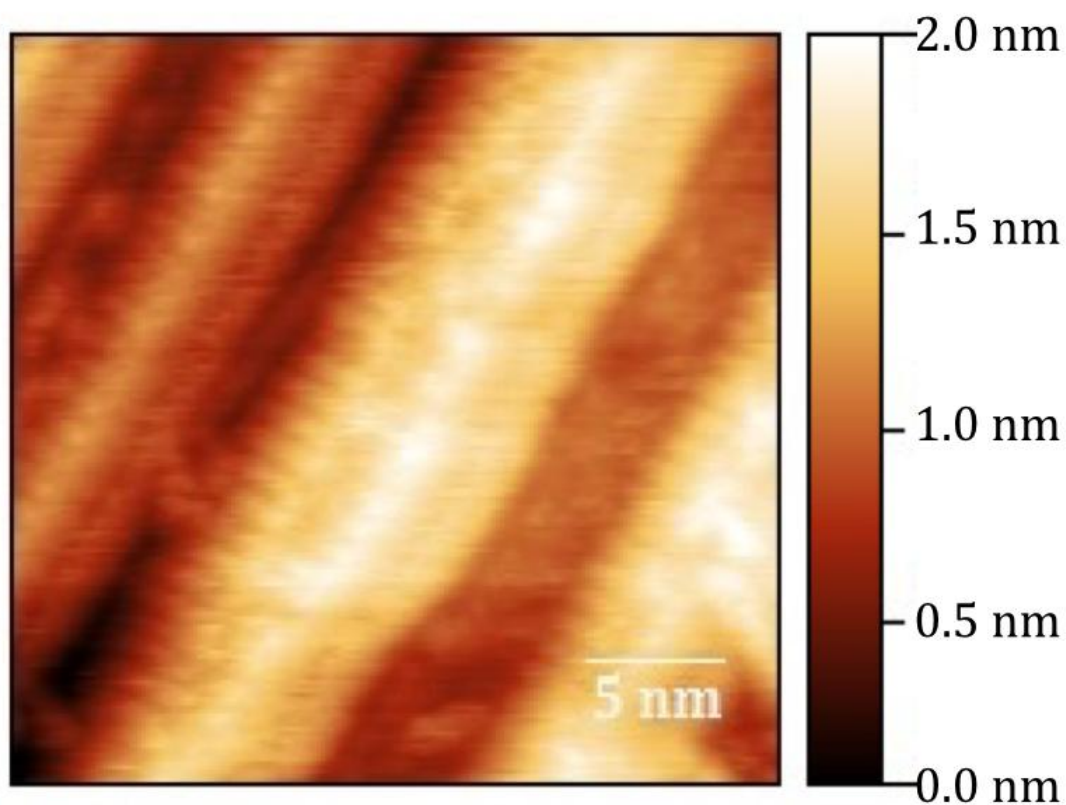

Figure 5.13: STM image showing two adjacent differently sized striped domains obtained at room temperature. The image was obtained with a sample bias of +0.5V and a tunnelling current of 1.2nA

Conclusions

In summary a range of structures formed when depositing Te onto Cu(100) have been studied using STM, LEED, XPS and UPS. The initial ordered structure agreed with previous work and was found to be a p(2×2) over-layer. The adsorption of tellurium increased the work function by 0.3eV with XPS revealing only one species present. As further tellurium was deposited a coincidence lattice was observed with the LEED corresponding to 5 Te surface lattice vectors = 6 Cu unit cell lattice vectors. Additional tellurium deposition sees the development of two striped domains of c(2×2) on the surface perpendicular to each other aligned along the [½ ½] direction of the surface. These were imaged with the STM and were shown to vary in width and height with the larger chains suggesting 3D growth. The lack of long range of order of these features is evident by the streaks observed in the LEED patterns. For the heaviest deposition we studied only this split c(2×2) structure was observed. At this coverage the large striped structures observed in the STM suggest 3D growth of the chains. The UPS data suggests it is similar to the Cu_3Te_2 phase alloy however we were not able to confirm the alloying with these techniques.

References

[1]   H. Uda, S. Ikegami, Sol. Energy Mater. Sol. Cells 50 (1998) p. 141

[2]   J.H. Yun, K.H. Kim, Sol. Energy Mater. Sol. Cells 75 (2003) p. 203

[3]   S.S. Hegedus, B.E. McCandless, Sol. Energy Mater. Sol. Cells 88 (2005) p. 75

[4]   X. Wu, J. Zhou, S. Thin Solid Films 515 (2006) p. 5798

[5]   K. Neyvasagam, N. Soundararajan, Vacuum 82 (2008) p. 72

[6]   X. Wu, Sol. Energy 77 (2004) p. 803

[7]   D.E. Andersson, S. Andersson, Surf. Sci. 23 (1970) p. 311

[8]   A. Salwén, J. Rundgren, Surf. Sci. 53 (1975) p. 523

[9]   P.D. Johnson, D.P. Woodruff, Surf. Sci. 129 (1983) p. 366

[10]   F. Comin, P. Citrin, P. Eisenberger, J. Rowe, Phys. Rev. B 26 (1982) p. 7060

[11]   B.V. Andryushechkin, Surf. Sci. 497 (2002) p. 59

[12]   H.C. Zheng, Surf. Sci. 177 (1986) p. 329

[13]   J. R. Patel, Phys. Rev. B 40 (1987) p. 1330

[14]   A.R. Alemozafar, R.J. Madix, J Phys. Chem. B 109(22)(2005) p. 11307

[15]   A.A. Cafolla, Surf. Sci. 544 (2003) p. 121

[16]   C. Argile and G. E. Rhead Thin Solid Films, 87 (1982) p. 265

[17]   E. AlShamaileh, Surf. Sci. 566–568 (2004) p. 52

[18]   H.Y. Xiao, X.T. Zu, X. He, Chemical Physics, 325 (2–3)(2006) p. 519

[19]   J. Wu, Phys. Chem. B 108(9) (2004) p. 2773

[20]   Gwyddion software version 3.27 http://gwyddion.net

[21]   S. Doniach, M. Sunjic, J. Phys. C 3 (1970) p. 285

[22]   A.J. Brunner, H. Bretscher, J. Phys. C 20 (1987) p. 5233

[23]   H. Neumann, M. Mast, J. Enderlein, Cryst. Res. Technol. 31 (1996) p. 75

[24]   A.J. Ricco, H.S. White, M.S. Wrighton, J. Vac. Sci. Technol. 2 (1984) p. 910

[25]   F. Debbagh, E.L. Ameziane, M. Azizan, Mater. Sci. Eng. 38 (1996) p. 223

[26]   M. Nahavandi, "Iodine induced structures on Cu(100)" Thesis 2012

[27]   M. Chang-Ki, New Journal of Physics 11 (2009) p. 103011

[28]   D. Westphal, A. Goldmann, Surf. Sci. 131 (1983) p. 113

[29]   S. Kashida, W. Shimosaka, M. Mori, J. Phys. Chem. Solids 64 (2003) p. 2357

[30]   J.K. Gimzewski, Phys. Rev. B 45 (1992) p. 12

[31]   T. A. Sorenson, J. of Electroanalytical Chemistry 467 (1999) p. 270

[32]   W. Hoesler, W. Moritz, Surf. Sci. 117 (1982) p. 196

Chapter 6

Effect of oxygen treatment on low index surfaces of In$_2$O$_3$

Abstract

The surface properties of the low index surfaces of singe crystal In$_2$O$_3$ samples has been studied by photoemission spectroscopy. The orbital character of the valence band was determined using a combination of synchrotron generated hard and soft X-rays. In order to understand the effect of oxygen vacancies on the electronic structure of In$_2$O$_3$ the valence band was probed using lab based UPS after three different treatments, sputtering the samples, and annealing them in both an oxygen poor and an oxygen rich environment.

Introduction

Indium oxide is a semiconducting material with many interesting applications, with applications in heterogeneous catalysis and chemical gas sensing as well as a transparent conducting oxide [1-4]. When the material is doped with tin it produces indium tin oxide (ITO), the prototypical transparent conducting oxide (TCO). ITO is a good TCO as it combines the two qualities needed; it has good transparency to light in the visible region while at the same time displaying electrical conductivity. Due to these characteristics and the fact it can be deposited in thin films mean it has many technological applications. It is used widely as a transparent film in solar cells, touch screens and liquid crystal displays. When integrating these materials into a device understating their surfaces is crucial for its optimization. In all of these devices a contact must be

166

made between the TCO and the rest of the device and so knowledge of the alignment of the bands of these materials is important to reduce possible barriers that may form, such as Schottky barriers. Gap states can also reduce the transparency of the material by effectively lowering the band gap.

It has been shown that at the surface certain metal oxides there exists a high mobility electron gas, these electronic states were found on In_2O_3 [5], CdO [6] and $SrTiO_3$ [7]. The presence of these excess electrons has been attributed to surface dipoles and lattice vacancies [8,9]. Several causes of this conductivity have been put forward in the past, including higher valence elements [10-12], defects such as vacancies within the lattice [13-15] and hydrogen incorporation [16,17]. Lany et al. showed that bulk vacancies cannot account for the large conductivities exhibited by these materials and showed their electrical properties are the result of charge carriers caused by surface donors [18]. Therefore understanding these surface donors is important when implementing these materials in working devices. A spectroscopic STM study revealed that as well as the presence of interstitial indium and oxygen the main defect contributing to the conductivity were oxygen vacancies [19].

One of the reasons for the lack of understanding of these oxides is that previously high quality single crystal samples have been hard to grow. Here we present work on molecular beam epitaxial In_2O_3 films of extremely good quality grown by HongLiang Zhang at the University of Oxford. We have tried to modify the low index surfaces to introduce oxygen vacancies to see their effect on the electronic structure. By reducing the amount of oxygen in the surface region the number of free carriers at the surface is increased, as the oxygen holds onto

these electrons when it is present in the structure. The situation is complicated however as modifying the surface can leave behind trap sites as well as oxygen vacancies, seen in valence band spectra as gap states. These gap states can not only effectively reduce the band gap of the material affecting its transparency, electrons trapped at the surface will not be able to contribute to the conductivity of the sample. Understanding these gap states therefore and their effect on electron accumulation is important for future device optimization. It has been shown previously that there is an electron accumulation region at the surface of indium oxide [5,20]. This was done by comparing hard and soft XPS spectra which probe different depths into the material. For the surface sensitive soft x-rays (1486.6eV) a well defined peak was observed at the Fermi level which was far weaker when viewed with the hard x-rays (6000ev) [20]. As the different faces of the indium oxide have different properties they react differently to the treatments applied. The three surfaces studied were the (100), (110) and (111) planes with the (100) plane having the highest surface energy and the (111) plane the lowest surface energy. Due to the bixbyite crystal structure of In_2O_3 the cleaving of the (100) plane leaves a polar surface while the (110) and the (111) planes are both non-polar [21]. The polar surface can be either indium or oxygen terminated however experiments have shown a preference for an oxygen termination, where the surface is considered to be stabilized through oxygen dimerization [22,23]. A theoretical study showed the work function of indium oxide can be increased by almost 2eV depending on the level of surface oxidation [24].

Previous work on samples

The samples were grown by molecular beam epitaxy on yttrium stabilized zirconate substrates. The samples studied have been previously studied to examine their crystalline quality [25]. The quality of the grown (111) epitaxial film was checked using X-ray diffraction. Figure 6.1 shows the θ-2θ scan with the inset showing the In_2O_3 (222) peak [20]. In the wide angle scan 4 peaks are seen, two originating from the yttrium stabilized zirconate substrate and two originating from the epitaxial film. This indicates a cubic In_2O_3 single crystalline film with the <111> direction of the epilayer parallel to the <111> direction of Y-ZrO_2. The full width at half maximum of the In_2O_3(222) peak is measured to be 0.115°, demonstrating the high crystal quality of the In_2O_3 epilayer. The quality of the films is reflected in a very low carrier concentration (1.0×10^{18} cm^{-3}) and high mobility (56 cm^{2}V^{-1}s^{-1}) as determined from single field Hall effect measurements. With an atomic force microscope atomically flat terraces were observed with triangular islands, which is consistent with a cubic (111) surface. LEED patterns obtained directly after growth showed sharp diffraction peaks displaying 3-fold symmetry. The lattice constant was found to be 14.0 ± 0.5 Å which is consistent with the cell side equaling $\sqrt{2}a$. This (1×1) surface could be reproduced ex-situ by cycles of argon sputtering followed by annealing in UHV at 600°C. STM studies on these ex-situ prepared surfaces showed flat terraces with hexagonal structures visible. These bright protrusions were attributed to the indium orbitals and showed the (1×1) termination of the sample.
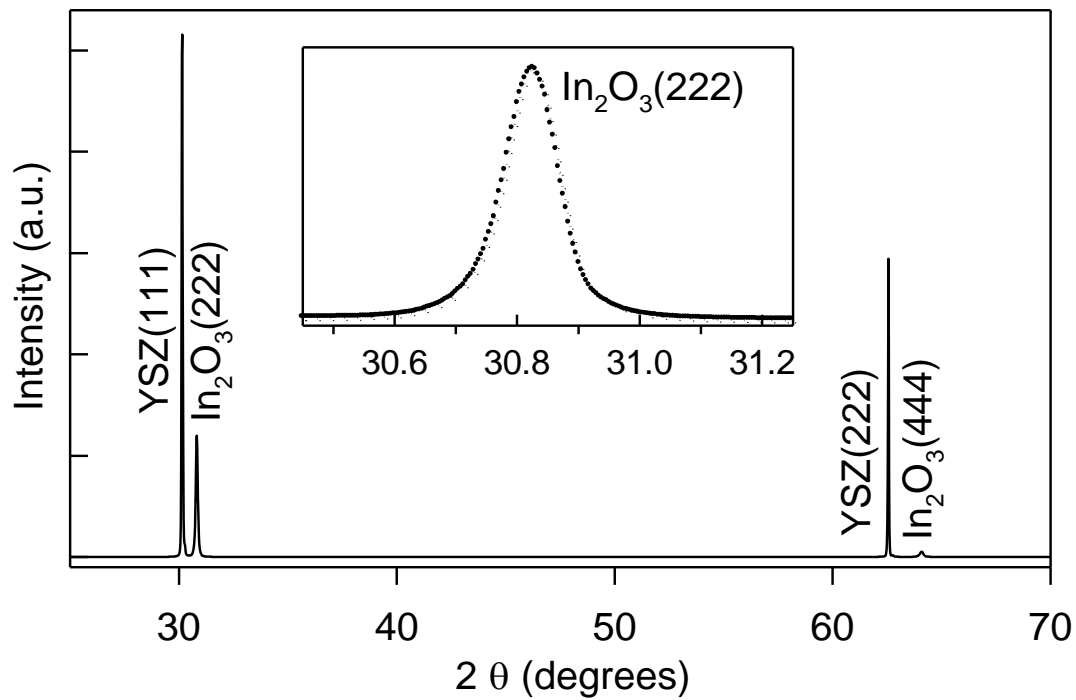
Figure 6.1: θ-2θ X-ray diffraction profile of an In₂O₃ thin film grown on yttrium stabilized zirconate (111) substrate taken without permission from [20]

In this chapter we have first confirmed the orbital character within the valence band for the (111) sample by comparing hard and soft x-rays using synchrotron radiation, revealing signals in the valence band arising from indium and oxygen. The 3 surfaces were then studied using lab-based photoemission after different sample preparations to investigate the effect annealing in oxygen has on the electronic structure and the work function of the surfaces.

Experimental

The In_2O_3 sample used were epitaxial thin films of grown on 1 cm × 1 cm yttrium stabilized zirconate Y-ZrO_2 substrates via molecular beam epitaxy. In-situ LEED was carried out in an analysis chamber connected to the growth chamber. These clean surfaces can be easily regenerated in another ex situ ultra high vacuum (UHV) system.

The (111) sample was studied using a combination of hard and soft XPS. This experiment was conducted on beam line I09 at Diamond Light Source, Uk. This beam line can provide photon energies from 230eV to 18keV and is equipped with a VG Scienta EW4000 electron analyser with an angular acceptance of +-30°. A silicon double crystal monochromator in combination with a channel cut silicon crystal was used to focus the beam line, producing a photon energy of 6054eV with an overall resolution <250mev. A plane grating monochromator was used for the soft X-rays providing a photon energy of 600eV with a resolution <300mev. The photon energy could be switched without the need to move the sample making comparisons between the two regimes clearer as sample preparations may not differ. The In_2O_3 samples were cleaned by repeated cycles of Ar+ sputtering (500eV) and annealing at 600^oC in UHV. The cleanliness of the final surface was confirmed by XPS, where no C 1s signal could be observed. For the UPS measurements the samples were annealed under two environments to probe the effect of oxygen vacancies. The samples were initially looked at after sputtering the sample. Due to the size difference between the oxygen and the indium at the surface the oxygen is preferentially removed during the bombardment. This leaves an oxygen deficient surface region

containing additional oxygen vacancies to the pristine surface. The samples were then studied after annealing under UHV conditions with an overall pressure of 1×10^{-9} mbar. They were then annealed in a more oxygen rich environment where the chamber was filled with oxygen to a pressure of 1×10^{-6} mbar. For these treatments the sample was held at a temperature of 600°C for 1 hour. The oxygen line was flushed 3 times prior to entry to the chamber with its cleanliness checked by a quadrupole mass spectrometer.

Results

The valence band of the (111) surface was studied using a combination of hard XPS (HAXPES) (6054eV) and soft XPS (SXPS) (600eV). This allows the orbital contributions of the valence band to be explored, with the hard X-rays probing far deeper into the sample whereas with the soft X-rays we are more sensitive to the surface. Another effect making the two energies suitable for this study is the change in ionisation cross-section [26]. The cross sections decrease for both the indium and the oxygen orbitals however the drop off is more severe for the oxygen cross section, meaning that the relatively the HAXPES measurements are more sensitive to indium 5s states than oxygen 2p states. The decrease in cross–section with increasing photon energy is shown in figure 6.2 The relative sensitivity factors were taken from Yeh and Lindau 1985 [27].
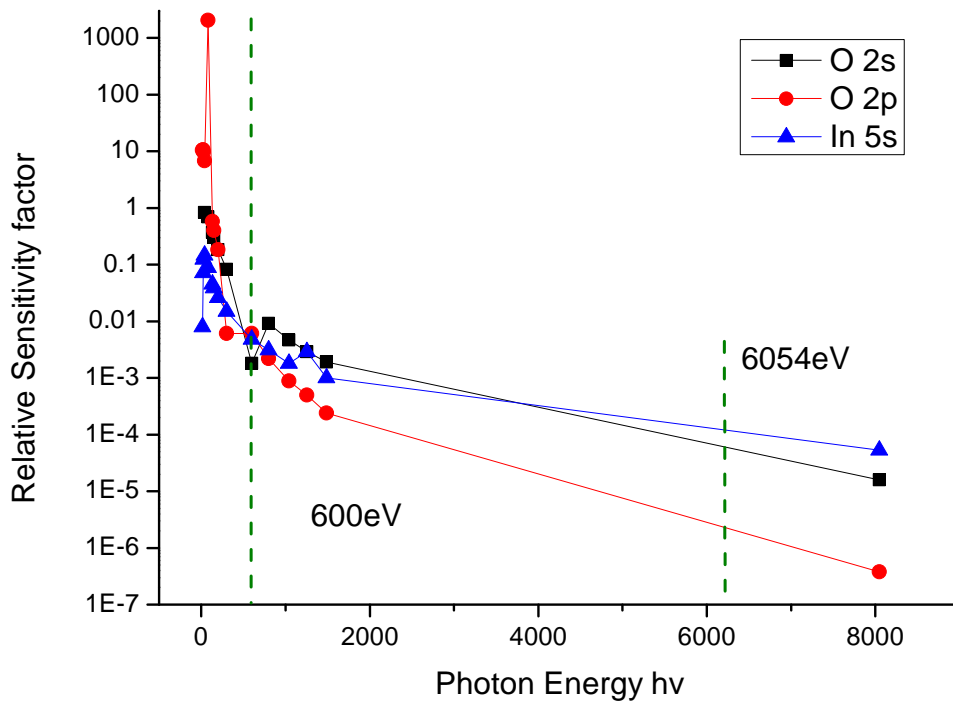
Figure 6.2: Change in relative sensitivity factors of the relevant indium and oxygen orbitals for different photon energies

This drop is mainly due to the fact that at higher photons energies *s* orbitals are more sensitive than higher *l* orbitals such as *p* and *d* orbitals. As can be seen in figure 6.2 there is a small change in relative intensity between the In 5s and the O 2s, however the largest relative change is between the O 2p and the In 5s orbital. At 600eV the relative cross sections given by Yeh and Lindau for O 2p and In 5s are 6.1×10^{-3} and 4.8×10^{-3} respectively. Increasing the photon energy to 8048eV sees the cross sections change to 3.8×10^{-7} and 5.3×10^{-5} respectively [27]. As can be seen the oxygen 2p sensitivity drops off far more relative to the indium 5s.

The spectra were collected with a pass energy of 100eV at room temperature and are shown in figure 6.3. Aligning the VBM of the 2 spectra it is clear that the HAXPES spectra is dominated by features from 5 - 10eV. The SXPS spectrum is dominated by signal arising from the VBM from 2 – 5eV. Previous density of states studies have shown that the lowest energy peak is comprised of mainly oxygen 2p orbitals, whereas the peak at ~ 8eV is attributed to hybridisation between the In 5s and the O 2p orbitals [28]. The region between these two features is attributed to mixed O 2p and In 5p orbitals. The features highlighted by HAXPES are attributed to indium 5s states while the features highlighted by SXPS are attributed to oxygen 2p which is in agreement with other studies [26].
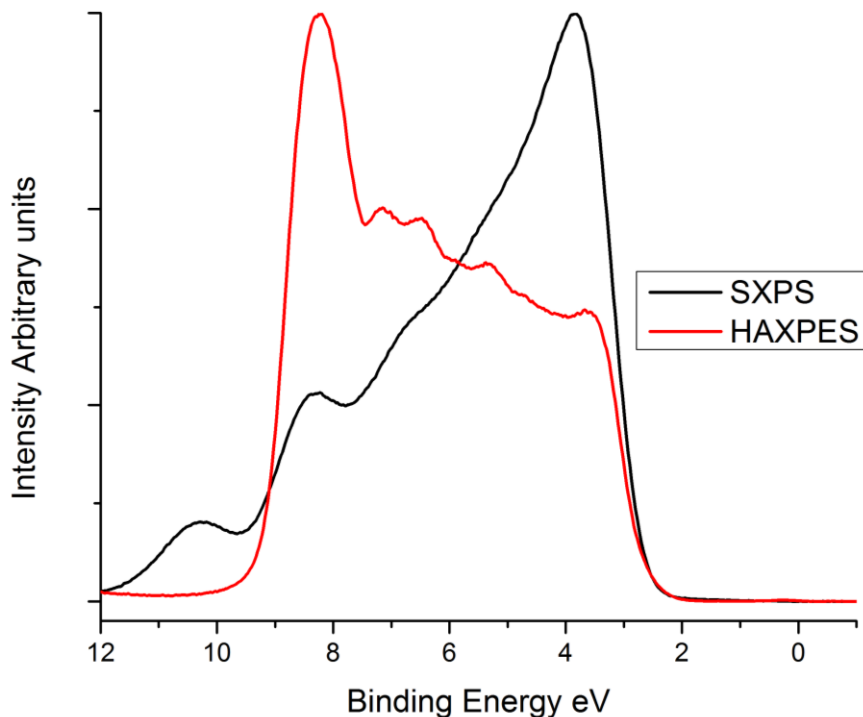

Figure 6.3: Comparison of the Valence band of the (111) sample investigated with 6054eV and 600eV photons.

Interestingly the HAXPES data showed a clear occupation of the conduction band in figure 6.4 that was not as strong with SXPS. In materials which are known to have an electron accumulation layer at the surface, as indium oxide does, it would be expected to be more sensitive to these surface electrons with the SXPS. This may be due to the fact that the surfaces were not cleaned prior to the measurements, as these facilities were not available on the beam line at that time, on the cleaned samples the population of the conduction band was seen with the SXPS [29].
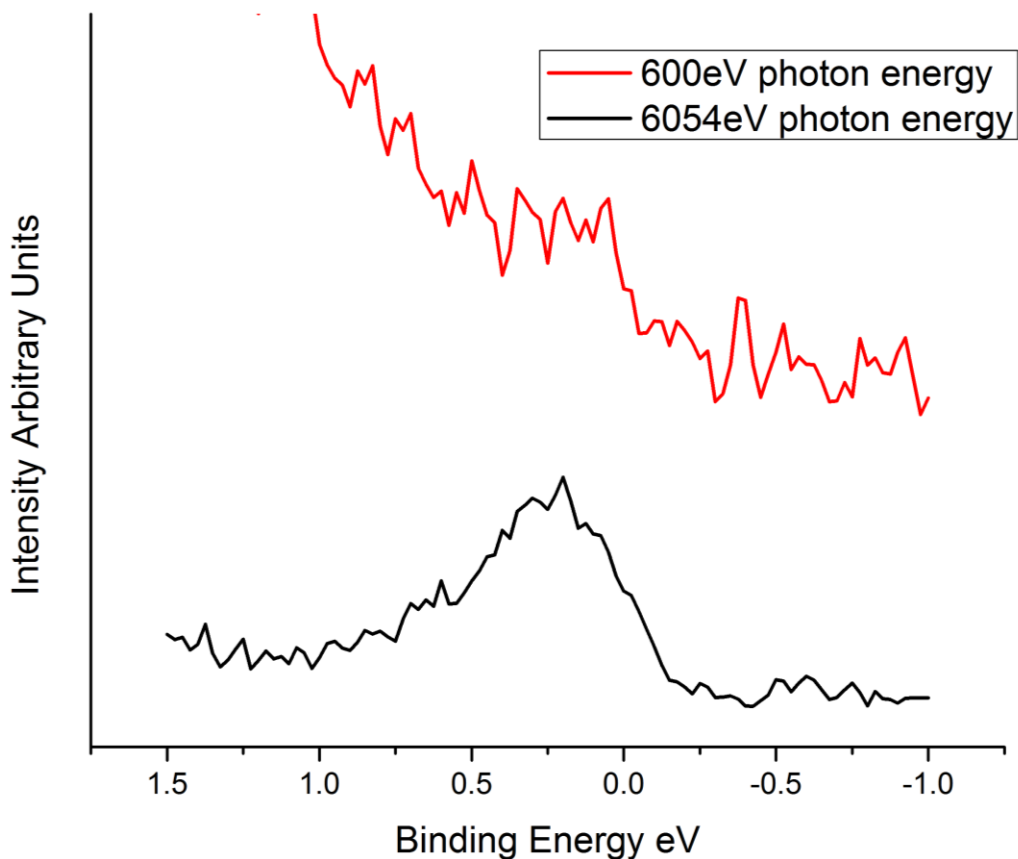

Figure 6.4: Fermi level for the different photon energies, showing much clearer occupied peak with HAXPES than SXPS, data has been offset for comparison

Lab Based PES

The effect of oxygen treatments on the electronic structure of indium oxide was investigated using both UPS and XPS. The spectra were taken after 3 different treatments, the samples were first sputtered in vacuum which left an oxygen deficient sample region as indicated by the ratio of the intensities of core levels from both indium and oxygen. The measured intensities were corrected with appropriate sensitivity factors [30]. The ideal ratio for indium oxide would be 3 indium atoms for 2 oxygen atoms. After sputtering the measured ratio decreased suggesting an indium rich surface and we therefore suggest that there are oxygen vacancies within the lattice at the surface region. This higher ratio of indium to oxygen may arise from other features such as islands of indium or indeed parts of the sample that are no longer stoichiometric. These features may be present in the sample after sputtering but after the samples have been annealed these features have not been found to occur in previous studies as the stoichiometry is restored when annealing. The samples were then annealed in either an oxygen rich environment or an oxygen deficient environment. For these annealing treatments the sample was held at 600°C for an hour in either an oxygen rich environment or oxygen deficient environment. For these different scenarios the atomic concentrations of the surfaces were calculated and listed in table 6.1. The XPS fitting was done using the Te $3d_{3/2}$ as there is a satellite from the non-monochromated source under the $3d_{5/2}$ orbital. The intensities and binding energies given for the Te $3d_{5/2}$ orbital are calculated from the $3d_{3/2}$ orbital using the known spin-orbit splitting and branching ratio for a *d*-orbital. The initial ratio before treatments was found to be O:In 1.56±0.01 however the

surface still had some contamination present, mainly carbon. However some of the measured signal from oxygen could also originate from surface contamination as opposed to stoichiometric oxygen within the lattice.

	110	100	111
Sputtered	1.42±0.01	1.30±0.01	1.31±0.01
Annealed in Vacuum	1.36±0.01	1.20±0.01	1.30±0.01
Annealed in Oxygen	1.59±0.01	1.43±0.01	1.38±0.01

Table 6.1: Atomic ratio of oxygen to indium as measured by XPS for the different sample treatments

As well as XPS revealing the atomic ratios present in the treated surfaces it can also give us an idea of their differences in carrier density. The measured XPS peaks for the In 3d core levels are asymmetric in shape. This asymmetry can arise from several mechanisms that have previously been suggested. Previous work on these samples has shown that there is an accumulation layer at the surface of these oxides [29]. This accumulation of electrons causes a space-charge region causing the energy bends to be bent downwards. The bending of the bands varies as a function of depth and so one would expect an asymmetric shape to the peaks due to the electrons originating from different depths having a slightly different separation from the Fermi level. Previous studies have also tried to take a more analytical approach to the fitting this asymmetry by fitting the peaks with two components [31], the two components relating to the screened and un-screened final states, with the shift between them interpreted as evidence for final state screening effects from the carriers in the conduction

band. Changes in the surface stoichiometry will affect the population of the conduction band and therefore will affect not only the intensity of the screened satellite but also its position, as this is a plasmon loss and the plasmon energy is dependent on among other variables the carrier density. The plasmon energy is calculated using equation 6.1

$$\omega_p^2 = \frac{ne^2}{m^*\varepsilon(\infty)\varepsilon_0}$$
(6.1)

where $\hbar\omega_p$ is the plasmon energy, n is the free carrier concentration, m^* is the effective mass of the electron, $\varepsilon(\infty)$ is the high frequency dielectric constant and ε_0 is the permittivity of free space. The value for the effective mass and the high frequency dielectric constant were taken from [26].

When the carrier density increase so does the plasmon energy and therefore the satellite peak should be shifted to higher binding energy. This fitting procedure was employed in a recent study on the CdO surface, a similar TCO to In_2O_3 [31]. In this study it was found that the plasmon peak shifted in energy by 0.15eV when increasing the carrier concentration from 1.8×10^{19} cm^{-3} to 2.4×10^{20} cm^{-3}. This is quite a large increase in carrier density, around 13 times larger, compared to what we expect for our differently annealed samples. If we assume all excess electrons at the surface originate from oxygen vacancies, and work out the difference in carrier concentrations for the 2 annealing environments the change in carrier concentration is of the order of 10-15%. This means the plasmon position should be virtually constant for the two different treatments. Fitting the spectra as such we found that the asymmetry does increase when annealing in vacuum but this difference is attributed to a different degree of

band bending as opposed to a different plasmon energy as shown in figures 6.5 and 6.6.

Screened

Fitting the spectra with a screened and un-screened component as in previous studies is shown in figures 6.5 and 6.6, the Plasmon energy being kept constant. The separation used was 0.4eV, this was determined by fitting the spectra with the most asymmetry. In order to make fitting simpler all the peaks of In 3d core levels were aligned to each other so that the changes in ratios could be observed. In these aligned spectra the In $3d_{5/2}$ for the unscreened component occurs at 444.9eV with the screened component 0.4eV higher in binding energy at 445.3eV. In previous work the FWHM of the screened peak was found to be 1.5 times bigger than the unscreened component so this was used as a constraint in the fitting parameters. Although all the presented graphs are for the $3d_{5/2}$ level the $3d_{3/2}$ level was also measured. This gives more certainty to the fitting of the $3d_{5/2}$ orbital when the branching ratio and known spin-orbit splitting are applied as a satellite peak from the X-ray source sits under the $3d_{5/2}$. This occurs 9.2eV below the real peak and so signal from the $3d_{3/2}$ satellite peak is buried under the $3d_{5/2}$ peak. Using the peak separation of the screened and un-screened components and with equation 6.1 the carrier concentration was calculated to be 1.6×10^{20}cm^{-3}. This is slightly lower than the previously reported value 2.6×10^{20}cm^{-3} [25] but this difference is most likely due to differences in the surface preparation.
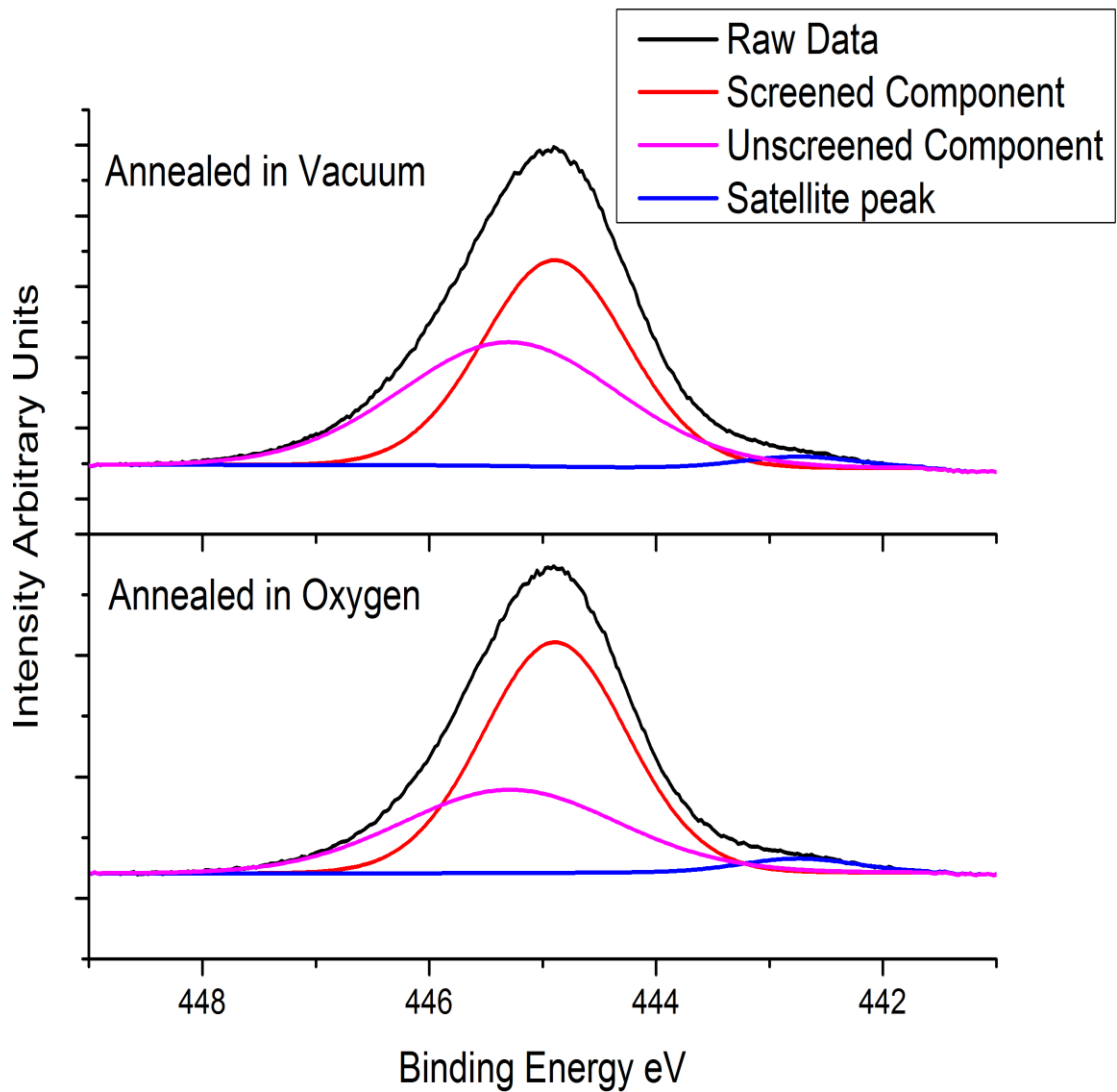
Figure 6.5: XPS indium 3d spectra for the annealed in vacuum and annealed in oxygen for the (111) sample fitted with screened and unscreened components

The oxygen 1s orbitals were also fitted with two components once again relating to the two final states separated by the same 0.4eV as for the indium orbital as this plasmon energy is related to the carrier concentration at the surface.
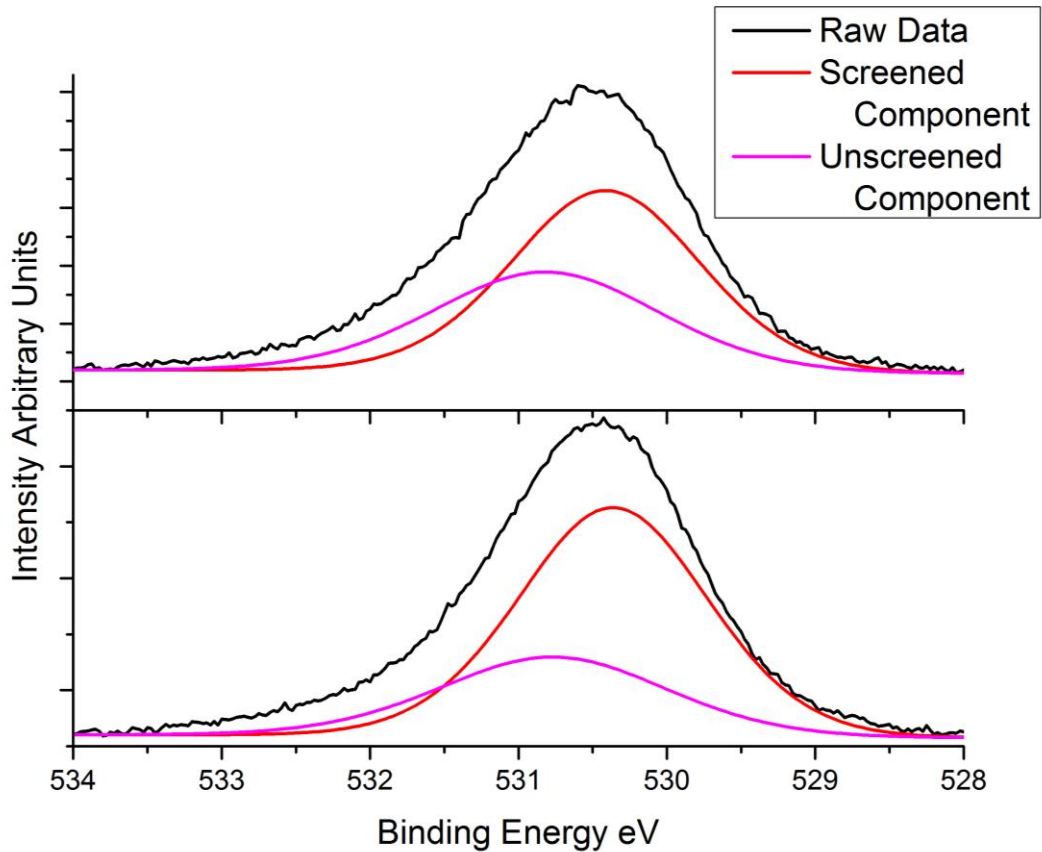
Figure 6.6: XPS oxygen 1s spectra for the annealed in vacuum and annealed in oxygen for the (111) sample fitted with screened and un-screened components

Asymmetry

Another way of linking line shape to carrier concentration is to look at the asymmetry of the experimentally observed peaks. For materials that exhibit downward band bending creating oxygen vacancies will generate excess carriers at the surface, this increases the surface potential and so increases the degree to which the bands are bent. So a higher surface carrier concentration should result in more asymmetric peaks as electrons originating from different depths

will have experience a different amount of band bending. Overlaying the spectra in figure 6.7 allows easy visualisation of this change in asymmetry. We also observe a shift in the centroid values for the samples annealed in oxygen. This can be attributed to the change in the position of the Fermi level brought about by excess charge carriers for the annealed in vacuum samples. This shift was found to be 0.2eV for all three of the surfaces.

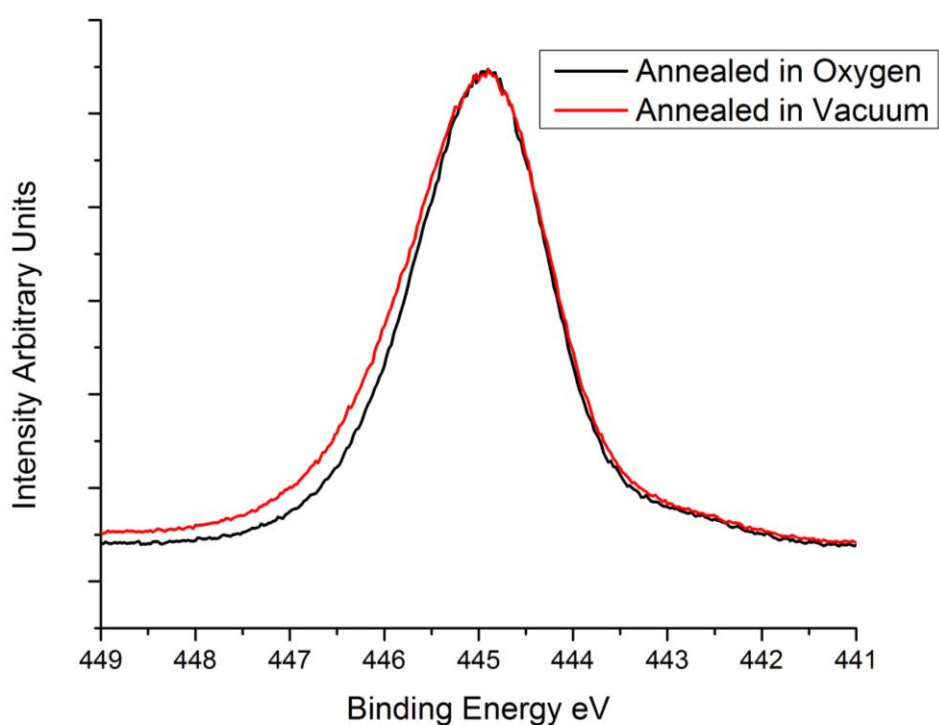
Figure 6.7: In 3d XPS spectrum showing the difference in asymmetry after annealing in oxygen

Before the XPS data was collected UPS measurements of the valence bands of the samples were made. The position of the secondary electron cut-off was

determined as shown in figure 6.8 and using equation 2.10 the work function of the surfaces was calculated.
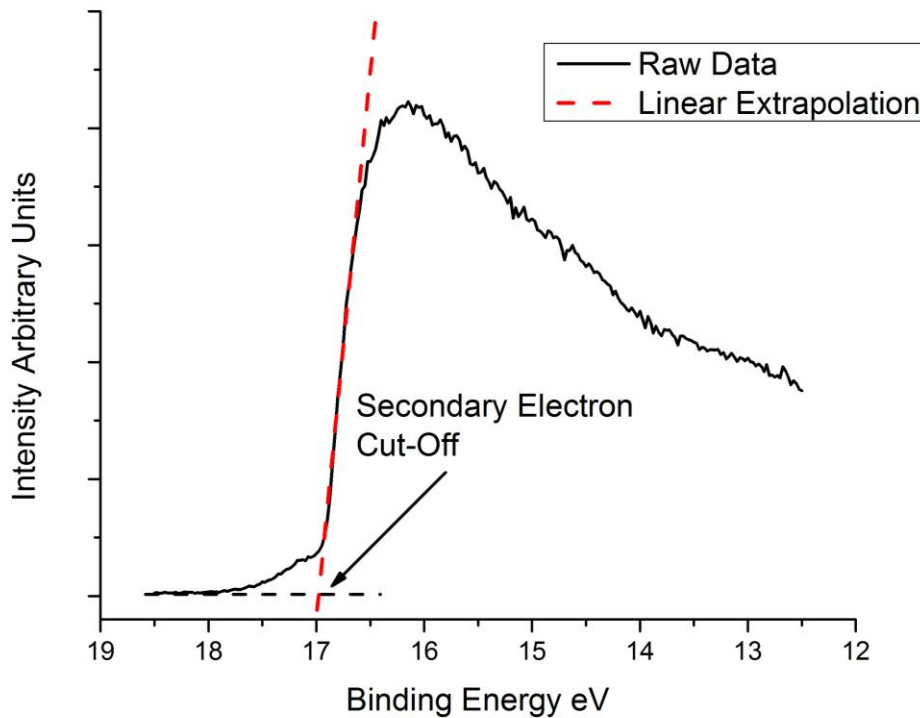
Figure 6.8: Secondary electron cut-off linear extrapolation

The calculated work functions for the different annealing conditions are shown in table 6.2. The measured values are consistent with previously reported values [32,33]. The trend is the same for all 3 surfaces, where annealing in oxygen increases the work function which agrees with previous studies [24]. This trend agrees with previous work where by increasing the carrier concentration pushes the Fermi level higher into the conduction band, meaning it is closer to the vacuum level and hence a lower work function is measured [34], as shown in figure 6.9.

	Work Function eV ±0.1
(110) Surface	
Sputtered	4.3
Annealed Vacuum	4.2
Annealed Oxygen	4.6
(100) Surface	
Sputtered	4.3
Annealed Vacuum	4.2
Annealed Oxygen	4.5
(111) Surface	
Sputtered	4.3
Annealed Vacuum	4.3
Annealed Oxygen	4.6

Table 6.2: Values for the work function after the 3 different treatments

It has been shown that post-deposition oxidation treatments can be employed to increase the work function of indium-based TCOs [35,36]. Comparison of the 3 surfaces with annealing and vacuum and oxygen is shown in figure 6.10. Upon the different treatments there are no major change in the observed orbitals away from the VBM. The population of the gap states at around 2-3eV is affected as well as the occupation of the conduction band, this is the reason the spectra are shifted to higher binding energies after annealing in vacuum. Cautiously we therefore assign the majority of the signal arising from gap states to be connected to oxygen vacancies at the surface.
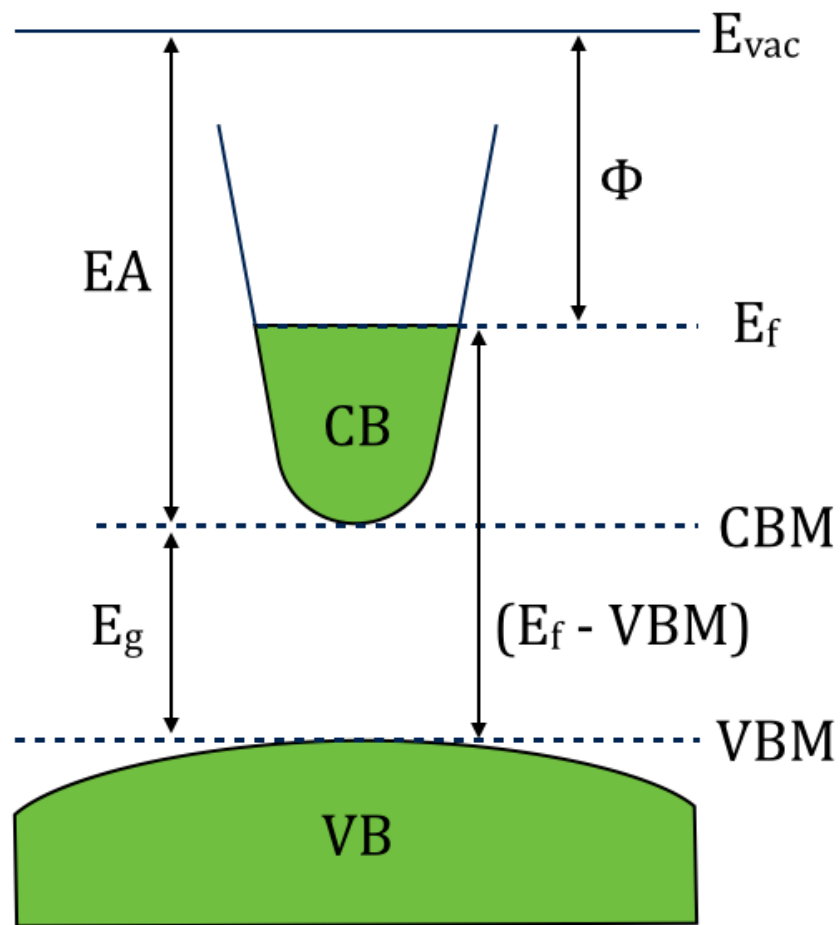
Figure 6.9: Energy diagram showing how the position of the Fermi level is related to the measured work function

Changes in the work function can come about for several reasons, the electrical potential the electron "feels" from the crystal may differ, for example if the oxidation state of a cation is increased. The work function also takes into account any surface dipoles that are present. These dipoles can act as energetic barriers when trying to remove an electron from a material and can be altered by altering the electric field at a surface or by adsorbents on the surface, either intentionally deposited or contaminants. By changing the carrier concentration you would also alter the work function, increasing the carrier concentration will push the Fermi level higher and therefore reduce the work function. This is the

process attributed to changes in our values of the work function as we see a similar shift for all three surfaces. Dipole formation at the surface would vary for the different surfaces due to their terminations.
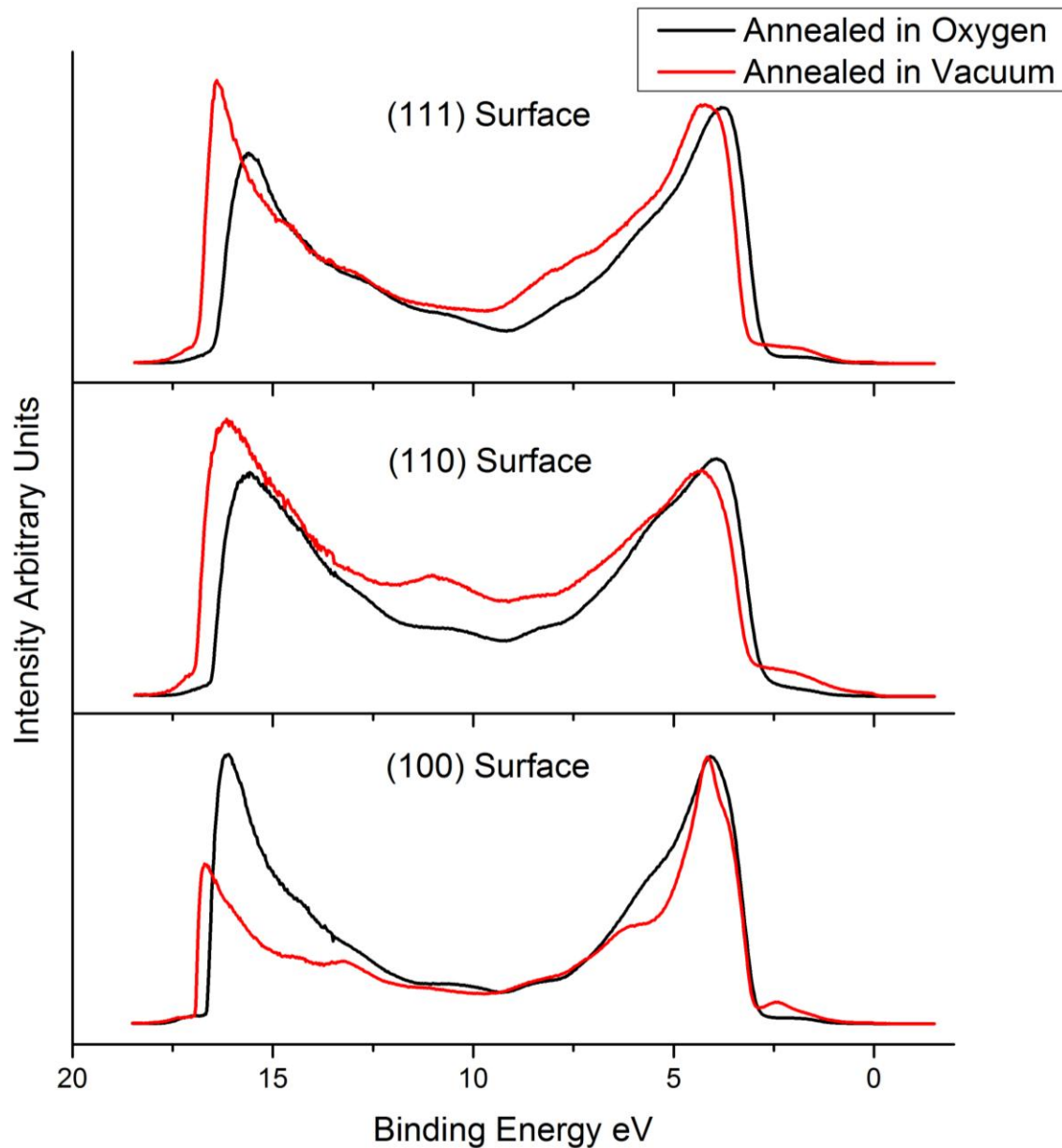

Figure 6.10: Valence band spectra for the 3 surfaces after annealing in vacuum and oxygen

The creating of oxygen vacancies will create gap states within the band, typically low lying donor levels [19]. These can affect the device performance by limiting

the optical transparency or by providing a pathway for electron flow, which is unwanted. To examine these gap states the plot below shows a high resolution scan around the VBM. The main state lies at an energy of ∼ 2eV below the Fermi level.
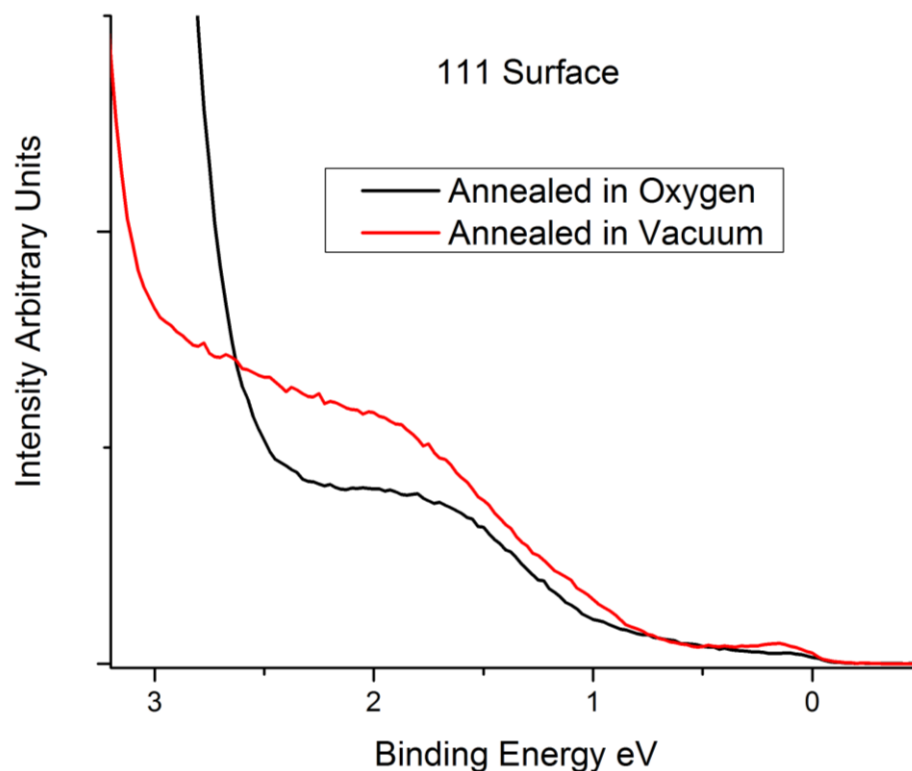
Figure 6.11: UPS spectra from VBM after both treatments. The intensity of the in-gap states is shown to depend on the oxygen environment during annealing

It can be seen in figure 6.11 that the intensity of these gap states is reduced when annealing in oxygen, this coincides with the loss of intensity at the Fermi level and a shift in the core XPS levels, all consistent with electron surface accumulation. We attribute these changes to a change in the number of oxygen vacancies present at the surface. It has been shown previously that these in-gap states can be attributed to oxygen vacancies as well as interstitial indium and

oxygen [19]. The creation of oxygen vacancies is a proposed mechanism for the electron accumulation layer observed in In_2O_3 where oxygen vacancies at the surface act as doubly ionized shallow donors and have been shown to provide free electrons to the accumulation layer. This accumulation region causes the downward band bending previously reported at the surfaces of indium oxide. By expanding the region around the Fermi level we can see a clear occupation of the CB for the sample annealed in vacuum shown in figure 6.12. This feature was not present in the sample that was annealed in oxygen. Its presence pushes the other levels down in energy as by populating this energy level the Fermi level of the system is shifted closer to the vacuum level. This surface accumulation is responsible for the asymmetric line shapes experienced in XPS.
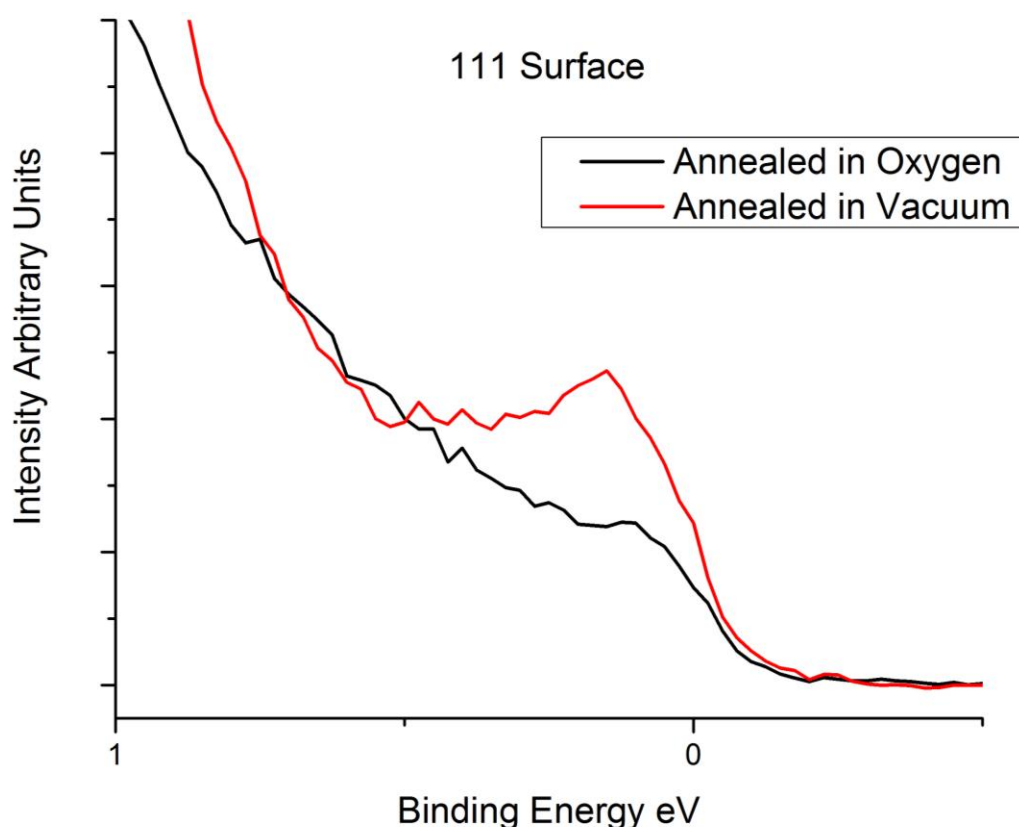

Figure 6.12: Fermi level region for the (111) sample after annealing in vacuum and oxygen

Conclusion

The surface electronic properties of indium oxide single crystal thin films has been investigated using Photoelectron spectroscopy. The orbital character of the (111) surface was confirmed using hard and soft x-rays and agrees with previous density of states work where the lower end of the valence band is mainly O 2p in character with the higher contribution coming from In 5s orbitals. The different treatments revealed that the work function of indium oxide can be easily modified. This change in the work function is attributed to the movement of the Fermi level as a result of additional free carriers at the surface. The gap states observed in the UPS spectra lowered in intensity when annealing in oxygen suggesting they are related to oxygen vacancies at the surface. This change in carrier concentration at the surface after different treatments is therefore attributed to oxygen vacancies.

References

[1]   R. Baetens, B. P. Jelle, Sol. Ene. Mat. Sol. Cel. 94 (2)(2010) p. 87

[2]   H. Mbarek, M. Saadoun, Physica Status Solidi C 4(2007) p. 1903

[3]   T. Minami, Thin Solid Films, 516(17)(2008) p. 5822

[4]   D. Ginley and C. Bright, MRS Bulletin, 25(2000) p. 15

[5]   P. D. C. King, T. D. Veal, Phys. Rev. Lett. 101(2008) p. 116808

[6]   P. D. C. King, T. D. Veal, Phys. Rev. Lett. 104(2010) p. 256803

[7]   W. Meevasana, P. D. C. King, Nat. Mater. 10 (2011) p.114

[8]   E. Dagotto, Nature, 469 (2011) p. 167

[9]   T. Tomita, K. Yamashita, Appl. Phys. Lett. 87 (2005) p. 051911

[10]   G. Frank and A. Kostlin, Appl. Phys. A 27 (1982) p. 197

[11]   G. B. Gonzalez, T.O. Mason, J. Appl. Phys. 96 (2004) p. 3912

[12]   S. Lany and A. Zunger, Phys. Rev. Lett. 98 (2007) p. 045501

[13]   F. A. Kroger, "The Chemistry of Imperfect Crystals", North-Holland, Amsterdam, (1974) 2nd edition

[14]   J. H. W. de Wit, J. Solid State Chem. 13 (1975) p.192

[15]   A. Ambrosini, G.B Palmer, Chem. Mater. 14 (2002) p. 52

[16]   C. G. van de Walle, Phys. Rev. Lett. 85 (2000) p. 1012

[17]   S. Limpijumnong, P. Reunchan, Phys. Rev. B 80 (2009) p. 193202

[18]   S. Lany A. Zakutayev et al., Phys. Rev. Lett. 108 (2012) p. 016802

[19]   D. Braun Phys. Status Solidi A 211 (2014) p. 59

[20]   K. H. L. Zhang, Chem. Mater. 21 (2009) p. 4353

[21]   A. Walsh, and C. Richard, J. Mater. Chem. 20 (2010) p. 10438

[22]   E. H. Morales and U. Diebold, Appl. Phys. Lett. 95 (2009) p. 253105

[23]   V. Golovanov, M. A. Maki-Jaskari, Sens. Actuators, B 106 (2005) p. 563

[24]   R. F. Minibaev, Nanotechnologies in Russia 5 (2010) p. 185

[25]   K.H.L. Zhang, "Structural and electronic investigations of In_2O_3 Nanostructures and Thin Films grown by MBE", doctoral thesis, 2011

[26]   C. Korber Phys. Rev. B 81 (2010) p. 165207

[27]   J.J. Yeh, I. Lindau, At. Data Nucl. Tables 32 (1985)

[28]   L. F. J. Piper App. Phys. Lett. 94 (2009) p. 022105

[29]   K.H.L. Zhang Phys Rev Lett. 110 (2013) p. 056803

[30]   C.D. Wagner, "Handbook of X-ray photoelectron spectroscopy", Perkin-Elmer Corporation (Physical Electronics) (1979) 1st edition

[31]   J.J. Mudd Physical Review B 89 (2014) p. 035203

[32]   E. Y. Wangand and L. Hsu, J. Electrochem. Soc. 125 (1978) p. 1329

[33]   W. G. Thompson and R. L. Anderson, Solid□-State Electron. 21(1978) p. 603

[34]   A. Klein, Materials 3 (2010) p. 4892

[35]   S.P. Harvey, A. Mason, Appl. Phys. Lett. 92 (2008) p. 252106

[36]   M. G. Mason, J. Appl. Phys. 86 (1999) p. 1688

Chapter 7

Conclusion

The results in this thesis have demonstrated that work function of materials with applications in solar cell technology can be controlled by means of altering the surface structure, by adsorbing materials onto them or by post-growth treatments. The growth mechanism for the single crystals studied can be useful to applied studies looking at more realistic polycrystalline materials, helping obtain better integration of these materials in to a device by reducing interfacial barriers formed upon contacting. One method for reducing this barrier height is to etch the CdTe surface leaving a Te layer. Cu is then deposited onto this Te layer to produce a Cu_xTe alloy. It has been shown that the phase of the Cu_xTe alloy can be controlled by varying the ratio of Cu:Te, these different phases vary in conductivity and stability that can lead to differences in the overall device performance [1]. Interestingly we found the adsorption behaviour of tellurium seemed to be somewhat substrate dependent, with the bulk alloy phase Cu_3Te_2 forming on the (111) surface but not on the (100) surface.

Tellurium deposited on to the (111) surface of copper was found to alloy from very low coverages producing a range of alloyed structure depending on tellurium coverage. For coverages between 0.08 and 0.17ML an ordered $(2\sqrt{3}\times2\sqrt{3})R30°$ structure was observed revealed to be a surface substitutional alloy. For a coverage of 0.33ML an ordered $(\sqrt{3}\times\sqrt{3})R30°$ alloyed structure was observed. LEED IV indicating that at this higher coverage the surface alloy is faulted with respect to the bulk, indicating that the surface alloy flips from the un-faulted to the faulted alloy at this coverage. The LEED IV results also found

that the best agreement between the theoretical model and the experimental data was achieved when using a mix of adsorption geometries. The most favourable mix being a ratio of 40:60 of HCP hollow sites to faulted alloy, this indicates that for the observed coverage the alloying process is not yet complete. For coverages greater than 0.6ML a bulk alloy was formed which closely resembles the Cu_3Te_2 phase of this system. The lattice vectors also agreed with that for the most common Cu_2Te phase however the atomic ratio's extracted from XPS favoured the Cu_3Te_2 phase.

On the Cu(110) surface an ordered c(2×2) structure was found for a coverage of 0.5ML which was imaged with STM. The XPS and LEED data suggests the surface may be alloying as the substrate lattice was found to expand in a similar manner to the (111) surface, however further efforts are needed to confirm this. Additional tellurium saw a compression of this over-layer along the [110] direction as indicated by spot splitting in the LEED. The size of this splitting indicated a coincidence lattice, for example where 5 Te unit meshes is equal to 6 Cu unit meshes. For coverages over 1ML 3d island growth was observed with the STM revealing two co-existing domains of the c(2×2) structure rotated by 30° with respect to each other. The UPS spectra for this coverage revealed a similarity to that reported for the Cu_3Te_2 bulk alloy phase. The LEED pattern for this phase showed hexagonal symmetry consistent with the observed STM images however the rotation of the domains was not detected with LEED. Further experiments on this surface would be to use LEED IV if the surface is alloying, and if so in which adsorption sites does the tellurium sit in. This will then allow a more direct comparison with the (111) surface.

Tellurium deposition on the Cu(100) surface produced a range of structures as the original p(2×2) over-layer becomes more compressed and transitions to a split c(2×2) phase. No change in the substrate lattice was observed as was on the (111) and (110) surface agreeing with previous studies where the Te was found to occupy the four-fold hollow sites for a coverage a 0.25ML and not form a surface alloy [2,3]. The split c(2×2) phase lacks long range order as indicated by the heavy streaking seen in the LEED patterns and the energy range over which they were viewable. These streaks coincided with the emergence of 2 striped domains in the STM, aligned perpendicular to each other. These chains were imaged at various sizes and the larger of these chains suggest a 3d growth mode. These chains are aligned along the [½ ½] direction of the substrate. The complicated growth modes at higher coverage means any further experiments would be difficult to analyse however one suggestion may be to anneal the samples to see if there are any kinetic barriers preventing the alloying process from occurring.

To create a surface alloy a substrate atom must first be removed from the surface, this requires the breaking of bonds. The more highly packed the surface the more energy is required to remove a surface atom, and therefore the easiest surface to alloy should be the (110) surface, then the (100) and finally the (111) surface according to their planar packing fractions of 0.56, 0.79 and 0.91 respectively. Another factor affecting the formation of an alloy is the effect of strain within the produced film. Incorporating a larger atom into the substrate lattice will lead to biaxial strain, if this strain becomes too high then the surface will not be stable. The strain is due to the lattice mismatch between the over-layer structure and the underlying substrate, and so if an alloyed structure has a

similar lattice constant to that of the underlying substrate then that alloyed structure may grow. The lattice constants for the (111) ($\sqrt{3}\times\sqrt{3}$)R30° and the (110) c(2×2) are 4.42Å and 4.40Å respectively, which both are similar to the surface lattice vectors of the most common alloy phase Cu_2Te 4.24Å and of the Cu_3Te_2 phase 4.28Å [4,5]. This lattice constant is also similar to the bulk hexagonal phase of tellurium whose lattice constant is 4.45Å [6]. This may suggest why these surfaces appear to alloy when the (100) surface does not, as the surface lattice vectors for the p(2×2) phase are 5.1Å and it does not posses hexagonal symmetry like the other two structures formed. One reason for the alloy not forming on the (100) surface could be due to strain from incorporating the larger Te atom within the Cu substrate. This 2d expansion of the surface introduces biaxial strain to the layer as seen in several systems such as the surface alloying of silver on Cu(100). In the case of silver adsorption on Cu(100) a surface alloy was found to occur for low coverages, however at higher coverages the biaxial strain is large enough to drive a de-alloying of the silver leading to the growth of islands [7]. Adsorbates can also cause the underlying substrate to facet, for example Te deposited on Pd(100) causes the Pd surface to re-arrange producing (210) facets [8]. From our data were are unable to determine if faceting could be the cause for the different behaviour of the (100) surface.

A similar behaviour has been observed for antimony adsorption on the low index (111) and (100) surfaces of copper. On the (111) surface a ($\sqrt{3}\times\sqrt{3}$) faulted surface alloy was also found while on the (100) surface they found a range of structures depending on annealing conditions with striped domains forming at higher coverages [9,10]. The XPS data also suggests a different behaviour of the

(100) surface where for the heavy deposition the Te $3d_{5/2}$ is similar to that of bulk Te, whereas on the other surfaces the peak position suggests a state of Te^{2-} agreeing with previous data for the alloyed phases. This trend toward the bulk value for the (100) surface as coverage increases could indicate 3d Te growth on the surface as the signal is dominated by Te-Te interactions more so than Te-Cu. The UPS spectra however measured on all 3 samples showed similar features.

The work function of all three surfaces was found to increase upon tellurium deposition with the largest change seen on the (110) surface, from 4.6 to 5.1eV. These changes in the work function are not high enough however to make an ohmic contact to the CdTe, the ideal value using equation 1.11 is 5.95eV. It has been shown however that small changes in the back contact barrier height can affect the fill factor of the overall device, a change of 0.2eV in the barrier height led to a calculated decrease in the fill factor of around 9% [11].

The effect of annealing high quality indium oxide films in two different oxygen environments was investigated using XPS and UPS. A combination of hard XPS and soft XPS allowed different orbitals within the valence band to be highlighted by utilising differences in ionisation cross sections. This confirmed that the valence band closest to the valence band maximum is comprised of mainly oxygen 2p orbitals while the higher portion of the valence band is derived from mainly indium orbitals. Using lab based PES changes to the valence band were observed when annealing the samples in vacuum or in an oxygen rich environment. All 3 of the surfaces studied showed an increase in work function when annealing in oxygen. This is attributed to the excess electrons present at the surface when the samples are annealed in the vacuum, which pushes the Fermi level closer to the vacuum energy level and hence the work function

decreases. One of the criteria for a TCO is that it has a high conductivity, increasing the work function by lowering the carrier density may be detrimental to the operation of the device. It has been shown that the work function of ITO can also modified by the similar post growth treatments to those shown here [12,13]. This ability to modify the carrier concentration in ITO may arise from the defect rich structure of the host In_2O_3 where oxygen vacancies are present both in the bulk and surface regions. No real changes to the shape of the valence band were detected other than those to the gap states. The gap states decrease in intensity when annealing in oxygen and we suggest that they are related to the presence of oxygen vacancies at the surface. This change in the carrier concentration is also noticeable from the shape of the XPS spectra. With a higher surface carrier concentration when annealing in vacuum the peaks are more asymmetric in shape. For all three surfaces we saw a reduction in the population of mid-gap states after annealing in oxygen. These mid-gap states can lower the transparency of TCO's and therefore controlling them is important.

References

[1]   X. Wu, J. Zhou, Thin Solid Films 515 (2007) p. 5798

[2]   Andersson D.E., Andersson S., Surf. Sci. 23 (1970) p. 311

[3]   A. Salwén, J. Rundgren, Surf. Sci. 53 (1975) p. 523

[4]   S. Kashida, W. Shimosaka, M. Mori, J. Phys. Chem. Solids 64 (2003) p. 2357

[5]   M.O. King, Surface Science 606 (2012) p. 1353

[6]   A. A. Opalenko, Z. Z Allam, physica status solidi B 99 (1980) p. K27

[7]   P.T. Sprunger, E. Laesgaard, Phys. Rev. B 54 (1996) p. 8163

[8]   D. Kolthoff, T. Dullweber, Surface Science 447 (2000) p. 259

[9]   D.P. Woodruff, J. Robinson, J. Phys. Condens. Matter 12 (2000) p. 7699

[10]   J. Wu, J. Wei, Journal Physical Chemistry 108 (2004) p. 2773

[11]   S.H. Demtsu, J.R. Sites, Thin Solid Films, 510 (2006) p. 320

[12]   Y. Gassenbauer, A. Klein, Solid State Ionics 173 (2004) p. 141

[13]   Y. Gassenbauer, R. Schafranek, A. Klein, Solid State Ionics 177 (2006) p. 3123